Investigating a role for EDI3 in tumor growth and metastasis in breast cancer using a doxycycline-inducible knockdown system

Dissertation

zur Erlangung des akademischen Grades des Doktors
der Naturwissenschaften (Dr. rer. nat.) an der Fakultät für Chemie und
Chemische Biologie der Technischen Universität Dortmund

Vorgelegt von

Annika Glotzbach (M.Sc.)

Dortmund 2022

1. Gutachter: Prof. Dr. Jan G. Hengstler

2. Gutachter: PD Dr. Leif Dehmelt

Veröffentlicht als Dissertationsschrift zur Erlangung des akademischen Grades des Doktors der Naturwissenschaften (Dr. rer. nat.) an der Fakultät für Chemie und chemische Biologie der TU Dortmund.

Promotionsort und Jahr: Dortmund, 2022

Tag der Disputation: 15.12.2022

Für meine Familie

Table of contents

ABSTRACT ..... **V**

ZUSAMMENFASSUNG ..... **VII**

1 INTRODUCTION **1**

1.1 BREAST CANCER – A HETEROGENOUS DISEASE **1**

1.2 CHOLINE METABOLISM **2**

1.3 GLYCEROPHOSPHOLIPID METABOLISM **4**

1.3.1 Structural membrane glycerophospholipids 4

1.3.2 Signaling lipids 6

1.3.2.1 DAG 6

1.3.2.2 PA 6

1.3.2.3 LPA 7

1.4 METABOLISM IN MALIGNANT TRANSFORMATION **8**

1.5 GLYCEROPHOSPHODIESTERASE EDI3 ..... **9**

1.6 METASTASIS FORMATION **12**

1.6.1 Metastatic organotropism in breast cancer 13

1.7 XENOGRAFT STUDIES IN MICE **14**

1.7.1 Subcutaneous CDX model 15

1.7.2 *In vivo* models for metastasis of blood-born cancer cells 16

1.7.3 *In vivo* model for peritoneal metastasis 16

1.8 NON-INVASIVE *IN VIVO* IMAGING **17**

1.9 AIM OF THE STUDY **19**

2 MATERIALS AND METHODS **21**

2.1 MATERIALS **21**

2.1.1 Technical equipment 21

2.1.2 Consumables 23

2.1.3 Chemicals 24

2.1.4 Commercial buffers, solutions and media 25

2.1.5 Prepared buffers and solutions 26

2.1.6 Commercial assays and kits 28

2.1.7 Cell lines 28

2.1.8 Cell culture medium and additives 29

2.1.9 Lentiviral vectors 30

2.1.10 Plasmids 30

2.1.11 Laboratory mice 30

2.1.12 Antibodies 31

2.2 METHODS 31
2.2.1 Cultivation of cell lines 31
2.2.2 Freezing and thawing of cell lines 32
2.2.3 Antibiotic kill-curve 32
2.2.4 Plasmid DNA transfection via Lipofectamine 3000 33
2.2.5 Inducible inhibition of gene expression via RNA interference 34
2.2.5.1 Transduction of cells with lentiviral particles 35
2.2.5.2 Dox-induction of shRNA mediated inhibition of gene expression 35
2.2.6 Single cell cloning 36
2.2.7 Luciferase assay 37
2.2.8 Cell assays 37
2.2.8.1 Wound closure assay 37
2.2.8.2 Adhesion assay 38
2.2.8.3 Viability assay 38
2.2.8.4 Anoikis assay 39
2.2.8.5 Colony formation assay 40
2.2.8.6 Proliferation assay 40
2.2.9 Housing conditions of mice 41
2.2.10 Doxycycline treatment of mice 41
2.2.11 Cell line-derived xenograft models 41
2.2.11.1 Preparation of cells 42
2.2.11.2 Subcutaneous injection 42
2.2.11.3 Tail vein injection 43
2.2.11.4 Intraperitoneal injection 43
2.2.12 Preparation of luciferin solution for *in vivo* imaging 43
2.2.13 *In vivo* imaging 44
2.2.14 *Ex vivo* imaging 44
2.2.15 Gene expression analysis 45
2.2.15.1 RNA isolation from cell culture 45
2.2.15.2 RNA isolation from tumor tissue 45
2.2.15.3 cDNA synthesis 45
2.2.15.4 Quantitative real-time polymerase chain reaction 46
2.2.16 Protein analysis 47
2.2.16.1 Protein extraction 47
2.2.16.1.1 Protein extraction from cell culture 47
2.2.16.1.2 Protein extraction from tumor tissues 47
2.2.16.2 Protein quantification 47
2.2.16.3 Western Blot 48
2.2.16.3.1 Sodium dodecyl sulfate polyacrylamide gel electrophoresis 48
2.2.16.3.2 Protein transfer on PVDF membrane 49
2.2.16.3.3 Immunodetection 49
2.2.17 Quantification of metabolites 50
2.2.17.1 Metabolite extraction from cell culture 50
2.2.17.2 LC-MS analysis of cell culture extracts 50

2.2.17.3 LC-MS analysis of fractionated cell culture extracts (SIMPLEX) ... 51

2.3 STATISTICAL DATA ANALYSIS ... 52

3 RESULTS ... 53

3.1 GENERATING LUCIFERASE-EXPRESSING CELL LINES FOR *IN VIVO* IMAGING ... 53

3.1.1 Generation of stable luciferase-expressing breast cancer cell lines ... 53

3.1.2 *In vivo* validation of luciferase-expressing breast cancer cell lines ... 54

3.1.3 Luciferase expression remains stable in the absence of antibiotic selection pressure ... 55

3.2 GENERATION OF DOXYCYCLINE-INDUCIBLE SHRNA-EXPRESSING CELL LINES ... 56

3.2.1 Optimization of transduction conditions ... 56

3.2.2 Establishing a doxycycline-inducible EDI3 knockdown in HCC1954_Luc breast cancer cells ... 58

3.3 OPTIMIZATION OF DOXYCYCLINE-INDUCIBLE EDI3 KNOCKDOWN ... 60

3.3.1 Doxycycline induction leads to time and dose dependent reduction in EDI3 expression ... 61

3.3.2 Doxycycline-induced EDI3 knockdown is reversible ... 63

3.4 *IN VITRO* CHARACTERIZATION OF DOXYCYCLINE-INDUCIBLE EDI3 KNOCKDOWN IN HCC1954_LUC CELLS ... 64

3.4.1 Doxycycline-induced EDI3 knockdown alters intracellular GPC/PCho ratio and glycerophospholipid metabolism ... 64

3.4.2 Inducibly silencing EDI3 leads to reduction in colony number and size ... 67

3.4.3 Inducible EDI3 knockdown shows a weak effect on adhesion ... 69

3.4.4 Induction of EDI3 knockdown reduces proliferation ... 71

3.4.5 Doxycycline-induced EDI3 knockdown reduces viability ... 75

3.4.5.1 Induced EDI3 knockdown reduces viability in adherent cells ... 75

3.4.5.2 Doxycycline-induced EDI3 knockdown leads to increased susceptibility to anoikis ... 76

3.4.6 Inducibly silencing EDI3 has no effect on migration ... 77

3.5 INVESTIGATING A ROLE FOR EDI3 IN TUMOR GROWTH AND METASTASIS *IN VIVO* ... 79

3.5.1 Investigating EDI3 in primary tumors ... 79

3.5.1.1 Optimization of growth conditions for subcutaneous tumors in mice ... 79

3.5.1.2 Doxycycline-induced EDI3 knockdown does not reduce primary tumor growth ... 80

3.5.2 Investigating EDI3 in a lung metastasis model ... 83

3.5.2.1 Doxycycline-induced EDI3 knockdown has no influence on early attached cells ... 83

3.5.3 Investigating EDI3 in a peritoneal metastasis model ... 84

3.5.3.1 Peritoneal metastasis formation does not differ between CD1 nude and NSG mice ... 85

3.5.3.2 *In vivo* imaging reveals reduced luminescence signal upon EDI3 knockdown induction ... 86

3.5.3.3 Doxycycline-induced EDI3 knockdown improves survival ... 88

3.5.3.4 Autopsies reveal liver and diaphragm infiltration in the majority of mice ... 89

3.5.3.5 Timed collection of metastases bearing mice reveals metastatic organotropism and lower metastatic burden in EDI3 knockdown condition ... 90

3.5.3.6 Doxycycline-induced EDI3 knockdown is associated with reduced ascites ... 95

4 DISCUSSION ... 97

4.1 ESTABLISHING A DOXYCYCLINE-INDUCIBLE EDI3 KNOCKDOWN SYSTEM IN LUCIFERASE-EXPRESSING HCC1954 CELLS 98

4.2 EDI3 INFLUENCES CHOLINE AND GLYCEROPHOSPHOLIPID METABOLISM 99

4.3 EDI3 INFLUENCES CLONOGENICITY, PROLIFERATION AND VIABILITY 101

4.4 EDI3 IN PRIMARY TUMORS 104

4.5 EDI3 IN METASTASIS FORMATION 105

4.6 FUTURE PERSPECTIVES 107

5 BIBLIOGRAPHY 111

6 APPENDIX 127

6.1 ABBREVIATIONS 127

6.2 LIST OF FIGURES 132

6.3 LIST OF TABLES 134

6.4 PUBLICATIONS 135

6.4.1 Articles 135

6.4.2 Contribution on congresses 135

6.5 EIDESSTATTLICHE VERSICHERUNG (AFFIDAVIT) 137

6.6 ACKNOWLEDGEMENT 139

Abstract

Metastasis remains a major problem for tumor therapy. In endometrial and ovarian cancer, metastasis and worse survival was found to be associated with elevated EDI3 (GPCPD1; GDE5; GDPD6) expression in primary tumors. EDI3 is a glycerophosphodiesterase which cleaves glycerophosphocholine (GPC) to form choline and glycerol-3-phosphate (G3P) and is therefore considered one of the key proteins involved in choline metabolism. Altered choline metabolism is a recognized metabolic hallmark of cancer and was reported in breast, ovarian, and prostate cancers. Previously, *in vitro* studies revealed that silencing EDI3 transiently in various breast cancer cell lines resulted in altered choline metabolism and impaired cellular migration, attachment, and spreading. Recent work showed that EDI3 expression is particularly high in the very specific ER-HER2+ breast cancer subtype, and that silencing EDI3 transiently led to reduced viability in these cells. However, stable constitutive EDI3 knockdown led to compensation of metabolite levels over time, which was accompanied by a loss of the migration phenotype. Therefore, in the present work a doxycycline (Dox) inducible EDI3 knockdown system was established in luciferase-expressing ER-HER2+ breast cancer cells, which reduces compensatory effects and allows to investigate EDI3 in tumor growth and metastasis *in vivo*.

To create cell lines in which EDI3 is inducibly silenced, stable luciferase-expressing HCC1954 and SkBr3 cell lines were first generated and subsequently evaluated *in vitro* and *in vivo* for their luminescence signal intensity and ability to form tumors. HCC1954_Luc cells were chosen for subsequent transduction with lentiviral particles, which resulted in three different Dox-inducible EDI3 knockdown cell lines containing independent EDI3-targeting shRNA oligos. Dox treatment led to a time and dose dependent decrease in EDI3 RNA and protein expression. Mass spectrometry analyses revealed that induced EDI3 knockdown also led to dose dependent alterations in endogenous choline metabolites and phospholipid levels. Using various *in vitro* assays, it could be shown that EDI3 knockdown resulted in significant reduction in colony formation and proliferation, processes which are relevant in the formation of metastasis. Furthermore, EDI3 silencing rendered cells more susceptible towards anoikis. However, Dox-induced EDI3 knockdown had only little effect on adhesion and no effect on migration.

To investigate EDI3's role in tumor growth and metastasis *in vivo*, different tumor models were established in immunodeficient mice. The subcutaneous tumor model showed no significant effect on primary tumor growth. However, in a mouse model for peritoneal metastasis, luminescence imaging revealed lower signals indicative of less metastasis formation in the

EDI3 knockdown condition. Furthermore, it could be shown that silencing EDI3 was associated with reduced tumor burden, less ascites fluid and longer survival time.

Altogether, this thesis provides, for the first time, *in vivo* evidence that supports a role for EDI3 in metastasis formation, which further emphasizes the importance of choline and glycerophospholipid metabolism in this process.

Zusammenfassung

Die Bildung von Metastasen stellt ein großes Problem in der Tumortherapie dar. Bei Endometrium- (Gebärmutter-) und Ovarialkarzinomen (Eierstockkrebs) wurde festgestellt, dass Metastasierung sowie schlechtere Überlebenschancen mit einer erhöhten EDI3 (GPCPD1; GDE5; GDPD6)-Expression in Primärtumoren assoziiert sind. EDI3 ist eine Glycerophosphodiesterase, die Glycerophosphocholin (GPC) zu Cholin und Glycerol-3-phosphat (G3P) spaltet und daher als eines der Schlüsselproteine im Cholinstoffwechsel gilt. Ein veränderter Cholinstoffwechsel ist ein anerkanntes Kennzeichen von Krebserkrankungen und wurde bereits bei Mamma- (Brust-), Ovarial- und Prostatakarzinomen festgestellt. Frühere *in vitro*-Studien zeigten, dass ein transienter EDI3-Knockdown in verschiedenen Brustkrebszelllinien zu einem veränderten Cholinstoffwechsel und einer Beeinträchtigung der Zellmigration, -adhäsion und -ausbreitung führte. In neueren Arbeiten konnte gezeigt werden, dass die EDI3-Expression speziell bei dem ER-HER2+-Brustkrebs-Subtyp erhöht ist und dass ein transienter EDI3-Knockdown zu einer verringerten Lebensfähigkeit in Zellen dieses Typs führte. Ein stabiler konstitutiver EDI3-Knockdown führte jedoch im Laufe der Zeit zu einer Kompensation der Metabolitenspiegel, was mit einem Verlust des Migrationsphänotyps einherging. Daher wurde in der vorliegenden Arbeit ein Doxycyclin (Dox)-induzierbares EDI3-Knockdown-System in Luciferase-exprimierenden ER-HER2+-Brustkrebszellen etabliert, welches kompensatorische Effekte reduziert und es ermöglicht, EDI3s Funktion in Tumorwachstum und Metastasierung *in vivo* zu untersuchen.

Um Zelllinien mit induzierbarem EDI3-Knockdown zu generieren, wurden zunächst stabile Luciferase-exprimierende HCC1954- und SkBr3-Zelllinien hergestellt, die im Anschluss *in vitro* und *in vivo* auf ihre Lumineszenz und ihre Fähigkeit, Tumore zu bilden, untersucht wurden. Für die anschließende Transduktion mit lentiviralen Partikeln wurden dann die HCC1954_Luc-Zellen verwendet. Insgesamt wurden drei verschiedene Dox-induzierbare EDI3-Knockdown-Zelllinien generiert, welche unabhängige EDI3-Targeting shRNA-Oligos enthielten. Die Dox-Behandlung dieser Zelllinien führte zu einer zeit- und dosisabhängigen Abnahme der EDI3 RNA- und Proteinexpression. Massenspektrometrische Analysen ergaben, dass die Induktion des EDI3-Knockdowns ebenfalls zu dosisabhängigen Veränderungen der endogenen Cholinmetaboliten und Phospholipidspiegel führte. Durch verschiedene *in vitro*-Assays konnte gezeigt werden, dass die Verringerung der EDI3-Expression in einer signifikanten Reduktion der Koloniebildung und Zellproliferation resultierte, welches Prozesse sind, die für die Metastasierung relevant sind. Darüber hinaus machte der EDI3-Knockdown

die Zellen anfälliger für Anoikis. Allerdings hatte der Dox-induzierte EDI3-Knockdown nur geringen Einfluss auf die Adhäsion und keine Wirkung auf die Migration der Zellen.

Um EDI3s Funktion in Tumorwachstum und Metastasierung *in vivo* zu untersuchen, wurden verschiedene Tumormodelle in immundefizienten Mäusen etabliert. Dabei zeigte die Reduktion der EDI3-Expression keine signifikante Wirkung auf das Wachstum von subkutanen Primärtumoren. In einem Modell für Peritonealmetastasen ergab die Lumineszenzbildgebung jedoch niedrigere Signale bei induziertem EDI3-Knockdown, was auf eine geringere Metastasierung hindeutet. Darüber hinaus konnte in diesem Modell gezeigt werden, dass die Reduktion der EDI3-Expression mit einer geringeren Tumorlast, weniger Aszitesflüssigkeit und einer längeren Überlebenszeit assoziiert war.

Insgesamt liefert diese Dissertation zum ersten Mal Hinweise aus *in vivo*-Experimenten, die eine Rolle für EDI3 bei der Metastasenbildung unterstützen, was wiederum die Bedeutung des Cholin- und Glycerophospholipid-Metabolismus in diesem Prozess weiter unterstreicht.

1 Introduction

1.1 Breast cancer – a heterogenous disease

Breast cancer is by far the most common cancer type among women with around 69,000 new cases diagnosed in Germany each year. Although advances in therapy have significantly improved the chances of survival, in Germany more than 18,000 women die from breast cancer per year (Robert Koch Institut, 2020). It is a highly heterogenous disease and prognosis as well as treatment options strongly depend on the stage at diagnosis and the molecular subtype of the tumor (Blows et al., 2010; Hennigs et al., 2016; Howlader et al., 2018). Based on the analysis of estrogen receptor (ER), progesterone receptor (PR) and human epidermal growth factor receptor 2 (HER2/Neu) status, as well as the expression of the proliferation marker Ki-67, which can be determined by immunohistochemistry (IHC) or gene expression profiling, breast cancer tumors can be classified into different molecular subtypes (Goldhirsch et al., 2011; Perou et al., 2000). In Figure 1.1 the four main intrinsic subtypes luminal A, luminal B, HER2-positive (HER2+) and basal-like with their specific hormone- and HER2 receptor status are presented and correlated with their prognostic outcome.

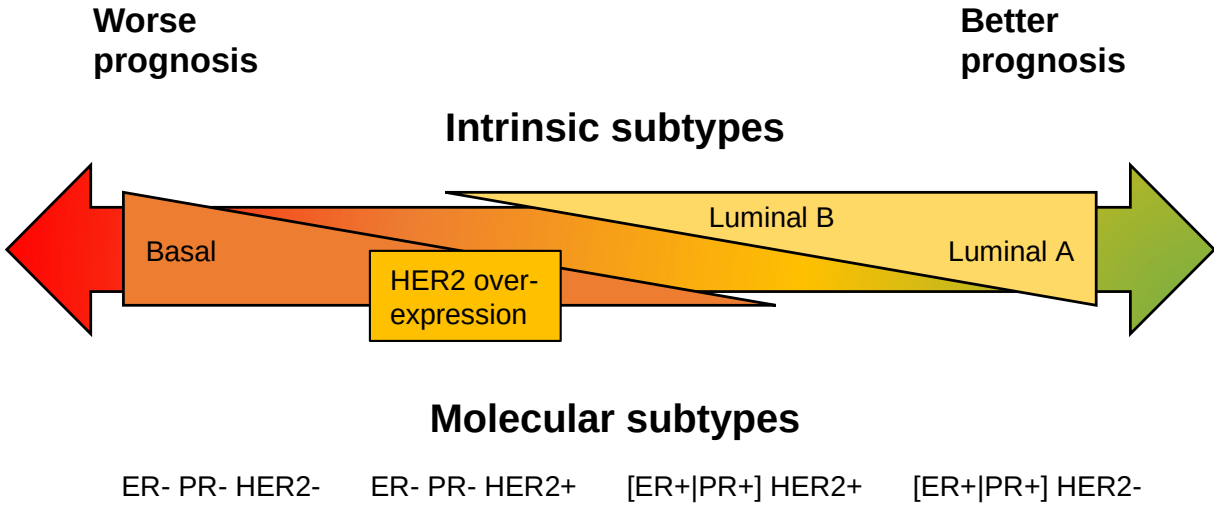

Figure 1.1: Breast cancer subtypes and their prognostic outcome (adapted from Dai et al., 2015).

The different subtypes of breast cancer originate from distinct cell types of the mammary epithelium, which consists of an inner layer of luminal epithelial and an outer layer of myoepithelial cells in direct contact with the basement membrane (Cristea & Polyak, 2018). Luminal tumors, categorized as luminal A and B, develop from epithelial cells that line the ducts and glands and are the most common subtypes, with luminal A occurring more often than luminal B (Blows et al., 2010; Fallahpour et al., 2017). Both subtypes are positive for ER or PR expression but differ in their HER2 receptor status. Luminal A tumors do not express the HER2

receptor, while luminal B tumors may be positive for HER2 receptor expression (Cheang et al., 2009; Vallejos et al., 2010). The prognosis for luminal tumors is generally good, although the prognosis for the luminal B subtype, which has a higher expression of proliferative genes, is significantly worse than that for luminal A tumors (Dai et al., 2015; Sørlie et al., 2003).

The HER2-positive subtype is characterized by high expression of HER2 and a common set of HER2-regulated genes, while the majority of these tumors is negative for PR and ER (Skibinski & Kuperwasser, 2015). HER2-expressing tumors can be targeted directly by therapy with anti-HER2 monoclonal antibody, trastuzumab, or dual tyrosine kinase inhibitor, lapatinib, which interrupts the HER2/Neu and epidermal growth factor receptor (EGFR) pathways (Higa & Abraham, 2007; Tai et al., 2010). However, most HER2 overexpressing tumors acquire or possess intrinsic mechanisms of resistance that allow escape from HER2 inhibition which leads to relapse and poor prognosis (Rexer & Arteaga, 2012). Therefore, this subtype would benefit from improvements in therapy, and by using additional targets in combined strategies to improve clinical outcome in the future (Dai et al., 2015).

The expression profile of the basal subtype resembles that of basal epithelial cells, which includes lacking or low expression of ER, PR and HER2 (triple negative), and high expression of basal markers and proliferation related genes (Perou et al., 2000). These aggressive tumors tend to grow rapidly and are associated with lower survival and high risk of relapse (Ho-Yen et al., 2012). Due to their triple negative receptor status, basal tumors do not respond to conventional targeted breast cancer therapies, which leaves chemotherapy the only option for treatment (Brenton et al., 2005).

1.2 Choline metabolism

Choline is an essential nutrient that plays a central role in many physiological pathways, including neurotransmitter synthesis, methyl-group metabolism, and lipid transport. As a precursor for several types of phospholipids, it is required for maintaining the structural integrity and signaling function of cellular membranes (Penry & Manore, 2008). In most tissues, up to 95% of choline is synthesized to phosphatidylcholine (PtdCho), the most abundant phospholipid in the cell membrane (Gibellini & Smith, 2010; van der Veen et al., 2017). The *de novo* biosynthesis of PtdCho happens via the CDP-choline pathway, also called the Kennedy pathway (Kennedy & Weiss, 1956), which consists of three enzymatic steps (Figure 1.2).

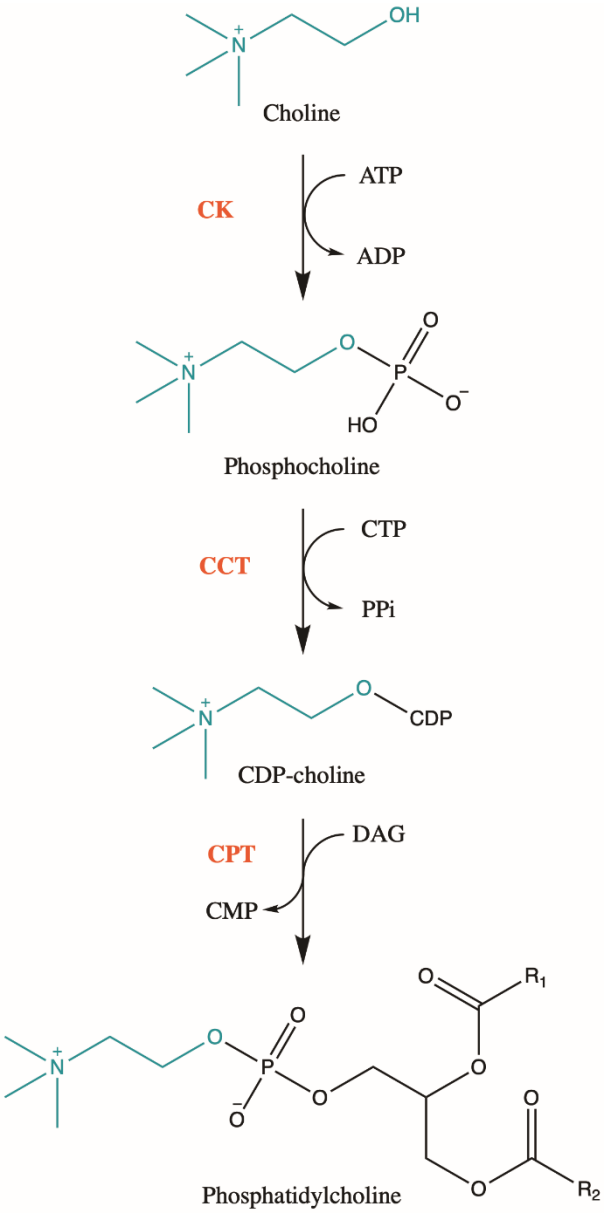

Figure 1.2: PtdCho *de novo* biosynthesis via the Kennedy pathway. Choline kinase (CK) phosphorylates choline to phosphocholine and CTP:phosphocholine cytidylyltransferase (CCT) converts phosphocholine to CDP-choline. CDP-choline and DAG are condensed by CDP-choline:DAG cholinephosphotransferase (CPT) to form phosphatidylcholine (PtdCho). ATP, adenosine triphosphate; ADP, adenosine diphosphate; CTP, cytidine triphosphate; CDP, cytidine diphosphate; PPi, pyrophosphate; DAG, diacylglycerol; CMP, cytidine monophosphate.

Choline is also present in the extracellular environment from where it can be transported into the cell via one of the three classes of choline transporters - the high-affinity transporter (CHT1), the intermediate-affinity transporters (CTL family) and the low-affinity organic cation transporters (OCT family). Once inside the cell, it is rapidly phosphorylated via choline kinase (CK) in an adenosine triphosphate (ATP)-dependent reaction forming phosphocholine (PCho) (Traiffort et al., 2013). CK is encoded by two distinct genes (*CHKA* and *CHKB*), that express choline kinases alpha and beta, respectively. In a second step, the cytidine-5'-triphosphate (CTP):phosphocholine cytidylyltransferase (CCT) uses PCho and CTP to form cytidine-5'-

diphosphocholine (CDP-choline), which is the rate-determining reaction in this pathway. The final step is catalyzed by the integral membrane protein CDP-choline:1,2-diacylglycerol cholinephosphotransferase (CPT), which transfers PCho from CDP-choline to diacylglycerol (DAG) to form PtdCho. For the synthesis of phosphatidylethanolamine (PE), the second most abundant phospholipid in cellular membranes, the analogous CDP-ethanolamine pathway is used, which involves ethanolamine instead of choline (Van der Veen et al., 2017; Gibellini and Smith, 2010).

Choline and choline metabolites can be restored by the controlled breakdown of PtdCho, which at the same time leads to the generation of several phospholipids that function as important signaling molecules and are described in more detail in chapter 1.3.2.

1.3 Glycerophospholipid metabolism

Phospholipids consist of a polar head group that is linked to two long-chain fatty acyl moieties and form the phospholipid bilayer that defines the permeability barrier of cells and organelles (Dowhan, 1997). Mammalian cell membranes contain different classes of phospholipids, of which the most abundant is PtdCho. Other important membrane constituents include PE, phosphatidylserine (PS), and sphingomyelin (SM). Besides phospholipids the mammalian cell membranes also contain other lipids, such as cholesterol and glycosphingolipids (Vance, 2015). The lipid composition defines the biology of the membrane, as phospholipids simultaneously serve as second messenger molecules, receptors for the recruitment of proteins to the membrane, chaperones to aid in protein folding, and direct modulators of protein function (McMaster, 2018).

1.3.1 Structural membrane glycerophospholipids

Phospholipids that are derivates of glycerol are called glycerophospholipids. Depending on their polar headgroup, different classes of glycerophospholipids exist, such as PtdCho, phosphatidylethanolamine (PE), phosphatidic acid (PA), phosphatidylserine (PS), phosphatidylglycerol (PG) and phosphatidylinositol (PI) (Huang & Freter, 2015). The general structure of glycerophospholipids as well as the main polar headgroups are presented in Figure 1.3A. The fatty acid composition of glycerophospholipids differs between cell types and tissues (MacDonald & Sprecher, 1991; Wood & Harlow, 1969; Yamashita et al., 1997). Fatty acids vary in chain length, level of unsaturation (double bond number) and double bond position (Figure 1.3B). Furthermore, the different combinations of the two fatty acids create the chemical diversity of glycerophospholipids (Harayama & Riezman, 2018).

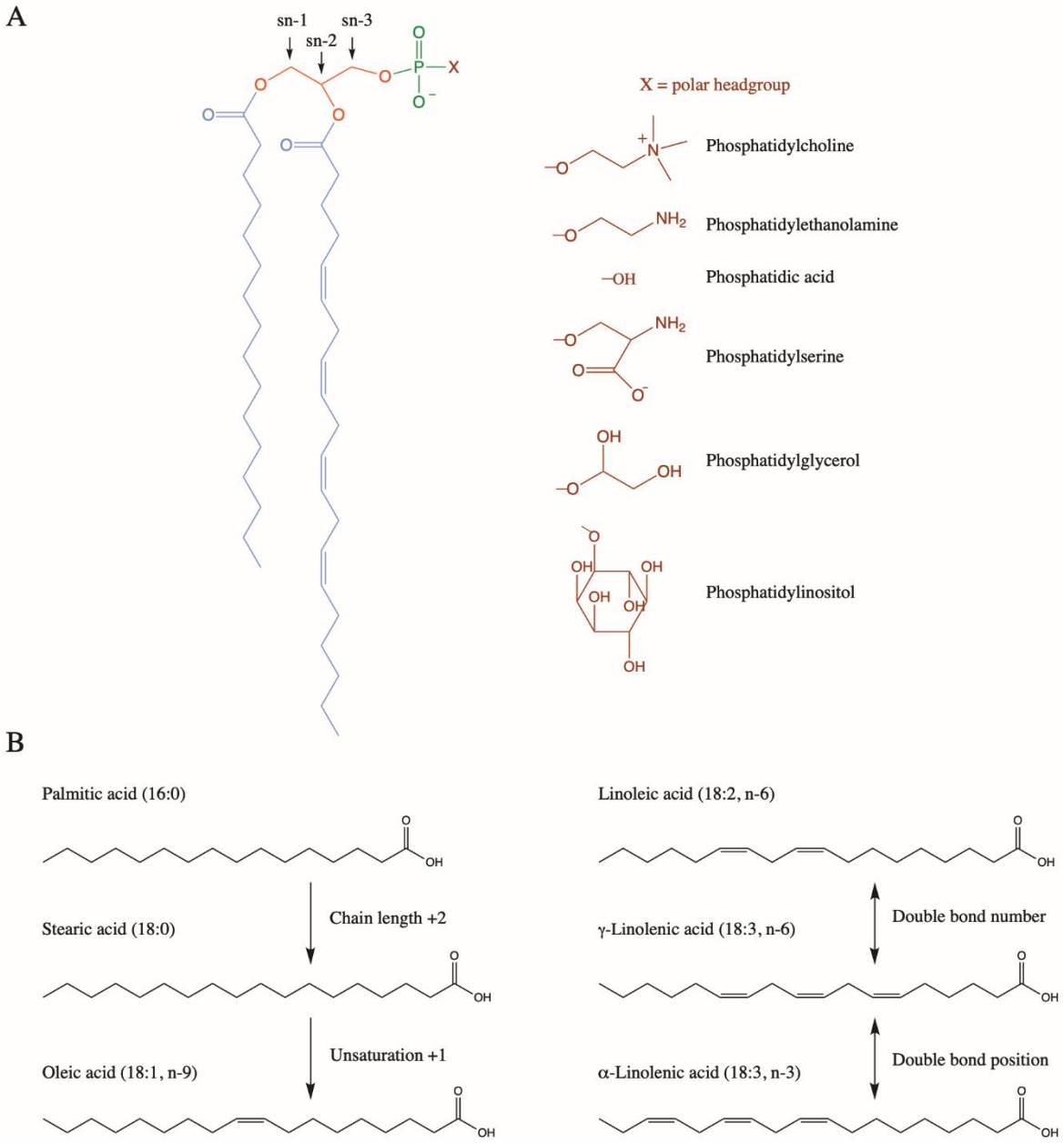

Figure 1.3: Glycerophospholipid structure. A) Fatty acids (blue) are linked to the glycerol backbone (red) at the sn-1 and sn-2 positions while the phosphate headgroup (green) is linked at the sn-3 position. Different variations of polar headgroups (brown) are presented. B) Fatty acids vary in chain length, level of unsaturation and the position of double bonds, illustrated as (XX:Y, n-Z), where XX represents the number of carbon atoms in the chain, Y denotes the number of double bonds and Z indicates the position of the first double bond from the omega end (modified from Harayama & Riezman, 2018).

De novo synthesis of glycerophospholipids by the Kennedy pathway (as described in chapter 1.2) results in formation of phospholipids with saturated and monounsaturated fatty acyl groups (Murphy & Folco, 2019). In order to establish diversity and asymmetry each of these phospholipid classes can be remodeled in the so-called Lands cycle, which consists of two enzymatic reactions (indicated in blue in Figure 1.4). First, phospholipase A (PLA) removes the fatty acyl group from the sn-2 position, which results in the formation of lysophospholipids. Subsequently, another fatty acyl group is covalently bound to the sn-2 position by

lysophospholipid acyltransferases (LPLATs) (Eto et al., 2012; Murphy & Folco, 2019). Remodeling of fatty acid composition was reported to be associated with alterations in cell biology (Harayama & Riezman, 2018; Simons & Toomre, 2000).

1.3.2 Signaling lipids

Glycerophospholipids are not only important for the structure and function of biological membranes but also serve as precursors of lipid mediators, such as DAG, PA and lysophosphatidic acid (LPA), that regulate multiple signaling pathways (Andresen et al., 2002; Momoi et al., 2020; Moolenaar et al., 2004; Turban & Hajduch, 2011). The metabolism of glycerophospholipids, including the production of signaling lipids, is presented in Figure 1.4.

1.3.2.1 DAG

DAG is produced from glycerophospholipids such as PtdCho either directly by phospholipase C (PLC) or by phospholipase D (PLD)-mediated hydrolyzation followed by dephosphorylation of the generated PA by phosphatidate phosphatase (PAP) or lipid phosphate phosphatases (LPPs) (Carrasco & Mérida, 2007; Dey et al., 2020; Han & Carman, 2010). It acts as a second messenger signaling lipid, which leads to activation of protein kinase C (PKC) which is in turn important for various signaling pathways, including cell proliferation and adhesion (Coleman & Lee, 2004; Turban & Hajduch, 2011). Impaired production or consumption of DAG have strong effects on cell growth and are associated with cancer (Carrasco & Mérida, 2007). DAG can be metabolized into triacylglycerol **(**TAG**)** by diacylglycerol acyltransferases (DAGATs) linking it to the *de novo* formation of lipid droplets (Coleman & Lee, 2004; Sonkar et al., 2019).

1.3.2.2 PA

Phosphorylation of DAG by diacylglycerol kinases (DAGKs) results in the production of PA, another lipid second messenger that affects cellular processes such as migration, adhesion, survival, proliferation, and membrane remodeling (Bruntz et al., 2014; Carrasco & Mérida, 2007; Chae et al., 2008; Momoi et al., 2020). Another important reaction that produces PA is the already mentioned hydrolysis of glycerophospholipids like PtdCho by PLD which results in the release of the head groups, e.g. choline. It has been shown that PA interacts with various proteins (Bruntz et al., 2014). Previous studies indicate that PA plays a critical role in regulating the activity of some members of Ras superfamily of small guanosine triphosphatases (GTPases), such as Ras, Rac and Arf by modulating membrane localization and activity of regulatory proteins as well as by directly binding small GTPases to the membrane (Y. Zhang & Du, 2009). Furthermore, it was shown that PA is involved in regulating the mTOR-mediated signals that promote cancer cell survival (Foster, 2009; C.-Y. Yang & Frohman, 2012).

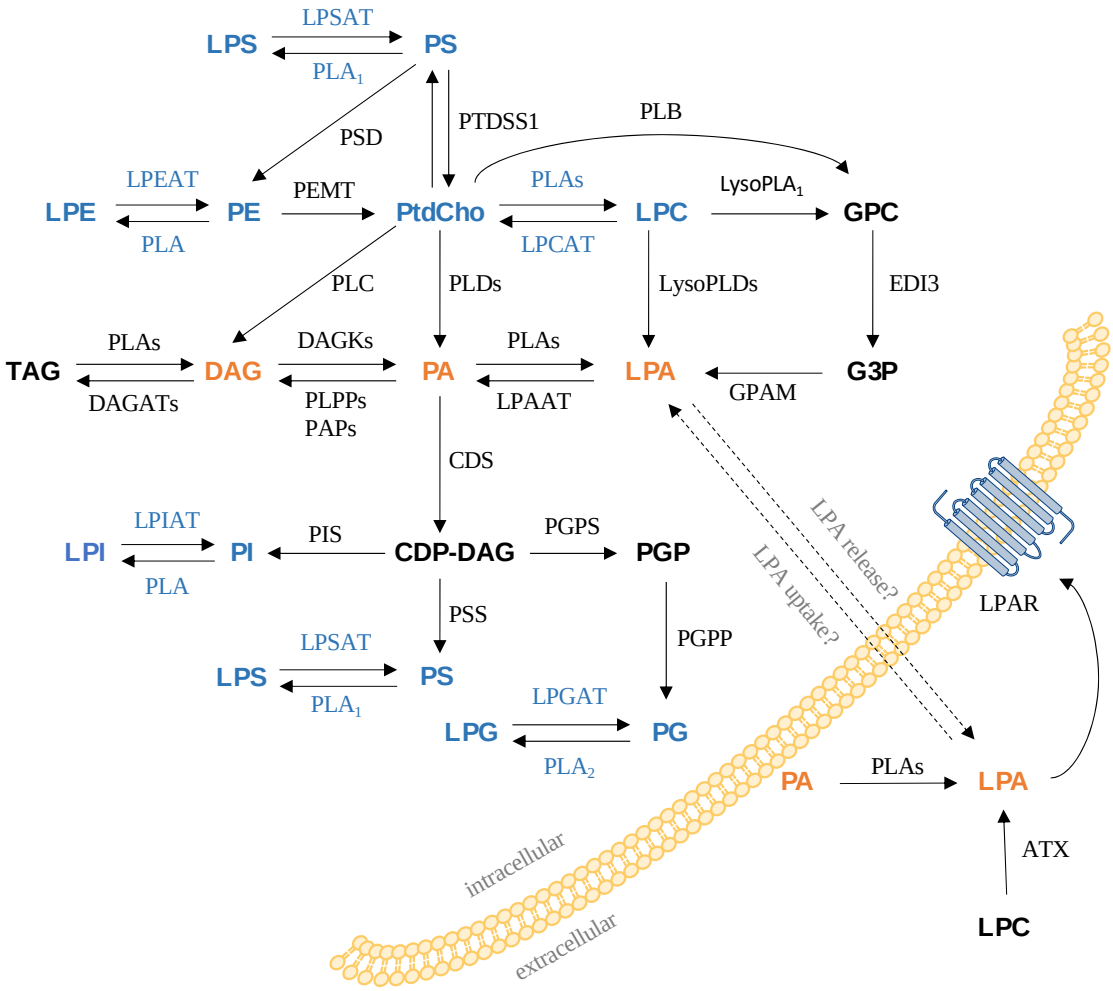

Figure 1.4: Schematic illustration showing the metabolism of glycerophospholipids. Overview of the glycerophospholipid metabolic pathways focusing on the Lands cycle for remodeling of the structural membrane lipids (blue) and the major signaling lipids (orange). LPS, lysophosphatidylserine; LPSAT, lysophosphatidylserine acyltransferase; PLA, phospholipase A; PS, phosphatidylserine; PSD, phosphatidylserine decarboxylase; PE, phosphatidylethanolamine; LPEAT, lysophosphatidylethanolamine acyltransferase; LPE, lysophosphatidylethanolamine; PEMT, phosphatidylethanolamine N-methyltransferase; PtdCho, phosphatidylcholine; LPCAT, lysophosphatidylcholine acyltransferase; LPC, lysophosphatidylcholine; PLB, phospholipase B; GPC, glycerophosphocholine; EDI3, endometrial differential 3; G3P, glycerol-3-phosphate; PLD, phospholipase D; GPAM, glycerol-3-phosphate acyltransferase; LPA, lysophosphatidic acid; LPAAT, lysophosphatidic acid acyltransferases; PA, phosphatidic acid; DAGK, diacylglycerol kinase; PLPP, phospholipid phosphatase; PAP, phosphatidate phosphatase; DAG, diacylglycerol; DAGAT, diacylglycerol acyltransferase; TAG, triacylglycerol; CDP-DAG, cytidine diphosphate diacylglycerol; CDS, CDP-diacylglycerol synthase; PIS, phosphatidylinositol synthase; PI, phosphatidylinositol; LPIAT, lysophosphatidylinositol acyltransferase; LPI, lysophosphatidylinositol; PGPS, phosphatidylglycerol phosphate synthase; PGP, phosphatidylglycerol phosphate; PGPP, phosphatidylglycerol phosphate phosphatase; PG, phosphatidylglycerol; LPGAT, lysophosphatidylglycerol acytransferase; LPG, lysophosphatidylglycerol; ATX, autotaxin; LPAR, lysophosphatidic acid receptor.

1.3.2.3 LPA

Deacylation of PA by PLA results in the formation of LPA, another important signaling lipid (Pagès et al., 2001). LPA can also be converted back to PA by lysophosphatidic acid

acyltransferases (LPAATs) (Yung et al., 2014; Zhukovsky et al., 2019). The main route for LPA production is via the hydrolyzation of glycerophospholipids, such as PtdCho by PLAs, which results in the formation of their corresponding lysophospholipids such as lysophosphatidylcholine (LPC). LPC can subsequently be converted to LPA by lysophospholipase D (lysoPLD) activity (Aikawa et al., 2015; Stack & Fishman, 2012; Yung et al., 2014). Alternatively, LPC can be converted by lysoPLA activity to GPC, which can be hydrolyzed by the glycerophosphodiesterase endometrial differential 3 (EDI3) to form glycerol-3-phosphate (G3P). Subsequent acylation of G3P produces LPA (Sonkar et al., 2019; Stewart et al., 2012).

Most studies thus far have focused on the role of extracellular LPA, which is produced by the secreted exo-enzyme autotaxin (AXT), also called ecto-nucleotide pyrophosphatase/phosphodiesterase-2 (ENPP-2) (Law et al., 2019; Nakamura et al., 2007). Extracellular LPA can bind and signal through six LPA-associated G protein-coupled receptors (GPCRs), lysophosphatidic acid receptor (LPAR) 1–6 and other GPCRs (such as P2Y10 and GRP87) (Choi et al., 2010; Geraldo et al., 2021; Knowlden & Georas, 2014). It was shown that LPA induces several cellular responses, such as proliferation, migration, and cytoskeletal reorganization (Geraldo et al., 2021; Moolenaar et al., 2004). LPA treatment of various cancer cell lines was found to stimulate the expression and release of angiogenic factor IL-8 (Hisano & Hla, 2019). Furthermore, by expressing either ATX or LPARs in the mammary epithelium of transgenic mice, Liu and colleagues demonstrated that the ATX-LPAR axis plays a causal role in breast tumorigenesis, invasion and metastasis (S. Liu et al., 2009).

Intracellular LPA on the other hand has been barely investigated. However, Marchan and colleagues could show that transfection of a breast cancer cell line with 18:1-LPA resulted in a 40-fold increase of intracellular LPA levels and had a positive effect on migration. These findings provided strong evidence that intracellular LPA is also an important factor in cellular migration (Marchan et al., 2017). Whether there is an exchange between the intracellular and extracellular LPA pools is still unknown.

1.4 Metabolism in malignant transformation

Changes to the metabolome that occur during cellular transformation and tumorigenesis are a recognized hall mark of cancer (Hanahan & Weinberg, 2011; Schulze & Harris, 2012). Altered choline metabolism, characterized by elevated levels of PCho and total choline (tCho), was found to be associated with oncogenesis and tumor progression in various cancer types, including breast cancer (Glunde et al., 2015; Mori et al., 2016; Sonkar et al., 2019).

Furthermore, high PCho levels have been associated with worse prognosis and decreased survival in breast carcinomas (Glunde et al., 2011). Changes in tCho and PCho can be detected non-invasively in patients by magnetic resonance spectroscopy (MRS) or positron emission tomography (PET) and are both helpful tools for diagnosis, prognosis, and monitoring of treatment responses (Glunde et al., 2011). In breast cancer, elevated PCho levels are accompanied by a decrease in GPC, which results in a decreased GPC/PCho ratio compared with normal tissue (Aboagye & Bhujwalla, 1999).

One of the most well-established molecular causes for the observed alterations in choline metabolism is the elevation of choline uptake by choline transporters (Eliyahu et al., 2007; Katz-Brull & Degani, 1996). Furthermore, several enzymes involved in choline metabolism have been identified to be overexpressed and/or activated in cancer cells and thereby contribute to the observed changes in metabolites. Among these are CHKA (Glunde et al., 2005; Ramírez de Molina et al., 2002), which phosphorylates choline to form PCho, PLD1 (Gadiya et al., 2014; Noh et al., 2000) that produces PA and choline by the hydrolysis of PtdCho, and EDI3 (GPCPD1; GDE5; GDPD6).

1.5 Glycerophosphodiesterase EDI3

EDI3, also known as glycerophosphocholine phosphodiesterase 1 (GPCPD1), is a glycerophosphodiesterase that hydrolyses GPC to produce choline and G3P (Figure 1.5) and is therefore considered a key enzyme linking phospholipid metabolism with choline metabolism (Stewart et al., 2012).

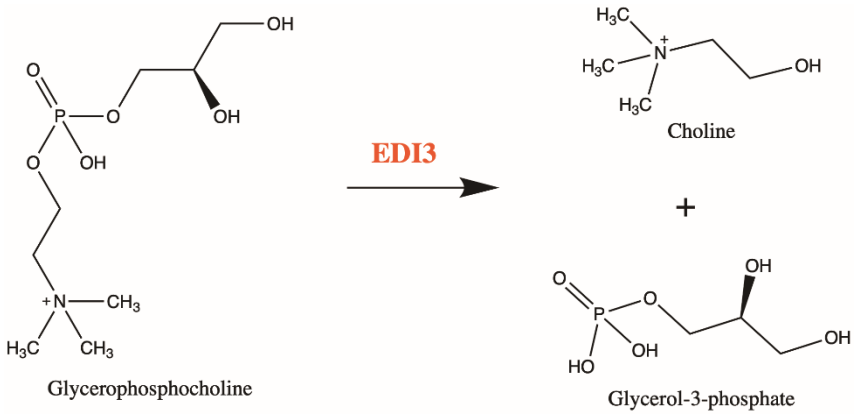

Figure 1.5: Reaction mechanism catalyzed by the glycerophosphodiesterase EDI3. Hydrolysis of glycerophosphocholine (GPC) results in choline as a substrate for the Kennedy pathway and glycerol-3-phosphate for glycerophospholipid synthesis.

It is a member of the mammalian glycerophosphodiesterase phosphodiesterase (GDE-PDE) family, of which so far seven members (GDE1-7) have been identified (Ohshima et al., 2015). Among these, EDI3 is the only one that does not contain a transmembrane membrane but is

localized to the cytoplasm instead. Besides EDI3, also another member of the family, GDE2, produces choline and G3P via GPC hydrolysis in the Kennedy pathway. Most of the work on GDE2 has focused on its role in motor neuron differentiation and regulating osmolarity in the kidney (Okazaki et al., 2010; Yanaka, 2007).

EDI3 was initially identified in a screen comparing non-metastasizing and metastasizing endometrial carcinomas, where EDI3 was found to be highly expressed in metastasizing primary tumors. Furthermore, it could be shown that high EDI3 expression was associated with worse prognosis in endometrial and ovarian cancer (Stewart et al., 2012). Subsequent phenotypic studies that were conducted in different cancer cell lines after altering EDI3 expression revealed that EDI3 positively influences cell migration, adhesion, and spreading, processes that are important in cancer and metastasis formation. Further analyses suggested that EDI3 expression is associated with PKCα signaling pathway and integrin β1 (Lesjak et al., 2014; Stewart et al., 2012). However, the exact mechanism how EDI3 influences these processes remained unknown.

Mass spectrometric analysis revealed that transiently silencing EDI3 in different cancer cell lines resulted in an increase in endogenous GPC accompanied by a decrease in choline and PCho levels, thereby correcting the low GPC/PCho ratio observed in various tumors and transformed cells. Furthermore, it was shown that EDI3 knockdown led to a decrease in the major membrane phospholipid PtdCho, as well as in the signaling lipids PA and LPA (Stewart et al., 2012). Interestingly, PtdCho synthesis via the Kennedy pathway is required for the formation of cellular membrane during tumor growth and PA and LPA are involved in different cellular processes, including migration, and are both known to be involved in cellular transformation and various cancer types (Foster, 2009; McMaster, 2018; Mills & Moolenaar, 2003). PA and LPA can be produced by several pathways (as described in more detail in chapter 1.3.2), for example by the acylation of EDI3's product G3P to LPA, which can subsequently be converted to PA by a second acylation step. It was also shown that the enzyme responsible for acylation of G3P, glycerol-3-phosphate acyltransferase (GPAM), as well as its product LPA are important for EDI3's role in migration (Marchan et al., 2017).

As illustrated in Figure 1.6, via its downstream metabolites EDI3 is linked to various cellular pathways, such as the production of structural and signaling phospholipids, triglyceride synthesis, the G3P shuttle, glycolysis, and the methylation cycle (Marchan et al., 2017).

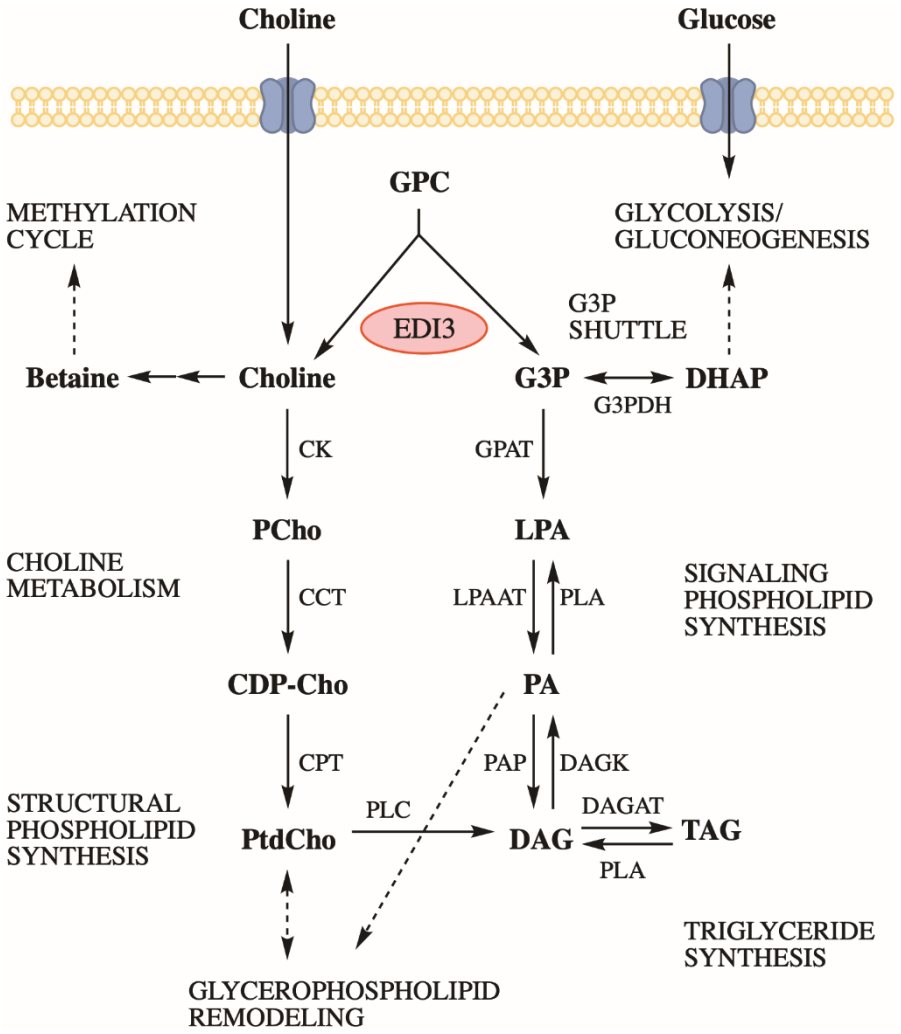

Figure 1.6: A role for EDI3 as a key enzyme linking different metabolic pathways. Via its downstream metabolites EDI3 is linked to various cellular pathways, such as choline metabolism, methylation cycle, synthesis of signaling and structural phospholipids, glycerophospholipid remodeling, triglyceride synthesis, G3P shuttle, glycolysis, and gluconeogenesis. GPC, glycerophosphocholine; EDI3, endometrial differential 3; CK, choline kinase; PCho, phosphocholine; CCT, CTP:phosphocholine cytidylyltransferase; CDP-choline, cytidine diphosphate-choline; CPT, CDP-choline:DAG cholinephosphotransferase; PtdCho, phosphatidylcholine; PLC, phospholipase C; DAG, diacylglycerol; DAGAT, DAG acyltransferase; DAGK, DAG kinase; TAG, triacylglycerol; PLA, phospholipase A; PA, phosphatidic acid; PAP, phosphatidate phosphatase; LPA, lysophosphatidic acid; LPAAT, lysophosphatidic acid acyltransferase; G3P, glycerol-3-phosphate; GPAT, G3P acyltransferase; G3PDH, G3P dehydrogenase; DHAP, dihydroxyacetone phosphate.

Due to its involvement in these different metabolic pathways and its association with several cancer and metastasis related processes, EDI3 is considered a potential target for cancer treatment. Consistently, a recent study could show that EDI3 levels are especially high in ER-HER2+ breast cancer tumors and cell lines and that altering HER2 expression, as well as pharmacological inhibition of HER2 in these cells indicated that EDI3 is regulated by HER2 signaling (Keller et al., in revision). Furthermore, inhibition of EDI3 in these cells led to a significant reduction in viability and tumor growth, suggesting EDI3 as a potential therapeutic target in tumors of this specific molecular subtype (Keller et al., in revision).

1.6 Metastasis formation

Despite early detection and advances in therapy that have significantly improved the chances of surviving breast cancer, metastasis from primary tumor remains a major cause of death among patients (Jin et al., 2018; Robert Koch Institut, 2020). In fact, approximately 20-30% of patients with early breast cancer eventually develop recurrent advanced or metastatic disease and 90% of cancer-related deaths can be attributed to metastasis (Lao et al., 2021; Liang et al., 2020).

To date, it is not fully understood when and how metastasis spread, but two models are widely acknowledged: The linear progression model states that cells in the primary tumor undergo a process of successive mutation and selection, and that the development of metastasis occurs relatively late at a point when cancer cells have acquired the mutational changes needed for survival and growth at distant sites (Craig et al., 2013; Navin & Hicks, 2010; Sims et al., 2006). On the other hand, according to the parallel progression model, tumor cells are supposed to acquire the necessary mutations very soon and metastases occur already at early stages so that both primary tumor and metastases progress in parallel (Nguyen et al., 2009; Paget, 1989).

Formation of metastasis is a multistep process initiated by the epithelial-to-mesenchymal transition (EMT) which is characterized by loss of epithelial characteristics accompanied by the gain of mesenchymal markers resulting in enhanced mobility and invasiveness of the cell (Christofori, 2006; Thiery et al., 2009). Important steps of metastasis formation are illustrated in Figure 1.7. They involve local invasion of tumor cells into the adjacent tissue, intravasation into the blood or lymphatic vessels, survival in the circulatory system as disseminated cells by resisting anoikis, followed by extravasation at a secondary site where they revert to epithelial cell phenotype by a phenomenon called mesenchymal-epithelial transition (MET) and colonize to proliferate into secondary tumors (Liang et al., 2020, p. 20; Yeeravalli & Das, 2021). Consequently, important qualities that cancer cells need for survival and growth at distant sites involve resistance towards anoikis, clonogenicity, and the ability to proliferate.

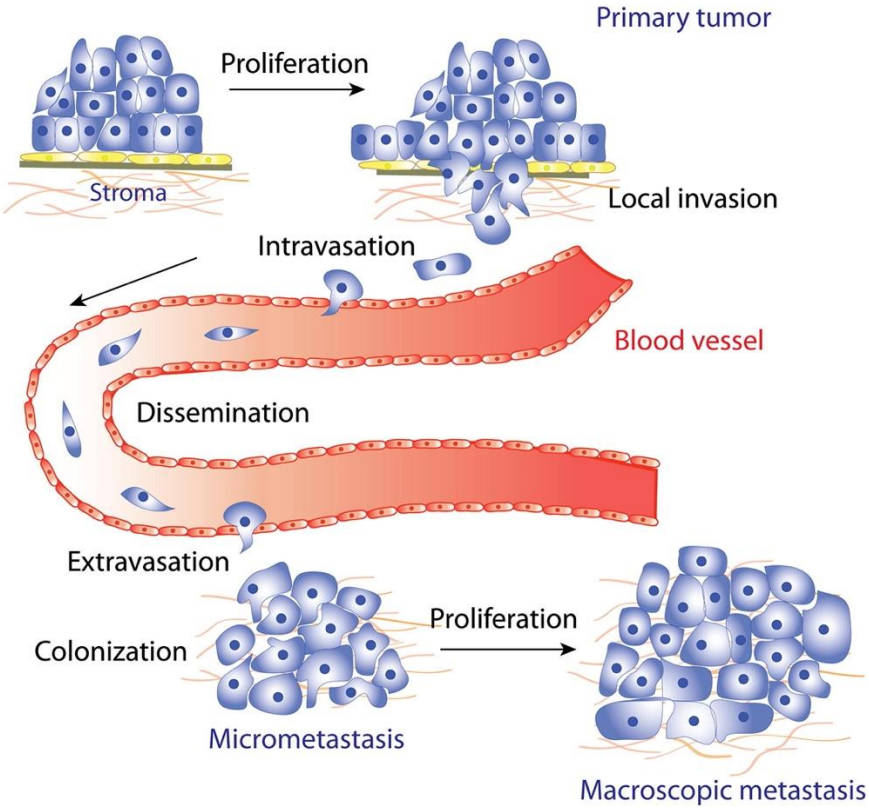

Figure 1.7: Schematic illustration of the multiple steps required for metastasis formation. Cancer cells from the primary tumor invade local tissue, disseminate into the blood stream followed by extravasation at a distant secondary site and colonization of a distant organ (Saxena and Christofori, 2013).

1.6.1 Metastatic organotropism in breast cancer

The seed and soil hypothesis postulates that metastatic tumor cells ("seed") will metastasize to a site where the local microenvironment ("soil") is favorable (Paget, 1989). In most cases distant metastases affect more than one site. The most common metastatic target sites for breast cancer, in order of frequency, have been described as bones (67.8%), liver (47.8%), lungs (42.6%) and brain (15.2%). Additionally, to a smaller extend, metastasis have been found in several other secondary sites, including the peritoneal cavity (7.6%) (Bertozzi et al., 2015).

Interestingly, different breast cancer subtypes show preference to certain organs. Luminal breast cancer preferably spreads to the bone (Kennecke et al., 2010) while basal-like tumors are reported to metastasize most often to the lungs and the brain (Luck et al., 2008; Wu et al., 2017). The ER−/PR−/HER2+ subtype is most prone to develop metastasis in brain and liver (Gong et al., 2017; Wu et al., 2017). So far, no such correlation has been reported regarding the prevalence of peritoneal metastasis. In fact, for long time peritoneal metastasis occurring from breast cancer was rarely mentioned in the literature. Metastases in the peritoneal cavity usually affect patients suffering intra-abdominal cancers originating from the gastrointestinal tract or

the female reproductive system (Flanagan et al., 2018). However, a recent study conducted by Flanagan and colleagues revealed that extra-abdominal cancers account for approximately 10% of diagnosed cases of peritoneal metastases. Furthermore, they could show that primary breast cancer is the most common extra-abdominal malignancy responsible for the development of peritoneal metastasis (40.8% of cases) (Flanagan et al., 2018). Metastases in the peritoneal cavity develop at late stages of breast cancer, usually several years after the first diagnosis, and therefore later than most non-peritoneal metastasis (Flanagan et al., 2018; Tuthill et al., 2009). They can lead to malignant ascites, the pathological accumulation of excessive fluid within the peritoneum.

The prognosis for breast cancer patients differs remarkably dependent on the location of metastasis. Brain and peritoneal metastases are associated with extremely poor survival that ranges from 2-25.3 months and 0.2-27 months, respectively, from the time of diagnosis (Flanagan et al., 2018; Leone & Leone, 2015; Tuthill et al., 2009). The five-year overall survival for patients affected by liver metastasis is 8.5% (Pentheroudakis et al., 2006), for lung metastasis 16.8% (Smid et al., 2008) and for bone metastasis 22.8% (Xiong et al., 2018).

1.7 Xenograft studies in mice

Although cell culture is a convenient model to study a variety of biological processes, it does not represent the microenvironment of a tumor which consists of a complex network of various cell types, extracellular matrix (ECM) and vasculature, all of which are relevant to study the process of cancer growth and metastasis formation. To overcome this limitation, human cancer cell lines can be transplanted into immunodeficient mice, such as CD1 nude or NOD SCID gamma (NSG) mice to generate cell line-derived xenograft (CDX) models. CD1 nude mice carry a genetic mutation in the *Foxn1* gene that results in the lack of the thymus gland (Z. Zhang et al., 2012). Consequently, these mice have a severely reduced number of T cells resulting in an impaired immune system, which facilitates the growth of many human cancer cell lines. The lack of thymus is accompanied by a lack of hair, which makes it easier to identify and measure tumors. NSG mice are among the most immunodeficient mice described to date (Shultz et al., 2007). These mice carry two different mutations, namely the severe combined immune deficiency (scid) mutation in the DNA repair complex protein (*Prkdc*) that leads to B- and T cell deficiency, as well as a $IL2rg^{null}$ mutation in the IL2 receptor common gamma chain, which prevents cytokine signaling through multiple receptors and renders the mice NK cell deficient (Shultz et al., 1995, 2005). In contrast to CD1 nude mice, these mice do still have hair.

CDX transplantation models are well-established tools for investigating breast cancer and the metastatic progress *in vivo* as they allow validation of target genes of interest and facilitate evaluation of a candidate anti-cancer drug and therapeutics (Park et al., 2018; Rygaard & Povlsen, 1969). Depending on the site of injection, different processes can be studied. Generally, three different types of CDX-models can be distinguished: the subcutaneous, metastatic and orthotopic CDX model (Park et al., 2018). For the subcutaneous model, cells are implanted subcutaneously into the flank of mice to study primary tumor growth. The metastatic models require injection of cells into the blood stream and allow to study metastasis formation at various sites. For the orthotopic breast cancer model, cells are injected into the mammary fat pad which results in primary tumor growth, that is usually followed by formation of metastasis at secondary sites.

In the current work, the subcutaneous and two different metastatic CDX-models were used as illustrated in Figure 1.8. both of which are explained in more detail in the following chapters.

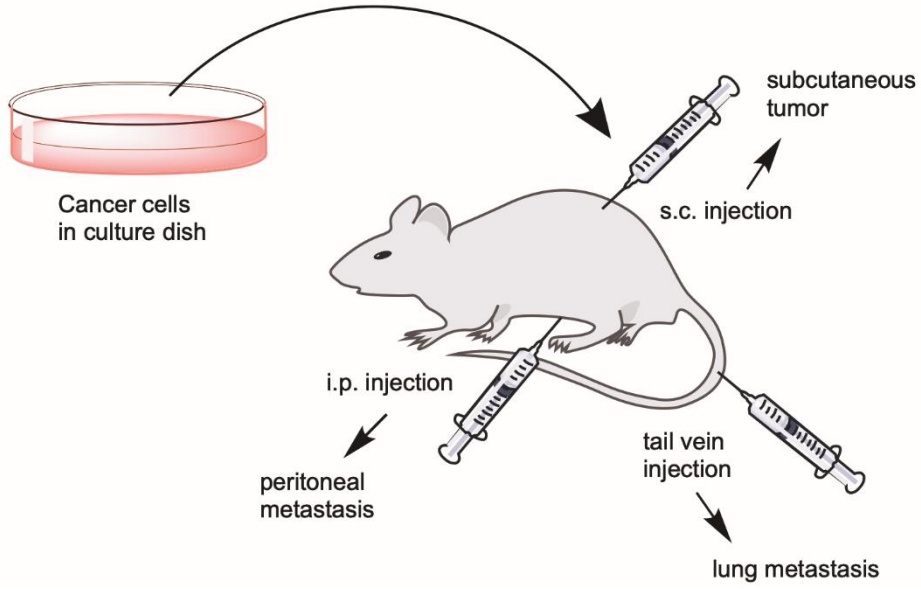

Figure 1.8: Schematic illustration of CDX-models established in this thesis. Injection of cancer cells into immunodeficient mice results in growth of tumor and metastasis in different microenvironments.

1.7.1 Subcutaneous CDX model

Subcutaneous injection of cancer cell lines into the flank of mice allows for the monitoring of primary tumor growth, which can be measured directly using a caliper. This technique has been successfully used to characterize different cell lines representing the common breast cancer subtypes (Holliday & Speirs, 2011). However, not all cancer cell lines lead to the formation of tumors and literature reveals a particular dearth of tumorigenic HER2+ lines (Holen et al., 2017; Holliday & Speirs, 2011). A downside of the subcutaneous model is that the tumors develop in

a peripheral site (under the skin) and not in their natural tumor microenvironment, which may alter their biology when compared to those grown in their natural environment. Furthermore, subcutaneous tumors usually do not metastasize (Y. Zhang et al., 2018). Therefore, other models need to be applied to study metastasis formation.

1.7.2 *In vivo* models for metastasis of blood-born cancer cells

In order to investigate metastasis in mice, cancer cells can be injected directly into the circulation. These cell seeding assays are also known as "experimental metastasis" (Elkin & Vlodavsky, 2001). Injection of cancer cells into the blood stream leads to the accumulation of cells in the capillary beds of different organs and mimics the process of extravasation of circulating tumor cells from blood vessels in target organs. Thereby, the metastatic potential of blood-borne cells is tested based on their ability to survive in and escape from the circulation, proliferate, and establish tumors.

Injection of cells into the lateral tail vein of mice delivers the cells to the lung. This lung seeding assay was extensively performed to study triple negative breast cancer cells, such as MDA-MB-231, which commonly metastasizes to the lungs (Jin et al., 2018; Sulaiman et al., 2019). After two to eight weeks, depending on the metastasis capacity of the cells, lungs can be excised and stained with Bouin's solution to make pulmonary tumor colonies macroscopically visible (Elkin & Vlodavsky, 2001). Depending on the route of injection, metastasis of blood-borne cancer cells to different organs can be investigated. For instance, injecting tumor cells into the portal vein introduces them directly into the murine liver. Liver metastasis can also be produced by the injection of cells into the splenic vein (intrasplenic), followed by the removal of the spleen to avoid the formation of splenic tumors (Goddard et al., 2016). Injecting tumor cells into the left ventricle (intracardiac) leads to their dissemination by the aorta resulting in multi-system metastases, and is a method commonly used to model bone and brain metastasis (Balathasan et al., 2013; Campbell et al., 2012). Another model for bone metastasis is the injection of cells into the iliac artery (intra-iliac) (Yu et al., 2016), and experimental brain metastasis can also be generated via the intracarotid injection of tumor cells (C. Zhang et al., 2017).

1.7.3 *In vivo* model for peritoneal metastasis

The peritoneum is a continuous membrane that lines the abdominal cavity. Metastases in the peritoneum are mainly caused by primary ovarian cancer (46% of cases) and other gastrointestinal or gynecological malignancies at advanced stages (Blackburn & Stanton, 2014). However, extra-abdominal cancers account for approximately 10% of diagnosed cases

of peritoneal metastases with breast cancer (41%) accounting for the majority (Flanagan et al., 2018) and several studies reported that the spread of primary breast cancer to the peritoneum is associated with extremely poor prognosis (Bertozzi et al., 2015; Caskey et al., 1991; Flanagan et al., 2018; Tuthill et al., 2009).

In order to model peritoneal metastasis in mice, cancer cells can be applied intraperitoneally (i.p.). In a previous study, Clinchy and colleagues compared the outcome of i.p. injection among several breast cancer cell lines. They reported that the HER2+ HCC1954 cell line resulted in the most severe metastatic phenotype with liver and kidney infiltration, large plaques of tumor cells growing on the peritoneal wall and accumulation of malignant ascites fluid within 8–15 weeks (Clinchy et al., 2000).

1.8 Non-invasive *in vivo* imaging

Whole animal imaging is an optical molecular imaging technique that allows non-invasive detection of luminescence or fluorescence emitting markers in mice. Consequently, bioluminescence imaging can be used to monitor the growth of luciferase-expressing cancer cells in mice over time.

In order to detect cells via luminescence imaging, cancer cells need to be genetically modified by the introduction of luciferase reporter enzymes. Firefly luciferase is one of many such luminescent proteins that was discovered in insects. It is the most frequently used and was isolated from the common North American firefly, *Photinus pyralis* (Close et al., 2010; Fraga, 2008). As illustrated in Figure 1.9A, the enzyme catalyzes the oxidation of D-luciferin to oxyluciferin in the presence of ATP-Mg^{2+} and oxygen thereby emitting a yellow-green light with a peak at 560 nm (Deluca, 1976). This rather long emission wavelength allows for highly sensitive imaging with low background in animal tissues as it is red-shifted compared to the endogenous autofluorescence of mice (Close et al., 2010; Lifante et al., 2020). Thus, firefly luciferase positive cells can be detected in deeper tissues and in the organs of mice, e.g. after intraperitoneal or intraorganellar injections. Another advantage of the firefly luciferase reporter is the quantitative correlation between signal strength and cell numbers (Close et al., 2010; Rettig et al., 2006).

In order to visualize the injected luciferase-expressing cancer cells in living mice, the substrate D-luciferin needs to be administered to the animals (see Figure 1.9B). Therefore, typically 150 mg/kg body weight D-luciferin are applied systemically by intraperitoneal injection. Application of the correct dose is essential for reproducible results, as the magnitude of

bioluminescence measured *in vivo* is dependent on the applied amount of D-luciferin (Burgos et al., 2003).

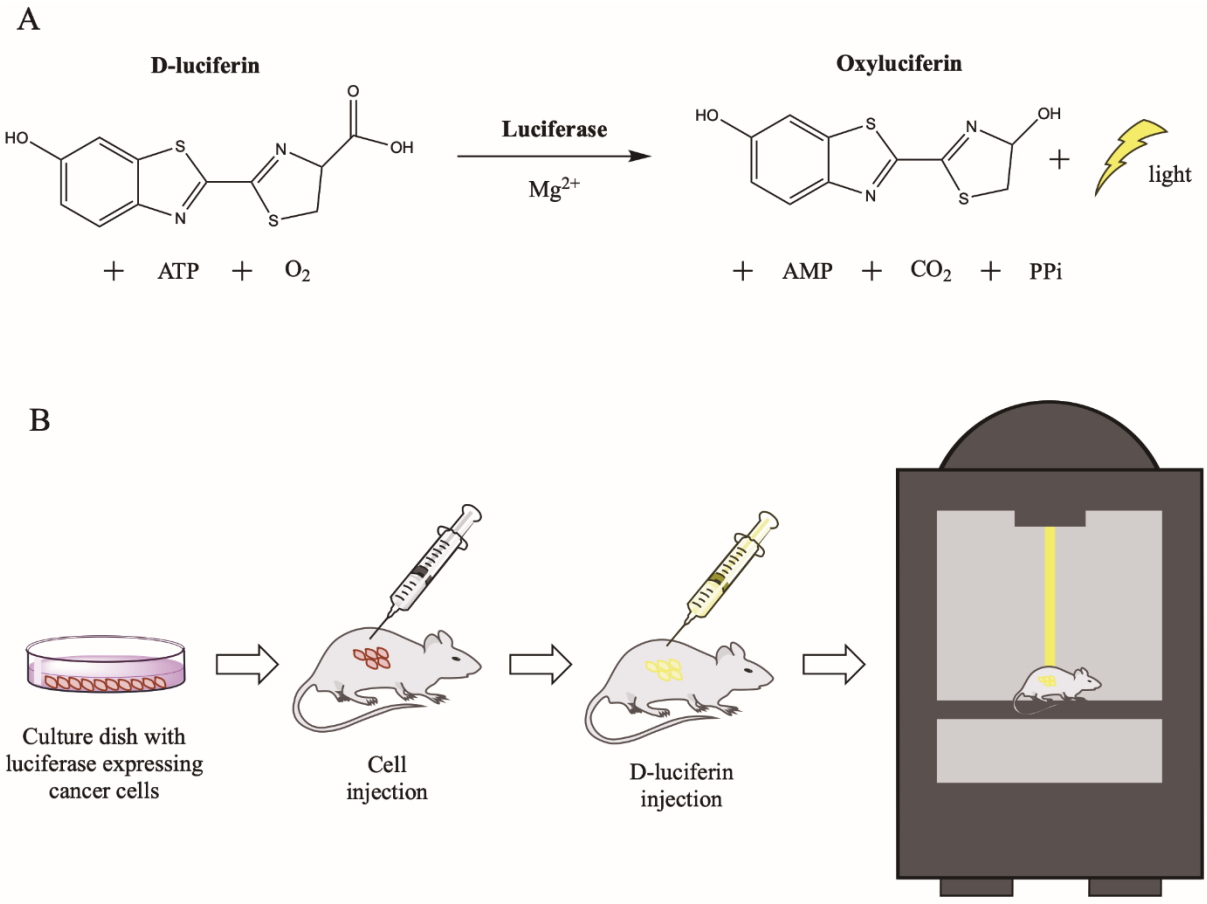

Figure 1.9: Non-invasive imaging of luciferase-expressing cells in mice. A) Light producing reaction of firefly luciferase enzyme transforming D-luciferin into oxyluciferin. B) Schematic illustration of the experimental steps required for *in vivo* imaging. Luciferase-expressing cells are injected into immunodeficient mice. Firefly luciferase's substrate is injected 10 min prior to bioluminescence imaging.

Another parameter that influences signal intensity is the pharmacokinetic of D-luciferin. After i.p. injection, D-luciferin is absorbed from the peritoneum into the blood, followed by systemic distribution in the body and uptake into cells via membrane transporters, where it is oxidized by luciferase (Sim et al., 2011; Y. Zhang et al., 2012). This results in a peak luminescence signal after approx. 10 min. Therefore, in order to achieve sufficient signal intensity and reproducibility, it is highly important to identify the optimal time for imaging post injection (Burgos et al., 2003; Rettig et al., 2006; Sim et al., 2011).

In contrast, fluorescence imaging is independent of substrate pharmacokinetics and allows true real-time imaging. However, endogenous fluorophores in the mouse tissue emit light, which results in autofluorescence of the imaged mouse. Furthermore, phytoestrogens that are contained in common mouse diets can emit fluorescence, which further increases autofluorescence in mouse tissue. To reduce this phenomenon, mice are fed a phytoestrogen

low diet (Miksicek, 1993). Since most endogenous fluorophores emit in the blue to green range of the electromagnetic spectrum, red-shifted reporters, such as turbo red fluorescent protein (tRFP) with excitation and emission maxima at 553 nm and 574 nm, respectively, can be used to avoid autofluorescence (Lifante et al., 2020).

For imaging, mice are anesthetized using isoflurane and placed in the light-tight imaging chamber of a whole animal imaging system, such as the IVIS Spectrum *In Vivo* Imaging System (PerkinElmer), where the photon emission of the luminescence or fluorescence markers is detected by a charge-coupled device (CCD) camera and matched with a photographic image of the subject. This enables localization of cancer cells and quantification of metastasis in deep tissues of mice, such as in the lung or in the peritoneal cavity, that cannot be measured using a manual caliper. Furthermore, it allows longitudinal monitoring of metastasis growth *in vivo* without the need to sacrifice mice at different time points, thereby reducing animal numbers that are needed for the experiment.

1.9 Aim of the study

EDI3 was identified in a screen for potential markers of metastasis in endometrial cancer, and was subsequently found to be associated with worse prognosis in both endometrial and ovarian cancer patients. Our research group could show that EDI3 functions as a glycerophosphodiesterase that hydrolyses GPC to form choline and G3P, thereby representing an important link between choline and glycerophospholipid metabolism. Previous experiments in different cancer cell lines showed that transient siRNA mediated EDI3 knockdown resulted in an increase in GPC accompanied by a decrease in choline and PCho levels, thereby correcting the low GPC/PCho ratio observed in various tumors and transformed cells. EDI3 knockdown also led to a decrease in glycerophospholipids PA and LPA, which are both known to be involved in cellular transformation. Furthermore, transient EDI3 knockdown was shown to result in a reduction of several cellular processes that play a role in metastasis formation, such as migration, adhesion and spreading.

Metastasis formation is a complex process that involves interaction of the tumor with its microenvironment and with the vascular system. Since all of EDI3's characterization so far was conducted *in vitro*, the major aim of this study was to investigate for the first time EDI3's role in tumor development and metastasis *in vivo*. In order to detect cancer cells in mice and to monitor metastasis growth, non-invasive bioluminescence imaging should be applied. Therefore, the first goal of this thesis was to generate stable luciferase expression in two different ER-HER2+ breast cancer cell lines (HCC1954 and SkBr3), which were recently

shown to have especially high EDI3 levels. Based on their luminescence intensity and tumor growth rate the more suitable cell line should be chosen for subsequent experiments.

Previous studies showed that a constitutive EDI3 knockdown, which could be used for long-term *in vivo* studies, led to a compensation of metabolite levels accompanied by loss of the migration phenotype over time. Therefore, the second goal of this work was to establish a Dox-inducible EDI3 knockdown system in the generated luciferase-expressing HCC1954_Luc breast cancer cells. This system allows for the induction of EDI3 knockdown only when needed, thus preventing compensational effects. For this purpose, cells should be transduced with lentiviral vectors containing different shRNA oligos under the control of a Dox-inducible promotor to generate different EDI3-targeting cell lines, as well as non-targeting negative control cells. These Dox-inducible cell lines should subsequently be investigated *in vitro* regarding the influence of EDI3 on choline and glycerophospholipid metabolite levels, as well as on various cellular processes that are relevant for metastasis formation.

After *in vitro* characterization, the aim was to use the generated cell lines to establish different cell line-derived xenograft models in immunocompromised mice in order to study EDI3's role in primary tumor growth and in the process of metastasis formation.

2 Materials and Methods

2.1 Materials

2.1.1 Technical equipment

Table 2.1: Equipment

Equipment	Company
ABI 7500 Fast Real-Time PCR System	Applied Biosystems
Autoclave VX-150	Systec
Autoclave 5075 ELV	Tuttenauer
Autosampler MPS-2	Gerstel
Blot imager Vilber Fusion Fx7	Vilber Lourmat
Changing station ARIA	Tecniplast
Compact portable balance CS 200	Ohaus
Cell counter Casy TT	OMNI life science
Centrifuge 5415R	Eppendorf
Centrifuge 400R	Heraeus
Centrifuge Megafuge 1.0R	Heraeus
Centrifuge MiniSpin	Eppendorf
Centrifuge MiniSpin plus	Eppendorf
Centrifuge 3-30K	Sigma
Confocal microscope (LSM 880)	Zeiss
CO2 incubator	Binder
Digital caliper gauge	Carl Roth
Electrophoresis unit Mini-PROTEAN®	BioRad
EVOS® FL Auto Imaging System	Life Technologies
Fume hood	Waldner
HPLC column: NUCLEOSHELL Bluebird RP 18 (125 x 3 mm, 2.7 µm)	Macherey-Nagel
HPLC Column: PerfectSil Target Sil 100 (125 x 3 mm, 3 µm)	MZ-Analysentechnik
Ice flake machine AF 100	Scotsman
Isoflurane Vaporizer	Northern Vaporisers
IVIS Spectrum *In Vivo* Imaging System	PerkinElmer
Laminar flow hood HERAsafe	Hereaus
Magnetic stirrer IKAMAG RCT	Ikamag

Micro scales	EW, Kern
Microscope BX41	Olympus
Microscope BZ-X800	Keyence
Microscope eclipse TS 100	Nikon
Microscope Primo Vert	Zeiss
Milli-Q® IQ Water Purification System	Millipore
Mini Vortex Mixer	Fisher Scientific
Mouse restrainer	Self-made
Multichannel pipette (300 µl)	Eppendorf
NanoDrop 2000	Thermo Fisher Scientific
NMR-Spectrometer Avance III	Bruker
Phase contrast microscope eclipse TS100	Nikon
pH meter	Schott Instruments
Pipets (2, 10, 20, 100, 200, 1000, 5000 µl)	Eppendorf
Pipetting aid	Integra Bioscience
Plate reader infinite M200 Pro	Tecan
Power pack HC	BioRad
Power pack P25T	Biometra
Precision balance EW150-3M	Kern
Precision balance ME235P	Sartorius
QExactive mass spectrometer	Thermo Fisher Scientific
Qtrap5500 mass spectrometer	Sciex
RAS-4 Rodent Anesthesia System	PerkinElmer
Rotating Wheel	VWR
Rocking Platform	VWR
Shaker KS 260 basic	IKA
Smart Flow IVC Air Handling Unit	Tecniplast
Sonicator sonoplus mini	Bandelin
Surgical Instruments	Fine Science Tools
Thermal cycler T3000	Biometra
Thermomixer	Eppendorf
Thermo shaker PHMT Grant-bio	Keison
Thermo shaker	peqlab
Trans-Blot® SD Semi-Dry Transfer Cell®	BioRad

UFLC system	Shimadzu
Vacuum pump	Vacuubrand
Vanquish Horizon UHPLC system	Thermo Fisher Scientific
Vortex-Genie2	Bender & Hobein
Water bath	GLF

2.1.2 Consumables

Table 2.2: Consumables

Consumable	**Company**
Biopsy punch	PFM Medical
Blot Filter Paper, 7 x 8.4 cm	Bio-Rad
CASY cups	Omni Life Sciences
Cell culture dishes (15 cm)	Sarstedt
Cell culture flasks (T25, T75, T175)	Sarstedt
Cell culture Inserts 24 well 8.0 µm pore	Falcon
Cell culture multiwell plates (6-, 12-, 24-, 96-well)	Sarstedt
Cell scraper (25 mm)	Sarstedt
Cryogenic Vials	Sarstedt
Culture-Insert 2 Well in µ-Dish (35 mm)	Ibidi
Falcon tubes (15, 50 ml)	Sarstedt
Filtertips (2.5 10, 100, 200, 1000, 5000 µl)	Sarstedt
Freezing container (Mr. Frosty)	Thermo Fisher Scientific
Glass Pasteur Pipettes	BRAND GmbH + Co
MicroAmp® Optical Adhesive Film	Thermo Fisher Scientific
MicroAmp® Optical 96-Well Reaction Plate	Thermo Fisher Scientific
Microplates 96-well, black	Thermo Scientific
Microplates, 96-well, clear	Greiner bio-one
Microplates, 96-well, white	Nunc
Minisart® syringe filters (0.45 µM)	Sartorius
µ-Slide 8 Well	Ibidi
NMR Inserts	Bruker
Pestle and Microtube	VWR
Pipet tips (10, 200, 1000 µl)	Sarstedt

PVDF membrane	PerkinElmer
Qiashredder columns	Qiagen
Reaction tubes (0.5, 1.5, 2, 5 ml)	Sarstedt
RNase-free Microfuge Tubes 1.5 ml	Thermo Fisher Scientific
Serological pipettes (5, 10, 25, 50 ml)	Sarstedt
Syringe (1 ml, 10 ml, 30 ml, 50 ml)	B.Braun
Syringe needle 20G	B.Braun
Syringe needle 26G, 30G	BD bioscience
Whatman-Paper 3 mm	VWR

2.1.3 Chemicals

Table 2.3: Chemicals

Chemical	**Company**
Ammonium persulfate	Sigma-Aldrich
Bovine serum albumin	Carl Roth
p-Coumaric acid	Sigma-Aldrich
Crystal violet	Sigma-Aldrich
Dimethyl sulfoxide	Sigma-Aldrich
Doxycycline hyclate	Sigma-Aldrich
Ethanol, absolute	Carl Roth
L-Glutamine	Sigma-Aldrich
Glycine	Carl Roth
Hydrogen peroxide 30%	Merck
Isoflurane	CP-Pharma
D-Luciferin potassium salt	PerkinElmer
Luminol	Sigma-Aldrich
β-Mercaptoethanol	Carl Roth
Methanol, HPLC grade	Carl Roth
Methyl-tert-butyl ether	Merck
Milk powder	Carl Roth
Nonidet P-40 substitute	Roche
Polybrene	Merckmillipore
Poly(2-hydroxyethyl methacrylate)	Sigma-Aldrich
Ponceau S	Carl Roth

Potassium chloride	Carl Roth
Potassium dihydrogen phosphate	Carl Roth
2-Propanol	Carl Roth
SDS pellets	Carl Roth
Sodium Chloride	AppliChem
Sodium deoxycholate	Carl Roth
Sodium hydrogen phosphate	Sigma-Aldrich
Tetramethylethylendiamine	Carl Roth
Tris	Carl Roth
Tris-HCl	Carl Roth
TritonX-100	Sigma-Aldrich
Tween20	AppliChem

2.1.4 Commercial buffers, solutions and media

Table 2.4: Commercial buffers, solutions and media

Buffer/solution/medium	**Company**
Acrylamide (30% (v/v))	Carl Roth
Buffer concentrate A	Carl Roth
Buffer concentrate K	Carl Roth
CASY ton	Omni Life Sciences
DMEM 4.5 g/l glucose	PAN-Biotech
Diethylpyrocarbonate treated (DEPC) water	Thermo Fisher Scientific
Fetal Bovine Serum	Gibco™ Thermo Scientific
Fibronectin bovine plasma	Sigma-Aldrich
Fluoroshield™ mounting medium	Sigma-Aldrich
Geneticin disulfate (G418) solution	Carl Roth
Loading buffer 4x	BioRad
Matrigel® Matrix High Concentration	Corning®
MEM Non-essential amino acids solution	Gibco™ Thermo Scientific
Paraformaldehyde 4%	Carl Roth
Phosphatase-Inhibitor-Cocktail II&III	Sigma-Aldrich
Precision Plus Protein Dual Colour Standard	BioRad
Protease-Inhibitor-Cocktail	Sigma-Aldrich
Puromycin	Gibco™ Thermo Scientific

RnaseZap™ Solution	Thermo Fisher Scientific
RPMI 1640	PAN Biotech
Sera Plus FCS	PAN Biotech
Sodium Pyruvate Solution	Sigma-Aldrich
Tetracycline-free FCS	PAN Biotech
Tris/Glycine/SDS Buffer (10x)	BioRad
Trypsin 0.05% / EDTA 0.02% in PBS	PAN Biotech

2.1.5 Prepared buffers and solutions

Table 2.5: Prepared buffers and solution for gel electrophoresis and western blot

Buffer/solution	**Composition**
Anode buffer	10% (v/v) Buffer concentrate A 20% (v/v) Methanol in ultrapure water
APS solution	10% (w/v) Ammonium persulfate in ultrapure water
Blocking solution (BSA)	5% (w/v) BSA in 1x TBS-T
Blocking solution (milk)	5% (w/v) Milk powder in 1x TBS-T
Cathode buffer	10% (v/v) Buffer concentrate K 20% (v/v) Methanol in ultrapure water
Enhanced chemiluminescent solution (ECL)	2.5 mM Luminol 0.2 mM p-Coumaric acid in 0.1 M Tris
Phosphate buffered saline (PBS 10x)	27 mM KCl 18 mM KH_2PO_4 100 mM Na_2HPO_4 1.37 M NaCl in ultrapure water
RIPA buffer	50 mM Tris-HCl (pH 7.5) 150 mM NaCl 1% NP-40

	0.5% Sodium deoxycholate 0.5% SDS 1% Protease-/Phosphatase-Inhibitor-Cocktail
SDS solution	10% (w/v) SDS in ultrapure water
Separation buffer	3 M Tris in ultrapure water pH 8.8
Stacking buffer	0.47 M Tris in ultrapure water pH 6.8
Stripping buffer	0.2 M Glycine 0.1% (w/v) SDS 1% (v/v) Tween20 in ultrapure water pH 2.2
Tris buffered saline (TBS 10x)	0.5 M Tris 1.5 M NaCl in ultrapure water pH 7.4
TBS-T	10% (v/v) TBS (10x) 0.1% (v/v) Tween20

Table 2.6: Prepared buffers and solutions for cell assays

Buffer/solution	**Composition**
1% BSA Blocking solution for adhesion assay	1% (w/v) BSA in 1x PBS
3% BSA Blocking solution for proliferation assay	3% (w/v) BSA in 1x PBS
Crystal violet fixation solution	0.1% (w/v) Crystal violet 20% (v/v) Ethanol in ultrapure water
Destaining solution for adhesion assay	0.2% (w/v) Triton X-100

	in H_2O
Permeabilization solution for proliferation assay	0.5% (w/v) Triton X-100 in 1x PBS

2.1.6 Commercial assays and kits

Table 2.7 Commercial assays and kits

Kits	Company
BCA Protein assay	Thermo Fisher Scientific
CellTiter-Blue® assay	Promega
Click-iT™ Plus EdU Cell Proliferation Kit for Imaging	Invitrogen
High-Capacity cDNA Reverse Transcription Kit	Thermo Fisher Scientific
Lipofectamine 3000 Transfection Kit	Invitrogen™
ONE-Glo™ Luciferase Assay System	Promega
QuantiFast SYBR® Green PCR Kit	Qiagen
RNase-Free-DNase kit	Qiagen
RNeasy Mini Kit	Qiagen

2.1.7 Cell lines

Table 2.8: Commercially available cell lines

Cell line	Information
HCC1954	This epithelial breast cancer cell line was derived from a primary stage IIA, grade 3 invasive ductal carcinoma with no lymph node metastases from a 61-year-old Asian woman in 1995 (Gazdar et al., 1998).
MCF7_Luc	The epithelial MCF7 cell line was isolated from the pleural effusion of a 69 year old Caucasian woman with metastatic adenocarcinoma of the breast in 1970 (Soule et al., 1973). This luciferase-expressing cell line was purchased from AMSBio.
SkBr3	This cell line was isolated from the pleural effusion of a 43-year-old Caucasian female with malignant adenocarcinoma of the breast in 1970 (Fogh et al., 1977).

Cell lines were purchased from ATCC (American Type Culture Collection) or DSMZ (German Collection of Microorganisms and Cell Cultures), unless stated differently.

Table 2.9: Cell line generated as part of this thesis

Cell line	Information
HCC1954_Luc	Stably luciferase-expressing HCC1954 cell line that was generated by transfection with the plasmid pGL4.51.
HCC1954_Luc shEDI3	Luciferase positive HCC1954 cell line with doxycycline inducible EDI3 silencing and RFP expression. It was created by transduction of HCC1954_Luc cells with SMARTvector™ Inducible Lentiviral shRNA.
HCC1954_Luc shNEG	Luciferase positive HCC1954 cell line with doxycycline inducible expression of scrambled shRNA and RFP. The cell line was generated by transduction of HCC1954_Luc cells with SMARTvector™ Inducible Non-targeting shRNA Control.
SkBr3_Luc	This stable luciferase-expressing SkBr3 cell line was created by transfection with the pGL4.51 plasmid.

All cell lines were authenticated by the Leibniz institute DSMZ.

2.1.8 Cell culture medium and additives

Table 2.10: Cell culture medium and additives

Cell line	Medium	Company
HCC1954	500 ml RPMI 1640	PAN Biotech
	+ Fetal Bovine Serum (10%)	Gibco™ Thermo Scientific
	+ Sodium Pyruvate (1%)	Sigma-Aldrich
HCC1954_Luc	500 ml RPMI 1640	PAN Biotech
	+ Fetal Bovine Serum (10%)	Gibco™ Thermo Scientific
	+ Sodium Pyruvate (1%)	Sigma-Aldrich
	+ G418 (200 µg/ml)	Carl Roth
HCC1954_Luc shEDI3/	500 ml RPMI 1640	PAN Biotech
HCC1954_Luc shNEG	+ Tetracycline-free FCS (10%)	PAN Biotech
	+ Sodium Pyruvate (1%)	Sigma-Aldrich
	+ G418 (200 µg/ml)	Carl Roth
	+ Puromycin (0.5 µg/ml)	Gibco™ Thermo Scientific
SkBr3	500 ml DMEM 4.5 g/l glucose	PAN Biotech
	+ Fetal Bovine Serum (10%)	Gibco™ Thermo Scientific
SkBr3_Luc	500 ml DMEM 4.5 g/l glucose	PAN Biotech
	+ Fetal Bovine Serum (10%)	Gibco™ Thermo Scientific
	+ G418 (400 µg/ml)	Carl Roth

2.1.9 Lentiviral vectors

Table 2.11: Lentiviral vectors

Target	Promotor	Fluorescence	Source Clone ID	Target Sequence
EDI3 #1	CMV	tRFP	V3IHSMCR_8692503	CCAGAAGATGTAGGGTTTA
EDI3 #2	CMV	tRFP	V3IHSMCR_10362897	GGAGTTAATGGTCTAATTT
EDI3 #3	CMV	tRFP	V3IHSMCR_5777679	GGTACAGCTTGTCTCTTAT
EDI3 #4	CMV	tRFP	V3IHSMCR_7594956	ATGTGGGATGGTAACTTAT
EDI3 #5	CMV	tRFP	V3IHSMCR_6267993	CGAGGTGCAGGAAACTCTA
EDI3 #6	CMV	tRFP	V3IHSMCR_10219776	AGTGCAGGCATTCACAGCC
Scrambled (control)	CMV	tRFP	VSC6585	
GAPDH (control)	CMV	tRFP	VSH6557	

All lentiviral vectors were purchased from Dharmacon.

2.1.10 Plasmids

Table 2.12: Plasmids

Plasmid	Company
pGL4.51[*luc2*/CMV/Neo]	Promega
pCMV6 [Neo] (empty vector)	ORIGENE-AMSBio

2.1.11 Laboratory mice

Table 2.13: Mice

Mouse	Full nomenclature	Gender	Age at arival	Company
CD-1® Nude	Crl:CD1-*Foxn1*^{nu}	female	5 weeks	Charles River
NSG® (NOD SCID gamma)	NOD.Cg-*Prkdc*^{scid} *Il2rg*^{tm1Wjl}/SzJ	female	5 weeks	Charles River

Table 2.14: Mouse feed

Feed	Company
Nude mouse diet fortified, γ-irradiated (25 kGy)	Ssniff
Rat/Mouse diet low phytoestrogen, γ-irradiated (25 kGy)	Ssniff
Rat/Mouse diet low phytoestrogen with doxycycline (625 / 720 mg/kg), γ-irradiated (25 kGy), green dye	Ssniff

2.1.12 Antibodies

Table 2.15: Primary antibodies

Antibody	Host	Cat#/Company
anti β-actin	Mouse	A5316, Sigma-Aldrich
anti EDI3	Mouse	Custom made (Clone 3B8G3), AMS Bio
anti RFP	Rabbit	R10367, Invitrogen

Table 2.16: Secondary antibodies

Antibody	Host	Cat#/Company
anti mouse HPR linked	Horse	#7076, Cell Signaling
anti rabbit HPR linked	Goat	#7074, Cell Signaling

2.1.10 QuantiTect Primer Assays

Target gene	Species	Primer ID	Company
EDI3	Human	QT00066598	Qiagen
ACTB	Human	QT00095431	Qiagen
18S	Human	QT00199367	Qiagen

2.2 Methods

2.2.1 Cultivation of cell lines

All cell lines were maintained under sterile conditions in a humidified incubator at 37 °C and 5% CO_2. All working steps were conducted in a laminar flow cabinet using only sterile materials and solutions. The cells were cultured using the media and supplements listed in Table 2.10 and cell medium was renewed every two to three days. Once the cells reached 80-90% confluency, they were sub-cultured to guarantee constant growth. Therefore, the medium was removed from the tissue flask and the adherent cells were carefully rinsed with 1x PBS.

Trypsin/EDTA (0.05%/0.02% in PBS) was added, and cells were incubated at 37 °C for 5 min to facilitate detachment of the cells. Subsequently, cells were resuspended in fresh medium and transferred into new culture flasks.

Before cells were seeded into plates for experiments, they were detached as described above. After resuspension in fresh media, the cell suspension was transferred into a tube and cells were pelleted for 5 min at 800 x g. The medium was aspirated to remove residual trypsin. The cell pellet was then resuspended in fresh media and the cells were counted with the CASY TT cell counter.

2.2.2 Freezing and thawing of cell lines

For storage in liquid nitrogen adherent cells with a confluency of approx. 70% were detached as described above. After resuspension in fresh full media, the cell number was determined using the CASY TT cell counter. Cells were pelleted for 5 min at 800 x g and the supernatant was removed. The pellet was resuspended in an appropriate volume of medium containing 5% DMSO to avoid ice crystal formation. One ml aliquots comprising 2-4 million cells were filled into cryo vials and placed in a freezing container, which was filled with 2-propanol and stored at -80 °C overnight. These containers provide a consistent cooling rate, which improves cryo preservation. Afterwards, the cells were placed into the gaseous phase of the liquid nitrogen tank for long-term storage.

For thawing, the cryovial was placed in a water bath of 37 °C. When the cell suspension was just defrosted the cells were pelleted for 5 min at 800 x g. The DMSO containing media was aspirated and the cell pellet was resuspended in 1 ml antibiotic free medium. The cell suspension was then transferred into a prepared T25 flask containing another 4 ml of fresh antibiotic free media. If needed, antibiotic containing medium was added to the cells 24 h after thawing. To conduct experiments, cells were at least sub-cultured twice after thawing from liquid nitrogen storage.

2.2.3 Antibiotic kill-curve

Mammalian cell sensitivity to antibiotics varies from one cell type to another. In order to generate stable cell lines by plasmid transfection or lentiviral transduction, it is important to determine the minimum concentration of antibiotic required to kill non-transfected or non-transduced cells. The pGL4.51 plasmid used in this thesis to create luciferase-expressing cells (2.2.4) contains a neomycin resistance gene and can be selected for by geneticin disulfate (G418), while the lentiviral vectors used for inducible gene silencing (2.2.5) contain a puromycin resistance and can then be selected for using puromycin.

For the antibiotic kill-curve, cells were plated at a density of $9x10^4$ cells per well in 0.5 ml full medium in 24-well plates to reach a confluency of approx. 70% on the next day. Increasing concentrations of antibiotic were prepared by diluting stock concentrations of 10 mg/ml puromycin as well as 50 mg/ml G418 in cell culture medium (Table 2.17). Twenty-four hours after plating, confluency was confirmed, and cells were rinsed with 1x PBS before increasing amounts of the antibiotic were added to duplicate wells. On subsequent days, the cells were examined for signs of visual toxicity using light microscopy. The antibiotic containing media was replaced every two to three days. If needed, cells were sub-cultured into new plates once a confluency of 90% was reached. To do so, cells were rinsed with 1x PBS followed by treatment with trypsin/EDTA at 37 °C for 5 min. Cells were re-suspended in 300 µl antibiotic containing media, 150 µl of the cell suspension was transferred into a new well and additional 350 µl antibiotic containing media was added. The lowest antibiotic concentration at which all of the cells were dead after one week of treatment was determined and used for antibiotic selection after transfection or transduction experiments.

Table 2.17: Concentrations of selection antibiotics tested

Antibiotic	**Tested concentrations [µg/ml]**
Puromycin	0, 0.5, 1, 2, 3, 4, 5, 6, 7, 8, 9, 10
Geneticin disulfate (G418)	0, 50, 100, 200, 300, 400, 500, 600, 700, 800, 900, 1000

2.2.4 Plasmid DNA transfection via Lipofectamine 3000

To generate luciferase-expressing cells, the breast cancer cell lines HCC1954 and SkBr3 were transfected with the firefly luciferase gene (*luc2*) encoding plasmid pGL4.51[luc2/CMV/Neo] (Promega) as well as with the pCMV6 [Neo] empty vector control.

The day before transfection, cells were plated in 500 µl medium into 24-well cell culture dishes at a density which resulted in approx. 70% confluency on the day of transfection (Table 2.18). 24 h after plating, the cells were transfected with plasmid DNA using the Lipofectamine 3000 Transfection Kit (Invitrogen™) according to the manufacturers' instructions. For transfection in a 24-well cell culture vessel, in a first tube 0.5 µl Lipofectamine 3000 reagent was added to 25 µl OptiMEM medium. In a second tube, 500 ng DNA as well as 1 µl P3000™ reagent were added to another 25 µl OptiMEM. Then, the contents of both tubes were combined and mixed well by vortexing. This mixture was then incubated for 15 min at room temperature to allow the DNA-Lipofectamine complexes to form. Afterwards, 50 µl of the prepared solution was added to the cells and the cell culture plate was swirled gently to ensure homogeneous

distribution of the complexes to the entire well. After 7 h the transfection media was replaced by regular cell culture media and 72 h later the media was replaced by fresh media containing the antibiotic geneticin disulfate (G418) at a concentration (Table 2.18) that was predetermined to successfully select for transfected cells as described in 2.2.3. After expansion of the cells, luciferase expression was confirmed by luciferase assay (2.2.7) and single cell cloning was performed with HCC1954_Luc and SkBr3_Luc cells (2.2.6). Luciferase positive clones were frozen and stored in liquid nitrogen (2.2.2).

Table 2.18: Lipofectamine 3000 transfection conditions

Cell culture vessel	Cell line	Cell number seeded	G418 [µg/ml]
24-well	HCC1954	$9.3x10^4$	200
24-well	SkBr3	$9.3x10^4$	400

2.2.5 Inducible inhibition of gene expression via RNA interference

RNA interference (RNAi) is a biological cellular response to double-stranded RNA that results in degradation of messengerRNA (mRNA) and can be used to inhibit the expression of target genes (Fire et al., 1998). By genomic integration of short hairpin RNA (shRNA) which is subsequently transcribed as short hairpin precursors (~70 nt), and processed into active 21-nt RNAs, continuous cell lines with heritable gene silencing can be constructed (Paddison et al., 2002).

To generate stable cell lines with inducible inhibition of gene expression, in this thesis SMARTvector™ lentiviral particles containing inducible gene-targeting shRNA oligos (Dharmacon) were used (Figure 2.1).

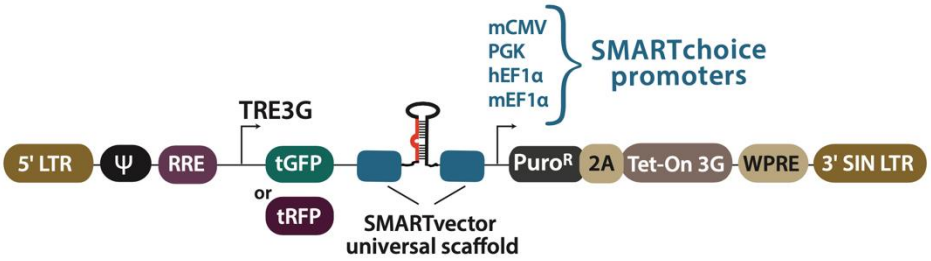

Figure 2.1: Elements of the SMARTvector inducible lentiviral shRNA vector. In the presence of Dox, the TRE3G promoter is bound and activated by the constitutively expressed Tet-On 3G transactivator protein which results in the expression of fluorescence marker and shRNA. 5' LTR5, 5' long terminal repeat; Ψ, Psi packaging sequence; RRE, reverse response element; TRE3G, inducible promoter with tetracycline response elements; tGFP or tRFP, TurboGFP or TurboRFP; SMARTvector universal scaffold, scaffold in which gene-targeting sequence is embedded; $Puro^R$, puromycin resistant gene; 2A, self-cleaving peptide; Tet-On 3G, encodes doxycycline-regulated transactivator protein; WPRE, woodchuck hepatitis post-transcriptional regulatory element; 3' SIN LTR, 3' self-inactivating long terminal repeat (Dharmacon, 2014).

These lentiviral vectors become integrated into the genome of the host cells and gene expression is controlled by a Tet-On 3G tetracycline-inducible system (Loew et al., 2010; Zhou et al., 2006). Consequently, shRNA mediated gene inhibition as well as the expression of the fluorescence marker TurboRFP (tRFP) is only activated upon induction with tetracycline or its analog doxycycline (Dox).

2.2.5.1 Transduction of cells with lentiviral particles

In this thesis, lentiviral vectors encoding six different shRNA oligos binding specifically to different exons of the *EDI3* gene were used to generate HCC1954_Luc cell lines with stable Dox inducible reduction of EDI3 expression. Additionally, a non-targeting scrambled shRNA control as well as a GAPDH-targeting positive control were used.

For the generation and cultivation of the inducible cell lines, all media were prepared with tetracycline-free FCS to prevent unintended induction. On the day before transduction $7.5x10^3$ cells were seeded into 96-well cell culture plates to ensure that cells were approximately 50% confluent on the day of transduction with the particles. Twenty-four hours later, the cells were transduced at a multiplicity of infection (MOI) of both three and five. For this purpose, lentiviral particles were diluted in serum-free medium without supplements according to the viral titer provided by the manufacturers to generate the transduction medium. Afterwards, the media was aspirated from the cells and replaced by 25 µl of transduction media per well. To prevent evaporation of the small media volume in the wells, the surrounding wells were filled with 200 µl medium each and the cell culture plates were wrapped in clingfilm before they were placed into the incubator. Sixteen hours after transduction, 100 µl tetracycline-free serum containing supplemented full media was added to the cells. The next day, media was replaced by selection medium containing 0.5 µg/ml puromycin which was predetermined to be sufficient for selection of stable integrants as described in 2.2.3. The remaining cells were expanded until an adequate cell number was achieved to freeze and store the cell lines (2.2.2). Puromycin was removed from the media once selection was complete after two weeks. Successful induction by Dox (2.2.5.2) was confirmed by expression of the fluorescence marker tRFP using fluorescence microscopy. Downregulation of EDI3 expression was determined using quantitative real-time polymerase chain reaction (qRT-PCR) and western blotting as described in 2.2.15 and 2.2.16, respectively.

2.2.5.2 Dox-induction of shRNA mediated inhibition of gene expression

To induce the transcription of shRNA in the transduced HCC1954_Luc cell lines, cells were seeded in full media in either cell culture flasks or well-plates at a density which resulted in

approx. 90% confluency after an induction time of 72 h (Table 2.19). The cells were placed in the incubator to fully attach overnight. Induction medium was freshly prepared by diluting a stock solution of 10 mg/ml Dox in full media to reach the desired concentrations. If not stated otherwise, for cellular assays a concentration of either 0.01 or 0.1 µg/ml Dox was used. Twenty-four hours after plating, media was aspirated, and cells were treated with Dox. Every 48 h the induction medium was replaced by freshly prepared Dox-containing medium.

Table 2.19: Induction conditions for shRNA mediated inhibition of EDI3 expression

Cell line	**Cell culture vessel**	**Cell number**	**Medium [ml]**	**Dox [µg/ml]**	**Induction time [h]**
HCC1954_Luc shEDI3 / shNEG/ shGAPDH	T175	¼ T175	25	0.01 / 0.1	72
	6-well	$3x10^5$	2	0.01 / 0.1	72
	24-well	$9x10^4$	1	0.01 / 0.1	72

2.2.6 Single cell cloning

To generate single cell clones containing a homogeneous genetic background from transfected or transduced cell cultures, two different dilution cloning approaches were performed. For the first approach, the heterogenous cells were serially diluted in their required full media in 5 ml tubes. From each dilution, 200 µl aliquots per well were transferred into two rows of a 96-well plate, resulting in replicates of 100, 10 and 1 seeded cells per well. Alternative, in the second approach, the heterogenous cell culture was diluted to 100 cells/ml in a 15 cm cell culture dish.

For both approaches, cell growth was monitored. Once single colonies became visible, they were rinsed with 1x PBS to remove unattached cells, fresh media was added, and clones were picked using a 200 µl pipette tip. In detail, the pipette tip was exhausted and placed on top of the colony, sealing it as much as possible from the surrounding media. Then, by filling up the pipette tip carefully with 200 µl, an undertow was created, that sucked cells from the colony into the tip. These cells were then transferred into a new 96-well plate. Growing cells were expanded until enough cells were achieved to confirm luciferase (2.2.7) or tRFP expression. The shRNA mediated downregulation of EDI3 expression was determined by quantitative real-time polymerase chain reaction (qRT-PCR) and western blotting as described in 2.2.15 and 2.2.16, respectively. Positive clones were frozen and stored in liquid nitrogen (2.2.2).

2.2.7 Luciferase assay

The ONE-Glo™ Luciferase Assay System (Promega) was used to confirm the expression of firefly luciferase in HCC1954_Luc and SkBr3_Luc cells after transfection with pGL4.51 plasmid. This assay utilizes the luciferin analog 5´-fluoroluciferin. Oxidation of 5´-fluoroluciferin by firefly luciferase results in the emission of luminescence.

On the day prior to the assay $1x10^4$ cells in 100 µl medium were seeded per well into a white 96-well microtiter plate. After the cells fully attached overnight, 100 µl of ONE-Glo™ Reagent was added per well. Cells were protected from light and incubated at room temperature for 3 min. The luminescence signal was subsequently measured in a plate reader (Infinite M200 Pro, Tecan).

2.2.8 Cell assays

2.2.8.1 Wound closure assay

A wound closure assay was applied to study how migration is affected by inducibly silencing EDI3 expression in HCC1954_Luc cells. The assay is based on determining the rate at which cells repopulate an artificial gap that was created in a confluent cell monolayer.

For this purpose, shRNA mediated EDI3 downregulation was induced in 6-well plates as described in 2.2.5.2. After 72 h of induction, cells were washed with 1x PBS and detached by treatment with trypsin/EDTA for 5 min at 37 °C. Cells were then pelleted at 800 x g for 5 min and resuspended in full media containing the appropriate Dox concentration to sustain the knockdown. The cell number was determined using the CASY TT cell counter after which $7x10^6$ cells in 70 µl were added per well into the 2 well silicone inserts (Ibidi) that were previously placed in the wells of 6-well plates. After 24 h, the cells were fully attached and the culture inserts were removed using sterile tweezers, leaving a clean gap between the two cell monolayers. The cells were then rinsed once with 1x PBS to remove any floating cells before 2 ml medium was added per 6-well. Directly upon removal of the insert, as well as on the following days, four photos per well were taken at the same position each day until the gap in the non-induced control cells was almost fully closed. The size of the gaps was determined using the “wound healing tool” of the ImageJ software. The average percentage of wound closure was calculated from all four positions photographed and compared to the non-induced control cells.

2.2.8.2 Adhesion assay

To evaluate the effect of EDI3 downregulation on cell adhesion, cells were re-plated on fibronectin-coated wells and the number of attached cells was determined at different time points.

For the fibronectin coating, a 20 µg/ml solution was prepared in H_2O and 50 µl were added per well to rows A-E of 96-well plates. The plates were shaken gently until the well surface was completely covered and kept at 4 °C overnight. On the next day, excessive fibronectin solution was removed from the wells and plates were left uncovered to dry under the sterile hood for approx. 15 min. Subsequently, 100 µl sterile blocking solution (1% BSA in 1x PBS) was added per well to rows A-H and the plate was kept again at 4 °C overnight. Immediately before cells were seeded, the wells were washed once with 1x PBS.

EDI3 downregulation in HCC1954_Luc cells was induced in T175 flasks as described in 2.2.5.2. After 72 h of induction, cells were detached using Trypsin/EDTA, resuspended in suspension medium (serum free regular medium) and transferred into 15 ml tubes. To end trypsinization, 0.5 µg/ml trypsin inhibitor was added, and cells were incubated for 10 min at room temperature while gently inverting the tube a few times. Cells were pelleted for 5 min at 800 x g at room temperature, resuspended in fresh suspension media, and rotated for 1 h at 37 °C in the incubator using the MacsMix rotator at full speed. After rotation, cell number was determined using the CASY TT cell counter and $5x10^4$ cells in 100 µl suspension medium were re-plated into five fibronectin-coated wells each, as well as into three BSA-blocked control wells. The cells were then incubated at 37°C for different time points ranging from 10 min to 1 h. After incubation, non-adherent cells were removed by washing the plate once with 1x PBS. The adherent cells were stained and fixed with a crystal violet solution for 20 min at room temperature. Excessive staining solution was removed by rinsing the plate carefully with tap water and the plates were left open to dry overnight at room temperature. Photos of the stained cells were taken with a phase-contrast microscope using a 10x objective. To quantify the adhered cells, they were destained with 0.2% Triton X-100 for 20 min on an orbital shaker at room temperature and absorption was measured at 570 nm in a plate reader (Infinite M200 Pro, Tecan).

2.2.8.3 Viability assay

To determine the viability of HCC1954_Luc shEDI3 cells after Dox induction of the shRNA mediated EDI3 knockdown, the CellTiter-Blue® viability assay (Promega) was applied. This assay uses the blue dye resazurin which is reduced by viable cells to the fluorescent dye

resorufin. Consequently, the generated fluorescence signal is proportional to the number of living cells in the sample.

HCC1954_Luc shEDI3 and HCC1954_Luc shNEG cells were seeded at an appropriate density into T175 cell culture flasks. After one day of attachment, the cells were induced with concentrations of 0, 0.01 and 0.1 µg/ml Dox (2.2.5.2). After 72 h of induction, cells were rinsed with 1x PBS and detached by trypsin/EDTA treatment for 5 min at 37 °C. Cells were pelleted at 800 x g for 5 min and resuspended in full media containing the corresponding amounts of Dox. The cell number was determined using the CASY TT cell counter and $5x10^3$ cells per well were re-plated into a 96-well plate. After 96 h, the medium was replaced by a 1:5 dilution of CellTiter-Blue® reagent in medium. The plate was incubated for 4.5 h until the blue color changed into pink. 100 µl of the cell supernatant was transferred into a microtiter plate with black walls and transparent, flat bottoms. The fluorescent signal was measured at $579_{Ex}/584_{Em}$ nm in a plate reader (Infinite M200 Pro, Tecan).

2.2.8.4 Anoikis assay

Anoikis is a form of apoptosis that is triggered in adherent cells when they detach from the surrounding extracellular matrix (ECM) (Frisch & Francis, 1994; Meredith et al., 1993). To determine if cells with reduced EDI3 expression are more susceptible towards anoikis, cells were incubated on plates coated with poly(2-hydroxyethyl methacrylate) (poly-HEMA), a polymer that prevents cell adhesion.

For that purpose, a poly-HEMA solution of 10 mg/ml was prepared in 95% ethanol by shaking vigorously at 37 °C overnight. After sterile filtration using a 0.2 µm filter, 6-well plates were coated with 750 µl poly-HEMA solution per well and plates were left without lid under the sterile hood to dry overnight. Plates were washed three times with 1x PBS before plating cells.

EDI3 downregulation in HCC1954_Luc cells was induced in T175 flasks as described in 2.2.5.2. After 72 h of Dox treatment, one million cells in 2 ml were replated per well of the poly-HEMA coated 6-well plates. The plates were placed in the incubator for 24 h. Afterwards, 100 µl CellTiter-Blue® reagent was added per well. The plate was incubated for another 40 min until the blue color of the non-induced control wells changed into pink. 100 µl of the cell supernatant was transferred into a microtiter plate with black walls and transparent, flat bottoms. The fluorescent signal was measured at $579_{Ex}/584_{Em}$ nm in a plate reader (Infinite M200 Pro, Tecan).

2.2.8.5 Colony formation assay

To evaluate the effect of Dox-induced EDI3 downregulation on the ability of the cells to form colonies out of a single cell, a colony formation assay was performed. Therefore, shRNA expression was induced with Dox in HCC1954_Luc shEDI3 and control cells (shNEG) in T175 flasks as described in 2.2.5.2. After 72 h of Dox treatment, 500 cells in 2.5 ml corresponding Dox-containing media per well were replated into 6-well plates and placed in the incubator for 14 days. Afterwards, the media was aspirated, cells were washed with 1x PBS and subsequently stained for 20 min with 500 µl crystal violet solution per well. Excess staining was removed by washing the wells thrice with tab water. After drying, pictures of each well were taken. The software ImageJ was used to determine the number and size of colonies.

2.2.8.6 Proliferation assay

To investigate if EDI3 knockdown affects proliferation, the Click-iT™ Plus EdU Cell Proliferation Kit for Imaging (Invitrogen) was used. With this kit, DNA synthesis can be measured in two steps. First, cells are labeled with EdU (5-ethynyl-2´-deoxyuridine), a nucleoside analog of thymidine that is incorporated into DNA during active DNA synthesis. Then, labeled proliferating cells can be detected using an Alexa Fluor® dye. This process is based on a copper-catalyzed click reaction resulting in a covalent bond between an alkyne, provided by EdU, and a picolyl azide, provided by the Alexa Fluor 488 dye (Salic & Mitchison, 2008).

EDI3 downregulation in HCC1954_Luc cells was induced in 6-well plates as described in 2.2.5.2. After 72 h of Dox treatment, cells were plated into 8-well chambers (Ibidi) in 300 µl corresponding Dox-containing media per well and placed in the incubator according to the cell numbers and incubation time listed in Table 2.20.

Table 2.20: Experimental conditions for proliferation assay

Experimental approach	Cell number plated	Incubation time until EdU treatment
Subconfluent cell layer	1500	24 h
Colony formation	150	7 d

Once the incubation time was over, half of the media per well was removed (150 µl) and 150 µl fresh medium containing 20 µM EdU was added, resulting in a final concentration of 10 µM EdU. The cells were placed back into the incubator for 2 h. Then, the media was completely aspirated, and cells were fixed with 4% PFA for 15 min at room temperature. The fixative was removed, and cells were washed twice with 3% BSA in 1x PBS for 5 min each. After the

washing steps, cells were permeabilized with of 0.5% Triton® X-100 in 1x PBS for 20 min at room temperature. Again, cells were washed twice with 3% BSA in PBS for 5 min each. Click-iT® reaction cocktail, containing Alexa Fluor™ 488 dye, was prepared as described in the manufacturers' manual and 200 µl were added per well. The well plate was rocked briefly to ensure even distribution followed by 30 min incubation at room temperature protected from light. After the click reaction, cells were washed once with 3% BSA in 1x PBS and subsequently with 1x PBS only for 5 min each. For DNA staining, the provided Hoechst 33342 solution was diluted 1:2000 in 1x PBS and 200 µl were added per well. Cells were incubated for 30 min at room temperature protected from light. Afterwards, cells were washed twice with 1x PBS for 5 min each and once with ultrapure H_2O, before each well was mounted with one drop each of Fluoroshoield histology mounting medium. Plates were left protected from light to dry. Fluorescence pictures were acquired using the LSM 880 confocal microscope (Zeiss) or the Keyence BZ-X800 microscope.

2.2.9 Housing conditions of mice

Mice were purchased at an age of five weeks from Charles River and allowed to acclimatize for one week. They had access to water and feed *ad libitum* and were kept in a 12 h day/night rhythm under specific pathogen-free conditions. The performed animal studies were approved by the animal welfare authority. All mice were handled in accordance with the Principles of Laboratory Care and the guidelines stipulated by the Society of Laboratory Animal Science (81-02.04.2020.A261, Gesellschaft für Versuchstierkunde, GV-SOLAS, Germany).

2.2.10 Doxycycline treatment of mice

In order to induce the EDI3-targeting or scrambled shRNA expression in HCC1954_Luc cells that were injected into mice to produce tumors or metastases, mice were treated with Dox. In the course of this work, two different application routes that were reported to result in successful induction of inducible gene expression in mouse xenograft models, were used (Cawthorne et al., 2007; Eger et al., 2004). Dox was administered to the mice either by a 625 mg/kg Dox containing diet (Ssniff) *ad libitum* or dissolved in drinking water. Fresh Dox containing water (7.5 mg/ml Dox in combination with 1% sucrose) was prepared every three days and constantly protected from light.

2.2.11 Cell line-derived xenograft models

Cell line-derived xenograft (CDX) models are based on the implantation of human tumor cells into immunodeficient mice to avoid graft versus host reaction of the mouse against the human tumor tissue. In this work, subcutaneous tumors were created to investigate a role for EDI3 in

primary tumor growth, whereas cell injection into the peritoneum or the tail vein provided information about EDI3's influence on metastasis formation in the peritoneal cavity and the lungs, respectively.

2.2.11.1 Preparation of cells

Cells were cultivated in T175 flasks resulting in a confluency of approx. 90% on the day of injection. If required, EDI3 knockdown or scrambled shRNA expression was induced with 0.1 µg/ml Dox 3-5 days in advance. Directly before injection, cells were washed with 1x PBS followed by trypsinization for 5 min at 37 °C. Cells were resuspended in full media and an aliquot was taken to confirm EDI3 knockdown on both RNA and protein level. Therefore, 1 ml of cell suspension was transferred into 1.5 ml tubes and pelleted at 800 x g for 5 min. The supernatant was aspirated, and the cell pellet was resuspended in 600 µl RLT lysis buffer for RNA analysis or 200 µl RIPA lysis buffer containing 1:100 protease inhibitor and phosphatase cocktail II and III for protein analysis. Lysates were vortexed and further processed as described in 2.2.15.1 and 2.2.16.1.1. The cell number of the remaining cell suspension was determined using the CASY-TT cell counter and cells were pelleted by centrifugation at 800 x g for 5 min. The cell pellet was resuspended with the appropriate amount of 1x PBS and/or Matrigel to result in the dilution necessary for the different routes of injection as described below.

2.2.11.2 Subcutaneous injection

Cells were cultivated and prepared as described in 2.2.11.1. The obtained cell pellet was resuspended in either 100% or 50% Matrigel. Matrigel was thawed overnight on ice and was handled on the day of injection only with pre-cooled tubes and pre-cooled cut 1000 µl pipette tips. For injection with 100% Matrigel, the appropriate amount was added directly to the cell pellet. For injection in 50% Matrigel (1:1 Matrigel/1x PBS), the cell pellet was resuspended in ice cold 1x PBS before the same volume of Matrigel was added. The cell suspension was mixed by carefully pipetting up and down and subsequently kept on ice. Directly before injection the cell suspension was mixed again by flicking and inverting the tube. Syringes were prepared under sterile conditions. Five million HCC1954_Luc cells in 150 µl were injected subcutaneously into the flank of six- to eight-week-old female CD1 nude or NSG mice. Tumor size was determined twice per week using a digital caliper and volume was calculated by $(L \times W^2)/2$ (Faustino-Rocha et al., 2013).

To induce expression of EDI3-targeting shRNA, cells and mice were pretreated with Dox three days in advance. Fluorescence imaging was performed as described in 2.2.13 to confirm successful Dox-induction based on the measured tRFA signal.

2.2.11.3 Tail vein injection

Cells were cultivated and prepared as described in 2.2.11.1 and subsequently resuspended in ice cold 1x PBS to obtain a dilution of 10 million cells/ml. The cell suspension was kept on ice until injection. Six- to eight-week-old female CD1 nude mice were placed into a mechanical restraint device with the tail protruding to make it accessible for injection. The tail was dipped in warm water to obtain better visibility due to vasodilation. Directly before injection, the cell suspension was mixed by inverting the tube several times. The tail was wiped with antiseptic solution and one million HCC1954_Luc cells with Dox-induced EDI3 knockdown vs. untreated control in 100 µl were injected into the lateral tail vein. The mice were removed from the restrainer and the luminescence signal was measured 10 min, 6 h and 24 h after injection using the IVIS Spectrum *In Vivo* Imager (PerkinElmer) as described in 2.2.13.

2.2.11.4 Intraperitoneal injection

All cells were cultivated and prepared as previously described (2.2.11.1). The cell pellet was resuspended in ice cold 1x PBS resulting in a dilution of 10 million cells/ml and kept on ice. Directly before injection the cell suspension was mixed by inverting the tube several times and syringes were prepared under sterile conditions. One million HCC1954_Luc cells in 100 µl 1x PBS were injected intraperitoneally into six- to eight-week-old female CD1 nude and NSG mice. To investigate the influence of EDI3 on metastasis formation, the expression of EDI3-targeting and scrambled non-targeting shRNA was induced in cells and mice three days before injection. Dox was administered to the mice in a Dox containing diet as described in 2.2.10. Luminescence signal was measured every one to two weeks using the IVIS Spectrum *In Vivo* Imager as described in 2.2.13. Mice were observed daily, and their overall condition was scored and tallied according to the conditions stipulated in the scoresheet, such as weight loss, ascites formation, abnormal behavior and unusual physical appearance. Once terminal endpoints were reached, mice were sacrificed, and autopsy was performed to analyze the spread of metastases.

For the timed organ collection six and eight weeks after intraperitoneal injection of the cells, mice were sacrificed after final *in vivo* luminescence imaging was performed and organs were collected and analyzed by *ex vivo* imaging as described in 2.2.14.

2.2.12 Preparation of luciferin solution for *in vivo* imaging

D-luciferin is a molecule which can be found in organisms that generate bioluminescence. ATP dependent oxidation of luciferin by firefly luciferase enzyme leads to the production of light. Since luciferin can penetrate cell membranes, it is suitable for *in vivo* imaging of cells that have been transformed to express luciferase. Fresh luciferin solution was prepared by dissolving

appropriate amounts of D-luciferin potassium salt (PerkinElmer) in 1x PBS to obtain a concentration of 15 mg/ml. The solution was sterile filtrated using a 0.2 µm filter and protected from light. To ensure stable luminescence signal, the solution was used within two weeks while avoiding repeated freezing and thawing.

2.2.13 *In vivo* imaging

Prior to luminescence imaging 10 µl/g body weight of luciferin solution were injected intraperitoneally into mice and allowed to distribute for 10 min. Three minutes before imaging, mice were placed into a chamber and anesthetized by inhalation of isoflurane in oxygene (2.5% (v/v)) at a flow of 1 l/min. Afterwards, the mouse was transferred into the IVIS Spectrum *In Vivo* Imager (PerkinElmer) and orientated in dorsal view for imaging of subcutaneous tumors located at the flank or in ventral view for imaging of lung and peritoneal metastasis. Ten minutes after luciferin injection the luminescent signal was measured by a CCD camera.

To confirm the Dox-induced expression of tRFP, the fluorescence signal was measured at a wavelength of 620 nm. No luciferin was administered prior to fluorescence imaging, as the emission interferes with the tRFP channel.

All results were evaluated using the Living Image® 4.7.2 software.

2.2.14 *Ex vivo* imaging

Organs were imaged to analyze the distribution of metastasis six and eight weeks after intraperitoneal injection of HCC1954_Luc cells comparing induced EDI3 knockdown to non-induced control cells. Directly after the last *in vivo* imaging was performed as described in 2.2.13, the mice were sacrificed by cervical dislocation. Ascites fluid, if present, was extracted using a syringe with a 26 G canula. Mice were fixed in a dorsal position on a surgical table and the abdominal cavity was opened longitudinally. Liver, diaphragm, kidneys, the complex of stomach, spleen, and pancreas, as well as the two gonadal white adipose tissues were excised and washed in 1x PBS in a petri dish. The organs were placed on a black non-reflecting Lexan foil, transferred into the IVIS Spectrum imager and luminescence was measured approx. 20 min after the mice were injected with luciferin. Afterwards, macroscopically visible tumors were counted, excised from the organs and their weight was determined. Imaging results were evaluated using the Living Image® 4.7.2 software.

2.2.15 Gene expression analysis

2.2.15.1 RNA isolation from cell culture

For RNA isolation from cells lines, the RNeasy kit (Qiagen) was used. Thereby, either 300 µl (24-well plate) or 600 µl (6-well plate) RLT lysis buffer was added per well. Cells were scraped and collected in 1.5 ml tubes. Cell lysates were vortexed for 30 sec and stored at -80 °C until further isolation. For RNA precipitation, lysates were thawed on ice, one volume 70% ethanol was added and mixed carefully by pipetting. The samples were transferred to mini-spin columns and centrifuged for 30 sec at 9,000 x g. The filtrate was discarded, and the columns were washed once with 350 µl RW1 buffer. For DNase treatment the RNase-Free DNase Set (Qiagen) was used. DNase I was reconstructed by adding 550 µl RNase free water to the lyophilized enzyme. Per RNA sample, a mixture of 10 µl DNase I and 70 µl RDD buffer were premixed, added to the column and incubated for 15 min at room temperature. Total RNA was then washed and eluted in RNase free water according to the manufacturers' protocol. RNA concentration was determined with a spectrophotometer (NanoDrop 2000) and samples were stored at -80 °C.

2.2.15.2 RNA isolation from tumor tissue

Snap-frozen pieces of tumor tissue were transferred into RNase-free 1.5 ml tubes containing 600 µl ice cold RLT lysis buffer. During the whole procedure, tubes were kept on dry ice. Per tube 6 µl β-mercaptoethanol was added and pestles were used to manually grind the tumor tissue. Once well ground, tubes were vortexed for 30 sec and lysates were added to Qiashredder columns. After centrifugation at 9,000 x g for 30 sec, RNA isolation from the filtrate was performed using the RNeasy kit and DNase treatment as described in 2.2.15.1.

2.2.15.3 cDNA synthesis

Prior to gene expression analysis by quantitative real-time polymerase chain reaction (qRT-PCR), isolated RNA was converted into complementary DNA (cDNA). For this purpose, the high capacity cDNA reverse transcription kit (Applied Biosystems) was used according to the manufacturers' instructions. Per reaction 500 ng – 2 µg RNA were mixed with a master mix containing the appropriate amounts of 10x RT-Buffer, 10x random primers, 25x dNTP mix and reverse transcriptase. DEPC water was used to adjust the total volume to 20 µl. The conditions for the subsequent PCR are listed in Table 2.21. After reverse transcription, all samples were diluted with DEPC water to a final concentration of 10 ng/µl and stored at -20 °C.

Table 2.21: Conditions for reverse transcription polymerase chain reaction

Step	Temperatur	Time
Incubation	25 °C	10 min
Reverse transcription	37 °C	120 min
Inactivation	85°C	5 min
Pause	4°C	∞

2.2.15.4 Quantitative real-time polymerase chain reaction

Quantitative real-time polymerase chain reaction (qRT-PCR) is a sensitive technique to detect and quantify alterations in gene expression of a target gene (Higuchi et al., 1993). In this work, the non-specific fluorescent dye SYBR green (QuantiFast SYBR® Green PCR Kit, Qiagen) was used to quantify the PCR products of gene specific oligonucleotides. As SYBR green intercalates into double stranded DNA, the intensity of the fluorescent signal measured after each PCR cycle is proportional to the amplified DNA concentration. The fluorescence is illustrated as a function of time and so-called Ct values. The latter describe the number of cycles necessary until the measured fluorescent signal crosses a threshold and enters the exponential phase and are used for quantification.

All gene expression measurements were performed with a 7500 Real-Time PCR System (Applied Biosystems) and all samples were measured at least in technical duplicates. Per reaction, 50 ng cDNA were mixed with 2x QuantiFast® SYBR Green reagent and 10x QuantiTect Primer Assay. The total reaction volume was adjusted to 25 µl with DEPC water. For each primer assay a negative control using water instead of cDNA was included. The standard conditions for the amplification are listed in Table 2.22.

Table 2.22: Parameters for QuantiFast SYBR® Green assays

Step	Temperature	Time	Cycles
	50 °C	2 min	1
Activation of DNA polymerase	95 °C	5 min	1
DNA Denaturation	94 °C	10 sec	40
Annealing and Elongation	60 °C	30 sec	

The $2^{-\Delta\Delta Ct}$ method (Livak & Schmittgen, 2001) was used to calculate the gene expression levels. This method for relative quantification compares the Ct values of the gene of interest (GOI) and of a housekeeping gene (HKG). Housekeeping genes are used as endogenous controls, and are characterized by their stable expression that is not affected by stress or modified

experimental conditions. In this work, the expression of *ACTB* or *18S* was used to normalize the expression of the GOI ($\Delta Ct = Ct_{GOI} - Ct_{HKG}$). For normalization, the ΔCt values of the treated samples were compared to an untreated control ($\Delta\Delta Ct = \Delta Ct_{treated} - \Delta Ct_{untreated}$). In a last step, $2^{-\Delta\Delta Ct}$ was applied to calculate the relative expression. Values >1 indicate an upregulation while values <1 indicate a downregulation of the GOI compared to the control.

2.2.16 Protein analysis

2.2.16.1 Protein extraction

In this work, proteins were extracted from tumor tissue, as well as from cell lines. Therefore, tissue and cells were lysed with RIPA lysis buffer containing 1:100 protease inhibitor and phosphatase cocktail II and III. All protein samples were stored at -80 °C.

2.2.16.1.1 Protein extraction from cell culture

Cell culture well plates were placed on ice and medium was aspirated. Cells were rinsed once with 1x PBS. Depending on the size of the well, 100 µl (24-well) or 200 µl (6-well) RIPA buffer were added. Cells were incubated for 1 min on ice, detached with a cell scraper and transferred into pre-cooled 1.5 ml tubes. After vortexing followed by 30 min rotation at 4 °C, cell lysates were centrifuged for 20 min at 15,000 x g and 4 °C. The supernatant containing soluble proteins was transferred into new tubes.

2.2.16.1.2 Protein extraction from tumor tissues

Pieces of tumors were kept in 1.5 ml tubes on ice and 300 µl RIPA buffer was added. The tissue was homogenized with a pestle and disrupted by sonification in a sonification bath for 3x 10 sec. After rotation for 1 h at 4 °C, the homogenates were centrifuged for 20 min at 15,000 x g and 4 °C. The supernatant was transferred into new tubes.

2.2.16.2 Protein quantification

To determine the protein concentration of the lysates the bicinchoninic acid (BCA) protein assay (Thermo Fisher Scientific) was used. In this assay, Cu^{2+} is reduced to Cu^{+} by peptide bonds under alkaline conditions as described by the Biuret reaction, followed by colorimetric detection of Cu^{+} with BCA. In detail, one Cu^{+} molecule and two BCA molecules form a purple chelate complex with an absorbance at 562 nm that is proportional to the protein concentration (Smith et al., 1985).

A standard curve of bovine serum albumin (BSA), ranging from 0 µg/ml to 2 mg/ml was prepared from a 2 mg/ml stock solution. Protein lysate samples were diluted 1:5 with ultrapure water. 5 µl each of standards and diluted samples were pipetted in triplicates into a 96-well

plate. Per well, 195 µl BCA working reagent consisting of 49 parts of solution A and one part of solution B were added. The plate was incubated at 37 °C for 30 min prior to measuring the absorbance at 562 nm in a plate reader (Infinite M200 Pro, Tecan). The protein concentration was calculated based on the BSA standard curve.

2.2.16.3 Western Blot

2.2.16.3.1 Sodium dodecyl sulfate polyacrylamide gel electrophoresis

For protein analysis sodium dodecyl sulfate polyacrylamide gel electrophoresis (SDS-PAGE) was performed. This technique allows to separate proteins only based on differences in their molecular weight (Shapiro et al., 1967).

1.5 mm thick 10% separation gels were freshly cast using the Mini-PROTEAN tetra electrophoresis system (BioRad). First, the separation gel was prepared as described in Table 2.23, mixed thoroughly and cast between two glass plates within a vertical frame. To avoid oxidation and evaporation, each gel was covered with 600 µl of 2-propanol. After polymerization was complete, the 2-propanol was carefully removed. The stacking gel was prepared according to Table 2.23 and cast on top of the separation gel. Combs, providing 10 or 15 loading wells, were added directly after casting. Gels were wrapped in damp paper towels and stored at 4 °C for up to two weeks.

Table 2.23: Gel preparation for SDS-PAGE

Components	**Per separation gel**	**Per stacking gel**
Ultrapure water	4 ml	4.8 ml
30% (v/v) Acrylamide solution	3.3 ml	1 ml
Separation buffer	2.5 ml	-
Stacking buffer	-	825 µl
10% (w/v) SDS	100 µl	67.5 µl
TEMED	4 µl	5 µl
10% (w/v) APS	100 µl	100 µl

For the gel electrophoresis equal amounts of protein from each sample were mixed with 4x Laemmli-buffer, denatured at 95 °C for 5 min and briefly centrifuged. The prepared gels were placed in a chamber filled with 1x Tris/Glycine/SDS Buffer and loaded with 6 µl protein standard (Precision Plus Protein Dual Colour Standard, BioRad) as well as with the denatured protein samples. Initially, a current of 20 mA/gel was applied, which was increased to 30 mA/gel once the samples reached the separation gel.

2.2.16.3.2 Protein transfer on PVDF membrane

After the protein separation by SDS-PAGE, proteins were transferred onto a polyvinylidene difluoride (PVDF) membrane for subsequent immunodetection. For this purpose, the Trans-Blot® SD Semi-Dry Transfer Cell® (Bio-Rad) was used. Per gel, three sheets of extra thick blot filter paper were equilibrated in the anode buffer and one sheet in the cathode buffer. The PVDF membrane was briefly activated in methanol and then transferred into the anode buffer. The gel was removed from the glass plates and equilibrated in cathode buffer. After equilibration, the three blotting papers soaked with anode buffer were placed on the anode plate of the transfer chamber. The activated membrane was placed on top, followed by the gel and the blotting paper soaked in the cathode buffer. After each layer was placed, air bubbles were carefully removed with a roller. The chamber was closed with the cathode plate and the protein transfer was performed for 30 min at 0.23 A per gel (5 mA/cm^2). Afterwards, the membrane was briefly washed in ultrapure water. To confirm successful protein transfer, the membrane was stained for 30 sec in Ponceau S followed by washing in ultrapure water to remove excess staining. To completely destain the membrane prior to the following steps of protein detection (2.2.16.3.3), the membrane was washed in 1x TBS-T.

2.2.16.3.3 Immunodetection

To block unspecific binding of antibodies, the membrane was incubated in either 5% BSA or 5% milk powder, depending on the primary antibody, in 1x TBS-T for 2 h. Subsequently, the membrane was incubated with specific primary antibodies diluted in blocking solution, overnight at 4 °C and constantly shaken. On the next day, the membrane was washed three times with 1x TBS-T for 10 min each followed by incubation with the secondary horseradish peroxidase (HRP) linked antibody, likewise diluted in blocking solution, for 2 h at room temperature. Information about all antibodies used and their appropriate dilutions in blocking solution are listed in Table 2.24. After the membrane was washed again three times with 1x TBS-T for 10 min each, protein detection was performed by chemiluminescence. Therefore, the membrane was placed into 5 ml enhanced chemiluminescence solution (ECL) to which 3 µl hydrogen peroxide was added. The HRP conjugated to the secondary antibody catalyzes the oxidation of luminol, which leads to the emission of light at 428 nm. The emitted light, illustrating the specific signal for the protein of interest, was detected using the Blot-Imager Vilber Fusion Fx7 (Vilber Luormat). If required, the probed antibodies were removed from the membrane by incubation in stripping buffer for 30 min at room temperature. Afterwards, the membrane could be blocked again and used for the analysis of additional proteins. For densitometric analysis of the protein signals, the software ImageJ was used.

Table 2.24: Parameters for antibody incubation (western blotting)

Primary antibody	Secondary antibody	Dilution	Incubation
anti β-actin	anti mouse	1:1500/1:10000 in BSA	ON 4 °C/ 2 h RT
anti EDI3	anti mouse	1:1000/1:9000 in milk	ON 4 °C/ 2 h RT
anti RFP	anti rabbit	1:1000/1:5000 in milk	ON 4 °C/ 2 h RT

Abbreviations: ON, overnight; RT, room temperature

2.2.17 Quantification of metabolites

2.2.17.1 Metabolite extraction from cell culture

The aim of this experiment was to investigate if inducibly silencing EDI3 in HCC1954_Luc cells leads to changes in intracellular metabolites, particularly in EDI3's substrate glycerophosphocholine (GPC), its direct products glycerol-3-phosphate (G3P) and choline, as well as in related downstream metabolites. Therefore, cells were plated in 6-well plates and EDI3 knockdown was induced as described in 2.2.5.2. After 72 h, well plates were placed on ice, medium was aspirated, and cells were washed with ice cold 1x PBS thrice. After the last washing step, PBS was removed, and cells were snap-frozen by placing the well plates on a thin layer of liquid nitrogen to ensure that metabolism is stopped immediately. Ice cold methanol spiked with internal standards was added to the wells. Cells were scraped, collected in 1.5 ml tubes, and kept on ice. Once the collected cell debris settled at the bottom of the tube, methanol supernatant was used to rinse the well a second time, to ensure collection of the maximum amount of metabolites. All extracts were stored at -80 °C until further processing. Choline metabolites were either measured directly (2.2.17.2) or after fractionation using the SIMPLEX protocol (2.2.17.3). Replicate wells for all conditions were used to determine the cell number per well. Therefore, media was removed, cells were rinsed once with 1x PBS and subsequently detached by trypsin/EDTA treatment for 5 min at 37 °C. Cells were resuspended in media and total cell number per well was determined using the CASY-TT cell counter.

2.2.17.2 LC-MS analysis of cell culture extracts

The extracted metabolite samples (2.2.17.1) were centrifuged at 21,100 x g for 3 min at room temperature before 20 µl of the supernatant was transferred to the vials used for LC-MS/MS analysis. Internal standards were used to create calibration curves ranging from 5-100 nmol/l for glycerophosphocholine and choline and from 50-1,000 nmol/l for phosphocholine. 2 µl per sample were subjected to LC-MS/MS on a QTrap 5500 triple quad mass spectrometer (Sciex) operated in positive mode, directly coupled to a UFLC system (Shimadzu). Selected-reaction-monitoring was used with the parameters stated in Table 2.25. The samples were injected into

a 150 mm long 3 mm I.D. Nucleoshell HILIC column with 2.7 µm particle diameter. All samples were separated isocratically in 50% solvent B (solvent A: acetonitrile; solvent B: 50% methanol, 5 mM ammonium formate) using a flow rate of 500 µl/min within 10 min. All data were interpreted using the Skyline Daily software (Adams et al., 2020).

Table 2.25: Transition data for measurement of choline-related metabolites

Analyte	Q1 mass [Da]	Q3 mass [Da]	Mode
choline	104.1	60.1	positive
d_9-choline	113.2	69.1	positive
phosphocholine	184.1	86.1	positive
d_9-phosphocholine	193.1	95.2	positive
glycerophosphocholine	258.1	125.0; 104.1; 86.1	positive
d_9-glycerophosphocholine	267.2	113.2	positive

2.2.17.3 LC-MS analysis of fractionated cell culture extracts (SIMPLEX)

The extracted metabolite samples (2.2.17.1) were fractionated using the simultaneous metabolite, protein, lipid extraction (SIMPLEX) protocol (Coman et al., 2016). Briefly, samples were supplemented with 300 µl of cold methyl-tert-butyl-ester (MTBE) and incubated at 4 °C for 1 h under agitation. 80 µl aqueous 0.1% ammonium formiate was added to induce phase separation and samples were centrifuged at 10,000 x g for 5 min. The upper phase (fraction 1), which contains most of the lipids, was collected, dried under nitrogen flow, and stored until reconstitution at -20 °C. The lower phase was mixed with 220 µl methanol and incubated for 2 h at -20 °C to achieve complete protein precipitation followed by centrifugation at 21,000 x g for 5 min. The supernatant (fraction 2), which contains choline metabolites as well as some lipids, was transferred into a new tube and evaporated to dryness. Fraction 1 was solubilized in 40 µl 80% acetonitrile/20% methanol with 1 mM phosphoric acid while fraction 2 was reconstituted using 40 µl methanol. Both fractions were measured in both positive and negative ion mode.

LC-MS/MS-analysis of the choline metabolites from fraction 2 was performed on a QExactive mass spectrometer (Thermo) directly coupled to a Vanquish Horizon UHPLC system (Thermo). From each sample, 1 µl was injected into a 125 mm long, 3 mm I.D. Nucleoshell Bluebird RP18 column with 2.7 µm particle diameter and separated using a binary gradient (solvent A: 0.1% formic acid; solvent B: 0.1% formic acid in acetonitrile) at a flow rate of 400 µl/min (0-1.5 min: 0% B; 1,5-2.5 min: 0-80% B; 2.5-4.0 min: 80% B; 4-7 min: 0% B). The mass spectrometer was operated in positive mode using the parameters presented in Table 2.25.

LC-MS/MS-analysis of the lipids contained in both fractions was accomplished on a QTrap 5500 mass spectrometer (Sciex) operating in (scheduled) MRM-mode coupled to a LC20 UFLC system (Shimadzu). Therefore, 1 µl per sample was injected into a 125 mm long, 3 mm PerfectSil Target 100 Sil column with 3 µm particle diameter. Samples were separated isocratically using 70% solvent A (acetonitrile) and 30% solvent B (50% methanol, 5 mM ammonium formiate, 0.1% formic acid) within 10 min. The settings used for lipid measurement are listed in Table 2.26.

All LC-MS/MS data were interpreted using the Skyline Daily software (Adams et al., 2020).

Table 2.26: Transition data for measurement of lipids

Analyte	**Q1 mass [Da]**	**Q3 mass [Da]**	**Mode**
16:0 lysophosphatidic acid	409.2	153.0	negative
17:1 lysophosphatidic acid	421.2	153.0	negative
32:0 phosphatidic acid	647.5	255.2	negative
17:0-14:1 phosphatidic acid	631.4	269.2	negative
16:0-16:0 diacylglycerol	586.5	313.3	positive
17:0-17:0 diacylglycerol	614.6	327.3	positive
32:0 phosphatidylcholine	734.6	184.1	positive
17:0-14:1 phosphatidylcholine	718.5	184.1	positive
16:0 lysophosphatidylcholine	496.3	184.1	positive
17:1 lysophosphatidylcholine	508.3	184.1	positive
16:0 lysophosphatidylserine	498.3	313.3	positive
17:1 lysophosphatidylserine	510.3	325.3	positive
16:0 lysophosphatidylglycerol	483.3	255.2	negative
17:1 lysophosphatidylglycerol	495.3	267.2	negative

2.3 Statistical data analysis

All experiments were performed with three or more biological replicates if not stated otherwise. The numeric numbers were represented as mean values with standard deviation or in box plots as median with the box representing 25^{th}-75^{th} percentiles and whiskers ranging from minimum to maximum. To evaluate if differences observed between conditions were significant, the unpaired T-test was applied if not mentioned otherwise. The statistical significance is indicated as follows: *, $p < 0.05$; **, $p < 0.01$; ***, $p < 0.001$ and ****, $p < 0.0001$.

3 Results

3.1 Generating luciferase-expressing cell lines for *in vivo* imaging

In vivo bioluminescence imaging is an optical molecular imaging technique that allows non-invasive detection of luciferase-expressing cells in mice. The enzyme luciferase catalyzes the oxidation of D-luciferin to oxyluciferin and thereby produces light emission that is detected at 560 nm (Deluca, 1976). By administering luciferin to mice that were injected with luciferase-expressing cancer cells, these cells can be visualized and tumor growth deep within tissues can be monitored over time. To enable the investigation of EDI3's influence on tumor growth and metastasis formation *in vivo*, in a first step luciferase-expressing breast cancer cells were generated in this thesis.

3.1.1 Generation of stable luciferase-expressing breast cancer cell lines

For the generation of stable luciferase-expressing cell lines for subsequent EDI3 silencing, HCC1954 and SkBr3 cells were chosen as they belong to the ER-HER2+ breast cancer subtype, which was shown to have especially high EDI3 expression (Keller et al., in revision). Transiently silencing EDI3 in these cells was also shown to significantly reduce viability (Keller et al., in revision). HCC1954 and SkBr3 cells were transfected with the firefly luciferase gene (*luc2*) encoding plasmid pGL4.51[*luc2*/CMV/Neo] using Lipofectamine 3000. Transfected cells were selected by the addition of G418 and cells were expanded until luciferase expression could be tested using the ONE-Glo™ Luciferase Assay System (Promega). Addition of luciferin to SkBr3_Luc and HCC1954_Luc cells resulted in high luminescence signals compared to the non-transduced parental cell lines (Figure 3.1), confirming successful transfection.

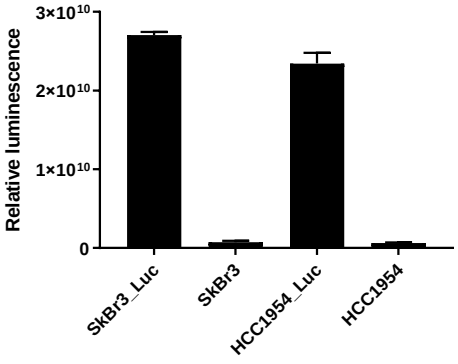

Figure 3.1: Cell lines stably-transfected with luciferase produce luminescence signal. Luciferase assay was performed with SkBr3_Luc and HCC1954_Luc cells in comparison to the non-transfected parental cell lines. Luminescence was measured 3 min after luciferin addition. Measurements represent mean ± SD of three technical replicates.

As the amount of plasmid taken up by an individual cell can vary, single cell cloning was performed to generate cell lines with a homogeneous genetic background. Once seven single cell clones per cell line were expanded, their luciferase expression was tested again by the luciferase assay. The observed intensity of the luminescence signal differed strongly among the individual clones (Figure 3.2). Only two SkBr3_Luc clones (left panel) exhibited luminescence levels equal to or higher than the stable luciferase-expressing MCF7_Luc cell line (AMSBio), which served as a positive control in this assay. SkBr3_Luc clone 1 showed the highest luminescence signal and was therefore used as the positive control in the subsequent assay with the HCC1954_Luc single cell clones (right panel). HCC1954_Luc clone 2 had a similar luminescence level as the SkBr3_Luc clone 1. Therefore, these two clones were chosen to be further tested *in vivo*.

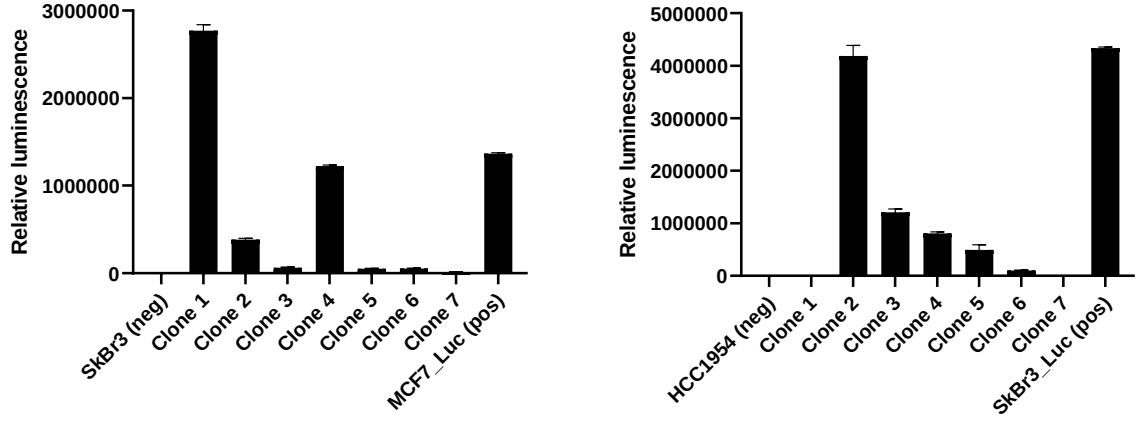

Figure 3.2: Screening of luciferase-expressing single cell clones reveals most promising clones. Luciferase assays were performed with seven clones each of SkBr3_Luc (left panel) and HCC1954_Luc (right panel). Relative luminescence was compared to non-transfected (neg) parental cell lines (SkBr3 and HCC1954) and to luciferase-expressing positive controls (MCF7_Luc and SkBr3_Luc). Luminescence was measured 3 min after luciferin addition. Measurements represent mean ± SD of three technical replicates.

3.1.2 *In vivo* validation of luciferase-expressing breast cancer cell lines

Since the cells needed to be detectable in mice for subsequent experiments, it was next tested if the cells form tumors and if their luminescence signal was strong enough to be measured by *in vivo* imaging. Therefore, five million cells per cell line were injected subcutaneously into CD1 nude mice. After five weeks, luciferin was administered to the mice and the luminescence signal was measured using the IVIS Spectrum. As shown in Figure 3.3, both cell lines formed detectable tumors. However, the signal in the SkBr3_Luc mice was very weak due to the extremely slow tumor growth (left panel), which did not increase over time (data not shown). Therefore, these cells were not further considered for the present work. In contrast,

HCC1954_Luc cells produced larger subcutaneous tumors in the same time period, and emitted a strong luminescence signal (right panel). Since the cells *in vivo* were no longer under antibiotic selection as they were *in vitro* with G418, the luminescence of HCC1954_Luc cells was next observed over the course of several weeks to ensure that the signal remains stable during long-term *in vivo* experiments.

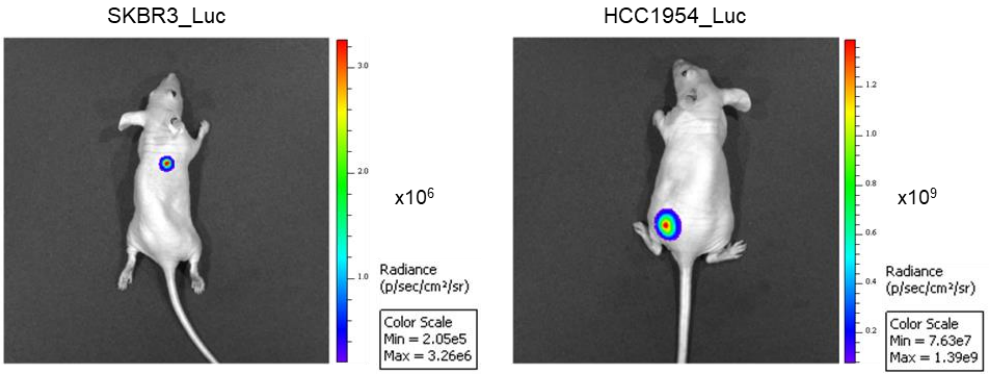

Figure 3.3: Tumors formed by luciferase-expressing cancer cell lines can be detected by *in vivo* luminescence imaging. Subcutaneous xenografts were generated in CD1 nude mice by injection of $5x10^6$ cells. After 5 weeks, mice were injected with 150 mg D-luciferin/kg body weight and luminescence signals were measured after 15 minutes using the IVIS Spectrum *In Vivo* Imaging System.

3.1.3 Luciferase expression remains stable in the absence of antibiotic selection pressure

As the cells were to be monitored in mice for up to 15 weeks for the subsequent *in vivo* experiments, it was important that the luciferase expression and thus luminescence signal remained stable over time, even if the selection antibiotic was not administered to the mice. For this reason, HCC1954_Luc cells were cultivated *in vitro* with and without G418 supplementation for 15 weeks and luminescence was measured over time by luciferase assays. The graph presented in Figure 3.4 revealed that the luminescence signal stayed stable and did not differ from G418-treated cells, even after 15 weeks without selection pressure. Thus, the results confirm that the HCC1954_Luc cells are suitable for long term experiments in mice.

Taken together, HCC1954_Luc cells were chosen over SkBr3_Luc cells to be used for the subsequent creation of the Dox-inducible EDI3 knockdown system as they provided better tumor growth and emitted a stable luminescence signal that was detectable in mice.

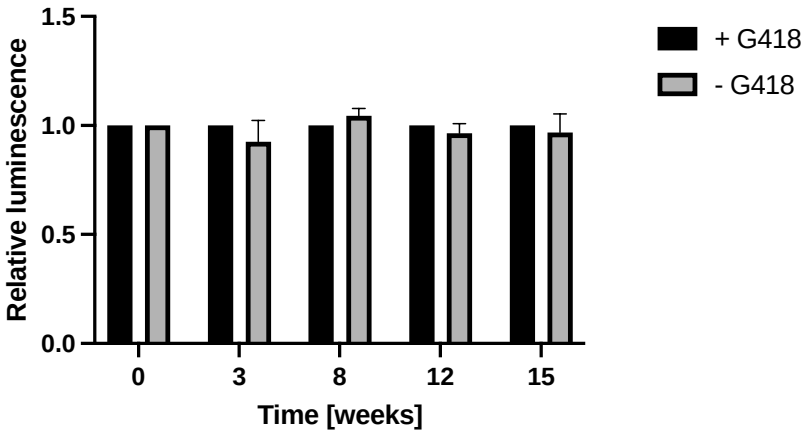

Figure 3.4: Luminescence signal remains stable in HCC1954_Luc cells in the absence of G418. Luciferase assays were performed with HCC1954_Luc cells cultured +/- G418 over time for up to 15 weeks. Luminescence was measured 3 min after luciferin addition. Measurements represent mean ± SD of three technical replicates.

3.2 Generation of doxycycline-inducible shRNA-expressing cell lines

Previous experiments using a constitutive knockdown to study EDI3 in MCF7 and AN3_CA cells resulted in compensation of the metabolite levels accompanied by minimal effect of the knockdown on the previously observed migration phenotype after cultivating the cells for longer time periods (data not published). Consequently, in this thesis the goal was to establish an inducible knockdown system to prevent the adaptation of any compensatory metabolic changes. Furthermore, a doxycycline (Dox) inducible knockdown is well suited for *in vivo* studies, as expression can be switched on or off as required, and can be maintained over longer periods of time by the administration of Dox to the mice.

In this thesis, the SMARTvector^{TM} Inducible Lentiviral shRNA system (Dharmacon) was used. These lentiviral vectors integrate into the host cell genome and contain shRNA oligos under the control of a Tet-On 3G tetracycline-inducible system (Loew et al., 2010; Zhou et al., 2006). Subsequent induction with Dox results in shRNA mediated gene inhibition, as well as the expression of the fluorescence marker TurboRFP (tRFP). In order to obtain a strong EDI3 knockdown effect, ER-HER2+ HCC1954_Luc breast cancer cells that express very high levels of EDI3 at both RNA and protein levels, as well as high EDI3 activity (Keller et al., in revision), were used.

3.2.1 Optimization of transduction conditions

The multiplicity of infection (MOI), referring to the number of virions that are added per cell during infection, is an important factor for knockdown efficiency. While higher MOIs may enhance gene silencing, they may also result in low-level gene knockdown in the absence of

Dox, which is referred to as leakiness. Thus, the optimal MOI had to be determined first, before establishing the inducible EDI3 knockdown cell lines.

For that purpose, GAPDH-targeting positive control particles were used to transduce HCC1954_Luc cells with MOIs of 0.3, 1, 3 and 5. One day after transduction, 0.5 µg/ml puromycin was added to select for successfully-transduced cells. Following the selection process, cells were induced with 0.1 µg/ml Dox, and after three days harvested for RNA analysis. *GAPDH* knockdown ranging from 80-90% was confirmed for all MOIs tested (Figure 3.5A). Higher MOIs (3 and 5) led only to a slight improvement of the knockdown efficiency compared to MOIs of 0.3 and 1. However, evaluation of the Dox-induced tRFP expression revealed that the amount of fluorescence positive cells increased with higher MOIs. Transduction with MOIs of 0.3 or 1 resulted in only 10% or 30% fluorescent cells respectively, while MOIs of 3 and 5 led to strong fluorescence signals in 80-90% of cells (Figure 3.5B). These results indicate that while a low MOI was already sufficient for a strong *GAPDH* knockdown, higher MOIs were needed to increase tRFP expression in order to enable detection of transduced cells by fluorescence. As a high number of viral particles per cell could result in increased leakiness of the promotor, it was also tested if the transduced cells showed any fluorescence expression in the absence of Dox. In Figure 3.5C, it is shown that even the highest viral copy number tested (MOI = 5) did not show any fluorescence signal, which suggests that there was no promotor leakage.

As transduction with MOIs of 3 and 5 resulted in a strong knockdown, as well as in a high level of tRFP induction, these conditions were chosen to transduce the HCC1954_Luc cells with EDI3-targeting lentiviral particles as described in the next chapter.

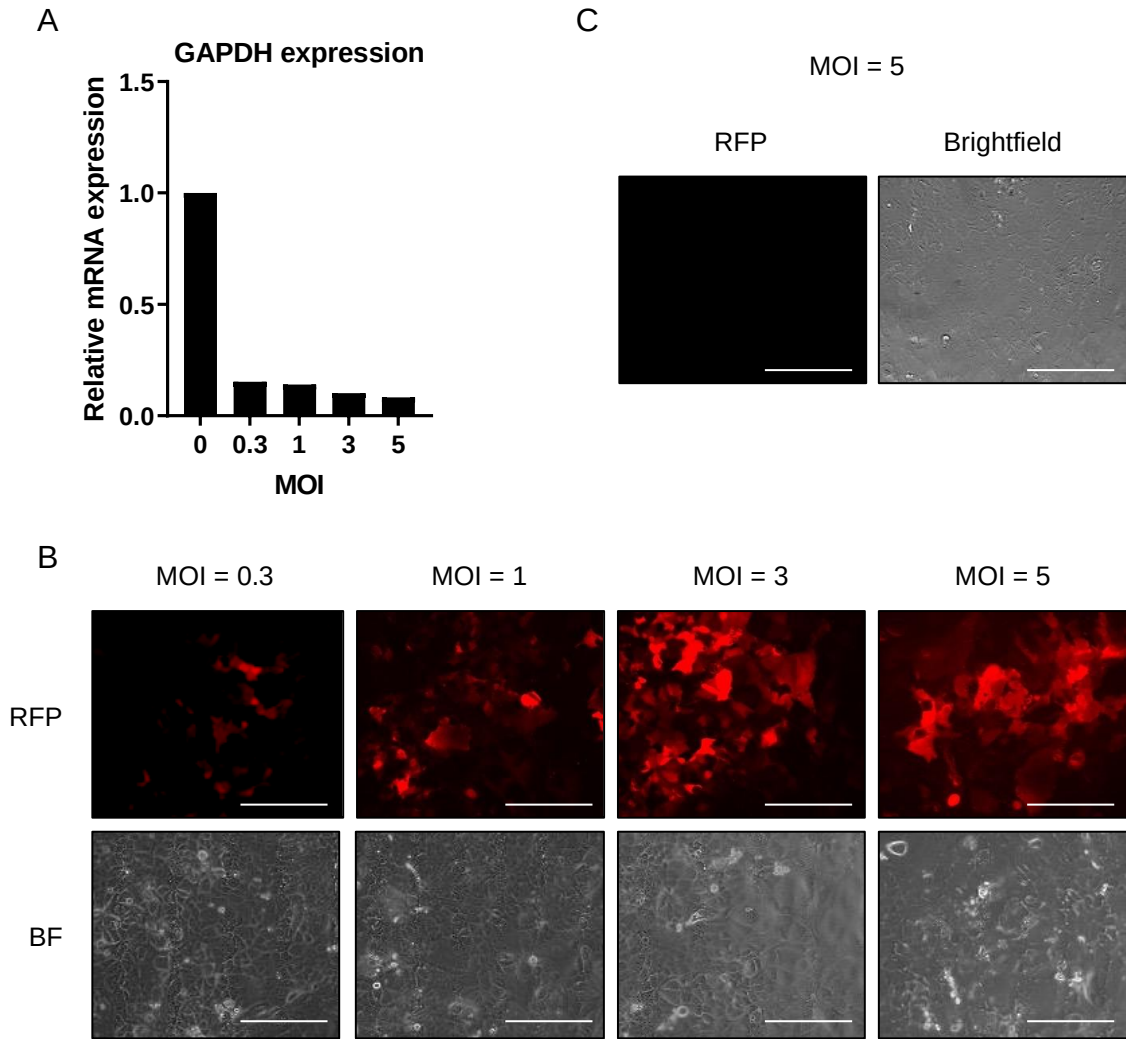

Figure 3.5: Lentiviral transduction of HCC1954_Luc cells with GAPDH-targeting shRNA results in Dox-inducible downregulation of *GAPDH* and increased expression of tRFP. HCC1954_Luc cells were transduced with different MOIs (0, 0.3, 1, 3 and 5) and selected with 0.5 µg/ml puromycin for three days, followed by induction with 0.1 µg/ml Dox for 72 h. A) RNA levels of *GAPDH* were analyzed by qRT-PCR 72 h after induction and normalized to non-transduced cells; *ACTB* was used as endogenous control. Representative fluorescence and brightfield images are shown of Dox-induced (B) and non-induced (C) cells. Scale bars represent 400 µm. MOI, multiplicity of infection; tRFP, turbo red fluorescent protein; BF, bright field.

3.2.2 Establishing a doxycycline-inducible EDI3 knockdown in HCC1954_Luc breast cancer cells

After the optimal MOI for transduction of HCC1954_Luc cells was selected on the basis of GAPDH-targeting control particles, Dox-inducible EDI3 knockdown cell lines were generated. To achieve this, HCC1954_Luc cells were transduced with lentiviral vectors encoding six different EDI3-targeting shRNA oligos (shEDI3 #1-6), as well as a non-targeting scrambled negative control oligo (shNEG) using MOIs of both 3 and 5. Successfully-transduced cells were selected with 0.5 µg/ml puromycin. EDI3 knockdown was induced with 0.1 µg/ml Dox for 72 h and *EDI3* expression was analyzed on RNA level. Results in Figure 3.6A show that oligos #1, #2 and #3 resulted in successful *EDI3* knockdown of 70-90% while oligos #4, #5 and #6 only

led to a decrease of 50% or less. As already seen in the GAPDH-targeting control particles, MOI of 5 only slightly improved knockdown efficiency compared to MOI 3 with all oligos. Furthermore, the results show that Dox itself did not alter *EDI3* expression in the non-targeting shNEG cells. Evaluation of the fluorescence signal revealed that Dox induction resulted in a strong tRFP expression in shNEG and shEDI3 #1-3 cells (Figure 3.6B). In contrast, non-induced cells did not fluoresce, which confirms that the viral transduction did not lead to a leaky expression in the absence of Dox.

Overall, three different Dox-inducible EDI3-targeting cell lines (shEDI3 #1-3), as well as one non-targeting negative control cell line (shNEG) were successfully established. In the following, EDI3 knockdown conditions were optimized as described in the next chapters.

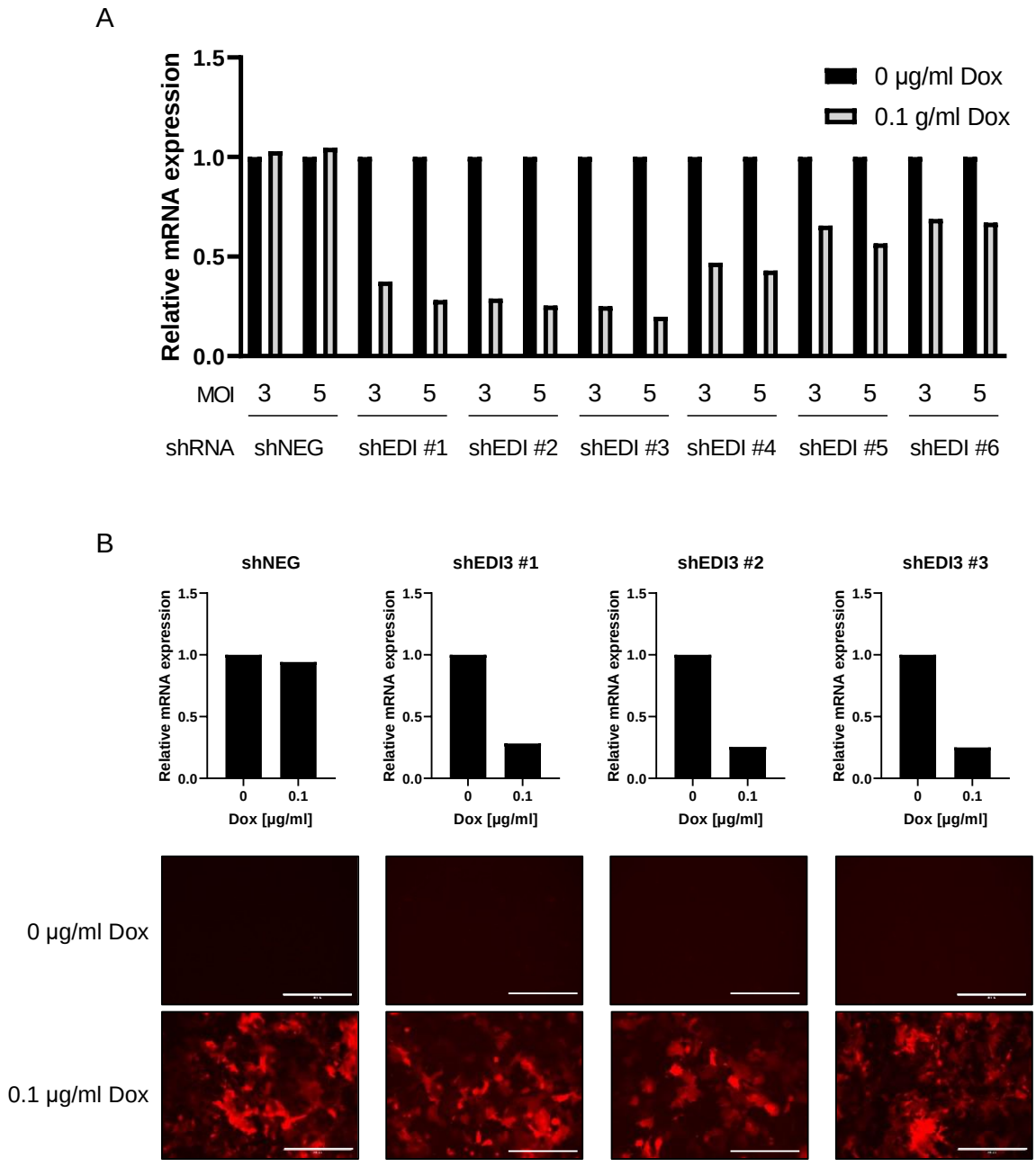

Figure 3.6: Screening of transduced HCC1954_Luc cells revealed efficient Dox-induced downregulation of *EDI3* and increased expression of tRFP with three different EDI3-targeting shRNA oligos. HCC1954_Luc cells were transduced with MOI = 3 and MOI = 5 using six shRNA oligos targeting different exons of the *EDI3* gene (shEDI3 #1-6) and a non-targeting scrambled shRNA oligo (shNEG). Transduced cells were selected with 0.5 µg/ml puromycin followed by induction with 0.1 µg/ml Dox for 72 h. A) RNA levels of *EDI3* for all tested oligos were analyzed by qRT-PCR relative to non-induced cells; *ACTB* was used as the endogenous control. B) Representative fluorescence images with corresponding *EDI3* RNA levels in shNEG cells, as well as the three cell lines with the best inducible EDI3 knockdown comparing Dox-induced and non-induced cells. Scale bars represent 400 µm.

3.3 Optimization of doxycycline-inducible EDI3 knockdown

Doxycycline (Dox) is a broad-spectrum antibiotic that belongs to the tetracycline family (Chopra et al., 1992; Gossen & Bujard, 1992). In biomedical research, it is widely used as a mediator of inducible gene expression systems. Since it was shown that Dox can cause

substantial changes in cellular metabolism and impair proliferative capacity of human cell lines in a dose-dependent way (Ahler et al., 2013), it was crucial to carefully optimize Dox-inducible systems in the current work in order to minimize the concentration of Dox used to induce shRNA expression. It was also essential to include non-targeting Dox-inducible controls (shNEG) in order to exclude any Dox-induced side effects.

3.3.1 Doxycycline induction leads to time and dose dependent reduction in EDI3 expression

In order to minimize the Dox concentration used for EDI3 knockdown induction, in a first step HCC1954_Luc shEDI3 cells were induced with two different Dox concentrations (0.01 µg/ml and 0.1 µg/ml) for different time points (6 h, 24 h, 48 h and 72 h). Successful induction was characterized by a reduction in EDI3 and an increase in tRFP expression. It could be shown that Dox treatment resulted in a time and dose dependent decrease in EDI3 protein expression with efficient knockdown after 72 h of treatment with 0.1 µg/ml Dox (Figure 3.7). Expression of tRFP was already detected after 6 h and increased over time. In addition, 0.1 µg/ml Dox resulted in a notably stronger tRFP signal than 0.01 µg/ml at all time points investigated.

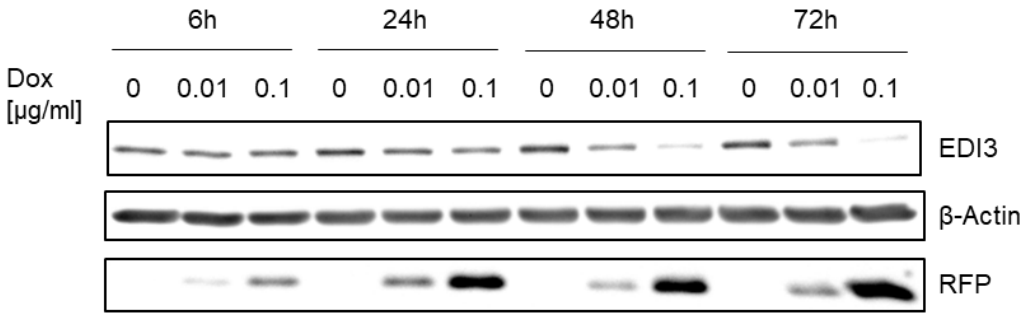

Figure 3.7: Dox-induction of EDI3 knockdown in HCC1954_Luc cells results in a time and dose dependent reduction in EDI3 protein expression and an increase in tRFP. Representative western blot of EDI3 and tRFP expression in shEDI3 #3 cells after Dox treatment compared to non-induced cells (n = 2). β-Actin was used as a loading control.

Furthermore, as presented in Figure 3.8A, dose dependent reduction in EDI3 protein expression was confirmed in two additional shEDI3 cell lines (shEDI3 #1 and #2) after treatment with three different Dox concentrations (0.01 µg/ml, 0.1 µg and 1 µg/ml) for 72 h. Moreover, mRNA expression levels in cells treated with Dox concentrations ranging from 0.01 µg/ml to 3.16 µg/ml (Figure 3.8B) revealed that 0.1 µg/ml Dox strongly improved *EDI3* knockdown compared to 0.01 µg/ml, thereby emphasizing that the higher Dox concentration is necessary for sufficient knockdown. On the other hand, the results showed that concentrations higher than 0.1 µg/ml Dox had no further effect on EDI3 downregulation. Importantly, Dox treatment alone had no effect on EDI3 expression in the non-targeting cells (shNEG) on protein (Figure 3.8A) or RNA level (Figure 3.8B). Based on these results, treatment with 0.1 µg/ml Dox for 72 h was

considered as the optimal condition for EDI3 knockdown and was used in all following experiments.

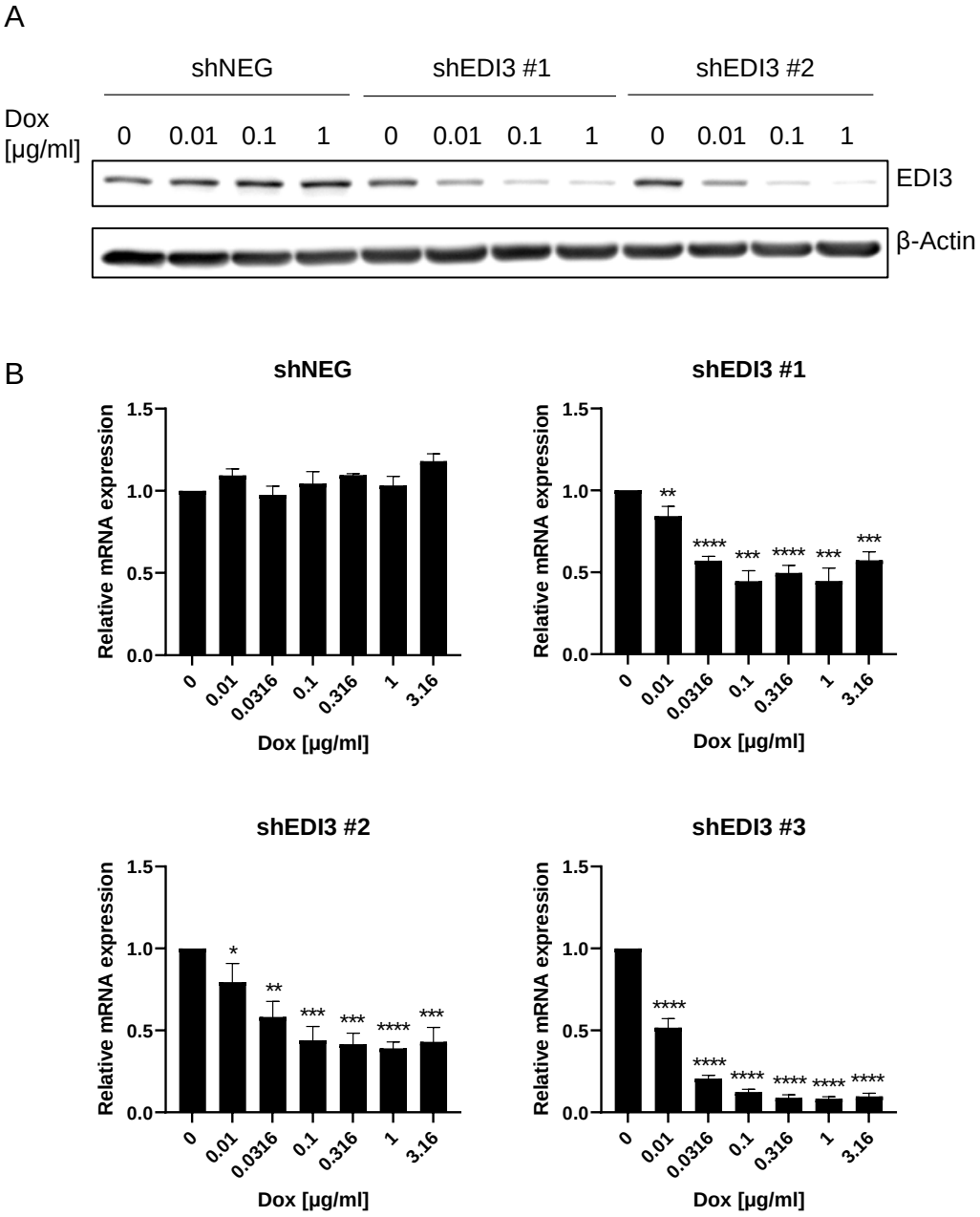

Figure 3.8: Dox-induction of EDI3 knockdown in HCC1954_Luc cells results in a dose-dependent reduction in EDI3 expression on RNA and protein level. A) Representative western blot of EDI3 expression in non-targeting (shNEG) and shEDI3 #1 & #2 cells after 72 h of Dox treatment (n = 3). β-Actin was used as a loading control. B) *EDI3* RNA expression in shNEG and three different EDI3-targeting cell lines (shEDI3 #1-3) after 72 h of Dox treatment relative to non-induced cells; *ACTB* was used as the endogenous control. Values in graphs represent mean ± SD from three independent experiments (*, $p < 0.05$; **, $p < 0.01$; ***, $p < 0.001$; ****, $p < 0.0001$).

3.3.2 Doxycycline-induced EDI3 knockdown is reversible

In order to determine the length of time the induced knockdown remained stable after removing Dox from the media and to test if expression can be fully restored, EDI3 knockdown was induced with 0.1 µg/ml Dox in three different EDI3-targeting cell lines. After 72 h, Dox was removed from the media. As illustrated in Figure 3.9A, samples for RNA analysis were collected from non-induced cells, as well as 72 h after induction and daily once Dox was removed. RNA analysis by qRT-PCR revealed that EDI3 knockdown remained stable for one day before *EDI3* expression began to increase on day two (Figure 3.9B). These results revealed that the generated cell lines were suitable for experiments that investigate the effects of restored EDI3 expression, which will be addressed in future experiments.

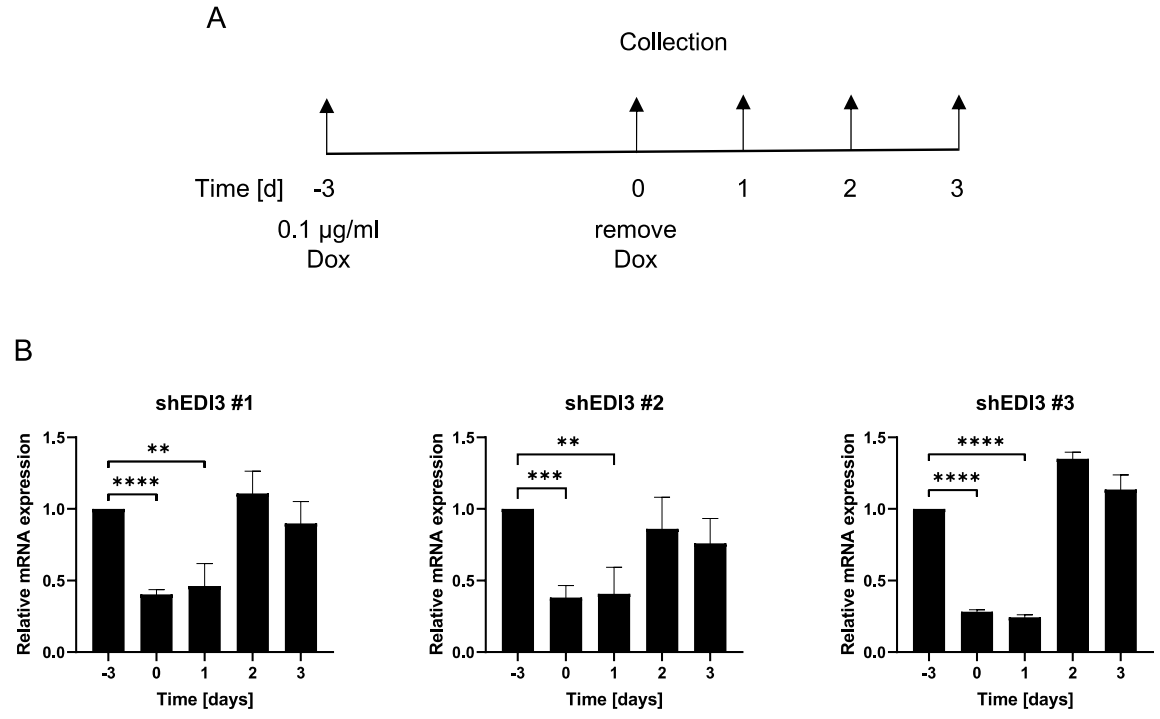

Figure 3.9: *EDI3* RNA expression in HCC1954_Luc cells is restored within two days after Dox removal. EDI3 knockdown was induced with 0.1 µg/ml Dox in three different EDI3-targeting cell lines. After 72 h, the induction media was replaced by Dox-free media. RNA samples were collected over time. A) Schematic overview of the experimental set up. B) *EDI3* RNA levels relative to non-induced cells; *ACTB* was used as the endogenous control. Values in graphs represent mean ± SD from three independent experiments (**, $p < 0.01$; ***, $p < 0.001$; ****, $p < 0.0001$).

3.4 *In vitro* characterization of doxycycline-inducible EDI3 knockdown in HCC1954_Luc cells

After successfully establishing three different Dox-inducible EDI3 knockdown cell lines in luciferase-expressing HCC1954 cells, each targeting a different exon of EDI3, and identifying the optimal conditions for Dox-induced knockdown, these cell lines were used in several cellular assays to analyze the effect of EDI3 knockdown on phenotypes that are crucial for tumor development and metastasis formation.

3.4.1 Doxycycline-induced EDI3 knockdown alters intracellular GPC/PCho ratio and glycerophospholipid metabolism

Since EDI3 hydrolyzes GPC to produce choline, which is subsequently phosphorylated by choline kinase alpha (CHKA) to form PCho, EDI3 might play a role in altered choline metabolism in cancer. In previous experiments, it was shown that siRNA mediated EDI3 knockdown in MCF7, MDA-MB-231 and AN3_CA cells resulted in increased endogenous concentrations of EDI3's substrate GPC and decreased PCho, with GPC levels being more profoundly affected than PCho levels (Marchan et al., 2017; Stewart et al., 2012). To confirm if inducible EDI3 knockdown in HCC1954 cells had similar effects, three different EDI3-targeting cell lines and non-targeting shNEG cells were treated with different Dox concentrations (0 µg/ml, 0.01 µg/ml and 0.1 µg/ml). After 72 h Dox treatment in both shNEG and shEDI3 cells, metabolites were extracted and GPC, choline and PCho levels were measured by liquid chromatography–mass spectrometry (LC-MS/MS).

In all three EDI3-targeting cell lines, Dox-induced knockdown resulted in a strong increase in GPC level (Figure 3.10), that ranged from 3- to 19-fold compared to non-induced conditions. Interestingly, the increase in GPC negatively correlated with residual EDI3 expression within the cells. Cells induced with higher Dox concentration (0.1 µg/ml) that had a consequently lower residual EDI3 expression (as it was shown in 3.3.1) had significantly higher GPC levels. Contrary to observations made previously in other cell lines (Marchan et al., 2017; Stewart et al., 2012), no decrease in choline or PCho levels was observed upon EDI3 knockdown. However, as reported in previous studies (Marchan et al., 2017; Stewart et al., 2012), there was a strong 3- to 18-fold dose-dependent increase in the intracellular GPC/PCho ratio upon EDI3 knockdown in all EDI3-targeting cell lines compared to non-induced control cells.

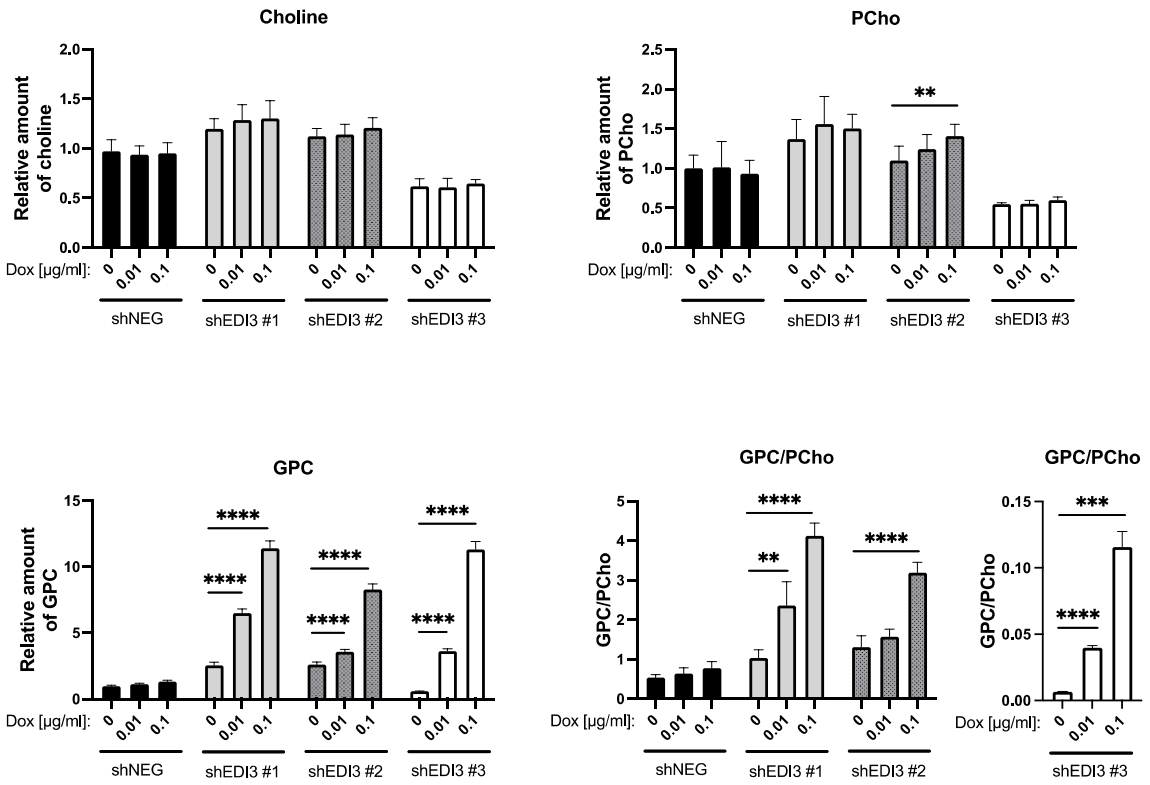

Figure 3.10: Dox-induced EDI3 knockdown in HCC1954_Luc alters intracellular GPC/PC ratio in a dose dependent manner. Metabolites were extracted after 72 h Dox treatment from three different EDI3-targeting cell lines compared to non-targeting cells (shNEG). GPC, choline and PCho levels were measured using LC-MS/MS and intracellular GPC/PCho ratios were calculated. Metabolite amounts were determined by forming the ratios of the integrated peaks of the endogenous metabolites and the internal standards. Quantities of metabolites were normalized to cell number and presented relative to untreated shNEG cells. Data represent mean ± SD from four to six technical replicates from one of at least two independent experiments (*, $p < 0.05$; **, $p < 0.01$; ***, $p < 0.001$; ****, $p < 0.0001$). PCho, Phosphocholine; GPC, Glycerophosphocholine.

In a next step, the influence of Dox-induced EDI3 knockdown on metabolites downstream of EDI3's second product glycerol-3-phosphate (G3P) was investigated. Acylation of G3P by G3P acyltransferases (GPATs) produces lysophosphatidic acid (LPA) which is further metabolized to phosphatidic acid (PA). Both LPA and PA are signaling lipids that play a role in several cellular processes, including cell migration (Geraldo et al., 2021; Momoi et al., 2020). It was reported in previous studies that transient silencing of EDI3 with siRNA in MCF7 cells led to a reduction in 16:0 LPA and 32:0 PA levels, (Marchan et al., 2017; Stewart et al., 2012). Therefore, EDI3 knockdown was induced in two different EDI3-targeting cell lines compared to non-targeting shNEG cells and the levels of metabolites related to LPA metabolism were determined by LC-MS/MS (Figure 3.11). Interestingly, with both oligos EDI3 knockdown with the highest Dox concentration resulted in a significant increase of approx. 1.5-fold in both 16:0 LPA and 32:0 PA. Furthermore, although not dramatic, levels of several lysophospholipids, namely 16:0 LPC (lysophosphatidylcholine), 16:0 LPS (lysophosphatidylserine) and 16:0 LPG (lysophosphatidylglycerol) significantly increased after EDI3 knockdown induction. Interestingly, Dox treatment of non-targeting shNEG cells resulted in a small but significant

reduction in LPS. No significant alterations were observed in diacylglycerol (16:0-16:0 DAG) and 32:0 PtdCho, which are both potential sources for 32:0 PA.

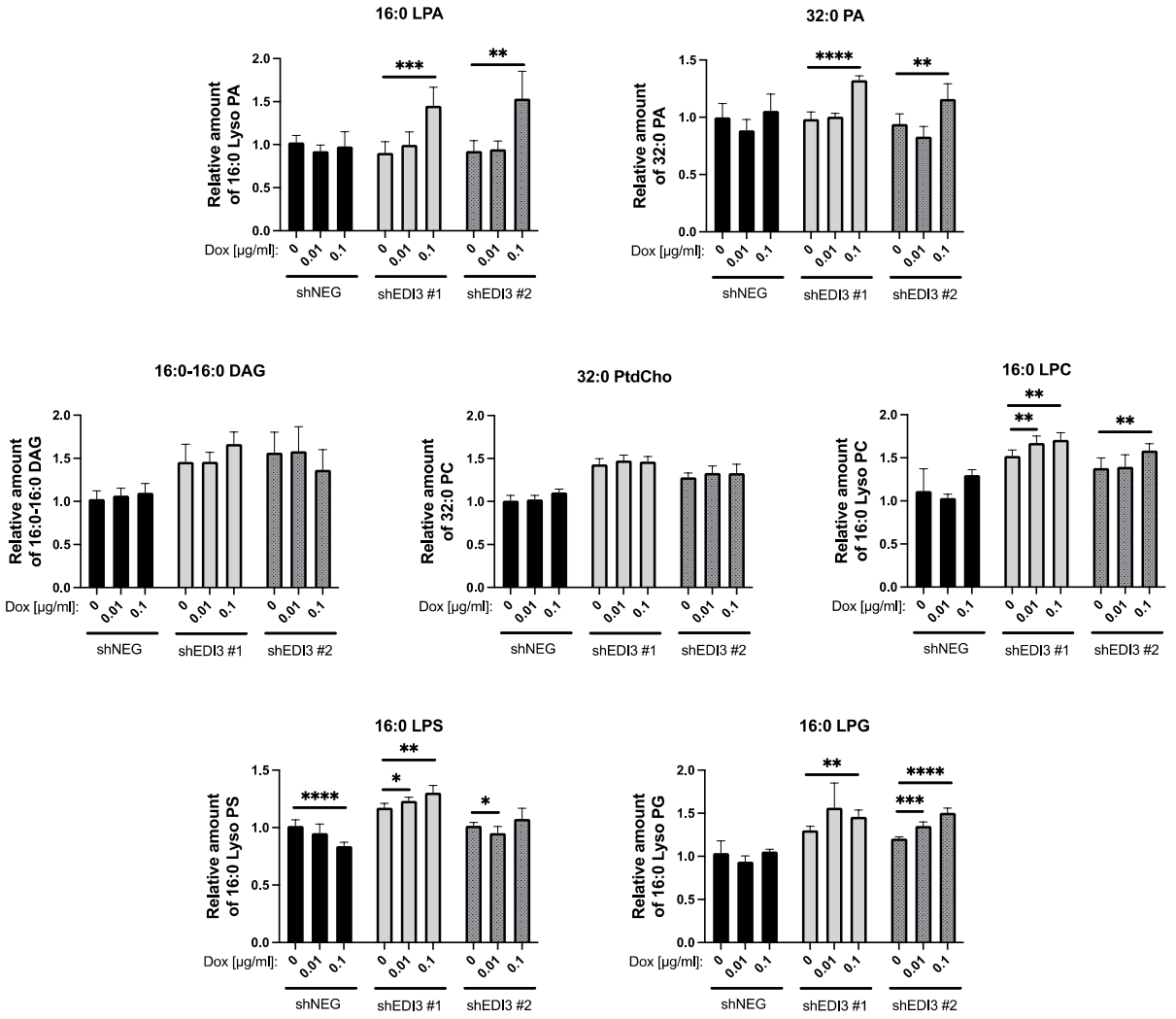

Figure 3.11: Inducibly silencing EDI3 in HCC1954_Luc cells alters intracellular glycerophospholipid levels. Metabolites were extracted 72 h after EDI3 knockdown from two different EDI3-targeting cell lines (shEDI3 #1 and shEDI3 #2) compared to non-targeting cells (shNEG). All metabolites were measured using LC-MS/MS. Metabolite levels were determined by calculating the ratios of the integrated peaks of the endogenous metabolites and the internal standards. Quantities of metabolites were normalized to cell number and presented relative to untreated shNEG cells. Data represent mean ± SD from four to six technical replicates from one of two independent experiments (*, $p < 0.05$; **, $p < 0.01$; ***, $p < 0.001$; ****, $p < 0.0001$). LPA, Lysophosphatidic acid; PA, Phosphatidic acid; DAG, Diacylglycerol; PtdCho, Phosphatidylcholine; LPC: Lysophosphatidylcholine; LPS: Lysophosphatidylserine; LPG: Lysophosphatidylglycerol.

Altogether, the observed changes in endogenous GPC/PCho ratio and glycerophospholipid levels further support EDI3 as a key enzyme linking choline and glycerophospholipid metabolism.

3.4.2 Inducibly silencing EDI3 leads to reduction in colony number and size

The colony formation or clonogenic cell survival assay is used to determine the ability of a cell to proliferate indefinitely to form a colony. Although initially developed for the field of radiobiology (Puck & Marcus, 1956), this assay has become a standard tool in cancer research to evaluate cellular growth and cytotoxicity with the formation of clones being interpreted as a characteristic of cancer cells with tumor-initiating capabilities (Munshi et al., 2005).

As described by Franken and colleagues who published a clonogenic assay protocol in Nature Protocols (Franken et al., 2006), there are different ways to perform the assay: Cells can either be pre-treated for a specified period and then re-plated at low densities, or they can be seeded at low densities before the treatment starts. To determine whether EDI3 influences colony formation and to understand mechanistically in which step of the process EDI3 is more relevant, in a first approach different time points for EDI3 knockdown induction were tested: HCC1954_Luc shEDI3 cells were either (1) pre-treated with Dox for 72 h to induce EDI3 knockdown before cells were re-plated for the assay or EDI3 knockdown was induced after re-plating. For the latter, Dox was added to the media of re-plated cells either (2) during the plating step or (3) 24 h later, when cells were already fully attached. Two different Dox concentrations were used for induction, resulting in a weaker (0.01 µg/ml) or stronger (0.1 µg/ml) EDI3 knockdown, as described in chapter 3.3.1. Colonies were fixed and stained with crystal violet after 14 days. Photographs of the colonies that were formed under the three different conditions are presented in Figure 3.12A. Quantitative analysis revealed that silencing EDI3 prior to re-plating (Dox pre-treated) resulted in a significant dose dependent reduction in colony number, and that the more efficient knockdown led to less colonies (Figure 3.12B). Furthermore, a decrease in colony size was also observed, although the latter was not significant (Figure 3.12C). When EDI3 knockdown was induced during the plating step (plated in +/- Dox) colony number also decreased in a dose dependent manner, but the effect did not reach significance. Colony size also decreased, but only with the higher Dox concentration, and this too did not reach significance. EDI3 knockdown induction 24 h after re-plating had no effect on colony formation. Together, these results indicate that EDI3 is important during the early steps of colony formation.

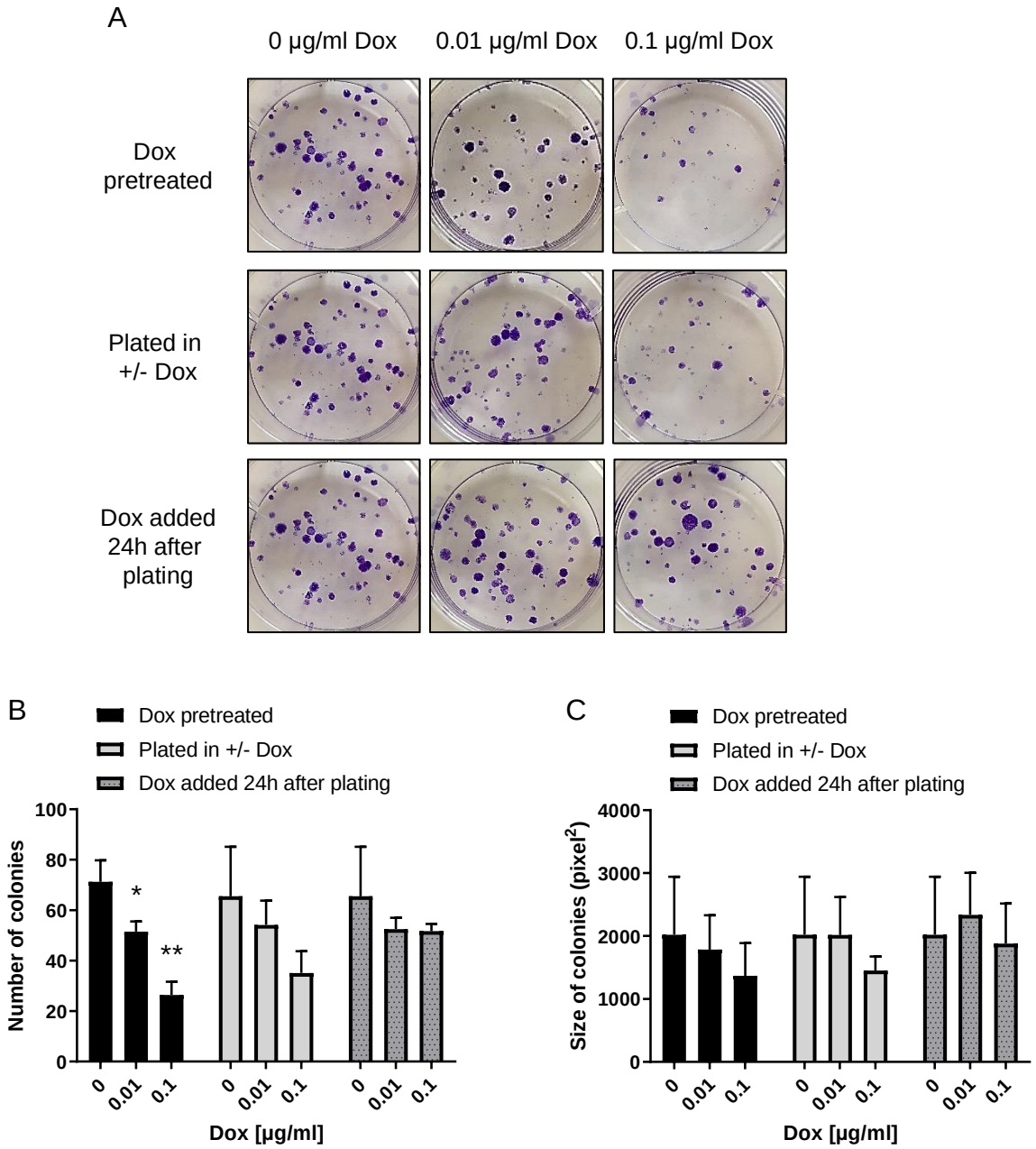

Figure 3.12: Colony formation assay reveals significant reduction in colony number only in Dox-pretreated cells. HCC1954_Luc shEDI3 #3 cells were either pretreated with Dox for 72 h before plating, or Dox was added during plating or 24 h after plating. Colonies were fixed and stained with crystal violet after 14 days. A) Representative pictures showing the formed colonies. B) & C) Quantitative analysis of colony number (B) and size (C). Values in graphs represent mean ± SD from three independent experiments (*, $p < 0.05$; **, $p < 0.01$).

As the strongest effects were achieved after pre-treatment with 0.1 µg/ml Dox, this condition was used to confirm the effect of EDI3 on colony formation by testing the three different EDI3-targeting inducible cell lines, as well as the non-targeting scrambled shRNA cells (shNEG). Photographs of the resulting colonies are presented in Figure 3.13A. Quantification of colonies confirmed that an established EDI3 knockdown at the time of cell seeding significantly reduced colony number by approx. two-third in all three different EDI3-targeting cell lines compared to

non-induced cells (0 µg/ml Dox) (Figure 3.13B). EDI3 knockdown also resulted in a reduction in colony size, which reached significance with two out of three tested oligos (Figure 3.13C).

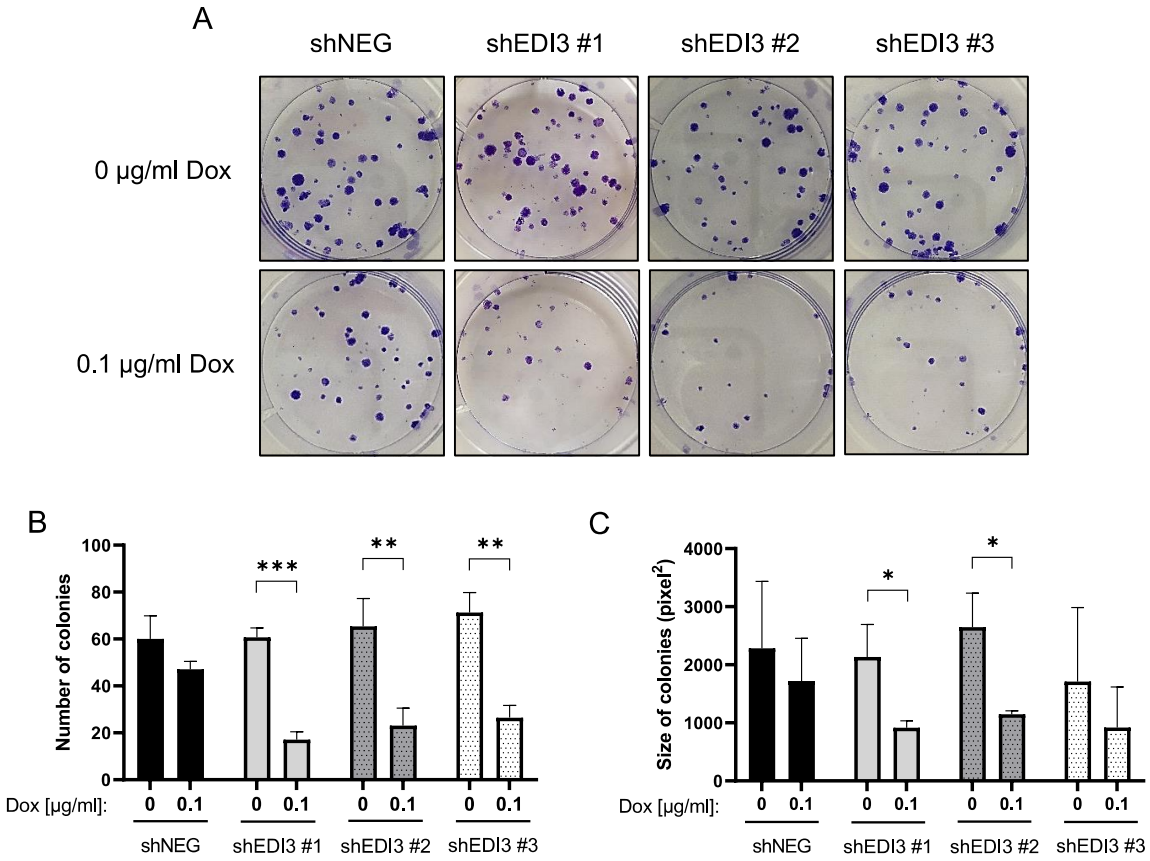

Figure 3.13: Dox-induced EDI3 knockdown in HCC1954_Luc reduces colony number and size. EDI3 knockdown was induced in three different EDI3-targeting cell lines and non-targeting cells (shNEG) before cells were replated for colony formation assay. Colonies were fixed and stained with crystal violet after 14 days. A) Representative pictures for each condition. B) & C) Quantitative analysis of colony number (B), and colony size (C). Values in graphs represent mean ± SD from three independent experiments (*, $p < 0.05$; **, $p < 0.01$; ***, $p < 0.001$).

These results confirm that EDI3 is important during the early phase of colony formation. Furthermore, they indicate that EDI3 may be relevant for the tumor-initiating capability of the cells. Based on these initial findings, subsequent experiments aimed to elucidate whether the reduced number of colonies observed upon EDI3 knockdown was due to impaired adhesion, decreased proliferation, or reduced viability of either the attached cells or cells in suspension (anoikis).

3.4.3 Inducible EDI3 knockdown shows a weak effect on adhesion

To elucidate if reduced colony formation upon EDI3 knockdown was caused by impaired adhesion, EDI3's influence on cell attachment was analyzed. Therefore, the ability of cells to attach on a fibronectin matrix was investigated based on a method that was previously established to investigate EDI3's role in adhesion (Lesjak et al., 2014).

For this purpose, two different EDI3-targeting HCC1954_Luc cell lines, as well as non-targeting shNEG cells were induced with 0.1 µg/ml Dox. After 72 h, induced and non-induced cells were harvested in FCS-free medium followed by rotation at 37 °C for one hour to allow regeneration of surface receptors after trypsinization. Then, cells were replated on a fibronectin matrix, and attached cells were stained with crystal violet 20 and 30 min after plating (Figure 3.14). For quantification, cells were subsequently destained and crystal violet absorption was measured at 570 nm. The results presented in Figure 3.14 (lower panel) show that there was a trend towards reduced adhesion when EDI3 was silenced compared to non-induced cells with both shEDI3 oligos, which reached significance only at 30 min with shEDI3 #1. Conversely, Dox treatment of the non-targeting shNEG cell line resulted in increased cell attachment, which was significant 20 min after cell seeding. Considering that Dox itself may promote adhesion, comparing the attachment of the induced shEDI3 cell lines to the induced shNEG cells indicated a significant decrease in adhesion at both time points with shEDI3 #1 oligo and a trend, albeit not significant ($p = 0.055$ at 20 min and $p = 0.064$ at 30 min), with shEDI3 #2 oligo. Thus, the results indicate that silencing EDI3 may lead to reduced adhesion, which might be obscured in this model by the adhesion-promoting effect of Dox itself.

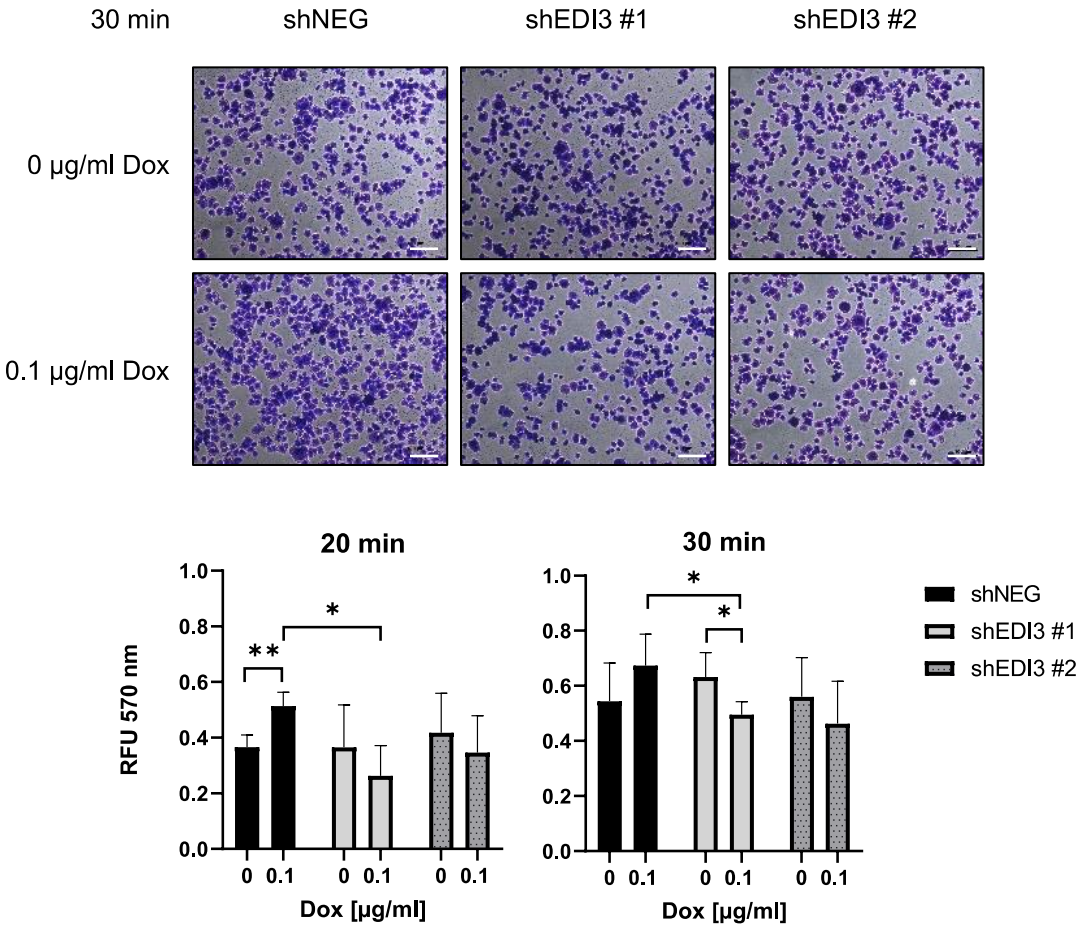

Figure 3.14: Dox-induced EDI3 knockdown in HCC1954_Luc reduces cell adhesion compared to Dox-treated control. EDI3 knockdown was induced in two different EDI3-targeting cell lines compared to non-targeting cells (shNEG) for 72 h and cells were replated on a fibronectin-matrix. Attached cells were stained with crystal violet solution 20 and 30 min after plating. Representative pictures of the 30 min time point are shown (top panel). Adhesion is shown as RFU after 20 and 30 minutes of adhesion, measured at 570 nm after destaining. Scale bars represent 100 µm. Values in graphs represent mean ± SD from three independent experiments (*, $p < 0.05$; **, $p < 0.01$). RFU, relative fluorescence units.

3.4.4 Induction of EDI3 knockdown reduces proliferation

To study if EDI3 knockdown affects cell proliferation, as indicated by the observed reduction in colony size, early time points in colony formation were investigated in more detail by analyzing the cell number per colony, as well as by labeling proliferating cells with EdU (5-ethynyl-2'-deoxyuridine), a nucleoside analog of thymidine that is incorporated into DNA during active DNA synthesis, followed by detection of EdU-positive cells with Alexa Fluor 488 dye via click reaction.

HCC1954_Luc shEDI3 #1 cells with Dox-induced EDI3 knockdown, as well as non-induced control cells were seeded for colony formation. Colonies were fixed and stained with crystal violet two, three, four and seven days after plating. Photos of representative colonies per time

point revealed how the colonies increased over time (Figure 3.15A). While most colonies in both conditions consisted of two cells two days after seeding, on subsequent days the number of cells per colony was lower when EDI3 was silenced (Figure 3.15B). The difference in cell number became more profound over time, indicating that EDI3 knockdown indeed slows down cell proliferation.

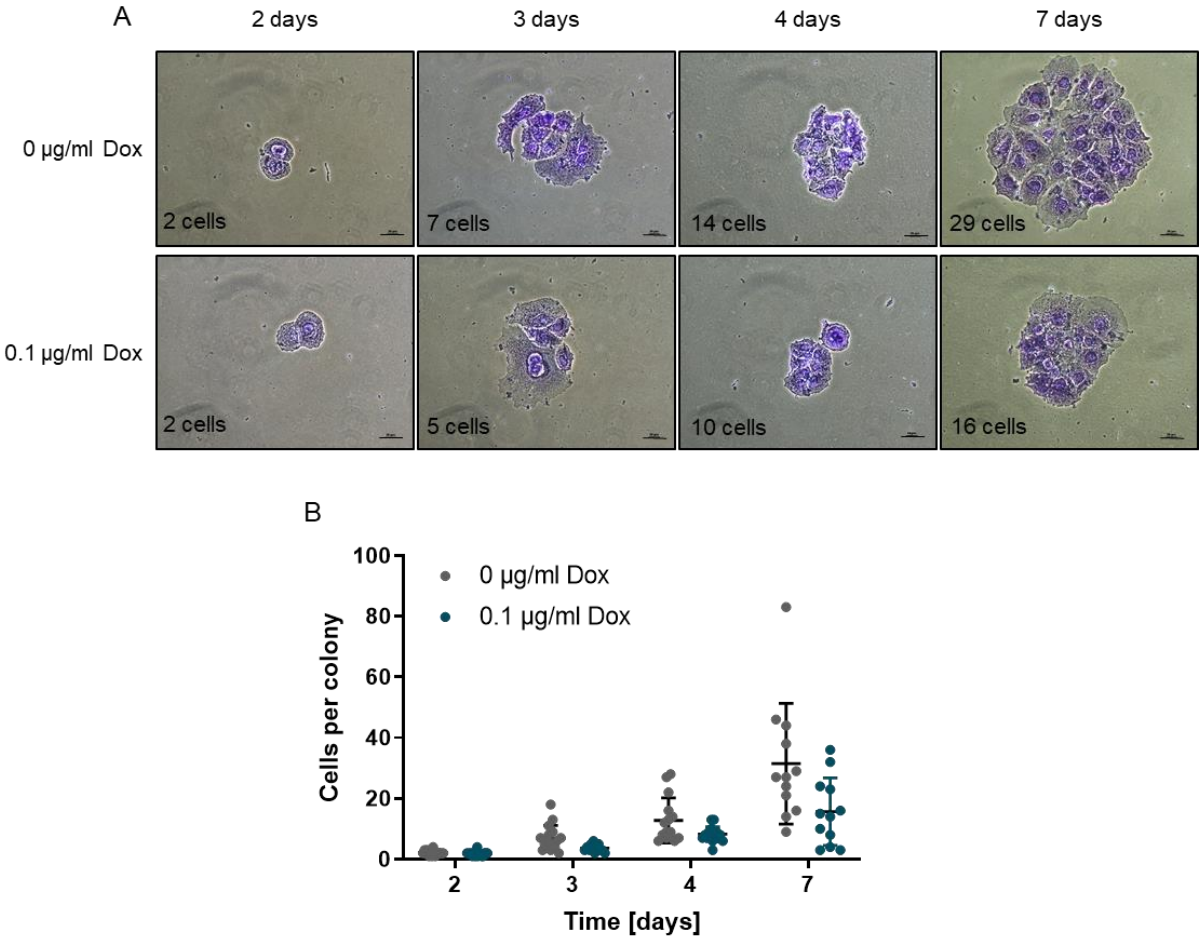

Figure 3.15: Induced EDI3 knockdown leads to a reduction in cell number per colony over time. Dox-induced and non-induced HCC1954_Luc shEDI3#1 cells were replated for colony formation assay. Colonies were fixed and stained with crystal violet 2, 3, 4 and 7 days after seeding. A) Representative pictures of colonies for each time point are shown. Number of cells within the colony is indicated. Scale bars represent 40 µm. B) Quantification of cell number per colony. Values in graphs represent mean ± SD from 12-15 counted colonies per time point.

To further elucidate that silencing EDI3 inhibits proliferation of the HCC1954 colonies, DNA synthesis was investigated. Here, two different shEDI3 cell lines, as well as non-targeting shNEG cells were induced with Dox for 72 h followed by replating for colony formation along with non-induced cells for each cell line. After seven days, proliferating cells were labeled for two hours with 10 nm EdU with results presented in Figure 3.16. Nuclei stained with Hoechst 33342 are displayed in blue. Representative fluorescence pictures show less proliferating EdU positive (green) cells in the Dox-induced EDI3 knockdown conditions. Quantification of the

proportion of EdU positive cells per colony normalized to the non-induced conditions (0 µg/ml Dox) revealed that silencing EDI3 led to a significant decrease in proliferation of 25-30% with both oligos. No effect on proliferation could be observed after Dox treatment of non-targeting shNEG cells.

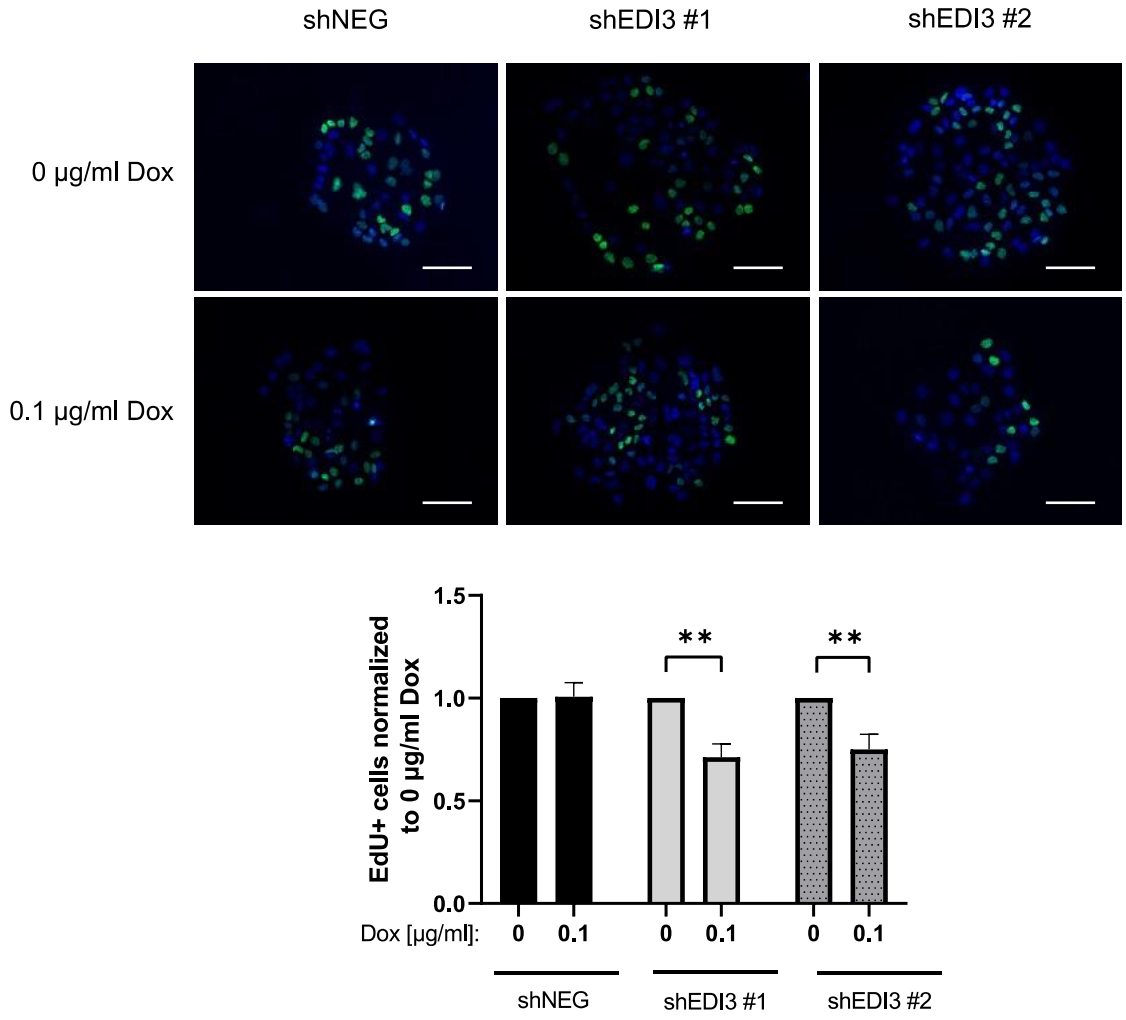

Figure 3.16: Induced EDI3 knockdown leads to a reduced number of proliferating cells in colonies. EDI3 knockdown was induced in two different shEDI3 cell lines and non-targeting cells (shNEG) before cells were replated for colony formation. After 7 d, cells were treated with 10 nm EdU for 2 h and proliferating cells were labeled with Alexa Fluor™ 488 dye (green). The nuclei were stained with Hoechst 33342 (blue). Representative pictures of colonies are shown (top panel). Scale bars represent 200 µm. The graph below represents the proportion of EdU positive cells per colony normalized to the control condition (0 µg/ml Dox). Values in graphs represent mean ± SD from three independent experiments (**, $p < 0.01$).

In order to investigate whether silencing EDI3 had a general effect on the proliferation of HCC1954 cells or was limited to colony formation, two Dox-induced shEDI3 cell lines, as well as induced shNEG cells were replated in a sub confluent cell layer compared to non-induced cells. EdU labeling was performed 24 h after plating. Less EdU positive proliferating cells were observed after EDI3 knockdown induction with Dox (Figure 3.17). Quantification of the proportion of EdU positive cells normalized to non-induced control (0 µg/ml Dox) shows that

proliferation in both EDI3-targeting cell lines was significantly reduced by approx. 25-30% when EDI3 was silenced. Again, Dox treatment had no effect on proliferation in the non-targeting shNEG cell line.

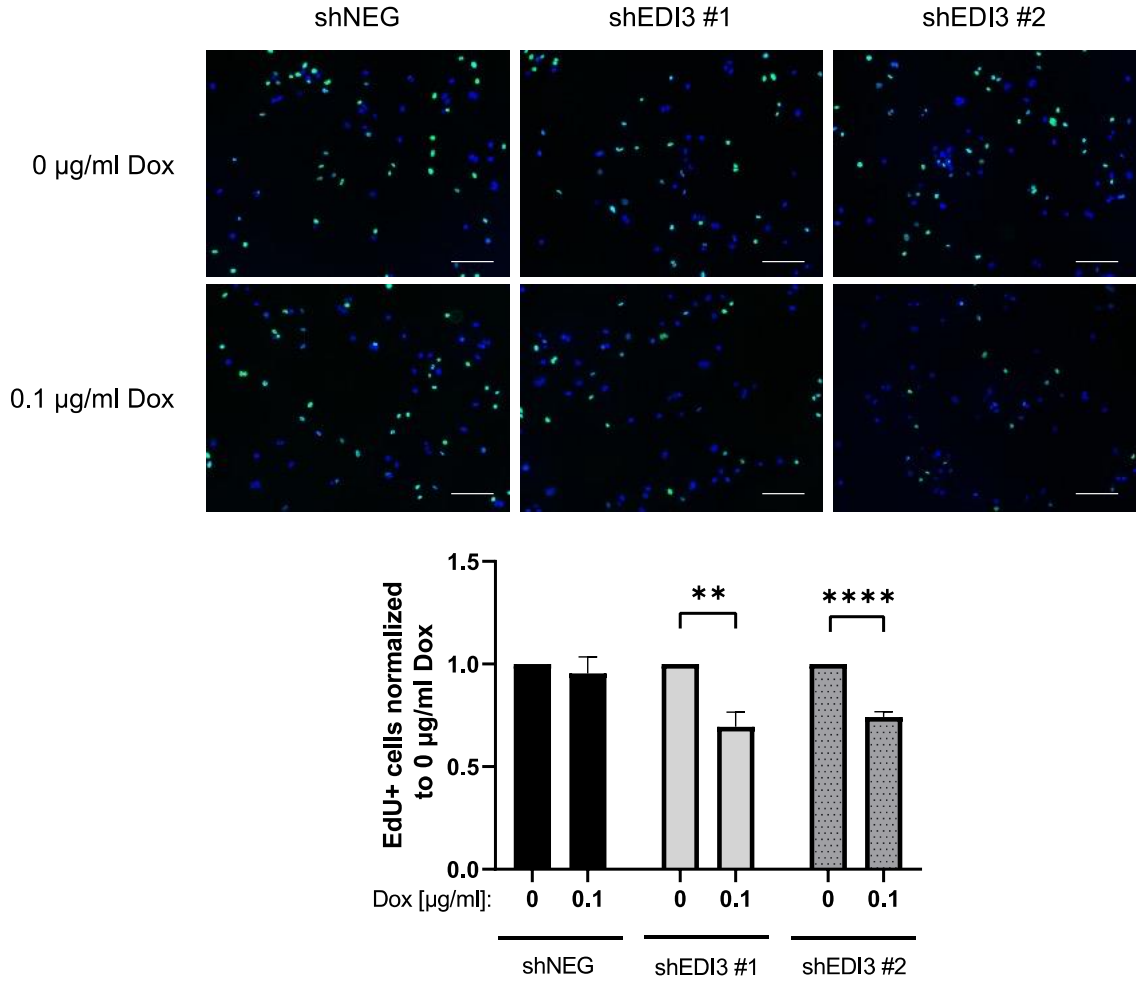

Figure 3.17: Induced EDI3 knockdown in HCC1954_Luc results in reduced proliferation in a subconfluent cell layer. EDI3 knockdown was induced in two different shEDI3 cell lines and non-targeting cells (shNEG). 24 h after replating, cells were treated with 10 nm EdU for 2 h and proliferating cells were labeled with Alexa Fluor™ 488 dye (green). The nuclei were stained with Hoechst 33342 (blue). Representative pictures per condition are shown (top panel). Scale bars represent 200 µm. The graph below represents the proportion of EdU positive cells normalized to the control condition (0 µg/ml Dox). Values in graphs represent mean ± SD from three independent experiments (**, $p < 0.01$; ****, $p < 0.0001$).

Altogether, these results show that EDI3 knockdown in HCC1954_Luc cells significantly reduced proliferation. Interestingly, the previously observed reduction in colony size was only significant in two out of three EDI3-targeting cell lines (described in chapter 3.4.2). At this point it should be noted that the measure of colony size is less precise than the number of cells per colony or the amount of EdU positive cells, as can be seen in Figure 3.15A where the two colonies consisting of either seven or 14 cells have a similar size.

3.4.5 Doxycycline-induced EDI3 knockdown reduces viability

3.4.5.1 Induced EDI3 knockdown reduces viability in adherent cells

Once the influence on proliferation was confirmed, viability assays were performed in order to investigate if the strong reduction in colony formation upon EDI3 knockdown was also associated with impaired cell survival.

For this purpose, two different EDI3-targeting HCC1954_Luc cell lines with and without induced EDI3 knockdown were replated along with non-targeting shNEG cells. After 96 h, CellTiter-Blue® viability assays were performed. In this assay, the dye resazurin is reduced to resorufin by metabolically active cells which results in a fluorescence signal that is proportional to the number of living cells in the sample. Compared to non-induced shEDI3 cells, viability was significantly decreased in the two independent shEDI3 cell lines after induction with Dox (Figure 3.18). However, Dox treatment alone also led to a significant reduction in cell viability in the non-targeting cell line (shNEG). Nevertheless, viability in shEDI3#1 cells was significantly lower when EDI3 was silenced than in the Dox-treated shNEG cells. Furthermore, the decrease in viability was more significant in both inducible shEDI3 cells than in the shNEG cells. Taken together, these results indicate that Dox-induced EDI3 kockdown led to a significant reduction in cell viability of the adherent HCC1954 cells.

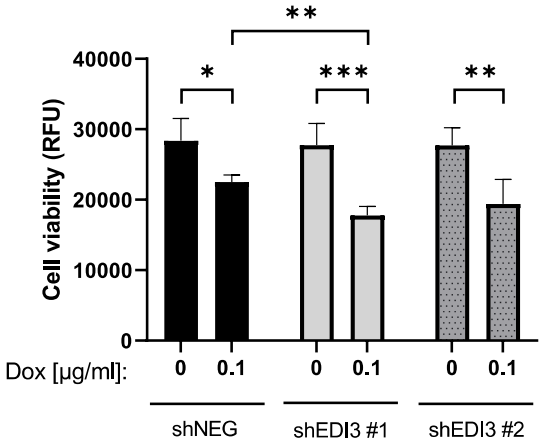

Figure 3.18: Inducible EDI3 knockdown in HCC1954_Luc reduces cell viability in adherent cells. Cells were replated after Dox-induction of EDI3 silencing in two different EDI3-targeting cell lines compared to non-targeting shNEG cells. Viability, shown as RFU, was determined with the Cell Titer Blue assay 96 h after plating. Values in graphs represent mean ± SD from three independent experiments (*, $p < 0.05$; **, $p < 0.01$; ***, $p < 0.001$). RFU, relative fluorescence units.

3.4.5.2 Doxycycline-induced EDI3 knockdown leads to increased susceptibility to anoikis

One important aspect of viability in cancer cells is their ability to prevent anoikis. Anoikis is a form of apoptosis that is induced when a cell detaches from the extracellular matrix (ECM), and serves as a critical mechanism to prevent adherent-independent cell growth and colonizing of distant organs (Frisch & Francis, 1994; Meredith et al., 1993). Cancer cells can develop several mechanisms to resist anoikis in order to progress towards malignancy and form metastases.

To investigate if EDI3 influences the ability of a cell to resist anoikis, EDI3 knockdown was induced in two different EDI3-targeting HCC1954_Luc cell lines and compared to non-targeting shNEG cells. After 72 h, induced as well as non-induced (shNEG and shEDI3) cells were replated on a poly(2-hydroxyethyl methacrylate) (poly-HEMA) matrix to prevent cell attachment. Cell viability was determined 24 h later by CellTiter-Blue® assay. Results in Figure 3.19 show that EDI3 knockdown significantly reduced survival of cells in suspension by approx. 15% (shEDI3 #1) and 25% (shEDI3 #2). In contrast to the results obtained in the classical viability assay with attached cells, Dox treatment alone had no effect on the non-targeting cell line. These results indicate that EDI3 may be involved in mechanisms that protect cells against anoikis.

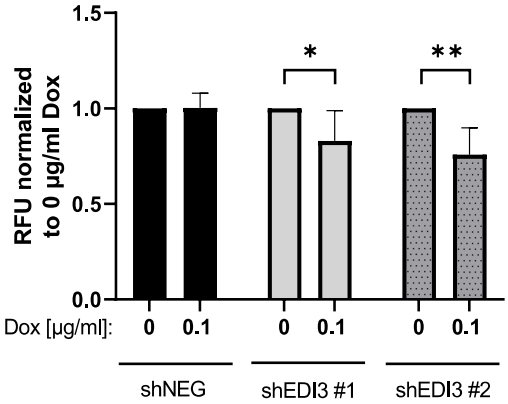

Figure 3.19: Inducible EDI3 knockdown decreases viability in HCC1954_Luc cells in suspension. After Dox induction of EDI3 knockdown with two different oligos compared to a non-targeting shNEG cell line, cells were replated on a Poly-HEMA matrix to prevent adhesion. Viability presented as RFU normalized to the non-induced controls (0 µg/ml Dox) was measured with the Cell Titer Blue assay 24 h after plating. Data represent mean ± SD from at least three independent experiments (*, $p < 0.05$; **, $p < 0.01$). RFU, relative fluorescence units.

3.4.6 Inducibly silencing EDI3 has no effect on migration

Enhanced migration can contribute to the invasion of tumor cells into the surrounding connective tissue and blood vessels, which is a key step in the metastatic spread of breast tumors. It was previously shown that silencing EDI3 decreased migration in several cell lines including MCF7, MDA-MB-231, HeLa, ES2 and AN3-CA cells (Marchan et al., 2017; Stewart et al., 2012).

To investigate if Dox-inducible EDI3 knockdown in HCC1954_Luc cells affects migration, the wound healing capability of the cells was tested. Two different EDI3-targeting cell lines and non-targeting shNEG cells were induced with 0.1 µg/ml Dox for 72 h before they were replated along with non-induced cells (0 µg/ml Dox) into Ibidi's culture inserts for wound healing. Twenty-four hours after seeding, inserts were removed, resulting in a defined 500 µm cell free gap within the cell layer. The percentage of wound closure was determined over time until the gap in the non-induced cells was completely closed. As presented in Figure 3.20, no differences in wound closure were visible between induced EDI3 knockdown and non-induced cells. Additionally, Dox treatment did not influence migration of non-targeting shNEG cells. Thus, the results suggest that EDI3 is not associated with migration in HCC1954_Luc cells.

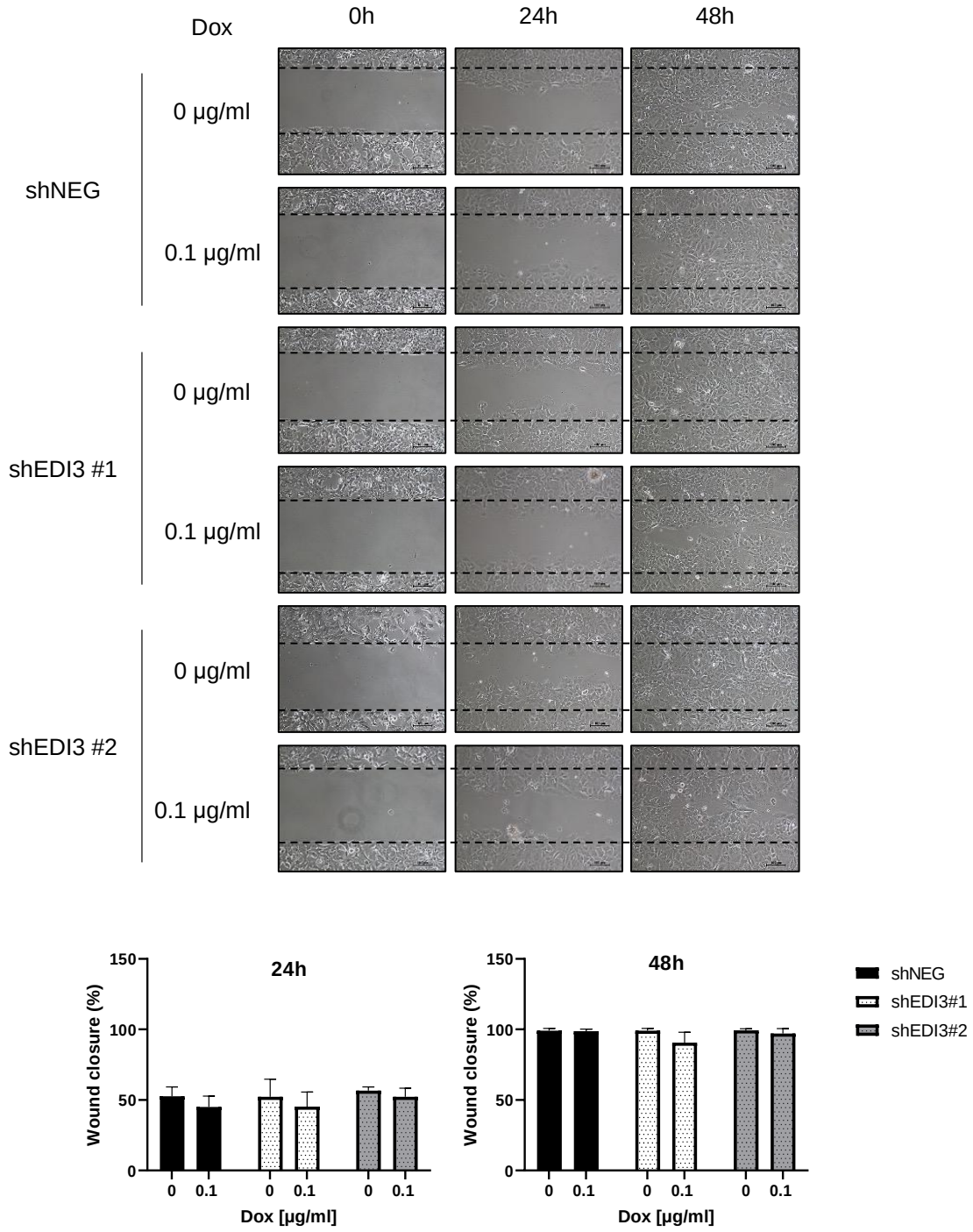

Figure 3.20: Inducibly silencing EDI3 in HCC1954_Luc has no effect on wound closure. Migration was analyzed with the wound healing assay after EDI3 knockdown induction with Dox comparing two different EDI3-targeting cell lines to non-targeting cells (shNEG). Representative pictures of the wound taken after 0 h, 24 h and 48 h are shown (top panel). Scale bars represent 100 µm. The graphs below show quantification of the wound closure in percentage after 24 h and 48 h. Values in graphs represent mean ± SD from three independent experiments.

3.5 Investigating a role for EDI3 in tumor growth and metastasis *in vivo*

In the current work, *in vitro* analysis of EDI3 in HCC1954_Luc cells revealed that Dox-induced EDI3 knockdown led to an increase in GPC/PCho ratio, which was previously assumed to be a switch towards a more untransformed phenotype (Stewart et al., 2012). Furthermore, a strong reduction in colony formation, likely caused by reduced cell proliferation, increased sensitivity to anoikis and a trend towards reduced adhesion capability was observed. Since these results indicate an overall reduction in tumor-initiating capabilities upon EDI3 knockdown, in the next step EDI3's effect on tumor growth and metastasis was investigated *in vivo*. Therefore, different xenograft and metastasis models were generated by injection of luciferase-expressing HCC1954 cells into immunocompromised mice in order to prevent rejection of human cells.

3.5.1 Investigating EDI3 in primary tumors

3.5.1.1 Optimization of growth conditions for subcutaneous tumors in mice

In order to investigate the effect of EDI3 on the growth of primary tumors, a subcutaneous (s.c.) xenograft model was used. HCC1954 cells are reported to grow slowly in this model (Clinchy et al., 2000), however, Clinchy and colleagues reported improved take rates for HCC1954 cells co-injected with 50% Matrigel (Clinchy et al., 2000), a solution rich in extracellular matrix (ECM) proteins and growth factors. In another study, s.c. HCC1954 xenografts were created by injecting cells in 100% Matrigel (Lopez-Albaitero et al., 2017). To optimize experimental conditions, in this thesis growth of HCC1954_Luc cells was tested with both 50% and 100% Matrigel. Furthermore, it was evaluated if the cells form tumors in immunocompromised nude mice (CD1 nude). Tumor take rates and growth were compared to the more immunodeficient NSG mice.

HCC1954_Luc cells in 50% (1:1 Matrigel/1x PBS) or 100% Matrigel were injected s.c. into the flank of six-week-old CD1 nude and NSG mice. Tumor growth was monitored using a digital caliper and the resulting growth curves are presented in Figure 3.21. All CD1 nude mice developed slow growing tumors with no significant differences between 50% and 100% Matrigel (Figure 3.21, left panel). In both conditions, an average tumor volume of 1000 mm^3 was reached approx. 8.5 weeks after injection. In contrast, only two out of four NSG mice injected with 100% Matrigel developed tumors. Tumor growth in NSG mice was improved by using 50% Matrigel (Figure 3.21, right panel). However, this effect was not significant as variability was very high among the mice. Due to fast tumor growth two of the NSG mice injected with 50% Matrigel had to be sacrificed after five weeks and the experiment had to be ended after 6.5 weeks because most tumors reached terminal size.

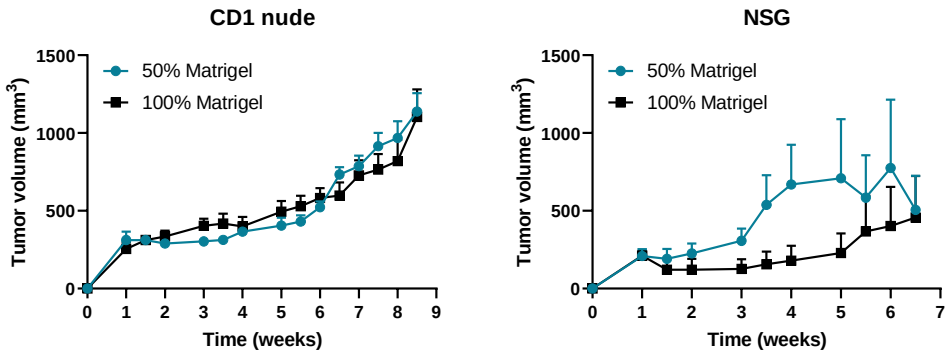

Figure 3.21: HCC1954_Luc cells form subcutaneous tumors in CD1 nude and NSG mice. Five million cells were injected subcutaneously in mixture of 1:1 PBS:Matrigel or 100% Matrigel and tumor volume was measured twice a week with a caliper. Two NSG mice injected with 50% Matrigel had to be sacrificed after five weeks, as tumors reached terminal size. Graphs represent mean ± SEM of the tumor volumes measured from four to five mice per condition.

This pre-test revealed that HCC1954_Luc tumors grew in CD1 nude mice with a take rate of 100%. Based on the obtained results, CD1 nude mice were chosen to be used for the subcutaneous xenograft model, because the tumor growth was less variable in this mouse strain. Since no significant differences were observed between the two Matrigel concentrations in CD1 nude mice, in the subsequent experiments s.c. xenografts were generated using 50% Matrigel, as this concentration facilitates easier sample handling, and diminishes consumption of Matrigel during cell preparation.

3.5.1.2 Doxycycline-induced EDI3 knockdown does not reduce primary tumor growth

Once the mouse strain and Matrigel concentration for the subcutaneous xenograft model were determined, the effect of EDI3 silencing on primary tumor growth was investigated. Since pre-silencing of EDI3 resulted in the most significant effects *in vitro* (see chapter 3.4.2), two different EDI3-targeting cell lines and non-targeting shNEG cells were induced with Dox 72 h prior to injection. Likewise, the mice were also treated with Dox three days before the injection of cells. As shown in the experimental plan in Figure 3.22A, pre-treated and non-induced cells were injected subcutaneously as described before and tumor growth was monitored over 12 weeks using a digital caliper. To verify Dox-induction in the tumors, the expression of Dox-dependent fluorescence marker tRFP was evaluated by *in vivo* fluorescence imaging. As shown in Figure 3.22B, fluorescence images comparing Dox-induced and non-induced mice confirm that Dox treatment was sufficient to induce a clear fluorescence signal in the subcutaneous tumors, while no signal was observed in non-induced mice.

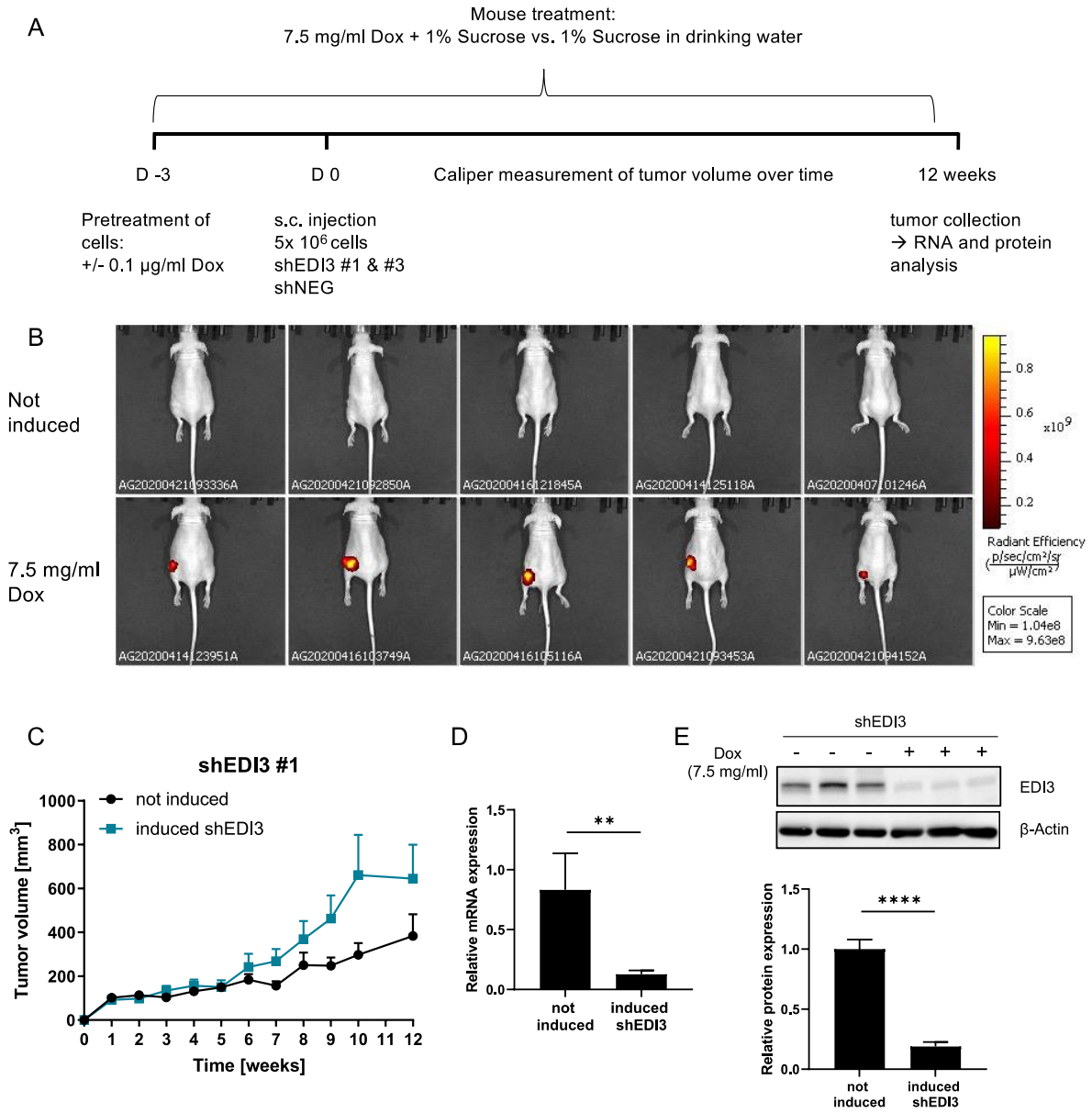

Figure 3.22: EDI3 knockdown does not decrease growth of subcutaneous tumors. A) Overview of the experimental plan. Three days after Dox induction of EDI3-targeting (shEDI3) and non-targeting (shNEG) HCC1954_Luc cells, induced and non-induced cells were injected subcutaneously into Dox-pretreated and untreated CD1 nude mice, respectively. Tumor volume was measured over 12 weeks and tRFP expression was confirmed by *in vivo* imaging. Tumors were collected and EDI3 expression was analyzed on RNA and protein level. B) Fluorescence images showing tRFP expression in Dox-induced and non-induced mice. C) Tumor volume measured for shEDI3 #1 cells comparing induced and non-induced conditions. D) *EDI3* mRNA expression in shEDI3 tumors was analyzed relative to expression of the housekeeping gene *18S*. E) Western blot and densitometric analysis of corresponding EDI3 protein expression normalized to β-actin. Data represent mean ± SEM (C) or mean ± SD of three (E) or five to six mice per condition (**, $p < 0.01$; ****, $p < 0.0001$).

In contrast to what was observed *in vitro*, growth curves showed an insignificant increase in tumor volume when EDI3 was silenced compared to non-induced shEDI3 cells with both EDI3-targeting oligos (shEDI3 #1 is shown representatively in Figure 3.22C). Tumor volume of the non-targeting shNEG cells was also slightly increased in the Dox-treated condition (data not shown). Since it was possible that despite the observed fluorescence signal, Dox treatment did

not result in a sufficient EDI3 knockdown in the tumors, EDI3 expression in the tumor tissue was verified. RNA analysis revealed an 85% reduction in *EDI3* expression in the Dox-induced tumors (Figure 3.22D) and western blot analysis confirmed sufficient EDI3 knockdown of 81% on protein level (Figure 3.22E).

To further elucidate why the tumor growth did not reflect the *in vitro* results, the mRNA expression of enzymes involved in GPC and choline metabolism in the tumor tissue was evaluated. As presented in Figure 3.23, expression of phospholipase B (*PLB*), the enzyme that produces GPC directly from PtdCho (Gallazzini & Burg, 2009), was significantly decreased in tumors with induced EDI3 knockdown, suggesting that silencing EDI3 resulted in an accumulation in GPC, as observed *in vitro*, which may consequently lead to a downregulation of the GPC producing enzyme. Interestingly, the expression of glycerophosphodiester phosphodiesterase 2 (*GDE2*), another enzyme that metabolizes GPC, was slightly, but insignificantly increased in tumors with induced EDI3 knockdown, while no changes were visible in non-targeting shNEG cells. This observation indicates that GDE2 may be upregulated to compensate for the loss of EDI3 and could explain why no reduction in tumor volume was observed. RNA expression levels of the choline kinases alpha and beta (*CHKA* and *CHKB*) on the other hand were not altered by Dox-induction.

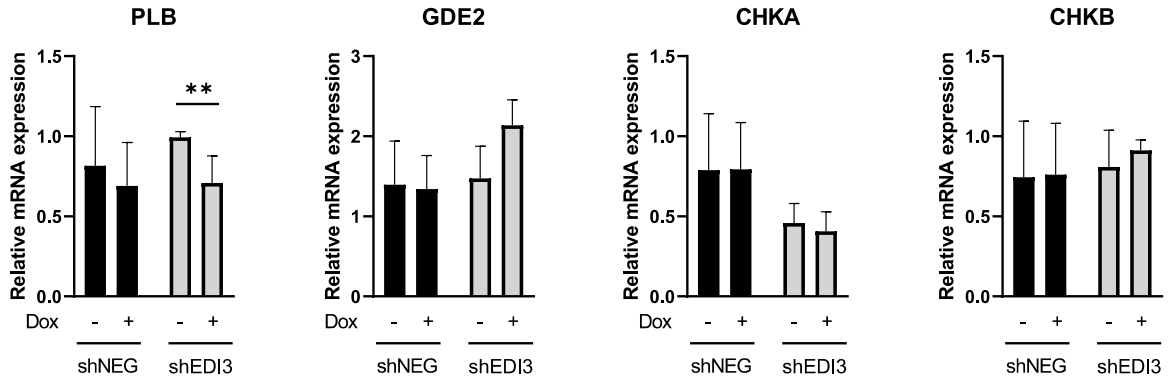

Figure 3.23: *PLB* mRNA expression is significantly reduced upon EDI3 knockdown in subcutaneous tumors. Gene expression of enzymes involved in GPC and choline metabolism was analyzed in subcutaneous tumors. *GDE2*, *PLB*, *CHKA* and *CHKB* mRNA expression is shown relative to expression of the housekeeping gene *18S*. Data represent mean ± SD of five mice per condition (**, $p < 0.01$). GDE2, Glycerophosphodiester phosphodiesterase 2; PLB, Phospholipase B; CHKA, Choline kinase alpha; CHKB, Choline kinase beta.

Taken together, in contrast to the *in vitro* results, silencing EDI3 insignificantly increased primary tumor growth *in vivo*. However, tumor growth of shNEG cells was also slightly increased upon Dox treatment, which indicates that Dox alone may have an influence on tumor growth that could obscure the influence of EDI3. In addition, gene expression analysis of *GDE2* suggests a compensation for the loss of EDI3, which may be reflected in the metabolite analysis

of the tumor tissue for which data are outstanding. It is worth noting that although subcutaneous xenograft models are a commonly used tool in the study of cancer, they do not represent the biological microenvironment of the tumors (Brand et al., 2020). Therefore, studying EDI3 in an orthotopic primary tumor model, where cells are injected directly into the mammary fat pad, might lead to more significant and relevant results and is being approached in future experiments. For this thesis, however, the focus for the subsequent experiments was on investigating EDI3 in metastasis formation.

3.5.2 Investigating EDI3 in a lung metastasis model

After silencing EDI3 showed no significant effect on primary tumor growth in a subcutaneous xenograft model, EDI3 was then investigated in metastasis formation. The method most frequently applied to evaluate the metastatic potential of tumor cells is the tail vein assay (Elkin & Vlodavsky, 2001). For this technique cancer cells are injected into the lateral tail vein of mice resulting in the accumulation of cells in the lung, one of the most common metastatic sites for breast cancer (Brown & Ruoslahti, 2004).

3.5.2.1 Doxycycline-induced EDI3 knockdown has no influence on early attached cells

In order to investigate EDI3's role in the formation of lung metastasis, EDI3-targeting cells were induced three days before injection as presented in the illustration of the experimental plan in Figure 3.24A. Dox-induced and non-induced shEDI3 cells were injected into the lateral tail vein of six-week-old female CD1 nude mice. To evaluate the effect of EDI3 on early attached cells, *in vivo* bioluminescence imaging was performed 10 min, 6 h and 24 h after injection.

As shown in the luminescence images in Figure 3.24B, strong signals could be detected in the lungs already 10 min after cell injection. After 24 h, signal intensity was strongly reduced, indicating that most of the cells did not attach to the lungs. As luminescence intensity varied among the individual mice, the signals measured for each mouse over time were normalized to the intensity of the first image, resulting in "relative total flux". Quantitative analysis of the luminescence signal measured 6 h and 24 h after injection revealed no differences between EDI3 knockdown and non-induced cells (Figure 3.24C). Unfortunately, long term effects of EDI3 on metastasis formation could not be studied with this model as the luminescence signal vanished completely after a couple of days and was still not detectable five weeks later.

Overall, the results suggest that EDI3 does not affect early attached cells in the investigated model. Furthermore, the absence of luminescence at later time points indicates that HCC1954_Luc cells did not form lung metastasis under the here tested experimental conditions. In order to study EDI3 during metastasis progression, a peritoneal model was then used.

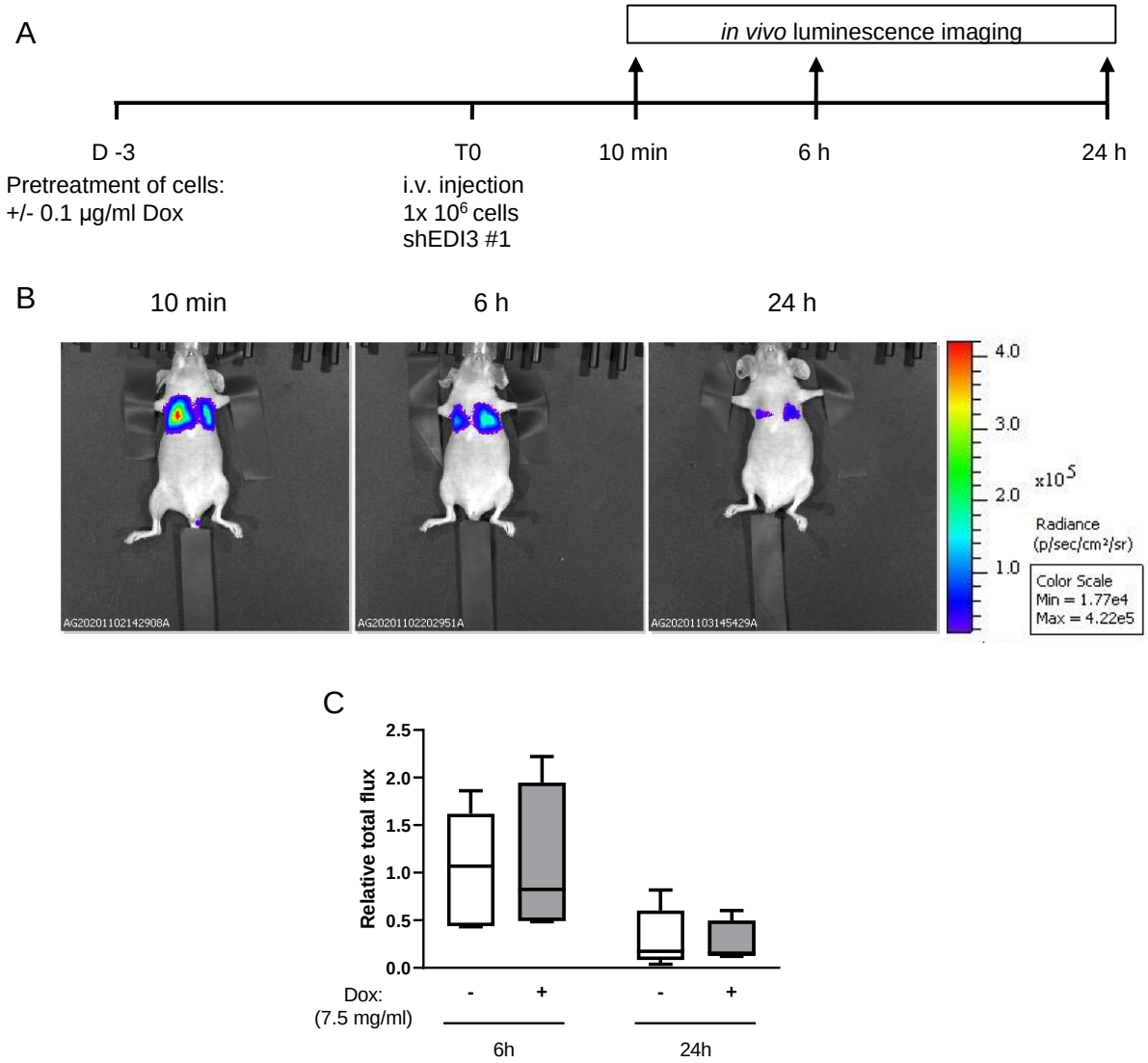

Figure 3.24: Silencing EDI3 has no effect on early attached cells in a mouse model for lung metastasis. A) Schematic illustration of experimental plan. Three days after Dox induction of EDI3-targeting (shEDI3) cells 1x10^6 induced and non-induced cells in 100 µl 1x PBS were injected into the tail vein of CD1 nude mice. Luminescence signal was measured 10 min, 6 h and 24 h after injection. B) Representative luminescence images showing the time dependent decrease of luminescence signal. C) Quantitative analysis of luminescence signal after 6 h and 24 h normalized to the signal intensity 10 min after injection comparing Dox-induced EDI3 knockdown with non-induced cells. Box plots: horizontal line, median; box, 25th-75th percentiles; whiskers, min to max. Data represent four to six mice per condition.

3.5.3 Investigating EDI3 in a peritoneal metastasis model

Since it was not possible to study the influence of EDI3 on later stages of metastasis in the applied lung metastasis model, an alternative model providing faster metastasis formation was needed. More specifically, a mouse model of peritoneal metastasis was used for the HCC1954 cells which were previously reported to grow aggressively when injected into the peritoneum of immunodeficient mice (Clinchy et al., 2000).

3.5.3.1 Peritoneal metastasis formation does not differ between CD1 nude and NSG mice

In order to establish a mouse model for peritoneal metastasis, it was first evaluated if HCC1954_Luc cells form metastases more efficiently in immunocompromised CD1 nude mice or the more immunodeficient NSG mice. Therefore, HCC1954_Luc cells were injected into the peritoneum of both strains of mice and luminescence was monitored over five weeks. The pictures obtained by luminescence imaging at T0 confirmed injection of cells into the peritoneum (Figure 3.25, top panel). In both CD1 nude and NSG mice, the luminescence signal increased over time indicating that HCC1954_Luc cells were able to survive and proliferate in both mouse strains. After five weeks, the median luminescence signal compared to the time of injection increased 8.1-fold in CD1 nude and 9.1-fold in NSG mice (Figure 3.25, lower panel). Since there were no significant differences in luminescence signal between the two mouse strains, CD1 nude mice were used for the peritoneal metastasis model in the subsequent experiments.

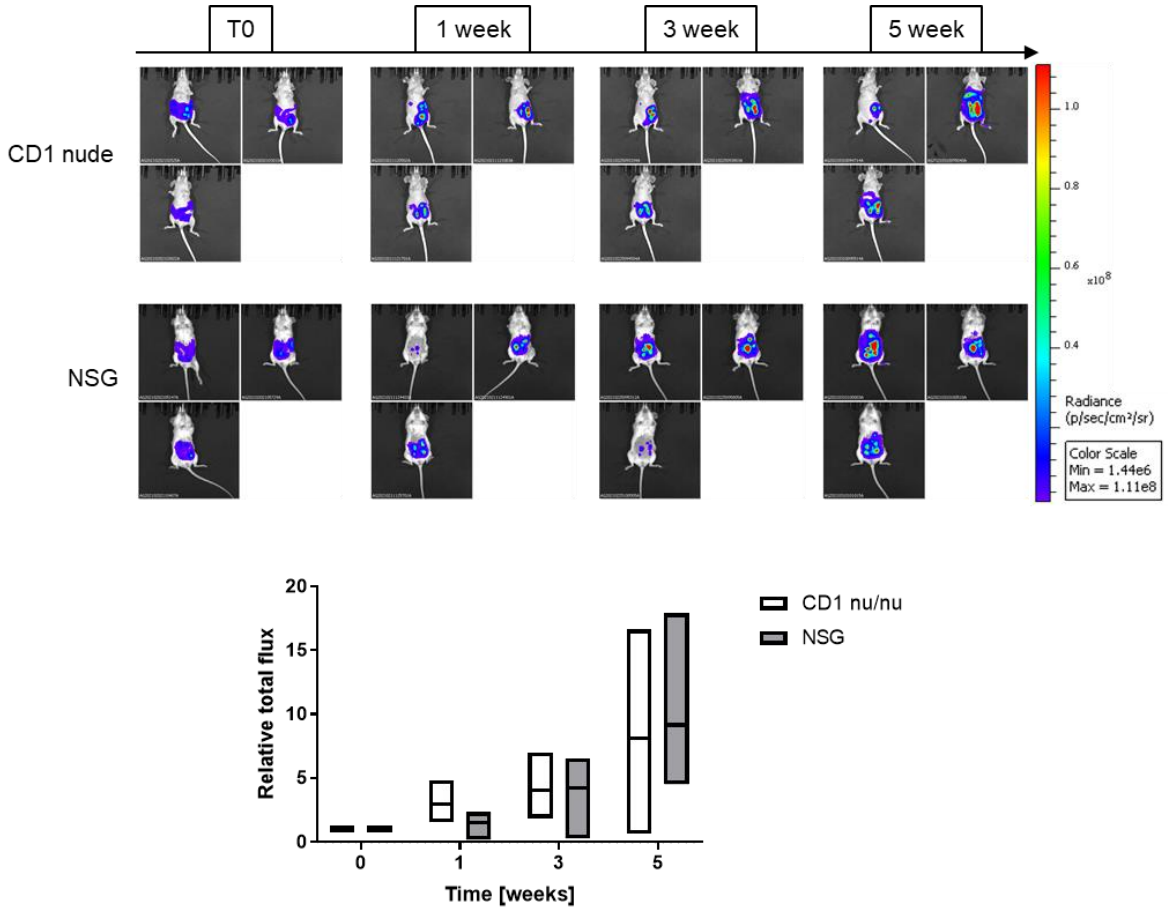

Figure 3.25: Growth of i.p. injected HCC1954 cells does not differ between CD1 nude and NSG mice. Non-induced EDI3-targeting (shEDI3 #1) cells were injected intraperitoneally, and luminescence signal was measured over five weeks. Pictures acquired by luminescence imaging and corresponding relative total flux normalized to T0 are shown. Floating bars: horizontal line, mean; box, min to max. n = 3 mice per mouse strain.

3.5.3.2 *In vivo* imaging reveals reduced luminescence signal upon EDI3 knockdown induction

Since it could be shown that HCC1954_Luc cells were growing in the peritoneum of CD1 nude mice, it was investigated next if silencing EDI3 influences formation of peritoneal metastasis. Since pre-silencing of EDI3 resulted in the most significant effects *in vitro* (see chapter 3.4.2), EDI3-targeting shEDI3 #1 and non-targeting shNEG cells were induced with Dox 72 h prior to injection, as illustrated in the experimental plan in Figure 3.26A. Dox-induced as well as non-induced cells were injected into the peritoneum of six-week-old Dox-treated and untreated control mice, respectively. To confirm that EDI3 knockdown induction was successful, RNA and protein were analyzed from shEDI3 cells collected at the time of injection. qRT-PCR analysis revealed that *EDI3* mRNA expression decreased by 74% in the Dox-induced cells compared to the non-induced control (Figure 3.26B). Successful EDI3 knockdown was also confirmed at the protein level by western blot analysis (Figure 3.26C).

The bioluminescence signal was monitored over 10 weeks. In Figure 3.26D, two representative luminescence images of mice per condition and time point are presented. At T0, luminescence could be observed in all mice, confirming successful cell injection into the peritoneum. Over time, the signal intensity increased strongly in mice injected with shNEG cells, as well as in mice injected with non-induced shEDI3 cells. Strikingly, there was no obvious increase in luminescence when EDI3 was silenced. Quantitative analysis of mice injected with shEDI3 cells confirmed that the luminescence signal was significantly reduced upon EDI3 knockdown compared to non-induced cells (Figure 3.26E). The signal intensity in most mice injected with non-induced shEDI3 cells started to increase at week five and resulted at week ten in a median foldchange of 4.7 (25^{th}-75^{th} percentiles ranging from 1.2-24.6) compared to T0. In contrast, the luminescence intensity stayed at a low level when EDI3 was silenced with a median foldchange of 0.49 (25^{th}-75^{th} percentiles ranging from 0.34-1.42) after ten weeks. Quantification of the luminescence in mice injected with non-targeting shNEG cells showed that the signal increased strongly over time in both the non-induced and induced conditions (Figure 3.26F). At ten weeks the median change in luminescence signal relative to the signal at T0 was 5.5-fold (25^{th}-75^{th} percentiles ranging from 0.57-40.68) for the non-induced and 3.7-fold (25^{th}-75^{th} percentiles ranging from 0.09-87.92) for the Dox-induced shNEG cells. The high luminescence levels in the Dox-treated shNEG mice confirm that Dox itself did not reduce luminescence nor growth of metastases. Taken together, despite the high variations in luminescence signals observed among the individual mice, the clear reduction in luminescence signal upon EDI3 knockdown suggests a role for EDI3 in metastasis formation.

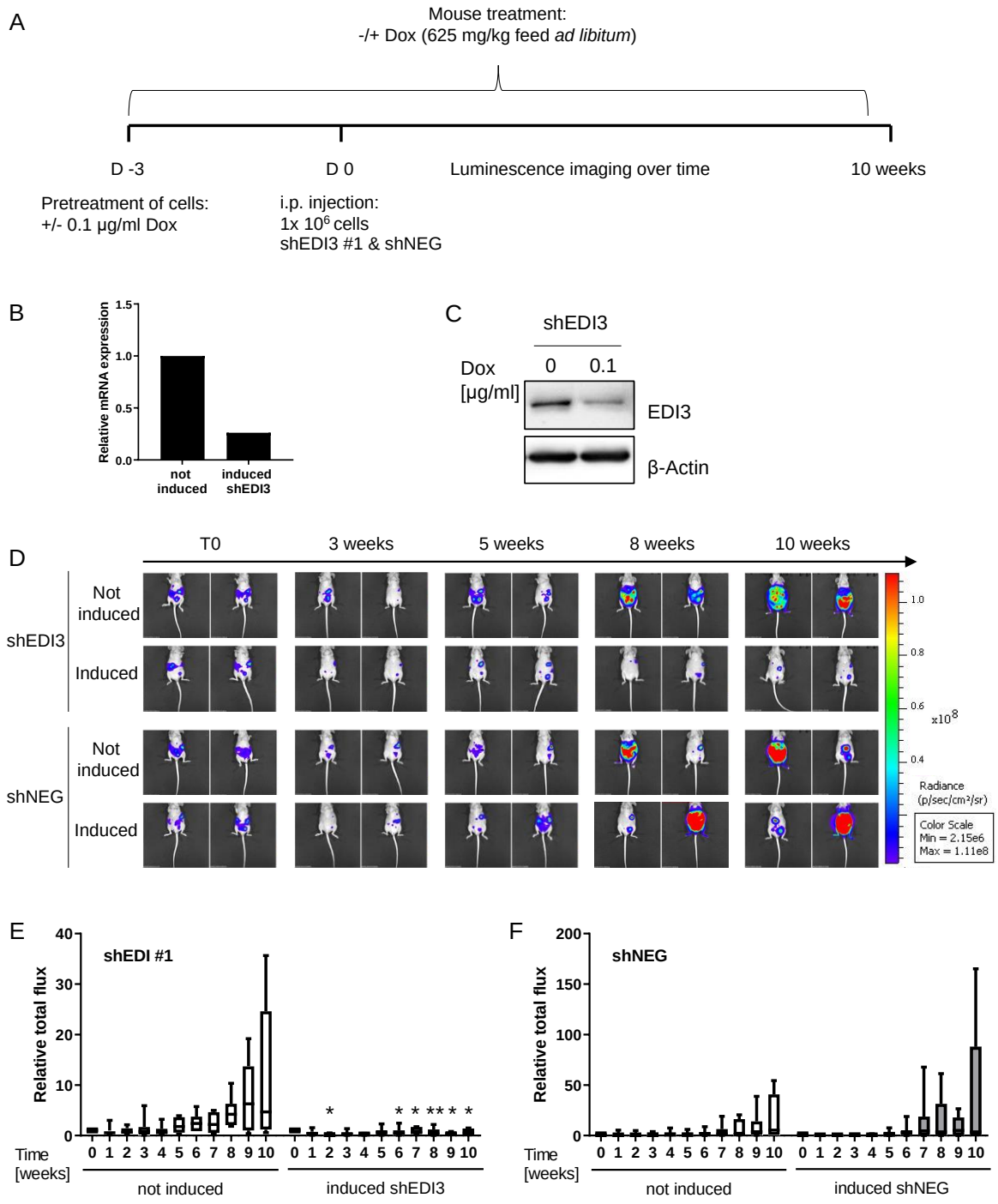

Figure 3.26: Silencing EDI3 in HCC1954 results in reduced luminescence signal after i.p. injection into mice. A) Schematic illustration of the experimental plan. EDI3-targeting (shEDI3 #1) and non-targeting (shNEG) cells were induced with Dox for three days. Induced and non-induced cells were injected i.p. into Dox pre-treated and untreated CD1 nude mice, respectively. Luminescence signal was measured over 10 weeks. B) *EDI3* RNA expression in the shEDI3 cells at time of injection analyzed by qPCR relative to *ACTB*. C) Corresponding western blot showing EDI3 protein expression. β-Actin was used as a loading control. D) Representative luminescence images of mice. E) & F) Corresponding quantitative analysis of luminescence signal for shEDI3 (E) and shNEG (F) normalized to T0. Box plots: horizontal line, median; box, 25th-75th percentiles; whiskers, min to max. n = 7 mice per condition (*, $p < 0.05$; **, $p < 0.01$).

3.5.3.3 Doxycycline-induced EDI3 knockdown improves survival

Since *in vivo* imaging indicated that the intraperitoneal metastasis burden with HCC1954_Luc cells is lower when EDI3 is silenced, the next aim was to investigate if EDI3 expression influenced survival. Therefore, CD1 nude mice injected i.p. with induced and non-induced EDI3-targeting (shEDI3) and non-targeting (shNEG) cells, were observed over a period of 15 weeks. Mice were weighed and monitored carefully for signs of ascites, the accumulation of excessive fluid within the peritoneal cavity. Once they developed ascites or their overall physical condition required termination of the experiment, the mice were sacrificed, and the dates noted, which were used to generate Kaplan-Meier survival curves (Figure 3.27). Data show that mice had a significantly higher probability of survival when EDI3 was silenced (left panel). More specifically, only 16.7% of these mice died within the first 15 weeks after injection, compared to the 58.3% that were injected with non-induced shEDI3 cells. Injection of both induced and non-induced shNEG cells resulted in a probability of survival of 42.9% (right panel), thereby excluding an influence of Dox treatment itself.

Altogether, the improved probability of survival observed upon EDI3 knockdown further supports a role for EDI3 in metastasis. In order to obtain information about the location of tumors (metastatic organotropism), autopsies were performed once mice had to be sacrificed. The corresponding analysis is presented in the next chapter.

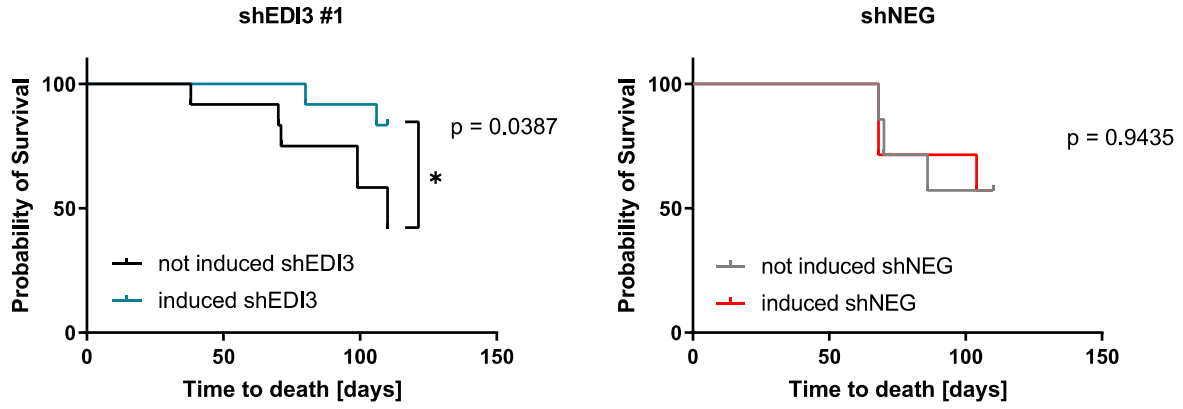

Figure 3.27: Induced EDI3 knockdown is associated with higher probability of survival in a peritoneal metastasis model. Survival of CD1 nude mice was observed for 15 weeks after i.p. injection with Dox inducible EDI3-targeting (shEDI3, left panel) and non-targeting cells (shNEG, right panel). Data represents 12 (shEDI3 #1) or seven (shNEG) mice per condition. P-values were determined by Gehan-Breslow-Wilcoxon test.

3.5.3.4 Autopsies reveal liver and diaphragm infiltration in the majority of mice

For a characterization of the peritoneal model, autopsies were performed once mice reached terminal conditions. It is important to note that this experiment was not designed to reveal information about EDI3's role in metastasis formation, but rather to give a general overview about the metastatic organotropism in the intraperitoneal metastasis model. For this reason, all mice were included into this evaluation, meaning both mice injected with EDI3-targeting (shEDI3) and non-targeting (shNEG) cells that were either Dox-induced or non-induced. Furthermore, the autopsies were performed when individual mice had to be sacrificed, with the result that the time after injection of cells varied over several weeks among the mice.

In total, 15 mice were analyzed and the number of mice that were positive for macroscopic metastasis or tumors in a certain organ was displayed as a percentage, as presented in Figure 3.28. Most mice developed metastases in the liver [12 (80%) out of 15] and the diaphragm [10 (66.7%) out of 15]. These tumors were mainly located at the connection site between these two organs. Kidneys were affected in six (40%) of 15 mice followed by the pancreas and the spleen [both 5 (33.3%) of 15]. Tumors at the peritoneal wall or at the colon were only found in one (6.7%) of 15 mice. No metastases were observed in the heart or the lungs, indicating that the cells were not able to pass through the diaphragm, but most mice (11 (73.3%) of 15] developed ascites (data not shown).

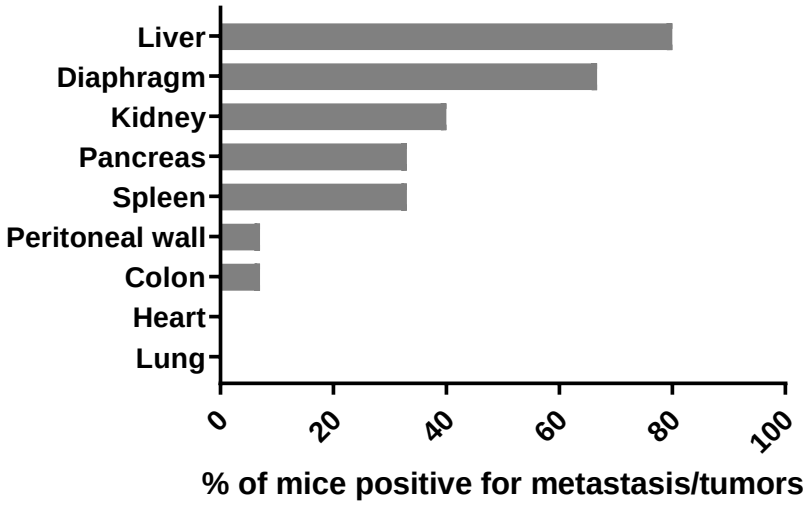

Figure 3.28: Metastatic organotropism observed in CD1 nude mice after i.p. injection of HCC1954 cells. Overview of organs affected by metastasis sorted according to prevalence as observed by autopsy once terminal conditions were reached (n = 15).

Once an overview of the organs affected by metastasis in the intraperitoneal model was obtained, as a next step timed organ collections were performed to investigate whether EDI3 influences location or size of the metastatic tumors.

3.5.3.5 Timed collection of metastases bearing mice reveals metastatic organotropism and lower metastatic burden in EDI3 knockdown condition

The results obtained thus far showed that silencing EDI3 led to a clear reduction in luminescence signal after intraperitoneal injection of HCC1954_Luc cells, indicating a decrease in metastasis formation. Furthermore, the organs affected by metastasis were identified. However, it was not clear yet how EDI3 influences metastasis formation. One possibility was that loss of EDI3 resulted in a general delay or reduction in metastasis growth. Alternatively, EDI3 may also influence the preferred location of metastases (metastatic organotropism) by facilitating growth in one tissue and preventing growth in another. Thus, the aim of this experiment was to collect organs from metastases bearing mice to determine both the overall metastatic burden and organotropism in the presence or absence of EDI3 based on *in vivo* and *ex vivo* luminescence imaging as well as on tumor weight analysis.

Therefore, EDI3-targeting (shEDI3) cells were pre-treated with Dox and mice were injected as described in chapter 3.5.3.2. Analysis of *EDI3* mRNA expression in the cells at the time of injection revealed a 65% knockdown in the Dox-treated cells compared to non-induced cells (Figure 3.29A). Successful EDI3 knockdown was also confirmed at protein level (Figure 3.29B). In the previous experiment, significant differences in luminescence between Dox-induced and untreated shEDI3 injected mice became visible at six weeks, while the differences were most significant at eight weeks; therefore, these two time points were chosen for the collection of organs. On the day of collection, first the luminescence intensity was determined by *in vivo* imaging. Luminescence images of seven mice per condition are presented in Figure 3.29C. At six weeks, the corresponding quantitative analysis (right panels) showed a lower luminescence signal in the mice injected with EDI3 silenced cells compared to non-induced cells, albeit not significant. After eight weeks, the reduction in luminescence signal was significant with a median foldchange of 1.53 (25^{th} percentile: 0.27; 75^{th} percentile: 3.98) when EDI3 was silenced compared to non-induced cells with a median foldchange of 12.65 (25^{th} percentile: 2.10; 75^{th} percentile: 22.98). Thus, the obtained *in vivo* luminescence results are consistent with the previous experiment.

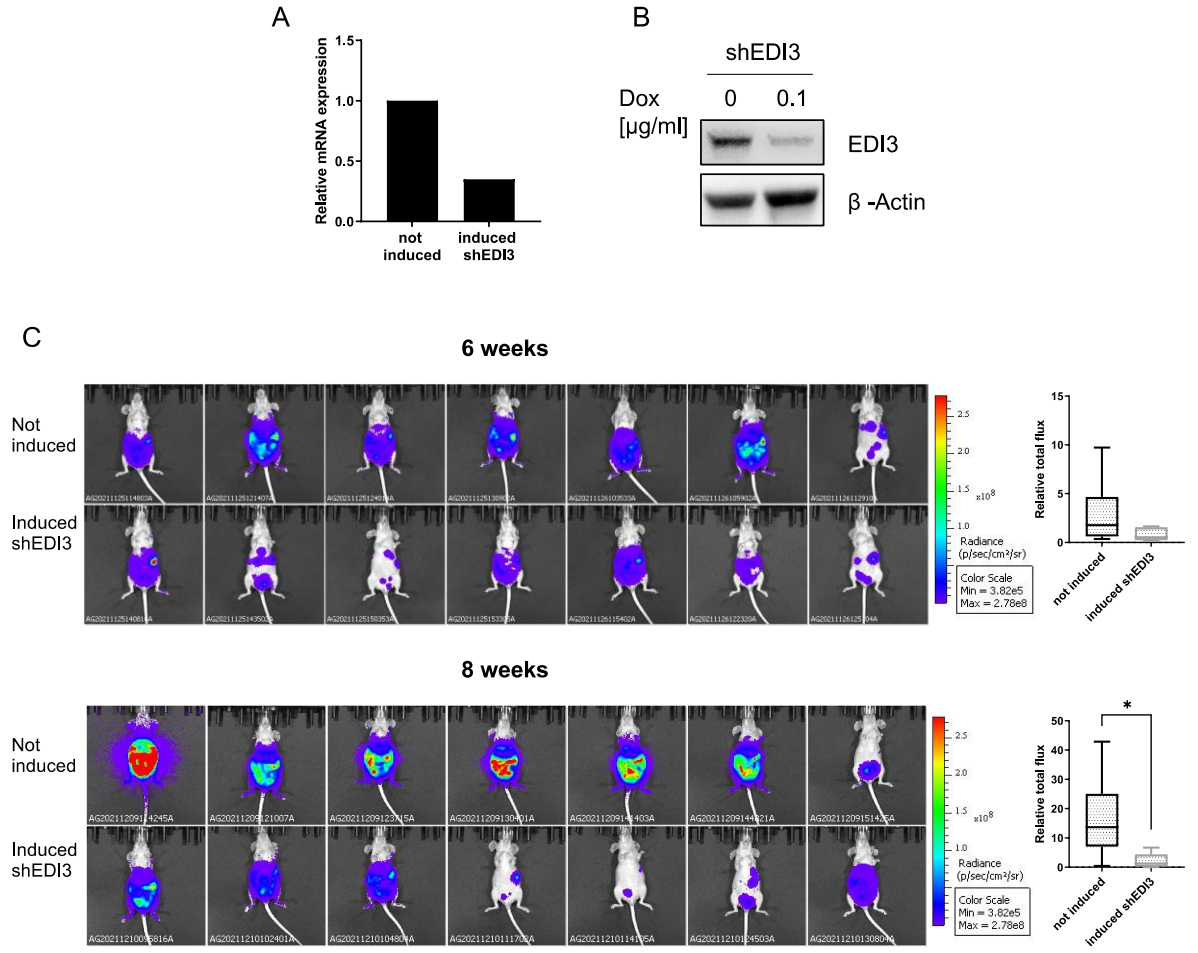

Figure 3.29: *In vivo* imaging confirms reduced luminescence upon EDI3 knockdown in the i.p. metastasis model for timed organ collection. After EDI3 knockdown induction shEDI3 #1 cells were injected i.p. into Dox-pretreated CD1 nude mice compared to non-induced control. A) *EDI3* RNA expression in the cells at time of injection analyzed by qPCR relative to *ACTB*. B) Corresponding western blot showing EDI3 protein expression. β-Actin was used as a loading control. C) *In vivo* luminescence imaging and corresponding quantitative analysis of CD1 nude mice directly before autopsy six or eight weeks after injection. Box plots: horizontal line, median; box, 25th-75th percentiles; whiskers, min to max. Data represent results of seven mice per condition (*, $p < 0.05$).

Directly after acquisition of the *in vivo* image the mouse was sacrificed, ascites fluid, if present, was extracted and organs were collected for *ex vivo* imaging. For this purpose, organs were washed in PBS to remove residual ascites and placed directly on a black non-reflecting Lexan foil along with 100 µl of the extracted ascites fluid. Luminescence photos of the organs are presented in Figure 3.30A for seven mice per condition. To determine the overall metastatic burden in the organs, the total luminescence detected in the combined organs per mouse was quantified (right panels). At six weeks, the total luminescence signal in the organs of mice injected with EDI3 silenced cells was reduced compared to non-induced cells, albeit not significant. Importantly however, after eight weeks the total flux was significantly reduced in the EDI3 knockdown condition. Thereby, the total luminescence in the organs indicates a lower metastatic burden when EDI3 was silenced which confirms the *in vivo* imaging results.

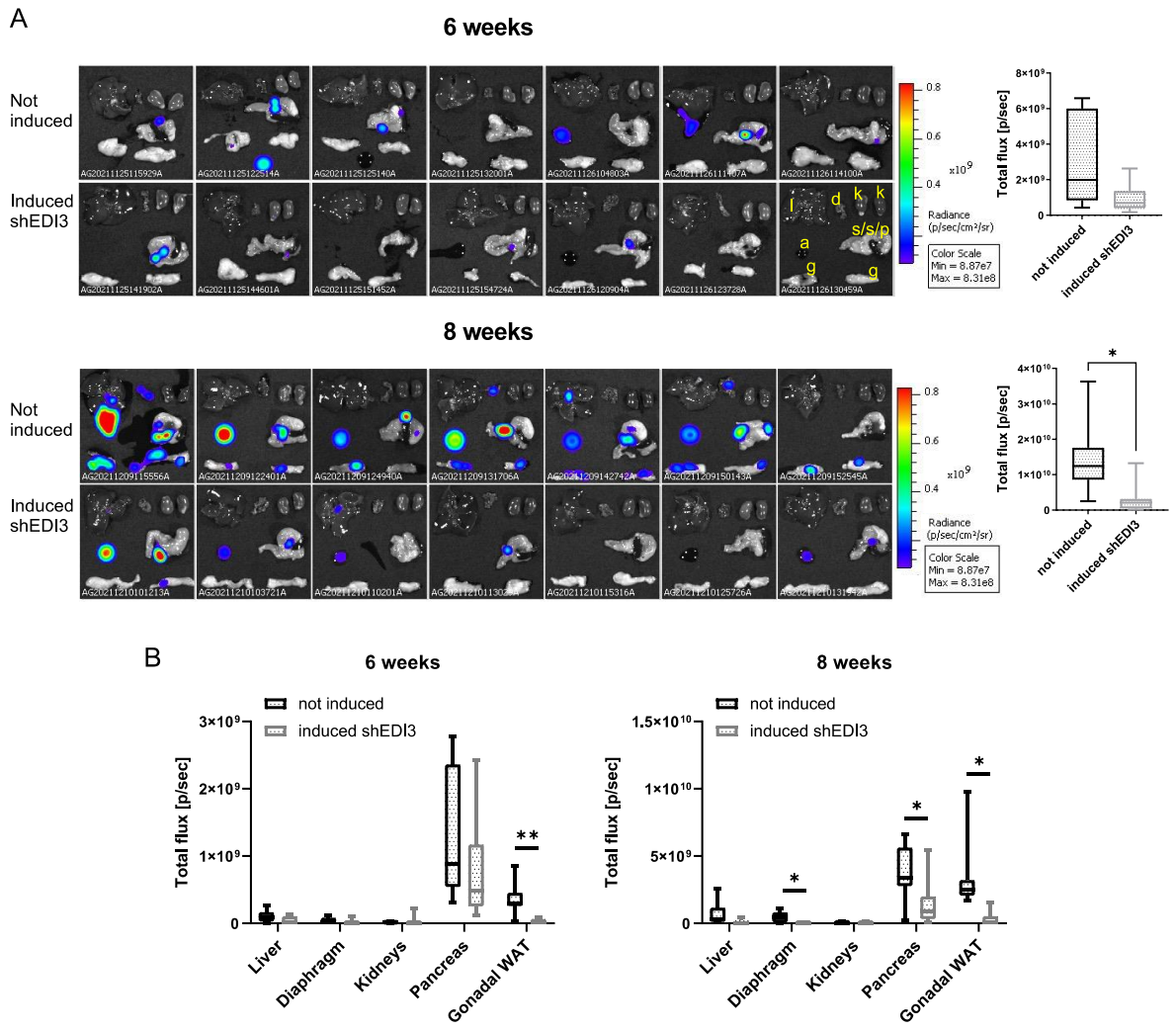

Figure 3.30: *Ex vivo* imaging of organs reveals metastatic organotropism and reduced metastatic burden in CD1 nude mice injected with EDI3 knockdown cells. A) *Ex vivo* luminescence imaging and corresponding quantitative analysis of organs and 100 µl ascitis fluid (if present) collected six and eight weeks after i.p. injection of induced and non-induced EDI3-targeting (shEDI3 #1) HCC1954_Luc cells. B) Quantitative analysis of luminescence signal analyzed per organ. Data represent results of seven mice per condition (*, $p < 0.05$; **, $p < 0.01$). l, liver; d, diaphragm; k, kidney; s/s/p, complex of spleen, stomach, and pancreas; a, ascites fluid; g, gonadal white adipose tissue (WAT).

Regarding the metastatic organotropism, *ex vivo* imaging revealed that in addition to the organs that were already identified on the basis of macroscopically visible tumors in the pre-experiment (liver, diaphragm, kidneys, pancreas, and spleen, as described in 3.5.3.4), luminescence signals could also be detected in the gonadal white adipose tissue (WAT) which surrounds the uterus and ovaries. Of note, the complex of stomach, spleen and pancreas was kept intact for imaging, but later analyses revealed that most of the luminescence signals registered in this complex were due to pancreas metastasis. In order to investigate the preferred location of metastases, the luminescence signal was then quantified per organ (Figure 3.30B). After six weeks, the strongest signal was detected in the pancreas. The gonadal WAT was found to be the second most common site of metastasis. For both locations, the luminescence signal

was lower when EDI3 was silenced, which was significant for the gonadal WAT. After eight weeks, in addition to the high signals observed in pancreas and gonadal WAT, increased luminescence was also detected in liver and diaphragm of non-induced mice. Closer examination of the latter revealed that the tumors were located close to the connection site between both organs. Importantly, when EDI3 was silenced, the metastatic burden was significantly reduced in the diaphragm, pancreas, and gonadal WAT, as well as the liver, although the latter did not reach significance. Thus, the *ex vivo* imaging results confirm the reduction in tumor burden when EDI3 was silenced and further reveal that metastatic organotropism was not altered by changes in EDI3 expression.

To verify the imaging results, all macroscopically visible tumors were excised from the organs. Prevalence and weight of tumors are presented in Figure 3.31. After six weeks, all mice were positive for pancreatic tumors (Figure 3.31A), but tumor weight was reduced, albeit not significantly, when EDI3 was silenced with a median weight of 8.42 mg compared to a median weight of 19.1 mg in the non-induced control (Figure 3.31B). Also, liver tumors were found in all mice, but as they were too small to be excised no quantitative analysis could be performed. Only one mouse per condition had visible tumors in the gonadal WAT. Eight weeks after cell injection, pancreatic tumors were once more found in all mice (Figure 3.31C); however, this time there was no difference in tumor weight between EDI3 knockdown and control (Figure 3.31D). Interestingly, the weight of liver tumors, which were present in all mice, was significantly reduced when EDI3 was silenced with a median weight of 10.86 mg compared to 22.57 mg in the non-induced control (Figure 3.31E). Furthermore, the prevalence of macroscopic tumors in the gonadal WAT and colon were slightly reduced in mice injected with EDI3 knockdown cells. Comparing the weight of all macroscopic tumors combined, tumor weight was reduced upon EDI3 knockdown, albeit not significantly (Figure 3.31F). Moreover, when all macroscopic tumor nodules that could be detected within a mouse were added together, the number of tumors per mouse was significantly lower in the EDI3 knockdown condition (Figure 3.31G).

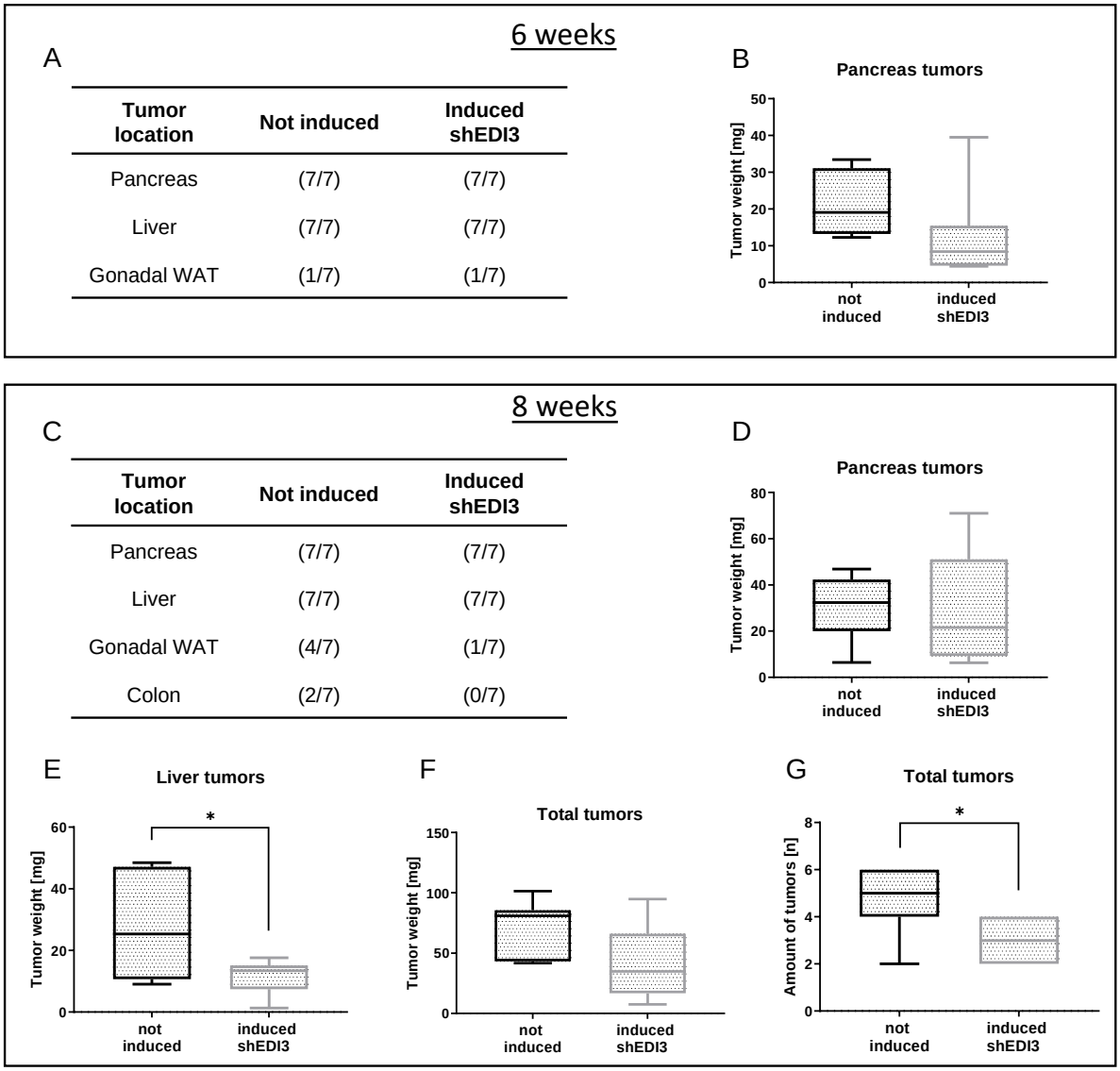

Figure 3.31: Tumor weight and prevalence indicate reduced metastatic burden after EDI3 knockdown induction in HCC1954_Luc. Upper panel: Results obtained six weeks after injection: A) Table representing the ratio of mice positive for macroscopically visible tumors at a certain organ compared to all mice. B) Weight of tumors found in the pancreas (the only measurable tumors at six weeks). Lower panel: Results obtained eight weeks after injection: C) Table showing the ratio of mice positive for macroscopically visible tumors at a certain organ compared to all mice. D) & E) Weight of tumors found in pancreas (D) and liver (E). F) & G) Combined weight (F) and amount (G) of all tumor nodules found. Data represent results of seven mice per condition (*, $p < 0.05$). WAT, white adipose tissue.

Overall, the weight and prevalence of macroscopic tumors support the *ex vivo* imaging results as no EDI3 dependent differences in metastatic organotropism were found. The results also indicate a reduction in metastatic burden after EDI3 knockdown, although the differences were not always significant. However, it should be noted that only tumors that reached a certain size could be successfully excised and weighed. Thereby, there is always the risk of inaccurate excision, which can result in falsely high or low tumor weights. Consequently, luminescence imaging is more precise, as it can also detect the signal of metastasis, that are still too small to be recognized by the naked eye. Altogether, the results suggest that while silencing EDI3 did not completely prevent metastases, it significantly reduced growth compared to the non-

induced condition. These results agree with the results obtained *in vitro*, showing that silencing EDI3 did not have a strong effect on adhesion but reduced proliferation.

3.5.3.6 Doxycycline-induced EDI3 knockdown is associated with reduced ascites

Malignant ascites is the pathological accumulation of excessive fluid within the peritoneal cavity caused by tumors that originate in or metastasize to the abdomen. The most common primary tumor leading to ascites is ovarian cancer (30-54% of cases), but primary breast cancer was also reported to cause peritoneal carcinomatosis and ascites (Parsons et al., 1996; Runyon et al., 1988; Sears & Hajdu, 1987).

In order to investigate differences in ascites production, the fluid from ascites bearing mice that can be identified by a swollen abdomen (Figure 3.32), was collected six and eight weeks after i.p. injection of HCC1954_Luc cells with Dox-induced EDI3 knockdown, as well as non-induced cells as described in the previous chapter (3.5.3.5). As presented in Figure 3.32B, the number of ascites bearing mice increased with the time after injection. At six weeks, four out of seven non-induced mice as well as three out of seven mice injected with EDI3 knockdown cells were found to be positive for ascites. At eight weeks, all mice injected with non-induced cells and six out of seven mice injected with EDI3 silenced cells developed ascites, suggesting that silencing EDI3 had no influence on the occurrence of ascites. However, EDI3 knockdown resulted in a reduction of ascites volume compared to non-induced control, which reached significance eight weeks after injection (Figure 3.32C). Furthermore, quantitative analysis of the luminescence detected in 100 µl ascites fluid revealed lower signal intensities when EDI3 was silenced, which also reached significance at eight weeks (Figure 3.32D). The observed reduction in luminescence indicates that the fluid contained less viable cancer cells.

As malignant ascites is caused by abdominal tumors, the reduced ascites volume matches the lower tumor burden observed in mice upon EDI3 knockdown (chapter 3.5.3.5). Furthermore, the reduced luminescence in ascites fluid from mice injected with EDI3 silenced cells, supports the *in vitro* results, which showed reduced viability of cells in suspension when EDI3 was silenced (chapter 3.4.5.2). Taken together, these results indicate that reduced EDI3 expression may result in less severe ascites conditions.

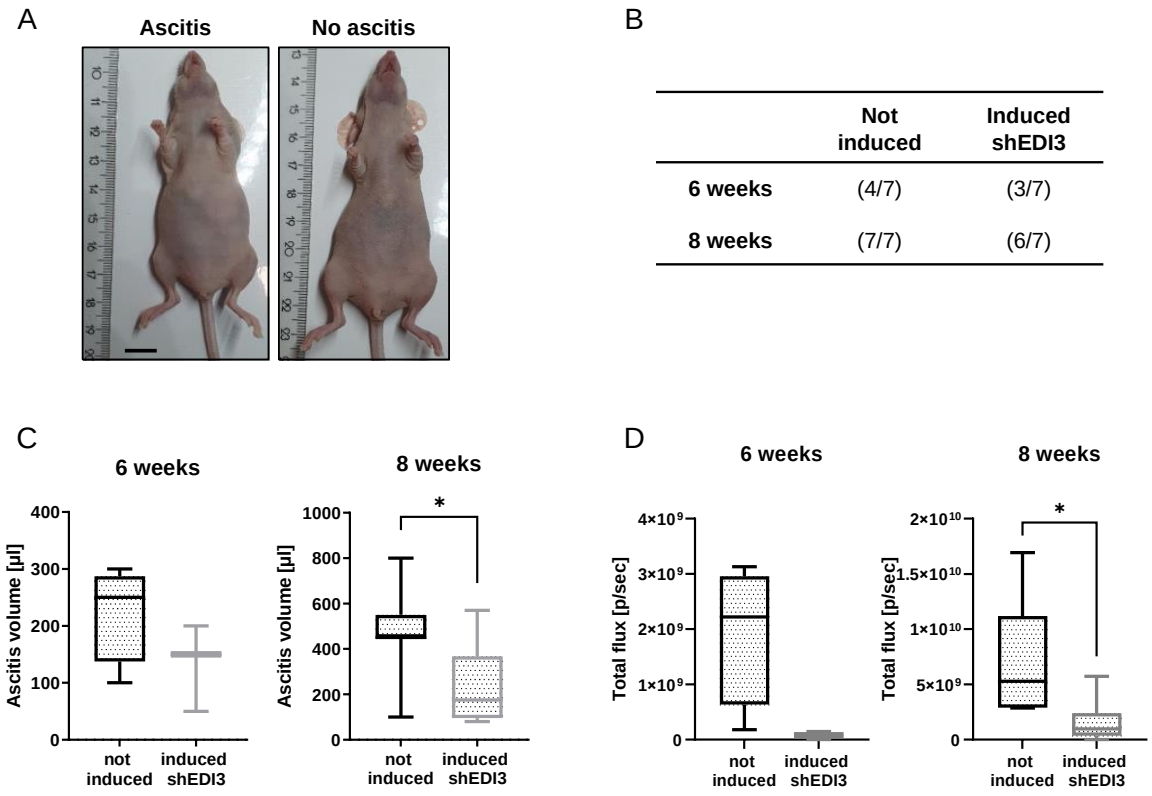

	Not induced	Induced shEDI3
6 weeks	(4/7)	(3/7)
8 weeks	(7/7)	(6/7)

Figure 3.32: Dox-induced EDI3 knockdown in HCC1954_Luc results in reduced ascites in CD1 nude mice eight weeks after i.p. injection. A) Representative photographs of mice with and without ascites. Scale bar represents 1 cm. B) Table representing the ratio of mice positive for ascites compared to all mice six and eight weeks after injection of Dox-induced EDI3 knockdown cells and non-induced control. C) Ascites volume measured in mice six and eight weeks after injection. D) Quantitative analysis of luminescence signal detected in 100 µl ascites fluid by *ex vivo* imaging. Data represent results of seven mice per condition (*, $p < 0.05$).

4 Discussion

Breast cancer is the most common cancer among women, and metastasis from primary tumor is by far the major cause of death among patients (Jin et al., 2018; Robert Koch Institut, 2020). Thus, finding new therapeutic targets that promote metastasis formation is of great importance. Metastasis and worse survival were found to be associated with elevated EDI3 expression in primary endometrial and ovarian tumors (Stewart et al., 2012). Therefore, in the last decade EDI3 was intensively studied to elucidate its role in metastasis. In fact, *in vitro* assays revealed that EDI3 positively influences migration, adhesion and spreading in several cancer cell lines, including breast cancer, while silencing EDI3 corrected the low GPC/PCho ratio reported in various tumors (Lesjak et al., 2014; Stewart et al., 2012). These results indicate that EDI3 plays a role in cancer and metastasis, thus making it a potential target for cancer treatment. However, so far all of EDI3's characterization has been conducted *in vitro*.

In the course of this PhD thesis, the impact of EDI3 on tumor growth and metastasis formation was investigated *in vivo*. For this purpose, stable luciferase-expressing cancer cell lines were generated to allow detection of cancer cells in mice by non-invasive luminescence imaging. The generated stable luciferase-expressing HCC1954_Luc breast cancer cells were subsequently used to establish Dox-inducible EDI3 knockdown cell lines. After optimization of the knockdown conditions, the cell lines were first evaluated *in vitro*. Mass spectrometry revealed that Dox-induced EDI3 knockdown led to an increase in the endogenous GPC/PCho ratio, as well as to alterations in glycerophospholipid levels. Moreover, it could be shown by various cell assays that silencing EDI3 reduced clonogenicity, proliferation and viability, thereby further supporting a role for EDI3 in metastasis formation. However, only little effect on adhesion and no effect on migration was observed.

In order to investigate EDI3 *in vivo*, several cell line-derived xenograft models were established. Primary tumor growth after subcutaneous injection of HCC1954_Luc cells in CD1 nude mice was not significantly affected by EDI3 knockdown. However, in the peritoneal metastasis model, *in vivo* imaging revealed that silencing EDI3 resulted in a decreased luminescence signal. Subsequent autopsy of the mice confirmed that EDI3 knockdown led to a reduction in metastatic burden and ascites. Furthermore, Dox-induced downregulation of EDI3 was found to be associated with longer survival of mice.

Taken together, the results indicate that EDI3 might not be relevant in the primary tumor but instead plays an important role in the process of metastasis formation. The most important findings are discussed below in detail.

4.1 Establishing a Doxycycline-inducible EDI3 knockdown system in luciferase-expressing HCC1954 cells

In vivo bioluminescence imaging facilitates the monitoring of the growth of luminescence-emitting cancer cells non-invasively in mice. In order to use this technique, stable luciferase-expressing ER-HER2+ breast cancer cell lines (HCC1954_Luc, SkBr3_Luc) were generated by introduction of the firefly luciferase gene. In contrast to other luciferase enzymes, firefly luciferase emission wavelength is red-shifted compared to the usual autofluorescence of mice which enables highly sensitive imaging with low background even in deeper tissues (Close et al., 2010; Lifante et al., 2020). Luciferase expression and sufficient luminescence signal could be confirmed *in vitro*, as well as *in vivo* (Figure 3.2 & Figure 3.3). Furthermore, it could be shown that luciferase expression remains stable over 15 weeks, which makes it suitable for long time *in vivo* studies without the need to administer selection antibiotics to the mice (Figure 3.4). As SkBr3_Luc tumors grew very slowly in mice, HCC1954_Luc cells were selected for subsequent experiments.

Previous experiments in breast (MCF7) and endometrial (AN3CA) cancer cell lines have shown that a stable constitutive EDI3 knockdown, which could be used for long term *in vivo* experiments, led to a compensation of metabolite levels over time accompanied by loss of the migration phenotype (data not published). In order to prevent compensatory effects, high EDI3-expressing HCC1954_Luc cells were transduced with lentiviral vectors containing different EDI3-targeting shRNA oligos under the control of a Dox-inducible promotor to generate Dox-inducible EDI3 knockdown cell lines. This system is well suited for *in vivo* studies, since it can be switched on at any time and can be maintained over long periods by administration of Dox to the mice (Cawthorne et al., 2007; Eger et al., 2004). Since it was previously reported that Dox can alter the metabolism and proliferative capacity of various human cell lines in a dose-dependent manner (Ahler et al., 2013), both Dox concentration and induction time points were optimized in order to minimize the concentration used. Analyses revealed that induction with Dox led to a dose-dependent downregulation of EDI3 on both RNA and protein level, which was sufficient using a concentration of 0.1 µg/ml for 72 h (Figure 3.7 & Figure 3.8). According to Ahler and colleagues, this concentration had only minor impact on all tested cell lines. Nevertheless, in the current work Dox-inducible non-targeting shNEG cells were implemented in every experiment to exclude any Dox-induced side effects.

As the efficiency of EDI3 knockdown is dependent on the Dox concentration, the generated cell lines offer the opportunity to manipulate EDI3 expression and study the resulting effect on

cell function. Moreover, the knockdown was reversible after removing Dox from the media, which allows for investigating the effect of restored EDI3 expression in future studies.

4.2 EDI3 influences choline and glycerophospholipid metabolism

As expected, and observed previously in MCF7, MDA-MB-231 and AN3_CA cells (Marchan et al., 2017; Stewart et al., 2012), silencing EDI3 in HCC1954_Luc cells strongly increased GPC as well as the GPC/PCho ratio (Figure 3.10). No effect was seen on choline or PCho levels, which may be due to compensation by alternative choline sources such as break down of PtdCho by PLD or PLC, or uptake from the extracellular media by choline transporters. However, repetition of the experiment in choline-free media did also not lead to a decrease in choline or PCho (data not shown).

Via its downstream products, EDI3 is linked to the synthesis of structural and signaling glycerophospholipids. Thus, the levels of various glycerophospholipids were analyzed with focus on lipids containing palmitic acid (16:0, 16:0-16:0 and 32:0), which is the most common saturated fatty acid found in humans (Carta et al., 2017). Dox-induced EDI3 knockdown resulted in a significant dose-dependent increase in signaling lipids LPA and PA (Figure 3.11). Conversely, a previous study reported that LPA and PA levels decreased upon transient EDI3 knockdown in MCF7 cells (Marchan et al., 2017). These contradicting observations could be explained by subtype dependent differences, since MCF7 cells belong to the luminal A subtype of breast cancer, and the here investigated HCC1954 cells belong to the HER2+ subtype. Subtype dependent differences in lipid metabolism between luminal and HER2+ subtype have been reported previously by Kang and colleagues (Kang et al., 2011).

Moreover, EDI3 knockdown induction resulted in elevated levels of several lysophospholipids, namely LPC, LPS and LPG (Figure 3.11). LPC is directly produced from PtdCho and is further metabolized to GPC by lysoPLA (Gallazzini & Burg, 2009). Previously, it was shown that high levels of GPC can lead to inhibition of lysoPLA by means of a negative feedback mechanism (Fallbrook et al., 1999). Since GPC levels are strongly elevated upon EDI3 knockdown induction, this negative feedback mechanism could explain the elevated LPC levels as illustrated in Figure 4.1. At the same time, lysoPLA inhibition and increased levels of LPC might result in an upregulation of LPA production, due to an increase in substrate availability. Furthermore, both the metabolism of LPC to LPA, as well as PtdCho to PA are catalyzed by PLDs and result in the production of free choline (Dey et al., 2020; Stack & Fishman, 2012). Thus, PLD activity might be upregulated to compensate for the reduced choline production

caused by EDI3 knockdown and could explain the increase in PA and LPA as well as the unchanged choline levels (see Figure 4.1).

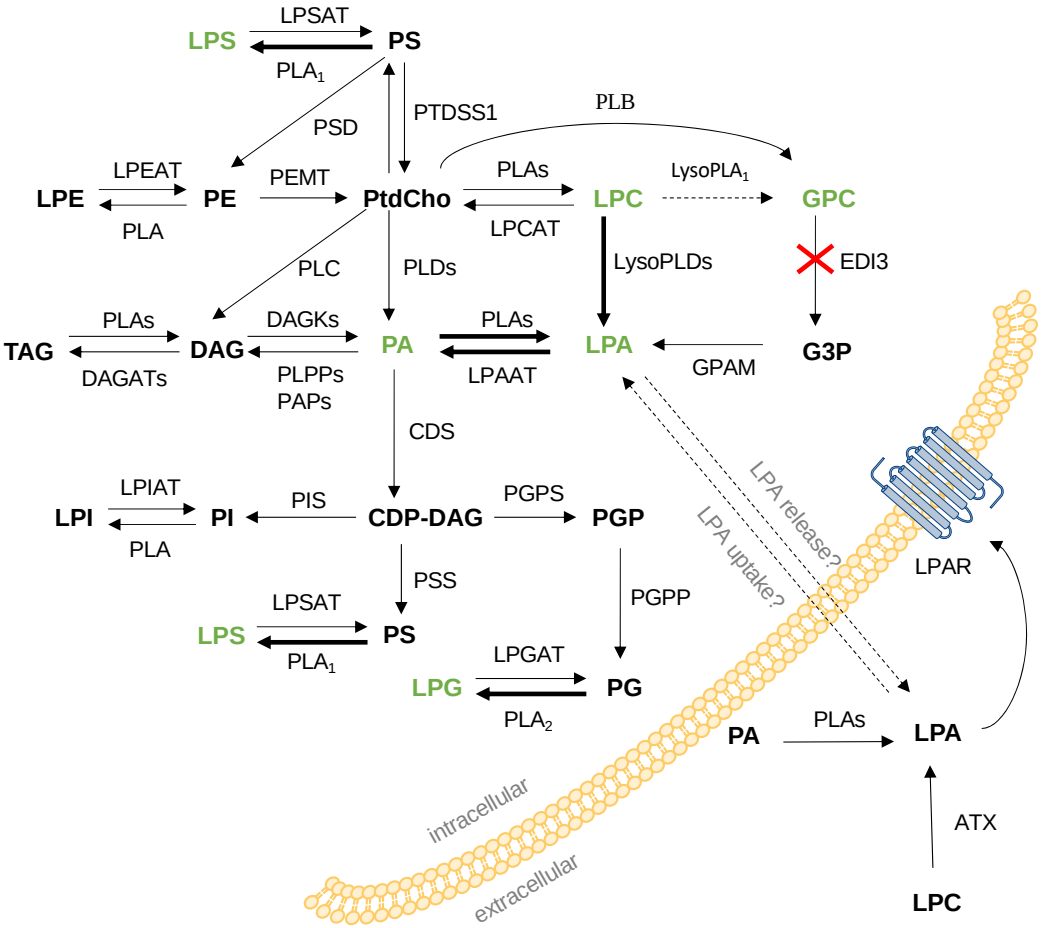

Figure 4.1: Hypothesis for the changes in glycerophospholipid metabolism observed upon EDI3 knockdown induction. Upregulated metabolites are displayed in green. Bold arrows indicate enhanced reactions, dashed arrow indicates impaired reaction. Abbreviations s. Figure 1.4.

LPA, LPC, LPS and LPG are involved in the Lands cycle, which is important for remodeling of phospholipid membranes (Eto et al., 2012; Murphy & Folco, 2019). Glycerophospholipids are synthesized *de novo* by the Kennedy pathway, which results in the formation of saturated and monounsaturated fatty acyl groups at the sn-1 and sn-2 positions (Murphy & Folco, 2019). The deacylation of glycerophospholipids to lysoglycerophospholipids by PLAs and subsequent reacylation by LPLATs signifies that this pathway provides the diversity of unsaturated, mono- and polysaturated fatty acid chains of different lengths that can be found in the membrane. Thus, the observed upregulation of lysoglycerophospholipids LPA, LPC, LPS and LPG might indicate enhanced remodeling of the cell membrane. Accordingly, previous studies reported that remodeling of fatty acid composition is associated with changes in cellular signaling and alters cell biology by affecting the physiochemical properties of membranes (Harayama &

Riezman, 2018; Simons & Toomre, 2000). Additionally, disruption of the remodeling pathway was reported to be associated with promoted tumorigenesis in the intestine (Wang et al., 2018). However, the molecular mechanism by which lipids affect biological functions has not yet been elucidated.

No significant differences were observed in the levels of structural membrane phospholipids, such as 32:0 PtdCho, 32:0 PE, 32:0 PS, 32:0 PG and 32:0 PI (data not shown). This observation supported previous findings by the group that endogenous 32:0 PtdCho levels did not change after siRNA mediated EDI3 down regulation in MCF7 cells (Stewart et al., 2012). However, it cannot be excluded that pools of structural membrane lipids with other fatty acid compositions are altered. In support, it was shown in several studies that changes in PtdCho fatty acid composition were found in many cancers (Narayan & Dahiya, 1991; Perrotti et al., 2016). For example, Narayan and Dahiya showed that 20:4 PtdCho was significantly decreased in prostatic cancer tissue compared to benign prostatic hyperplasia (Narayan & Dahiya, 1991).

4.3 EDI3 influences clonogenicity, proliferation and viability

Since previous findings suggest a role for EDI3 in cancer and metastasis, Dox-inducible EDI3 knockdown in HCC1954_Luc cells was investigated *in vitro* using several cellular assays that model processes which are relevant for metastasis formation.

The ability of a cell to survive and proliferate indefinitely to form a colony is an indicator of its tumor-initiating capabilities (Munshi et al., 2005). EDI3 knockdown resulted in a dose dependent reduction in colony number and size when induced before (pre-treated) or at the time of seeding, but not when induced 24 h later (Figure 3.12). This indicates that EDI3 is important in the early steps of colony formation, more specifically for adhesion, proliferation, and/or survival of the cells. Strong significant reduction in colony number in the pre-treated cells could be confirmed with three independent EDI3-targeting oligos, while no significant effect was observed in the non-targeting shNEG cells, thereby excluding Dox-induced off target effects (Figure 3.13). The reduction in colony size was only significant with two out of three oligos. However, further analysis indicated that the number of cells within a colony is not always reflected by its size, since the size of individual cells as well as the cell density within the colony can differ (Figure 3.15). Thus, a more precise approach to compare colony size would be to determine the number of cells per colony, which was used in subsequent assays. Taken together, the reduction in colony formation indicates that EDI3 might be relevant for the tumor-initiating capability of HCC1954 cells. To further elucidate which process during the formation of

colonies is affected by EDI3 knockdown, its influence on adhesion, proliferation and viability was investigated.

Adhesion is a relevant step in the process of colony formation and decreased adhesion upon transient siRNA mediated EDI3 knockdown was previously reported in MCF7 breast cancer and OVCAR3 ovarian cancer cells (Lesjak et al., 2014). Dox-induced EDI3 knockdown in the HCC1954-Luc cells resulted in a trend towards reduced attachment compared to non-induced cells which was significant only after 30 min with one out of two tested EDI3-targeting oligos. However, Dox treatment of non-targeting shNEG cells led to a significant increase in adhesion and comparing EDI3 knockdown with Dox-treated non-targeting cells revealed a stronger reduction in adhesion which was significant at both tested time points with one out of two independent EDI3-targeting oligo (Figure 3.14). Therefore, it is likely that the attachment-promoting effect of Dox itself may obscure EDI3's role in adhesion.

To elucidate if EDI3 is important for proliferation in HCC1954_Luc, as one possible explanation for the smaller colonies observed after EDI3 knockdown, cells were labeled with EdU, a nucleoside analog of thymidine that is incorporated into DNA during active DNA synthesis. Indeed, EDI3 silencing led to a significant reduction in proliferation with two independent EDI3-targeting shRNA oligos compared to non-induced controls (Figure 3.16 & Figure 3.17). Impaired proliferation was previously reported as a side effect of Dox (Ahler et al., 2013; Y.-F. Chen et al., 2022). However, this could be excluded in the present study since Dox treatment alone did not affect proliferation in non-targeting control cells. Interestingly, previous studies investigating EDI3 knockdown in AN3-CA and MCF7 cells reported no effect on proliferation (Sonkar et al., 2019; Stewart et al., 2012). This discrepancy may be due to the difference in cancer type and breast cancer subtype, respectively. The observed reduction in proliferation might seem contradictory to the increase in LPA levels upon EDI3 knockdown since LPA is associated with increased proliferation (Geraldo et al., 2021; Moolenaar et al., 2004). In a recent study however, it was shown that cells of different breast cancer subtypes respond differently to LPA. Intriguingly, no stimulatory effect of LPA on proliferation could be observed in HER2+ SkBr3 cells (Hauck et al., 2022), but the effect of LPA on HCC1954 cells was not tested in that study. Additionally, previous studies described very low LPAR1 and LPAR3 expression in HER2+ cell lines and no stimulatory effect of LPA in chemotaxis assays (M. Chen et al., 2007; Schmid et al., 2018). Altogether, the results indicate that the reduced proliferation observed upon EDI3 knockdown is independent of LPA levels.

Viability assays with adherent HCC1954_Luc cells revealed that Dox itself reduced cell viability in non-targeting shNEG cells (Figure 3.18). Consistently, increased apoptosis after Dox treatment has been described before in several cell lines (Ahler et al., 2013; Fife et al., 1998; Son et al., 2009). Nevertheless, silencing EDI3 resulted in a significant additional reduction in viability with one out of two tested EDI3-targeting shRNA oligos. This finding is consistent with data from a recent study reporting that transient siRNA mediated EDI3 knockdown significantly decreased survival in HER2+ HCC1954 and SkBr3 cells (Keller et al., in revision). In addition, Dox-induced EDI3 knockdown led to significantly reduced viability in cells that are in suspension (Figure 3.19), which indicates that EDI3 influences mechanisms that are involved in resistance to anoikis. Anoikis is a form of apoptosis that is induced when a cell loses contact to the ECM, thus preventing adherent-independent cell growth (Frisch & Francis, 1994; Meredith et al., 1993). In order to form metastases, cancer cells develop several mechanisms to resist anoikis. A variety of factors were identified to be involved in mediating anoikis resistance in breast cancer. Among these are alterations in metabolic pathways, such as glucose (Mason et al., 2021; Palorini et al., 2016; L. Yang et al., 2018) and fatty acid metabolism (van Weverwijk et al., 2019), as well as the upregulation of signaling pathways, such as PI3K/Akt signaling (Lu et al., 1999). Moreover, HER2 overexpression, a characteristic of HCC1954 cells, is known to promote anoikis resistance which is associated with maintained ERK and AKT signaling in the absence of proper cell adhesion (Reginato et al., 2003; Whelan et al., 2013). Interestingly, a recent study suggested that EDI3 expression is induced by HER2 pathway via PI3K/Akt/mTOR signaling (Keller et al., in revision), but how EDI3 specifically is involved in anoikis resistance is unclear and needs to be further elucidated.

No effect was observed on cell migration with two independent EDI3-targeting shRNA oligos (Figure 3.20). In contrast to the present findings, a reduction in migration upon siRNA mediated EDI3 knockdown was previously reported in several cancer cell lines, including MCF7 and MDA-MB-231 breast cancer cells (Marchan et al., 2017; Stewart et al., 2012). Moreover, it was shown that EDI3 knockdown in these cell lines resulted in decreased levels of the signaling lipid LPA, and that this decrease in LPA was relevant for EDI3's role in migration (Marchan et al., 2017). However, as discussed in chapter 4.2, no reduction in LPA was observed upon EDI3 knockdown induction in the here investigated HCC1954_Luc cells, which may explain why no effect on migration could be observed.

Overall, the *in vitro* results suggest that EDI3 is important for the tumor-initiating capabilities of HCC1954 cells. This effect is most likely mediated by EDI3 influencing cell proliferation, viability and mechanisms that provide resistance to anoikis. Additionally, EDI3 seems to be

involved in adhesion, although the true effect may be obscured by Dox. The molecular mechanism by which EDI3 is relevant in these processes is still unknown. As discussed in chapter 4.2, EDI3 knockdown resulted in altered glycerophospholipid levels, indicating a reassembling of the lipid membrane composition, which will have implications on cellular processes. If these changes are relevant for the observed phenotypes will be elucidated in the future. Nevertheless, the obtained results support previous findings that EDI3 appears to be important in tumor development and metastasis formation, which was subsequently investigated *in vivo*.

4.4 EDI3 in primary tumors

In order to investigate EDI3's role in primary tumor growth, a subcutaneous CDX-model was established in immunodeficient mice. Successful EDI3 knockdown in the tumors was confirmed on both RNA and protein level; however, there was no reduction in primary tumor growth when EDI3 was silenced compared to non-induced cells (Figure 3.22). Since GDE2, another glycerophosphodiesterase that cleaves GPC to produce choline and G3P, was slightly upregulated in the tumors upon EDI3 knockdown (Figure 3.23), it is possible that a compensation on metabolite level took place, but the increase in *GDE2* mRNA expression was not significant. In order to elucidate if there was compensation at the metabolite level within the tumors, metabolite measurements are ongoing. Interestingly, Dox treatment of non-targeting shNEG xenografts resulted in increased tumor growth (data not shown), indicating that Dox itself may have a promoting effect which could obscure EDI3's influence. Moreover, in a recent study our group could show that inhibiting EDI3 with the general phosphodiesterase (PDE) inhibitor dipyridamole significantly decreased tumor volume of HCC1954 xenografts (Keller et al., in revision). However, as dipyridamole is not specific towards EDI3, the observed effect might not be due to inhibiting EDI3 alone. Thus, EDI3's role in the primary tumor is not yet fully elucidated.

Importantly, the *in vitro* set up, where silencing EDI3 led to a reduction in colony formation and proliferation, differs dramatically from the *in vivo* conditions. *In vitro*, cells were highly diluted and plated subconfluently, while for the s.c. tumors millions of cells were implanted in mixture with Matrigel which contains ECM proteins and growth factors. Moreover, it is well known that high confluency and tumor cell density affect cell behavior and protein expression, which might explain these contradicting results (Jayatilaka et al., 2018; Sharif & Wellstein, 2015; Topman et al., 2011).

Since the *in vitro* and *in vivo* results obtained in the current work indicate that EDI3 might rather be relevant for the clonogenic potential of single cells than in dense primary tumors, the subsequent work in this thesis focused on investigating EDI3 in metastasis.

4.5 EDI3 in metastasis formation

Since its identification, EDI3 has been linked to tumor metastasis (Stewart et al., 2012). This was further substantiated by *in vitro* studies in various cell lines describing a role for EDI3 in migration and adhesion (Lesjak et al., 2014; Stewart et al., 2012), but until the present work, a role for EDI3 in metastasis *in vivo* was not investigated. Therefore, a mouse model for lung metastasis was established in the current thesis by tail vein injection of HCC1954_Luc cells. Despite one previous study reporting microscopically visible metastasis four weeks after tail vein injection of HCC1954 cells (Baldassarre et al., 2017), under the here-tested experimental conditions, no metastases were observed. This may be due to differences in mouse strains, as Baldassarre and colleagues used the more immunodeficient $Rag2^{-/-}$:$IL2R\gamma c^{-/-}$ mice in their study. Thus, the model would need further optimization. However, the lung metastasis model is not commonly used to study HCC1954 metastasis. Instead, Clinchy and colleagues reported that HCC1954 cells grew aggressively in a model for peritoneal metastasis (Clinchy et al., 2000). Peritoneal metastases usually occur in late-stage breast cancer and are associated with very poor survival (Bertozzi et al., 2015; Flanagan et al., 2018; Lin et al., 2004; Quigley et al., 2013; Tham et al., 2006; Tuthill et al., 2009). It was shown that in this model HCC1954 cells form metastases in the liver (Clinchy et al., 2000), which is the most common metastatic site for ER−|PR−|HER2+ subtype of breast cancer (Gong et al., 2017; Wu et al., 2017). Therefore, for this thesis, a mouse model for peritoneal metastasis was established. Serial *in vivo* imaging revealed a significant reduction in luminescence signal after i.p. injection of Dox-induced EDI3 knockdown cells compared to non-induced cells (Figure 3.26). Since Dox itself can reduce cell proliferation (Ahler et al., 2013), it was necessary to exclude that the decreased signal was due to Dox itself. *In vivo* imaging showed that Dox treatment of non-targeting shNEG cells even resulted in a slight increase of the luminescence signal, confirming that the previously observed reduction in luminescence was indeed caused by silencing EDI3. Interestingly, EDI3 knockdown significantly increased survival of mice, while Dox treatment of non-targeting shNEG cells had no effect (Figure 3.27). Improved survival and reduced luminescence upon EDI3 silencing were the first hint that EDI3 may indeed be relevant for tumor growth in this metastasis model. Subsequent autopsy of mice followed by *ex vivo* imaging of organs and analysis of tumor weight confirmed that silencing EDI3 resulted in a reduced tumor burden (Figure 3.30, Figure 3.31).

In vivo and *ex vivo* imaging not only revealed that the luminescence is generally lower when EDI3 is silenced, but also that the difference in signal intensity between EDI3 knockdown and control gets stronger over time. Therefore, it appears that silencing EDI3 does not completely prevent metastases but reduces metastasis growth. These results are in agreement with the results obtained *in vitro*, showing that Dox-induced EDI3 knockdown reduces proliferation. In addition to the metastatic burden, ascites volume was also significantly reduced upon EDI3 knockdown (Figure 3.32). Since malignant ascites is caused by abdominal tumors, the reduced volume matches with the reduction in tumor burden. Furthermore, luminescence imaging revealed that the ascites fluid contained viable cancer cells. Interestingly, the luminescence signal was significantly lower in the EDI3 knockdown condition, which indicates that the number of viable cells was reduced. This observation corresponds with the reduced viability of cells in suspension after EDI3 knockdown that was seen *in vitro*. Thus, the *in vivo* findings further support the hypothesis that EDI3 influences mechanisms that provide resistance towards anoikis.

Looking at the metastatic organotropism, *ex vivo* imaging revealed that high metastatic burden was predominantly found in the pancreas and gonadal white adipose tissue (WAT), as well as in the liver and diaphragm (Figure 3.30). Liver infiltration after i.p. injection of HCC1954 cells was previously reported by Clinchy and colleagues (Clinchy et al., 2000); however, metastasis in pancreas, gonadal WAT or diaphragm was not described. Since the authors investigated most of the organs macroscopically, they may have missed micro metastases that could be detected by *ex vivo* luminescence imaging. They also identified large plaques of tumor cells on the peritoneal wall and kidney metastasis 8-15 weeks after i.p. injection, which was also observed in the current work up to 15 weeks after injection (Figure 3.28). Interestingly, in contrast to the here-obtained results, metastases were also found in the lungs, which may be due to the more immunodeficient mouse strain used in their study. The distribution of metastases to certain organs is regulated by multiple factors, such as breast cancer subtype, host organ microenvironment, and cancer cells-organ interactions (W. Chen et al., 2018). Crosstalk between cancer cells and host organs, as well as various factors released from cancer cells facilitate the formation of the premetastatic niche, which is also influenced by the specific organ microenvironment (W. Chen et al., 2018; Y. Liu & Cao, 2016). Strikingly, no differences in metastatic organotropism could be observed upon EDI3 knockdown, suggesting. that EDI3 does not affect mechanisms involved in premetastatic niche formation and organotropism.

Overall, the results obtained from the peritoneal metastasis model show that EDI3 knockdown reduces metastatic burden, ascites volume, and the amount of viable cancer cells contained in

the ascites fluid, probably due to its influence on proliferation and resistance to anoikis, which consequently results in prolonged survival. Thus, the *in vivo* results further support the results obtained *in vitro* suggesting that EDI3 plays a role in metastasis formation which makes it a potential therapeutic target to reduce the severity of metastatic disease and increase survival.

4.6 Future perspectives

This thesis provided *in vitro* and *in vivo* evidence that EDI3 is important for the tumor-initiating capabilities of HCC1954 cells. Moreover, it was shown that this effect is most likely mediated by reduced proliferation and increased susceptibility towards anoikis upon EDI3 knockdown. However, subsequent analyses are needed to elucidate the mechanisms by which EDI3 influences these processes.

Most strikingly, silencing EDI3 resulted in a reduction in tumor burden and ascites in a mouse model of peritoneal metastasis. As a next step, the collected tumors will be analyzed to investigate the differences between metastases with normal and reduced EDI3 expression. RNA-sequencing (RNAseq) and proteomics of the extracted tumors may identify EDI3-induced changes in expression levels and could reveal relevant pathways that are altered. Furthermore, differences in tumor proliferation will be elucidated by examining the expression of proliferation markers, such as Ki-67, to confirm EDI3's role in proliferation. For this purpose, cryo slides will also be prepared and stained with the respective antibodies to obtain spatial information about proliferation within the tumor tissue. Additionally, staining of cleaved-caspase-3 may provide information about apoptosis. To investigate if the reduction in metastasis burden is mediated by changes in metabolites, infiltrated organs will be analyzed by MALDI mass spectrometry imaging (MALDI-MSI). This technique combines mass spectrometry with traditional histology and provides information about the spatial localization of metabolites within the tumor and adjacent tissue. Besides targeted analysis of choline metabolites and glycerophospholipids, untargeted analyses will be performed to identify any significant changes in the cells upon EDI3 knockdown that influence proliferation. Thus, MALDI-MSI could reveal differences within the tumor cell, at the invading edge of the tumor cells into the tissue. Moreover, the ascites fluid will be analyzed regarding the metabolite levels to reveal EDI3 expression-dependent differences. It was shown previously that overexpression of active focal adhesion kinase (FAK; *PTK2*) or integrin-linked kinase (ILK) blocks anoikis in suspended cells and consequently serves as a marker for anoikis protection (Frisch et al., 1996; Frisch & Francis, 1994; Hungerford et al., 1996; Ilić et al., 1998; Paoli et al., 2013). To further investigate EDI3's influence on anoikis *in vivo*, RNA will be isolated from the tumor cells

contained in the ascites fluid to measure the expression levels of anoikis-suppressing markers *PTK2* and *ILK*, as well as apoptosis markers.

In vitro results obtained in this thesis from metabolomic analysis after silencing EDI3 revealed alterations in glycerophospholipids that might indicate increased remodeling of membrane lipid composition. Alterations of membrane lipid composition are known to be associated with changes in cellular signaling (Simons & Toomre, 2000). In order to elucidate the mechanism behind the *in vivo* observations, it is of high interest to further investigate *in vitro* how modification of EDI3 expression affects this process. Alterations in membrane lipid composition, characterized by the degree of lipid packing, could be assessed using polarity sensitive fluorescent probes, such as di-4-ANEPPDHQ which changes its conformation depending on the fluidity of the membrane and can be detected by flow cytometry or confocal microscopy (Owen et al., 2011; Waddington et al., 2019). Furthermore, RAMAN microscopy could be used which allows detection of single membrane components and could reveal more detailed information about changes in membrane lipids and fatty acid composition. Moreover, transcriptome and proteome analysis could also reveal EDI3-induced changes in enzymes involved in phospholipid metabolism to confirm observed alterations.

In the current work, no significant differences in primary tumor growth were observed in the subcutaneous tumor model. However, subcutaneous tumors are not located in their natural microenvironment which may lead to differential effects on their biology. In an ongoing experiment, an orthotopic mouse model has been established, which allows to study both primary tumor growth in the mammary fat pad as well as metastasis formation at secondary sides; thus, representing the whole metastatic process. In this experiment an additional approach was used to study EDI3's influence on growth and metastasis that may better reflect the human situation: Mice were first injected with tumor cells, and then treated with Dox to silence EDI3. Primary tumors were allowed to develop, then surgically resected once a certain size was reached, and the effect of EDI3 silencing on primary tumor recurrence and metastasis development is being monitored by *in vivo* luminescence and µCT imaging. Initial results from this experiment suggest a significant decrease in primary tumor growth and significantly reduced formation of lung metastasis when EDI3 is silenced. Eventually, regrown primary tumors and infiltrated organs will be collected for further analysis. Harvested tumors will be analyzed by RNAseq, proteomics, metabolomics and MALDI-MSI to access differences between primary tumor and metastasis, which may reveal why EDI3 knockdown led to a reduction in metastasis burden but did not show any effect on primary tumor growth. Furthermore, blood will be collected from the heart of the mice, in order to isolate circulating

tumor cells (CTCs). These cells can be quantified by qRT-PCR using human specific primers of highly expressed genes such as *HER2* or *luc2* (Na et al., 2020) to investigate if silencing EDI3 affects the number of CTCs in the blood. In addition, mRNA expression of anoikis-suppressing and apoptosis markers in CTCs will be analyzed to further elucidate a role for EDI3 in anoikis.

Since HCC1954 cells belong to the ER-PR-HER2+ breast cancer subtype that most often metastasizes to the brain and liver (Gong et al., 2017; Wu et al., 2017), additional mouse models for organ specific metastasis could be used to confirm the results obtained by the peritoneal model, namely injection of cells to the carotid artery for the brain and the portal vein for the liver. Furthermore, EDI3 could be investigated in other HER2-positive breast cancer cell lines, such as SUM190PT, to confirm results for this particular subtype.

The findings obtained in this thesis suggest that EDI3 may be a potential target for cancer treatment. By using a variety of approaches and methodologies in the proposed next steps, the goal is to not only understand the mechanism by which EDI3 influences tumor metastasis, but also to determine whether EDI3 itself and the metabolic pathways it influences can eventually be targeted therapeutically in HER2+ breast cancer. Therefore, the identification of inhibitors that specifically target EDI3 would be a critical next step. Small molecule inhibitors or EDI3-targeting oligonucleotides (e.g. FANA-ASO, AUM BioTech) can then be delivered directly into animals via injection into the bloodstream to silence EDI3 in tumor-bearing mice.

5 Bibliography

Aboagye, E. O., & Bhujwalla, Z. M. (1999). Malignant transformation alters membrane choline phospholipid metabolism of human mammary epithelial cells. *Cancer Research*, *59*(1), 80–84.

Adams, K. J., Pratt, B., Bose, N., Dubois, L. G., St. John-Williams, L., Perrott, K. M., Ky, K., Kapahi, P., Sharma, V., MacCoss, M. J., Moseley, M. A., Colton, C. A., MacLean, B. X., Schilling, B., Thompson, J. W., & Alzheimer's Disease Metabolomics Consortium. (2020). Skyline for Small Molecules: A Unifying Software Package for Quantitative Metabolomics. *Journal of Proteome Research*, *19*(4), 1447–1458. https://doi.org/10.1021/acs.jproteome.9b00640

Ahler, E., Sullivan, W. J., Cass, A., Braas, D., York, A. G., Bensinger, S. J., Graeber, T. G., & Christofk, H. R. (2013). Doxycycline Alters Metabolism and Proliferation of Human Cell Lines. *PLoS ONE*, *8*(5), e64561. https://doi.org/10.1371/journal.pone.0064561

Aikawa, S., Hashimoto, T., Kano, K., & Aoki, J. (2015). Lysophosphatidic acid as a lipid mediator with multiple biological actions. *The Journal of Biochemistry*, *157*(2), 81–89. https://doi.org/10.1093/jb/mvu077

Andresen, B. T., Rizzo, M. A., Shome, K., & Romero, G. (2002). The role of phosphatidic acid in the regulation of the Ras/MEK/Erk signaling cascade. *FEBS Letters*, *531*(1), 65–68. https://doi.org/10.1016/s0014-5793(02)03483-x

Balathasan, L., Beech, J. S., & Muschel, R. J. (2013). Ultrasonography-Guided Intracardiac Injection: An Improvement for Quantitative Brain Colonization Assays. *The American Journal of Pathology*, *183*(1), 26–34. https://doi.org/10.1016/j.ajpath.2013.03.003

Baldassarre, T., Truesdell, P., & Craig, A. W. (2017). Endophilin A2 promotes HER2 internalization and sensitivity to trastuzumab-based therapy in HER2-positive breast cancers. *Breast Cancer Research: BCR*, *19*(1), 110. https://doi.org/10.1186/s13058-017-0900-z

Bertozzi, S., Londero, A. P., Cedolini, C., Uzzau, A., Seriau, L., Bernardi, S., Bacchetti, S., Pasqual, E. M., & Risaliti, A. (2015). Prevalence, risk factors, and prognosis of peritoneal metastasis from breast cancer. *SpringerPlus*, *4*, 688. https://doi.org/10.1186/s40064-015-1449-x

Blackburn, S. C., & Stanton, M. P. (2014). Anatomy and physiology of the peritoneum. *Seminars in Pediatric Surgery*, *23*(6), 326–330. https://doi.org/10.1053/j.sempedsurg.2014.06.002

Blows, F. M., Driver, K. E., Schmidt, M. K., Broeks, A., van Leeuwen, F. E., Wesseling, J., Cheang, M. C., Gelmon, K., Nielsen, T. O., Blomqvist, C., Heikkilä, P., Heikkinen, T., Nevanlinna, H., Akslen, L. A., Bégin, L. R., Foulkes, W. D., Couch, F. J., Wang, X., Cafourek, V., … Huntsman, D. (2010). Subtyping of Breast Cancer by Immunohistochemistry to Investigate a Relationship between Subtype and Short and Long Term Survival: A Collaborative Analysis of Data for 10,159 Cases from 12 Studies. *PLoS Medicine*, *7*(5), e1000279. https://doi.org/10.1371/journal.pmed.1000279

Brand, M., Laban, S., Theodoraki, M.-N., Doescher, J., Hoffmann, T. K., Schuler, P. J., & Brunner, C. (2020). Characterization and Differentiation of the Tumor Microenvironment (TME) of Orthotopic and Subcutaneously Grown Head and Neck Squamous Cell Carcinoma

(HNSCC) in Immunocompetent Mice. *International Journal of Molecular Sciences*, *22*(1), E247. https://doi.org/10.3390/ijms22010247

Brenton, J. D., Carey, L. A., Ahmed, A. A., & Caldas, C. (2005). Molecular classification and molecular forecasting of breast cancer: Ready for clinical application? *Journal of Clinical Oncology: Official Journal of the American Society of Clinical Oncology*, *23*(29), 7350–7360. https://doi.org/10.1200/JCO.2005.03.3845

Brown, D. M., & Ruoslahti, E. (2004). Metadherin, a cell surface protein in breast tumors that mediates lung metastasis. *Cancer Cell*, *5*(4), 365–374. https://doi.org/10.1016/s1535-6108(04)00079-0

Bruntz, R. C., Lindsley, C. W., & Brown, H. A. (2014). Phospholipase D signaling pathways and phosphatidic acid as therapeutic targets in cancer. *Pharmacological Reviews*, *66*(4), 1033–1079. https://doi.org/10.1124/pr.114.009217

Burgos, J. S., Rosol, M., Moats, R. A., Khankaldyyan, V., Kohn, D. B., Nelson, M. D., & Laug, W. E. (2003). Time course of bioluminescent signal in orthotopic and heterotopic brain tumors in nude mice. *BioTechniques*, *34*(6), 1184–1188. https://doi.org/10.2144/03346st01

Campbell, J. P., Merkel, A. R., Masood-Campbell, S. K., Elefteriou, F., & Sterling, J. A. (2012). Models of Bone Metastasis. *Journal of Visualized Experiments : JoVE*, *67*, 4260. https://doi.org/10.3791/4260

Carrasco, S., & Mérida, I. (2007). Diacylglycerol, when simplicity becomes complex. *Trends in Biochemical Sciences*, *32*(1), 27–36. https://doi.org/10.1016/j.tibs.2006.11.004

Carta, G., Murru, E., Banni, S., & Manca, C. (2017). Palmitic Acid: Physiological Role, Metabolism and Nutritional Implications. *Frontiers in Physiology*, *8*, 902. https://doi.org/10.3389/fphys.2017.00902

Caskey, C. I., Scatarige, J. C., & Fishman, E. K. (1991). Distribution of metastases in breast carcinoma: CT evaluation of the abdomen. *Clinical Imaging*, *15*(3), 166–171. https://doi.org/10.1016/0899-7071(91)90071-3

Cawthorne, C., Swindell, R., Stratford, I. J., Dive, C., & Welman, A. (2007). *Comparison of Doxycycline Delivery Methods for Tet-Inducible Gene Expression in a Subcutaneous Xenograft Model*. *18*(2), 4.

Chae, Y. C., Kim, J. H., Kim, K. L., Kim, H. W., Lee, H. Y., Heo, W. D., Meyer, T., Suh, P.-G., & Ryu, S. H. (2008). Phospholipase D activity regulates integrin-mediated cell spreading and migration by inducing GTP-Rac translocation to the plasma membrane. *Molecular Biology of the Cell*, *19*(7), 3111–3123. https://doi.org/10.1091/mbc.e07-04-0337

Cheang, M. C. U., Chia, S. K., Voduc, D., Gao, D., Leung, S., Snider, J., Watson, M., Davies, S., Bernard, P. S., Parker, J. S., Perou, C. M., Ellis, M. J., & Nielsen, T. O. (2009). Ki67 Index, HER2 Status, and Prognosis of Patients With Luminal B Breast Cancer. *JNCI Journal of the National Cancer Institute*, *101*(10), 736–750. https://doi.org/10.1093/jnci/djp082

Chen, M., Towers, L. N., & O'Connor, K. L. (2007). LPA2 (EDG4) mediates Rho-dependent chemotaxis with lower efficacy than LPA1 (EDG2) in breast carcinoma cells. *American Journal of Physiology. Cell Physiology*, *292*(5), C1927-1933. https://doi.org/10.1152/ajpcell.00400.2006

Chen, W., Hoffmann, A. D., Liu, H., & Liu, X. (2018). Organotropism: New insights into molecular mechanisms of breast cancer metastasis. *NPJ Precision Oncology*, *2*, 4. https://doi.org/10.1038/s41698-018-0047-0

Chen, Y.-F., Yang, Y.-N., Chu, H.-R., Huang, T.-Y., Wang, S.-H., Chen, H.-Y., Li, Z.-L., Yang, Y.-C. S. H., Lin, H.-Y., Hercbergs, A., Whang-Peng, J., Wang, K., & Davis, P. J. (2022). Role of Integrin αvβ3 in Doxycycline-Induced Anti-Proliferation in Breast Cancer Cells. *Frontiers in Cell and Developmental Biology*, *10*. https://www.frontiersin.org/articles/10.3389/fcell.2022.829788

Choi, J. W., Herr, D. R., Noguchi, K., Yung, Y. C., Lee, C.-W., Mutoh, T., Lin, M.-E., Teo, S. T., Park, K. E., Mosley, A. N., & Chun, J. (2010). LPA receptors: Subtypes and biological actions. *Annual Review of Pharmacology and Toxicology*, *50*, 157–186. https://doi.org/10.1146/annurev.pharmtox.010909.105753

Chopra, I., Hawkey, P. M., & Hinton, M. (1992). Tetracyclines, molecular and clinical aspects. *The Journal of Antimicrobial Chemotherapy*, *29*(3), 245–277. https://doi.org/10.1093/jac/29.3.245

Christofori, G. (2006). New signals from the invasive front. *Nature*, *441*(7092), 444–450. https://doi.org/10.1038/nature04872

Clinchy, B., Gazdar, A., Rabinovsky, R., Yefenof, E., Gordon, B., & Vitetta, E. S. (2000). The growth and metastasis of human, HER-2/neu-overexpressing tumor cell lines in male SCID mice. *Breast Cancer Research and Treatment*, *61*(3), 217–228. https://doi.org/10.1023/A:1006494001861

Close, D. M., Xu, T., Sayler, G. S., & Ripp, S. (2010). In Vivo Bioluminescent Imaging (BLI): Noninvasive Visualization and Interrogation of Biological Processes in Living Animals. *Sensors (Basel, Switzerland)*, *11*(1), 180–206. https://doi.org/10.3390/s110100180

Coleman, R. A., & Lee, D. P. (2004). Enzymes of triacylglycerol synthesis and their regulation. *Progress in Lipid Research*, *43*(2), 134–176. https://doi.org/10.1016/s0163-7827(03)00051-1

Coman, C., Solari, F. A., Hentschel, A., Sickmann, A., Zahedi, R. P., & Ahrends, R. (2016). Simultaneous Metabolite, Protein, Lipid Extraction (SIMPLEX): A Combinatorial Multimolecular Omics Approach for Systems Biology. *Molecular & Cellular Proteomics*, *15*(4), 1435–1466. https://doi.org/10.1074/mcp.M115.053702

Craig, D. W., O'Shaughnessy, J. A., Kiefer, J. A., Aldrich, J., Sinari, S., Moses, T. M., Wong, S., Dinh, J., Christoforides, A., Blum, J. L., Aitelli, C. L., Osborne, C. R., Izatt, T., Kurdoglu, A., Baker, A., Koeman, J., Barbacioru, C., Sakarya, O., De La Vega, F. M., … Carpten, J. D. (2013). Genome and transcriptome sequencing in prospective metastatic triple-negative breast cancer uncovers therapeutic vulnerabilities. *Molecular Cancer Therapeutics*, *12*(1), 104–116. https://doi.org/10.1158/1535-7163.MCT-12-0781

Cristea, S., & Polyak, K. (2018). Dissecting the mammary gland one cell at a time. *Nature Communications*, *9*(1), Article 1. https://doi.org/10.1038/s41467-018-04905-2

Dai, X., Li, T., Bai, Z., Yang, Y., Liu, X., Zhan, J., & Shi, B. (2015). Breast cancer intrinsic subtype classification, clinical use and future trends. *American Journal of Cancer Research*, *5*(10), 2929–2943.

Deluca, M. (1976). Firefly luciferase. *Advances in Enzymology and Related Areas of Molecular Biology*, *44*, 37–68. https://doi.org/10.1002/9780470122891.ch2

Dey, P., Han, G.-S., & Carman, G. M. (2020). A review of phosphatidate phosphatase assays. *Journal of Lipid Research*, *61*(12), 1556–1564. https://doi.org/10.1194/jlr.R120001092

Dharmacon. (2014). *SMARTvectorTM Inducible Lentiviral shRNA - Technical Manual*. https://horizondiscovery.com/-/media/Files/Horizon/resources/Technical-manuals/smartvector-inducible-lentiviral-shRNA-manual.pdf

Dowhan, W. (1997). Molecular basis for membrane phospholipid diversity: Why are there so many lipids? *Annual Review of Biochemistry*, *66*, 199–232. https://doi.org/10.1146/annurev.biochem.66.1.199

Eger, K., Hermes, M., Uhlemann, K., Rodewald, S., Ortwein, J., Brulport, M., Bauer, A. W., Schormann, W., Lupatsch, F., Schiffer, I. B., Heimerdinger, C. K., Gebhard, S., Spangenberg, C., Prawitt, D., Trost, T., Zabel, B., Sauer, C., Tanner, B., Kolbl, H., … Hengstler, J. G. (2004). 4-Epidoxycycline: An alternative to doxycycline to control gene expression in conditional mouse models. *Biochemical and Biophysical Research Communications*, *323*(3), 979–986. https://doi.org/10.1016/j.bbrc.2004.08.187

Eliyahu, G., Kreizman, T., & Degani, H. (2007). Phosphocholine as a biomarker of breast cancer: Molecular and biochemical studies. *International Journal of Cancer*, *120*(8), 1721–1730. https://doi.org/10.1002/ijc.22293

Elkin, M., & Vlodavsky, I. (2001). Tail vein assay of cancer metastasis. *Current Protocols in Cell Biology*, *Chapter 19*, 19.2.1-19.2.7. https://doi.org/10.1002/0471143030.cb1902s12

Eto, M., Shindou, H., Koeberle, A., Harayama, T., Yanagida, K., & Shimizu, T. (2012). Lysophosphatidylcholine acyltransferase 3 is the key enzyme for incorporating arachidonic acid into glycerophospholipids during adipocyte differentiation. *International Journal of Molecular Sciences*, *13*(12), 16267–16280. https://doi.org/10.3390/ijms131216267

Fallahpour, S., Navaneelan, T., De, P., & Borgo, A. (2017). Breast cancer survival by molecular subtype: A population-based analysis of cancer registry data. *CMAJ Open*, *5*(3), E734–E739. https://doi.org/10.9778/cmajo.20170030

Fallbrook, A., Turenne, S. D., Mamalias, N., Kish, S. J., & Ross, B. M. (1999). Phosphatidylcholine and phosphatidylethanolamine metabolites may regulate brain phospholipid catabolism via inhibition of lysophospholipase activity. *Brain Research*, *834*(1–2), 207–210. https://doi.org/10.1016/S0006-8993(99)01570-X

Faustino-Rocha, A., Oliveira, P. A., Pinho-Oliveira, J., Teixeira-Guedes, C., Soares-Maia, R., da Costa, R. G., Colaço, B., Pires, M. J., Colaço, J., Ferreira, R., & Ginja, M. (2013). Estimation of rat mammary tumor volume using caliper and ultrasonography measurements. *Lab Animal*, *42*(6), 217–224. https://doi.org/10.1038/laban.254

Fife, R. S., Sledge, G. W., Roth, B. J., & Proctor, C. (1998). Effects of doxycycline on human prostate cancer cells in vitro. *Cancer Letters*, *127*(1–2), 37–41. https://doi.org/10.1016/s0304-3835(98)00003-2

Fire, A., Xu, S., Montgomery, M. K., Kostas, S. A., Driver, S. E., & Mello, C. C. (1998). *Potent and specific genetic interference by double-stranded RNA in Caenorhabditis elegans*. *391*, 6.

Flanagan, M., Solon, J., Chang, K. H., Deady, S., Moran, B., Cahill, R., Shields, C., & Mulsow, J. (2018). Peritoneal metastases from extra-abdominal cancer—A population-based study. *European Journal of Surgical Oncology: The Journal of the European Society of Surgical Oncology and the British Association of Surgical Oncology*, *44*(11), 1811–1817. https://doi.org/10.1016/j.ejso.2018.07.049

Fogh, J., Fogh, J. M., & Orfeo, T. (1977). One hundred and twenty-seven cultured human tumor cell lines producing tumors in nude mice. *Journal of the National Cancer Institute*, *59*(1), 221–226. https://doi.org/10.1093/jnci/59.1.221

Foster, D. A. (2009). Phosphatidic acid signaling to mTOR: Signals for the survival of human cancer cells. *Biochimica Et Biophysica Acta*, *1791*(9), 949–955. https://doi.org/10.1016/j.bbalip.2009.02.009

Fraga, H. (2008). Firefly luminescence: A historical perspective and recent developments. *Photochemical & Photobiological Sciences: Official Journal of the European Photochemistry Association and the European Society for Photobiology*, *7*(2), 146–158. https://doi.org/10.1039/b719181b

Franken, N. A. P., Rodermond, H. M., Stap, J., Haveman, J., & van Bree, C. (2006). Clonogenic assay of cells in vitro. *Nature Protocols*, *1*(5), 2315–2319. https://doi.org/10.1038/nprot.2006.339

Frisch, S. M., & Francis, H. (1994). Disruption of epithelial cell-matrix interactions induces apoptosis. *The Journal of Cell Biology*, *124*(4), 619–626. https://doi.org/10.1083/jcb.124.4.619

Frisch, S. M., Vuori, K., Kelaita, D., & Sicks, S. (1996). A role for Jun-N-terminal kinase in anoikis; suppression by bcl-2 and crmA. *Journal of Cell Biology*, *135*(5), 1377–1382. https://doi.org/10.1083/jcb.135.5.1377

Gadiya, M., Mori, N., Cao, M. D., Mironchik, Y., Kakkad, S., Gribbestad, I. S., Glunde, K., Krishnamachary, B., & Bhujwalla, Z. M. (2014). Phospholipase D1 and choline kinase-α are interactive targets in breast cancer. *Cancer Biology & Therapy*, *15*(5), 593–601. https://doi.org/10.4161/cbt.28165

Gallazzini, M., & Burg, M. B. (2009). What's new about osmotic regulation of glycerophosphocholine. *Physiology (Bethesda, Md.)*, *24*, 245–249. https://doi.org/10.1152/physiol.00009.2009

Gazdar, A. F., Kurvari, V., Virmani, A., Gollahon, L., Sakaguchi, M., Westerfield, M., Kodagoda, D., Stasny, V., Cunningham, H. T., Wistuba, I. I., Tomlinson, G., Tonk, V., Ashfaq, R., Leitch, A. M., Minna, J. D., & Shay, J. W. (1998). Characterization of paired tumor and non-tumor cell lines established from patients with breast cancer. *International Journal of Cancer*, *78*(6), 766–774. https://doi.org/10.1002/(SICI)1097-0215(19981209)78:6<766::AID-IJC15>3.0.CO;2-L

Geraldo, L. H. M., Spohr, T. C. L. de S., Amaral, R. F. do, Fonseca, A. C. C. da, Garcia, C., Mendes, F. de A., Freitas, C., dosSantos, M. F., & Lima, F. R. S. (2021). Role of lysophosphatidic acid and its receptors in health and disease: Novel therapeutic strategies. *Signal Transduction and Targeted Therapy*, *6*(1), Article 1. https://doi.org/10.1038/s41392-020-00367-5

Gibellini, F., & Smith, T. K. (2010). The Kennedy pathway—De novo synthesis of

phosphatidylethanolamine and phosphatidylcholine. *IUBMB Life*, *62*(6), 414–428. https://doi.org/10.1002/iub.337

Glunde, K., Bhujwalla, Z. M., & Ronen, S. M. (2011). Choline metabolism in malignant transformation. *Nature Reviews Cancer*, *11*(12), Article 12. https://doi.org/10.1038/nrc3162

Glunde, K., Penet, M.-F., Jiang, L., Jacobs, M. A., & Bhujwalla, Z. M. (2015). Choline metabolism-based molecular diagnosis of cancer: An update. *Expert Review of Molecular Diagnostics*, *15*(6), 735–747. https://doi.org/10.1586/14737159.2015.1039515

Glunde, K., Raman, V., Mori, N., & Bhujwalla, Z. M. (2005). RNA interference-mediated choline kinase suppression in breast cancer cells induces differentiation and reduces proliferation. *Cancer Research*, *65*(23), 11034–11043. https://doi.org/10.1158/0008-5472.CAN-05-1807

Goddard, E. T., Fischer, J., & Schedin, P. (2016). A Portal Vein Injection Model to Study Liver Metastasis of Breast Cancer. *Journal of Visualized Experiments: JoVE*, *118*. https://doi.org/10.3791/54903

Goldhirsch, A., Wood, W. C., Coates, A. S., Gelber, R. D., Thürlimann, B., & Senn, H.-J. (2011). Strategies for subtypes—dealing with the diversity of breast cancer: Highlights of the St Gallen International Expert Consensus on the Primary Therapy of Early Breast Cancer 2011. *Annals of Oncology*, *22*(8), 1736–1747. https://doi.org/10.1093/annonc/mdr304

Gong, Y., Liu, Y.-R., Ji, P., Hu, X., & Shao, Z.-M. (2017). Impact of molecular subtypes on metastatic breast cancer patients: A SEER population-based study. *Scientific Reports*, *7*, 45411. https://doi.org/10.1038/srep45411

Gossen, M., & Bujard, H. (1992). Tight control of gene expression in mammalian cells by tetracycline-responsive promoters. *Proceedings of the National Academy of Sciences*, *89*(12), 5547–5551. https://doi.org/10.1073/pnas.89.12.5547

Han, G.-S., & Carman, G. M. (2010). Characterization of the human LPIN1-encoded phosphatidate phosphatase isoforms. *The Journal of Biological Chemistry*, *285*(19), 14628–14638. https://doi.org/10.1074/jbc.M110.117747

Hanahan, D., & Weinberg, R. A. (2011). Hallmarks of cancer: The next generation. *Cell*, *144*(5), 646–674. https://doi.org/10.1016/j.cell.2011.02.013

Harayama, T., & Riezman, H. (2018). Understanding the diversity of membrane lipid composition. *Nature Reviews Molecular Cell Biology*, *19*(5), 281–296. https://doi.org/10.1038/nrm.2017.138

Hauck, T., Kadam, S., Heinz, K., Garcia Peraza, M., Schmid, R., Kremer, A. E., Wolf, K., Bauer, A., Horch, R. E., Arkudas, A., & Kengelbach-Weigand, A. (2022). Influence of the autotaxin-lysophosphatidic acid axis on cellular function and cytokine expression in different breast cancer cell lines. *Scientific Reports*, *12*(1), Article 1. https://doi.org/10.1038/s41598-022-09565-3

Hennigs, A., Riedel, F., Gondos, A., Sinn, P., Schirmacher, P., Marmé, F., Jäger, D., Kauczor, H.-U., Stieber, A., Lindel, K., Debus, J., Golatta, M., Schütz, F., Sohn, C., Heil, J., & Schneeweiss, A. (2016). Prognosis of breast cancer molecular subtypes in routine clinical care: A large prospective cohort study. *BMC Cancer*, *16*, 734. https://doi.org/10.1186/s12885-016-

2766-3

Higa, G. M., & Abraham, J. (2007). Lapatinib in the treatment of breast cancer. *Expert Review of Anticancer Therapy*, *7*(9), 1183–1192. https://doi.org/10.1586/14737140.7.9.1183

Higuchi, R., Fockler, C., Dollinger, G., & Watson, R. (1993). Kinetic PCR Analysis: Real-time Monitoring of DNA Amplification Reactions. *Nature Biotechnology*, *11*(9), 1026–1030. https://doi.org/10.1038/nbt0993-1026

Hisano, Y., & Hla, T. (2019). Bioactive lysolipids in cancer and angiogenesis. *Pharmacology & Therapeutics*, *193*, 91–98. https://doi.org/10.1016/j.pharmthera.2018.07.006

Holen, I., Speirs, V., Morrissey, B., & Blyth, K. (2017). In vivo models in breast cancer research: Progress, challenges and future directions. *Disease Models & Mechanisms*, *10*(4), 359–371. https://doi.org/10.1242/dmm.028274

Holliday, D. L., & Speirs, V. (2011). Choosing the right cell line for breast cancer research. *Breast Cancer Research: BCR*, *13*(4), 215. https://doi.org/10.1186/bcr2889

Howlader, N., Cronin, K. A., Kurian, A. W., & Andridge, R. (2018). Differences in Breast Cancer Survival by Molecular Subtypes in the United States. *Cancer Epidemiology, Biomarkers & Prevention*, *27*(6), 619–626. https://doi.org/10.1158/1055-9965.EPI-17-0627

Ho-Yen, C., Bowen, R. L., & Jones, J. L. (2012). Characterization of basal-like breast cancer: An update. *Diagnostic Histopathology*, *18*(3), 104–111. https://doi.org/10.1016/j.mpdhp.2011.12.002

Huang, C., & Freter, C. (2015). Lipid Metabolism, Apoptosis and Cancer Therapy. *International Journal of Molecular Sciences*, *16*(1), 924–949. https://doi.org/10.3390/ijms16010924

Hungerford, J. E., Compton, M. T., Matter, M. L., Hoffstrom, B. G., & Otey, C. A. (1996). Inhibition of pp125FAK in cultured fibroblasts results in apoptosis. *Journal of Cell Biology*, *135*(5), 1383–1390. https://doi.org/10.1083/jcb.135.5.1383

Ilić, D., Almeida, E. A. C., Schlaepfer, D. D., Dazin, P., Aizawa, S., & Damsky, C. H. (1998). Extracellular Matrix Survival Signals Transduced by Focal Adhesion Kinase Suppress p53-mediated Apoptosis. *The Journal of Cell Biology*, *143*(2), 547–560.

Jin, L., Han, B., Siegel, E., Cui, Y., Giuliano, A., & Cui, X. (2018). Breast cancer lung metastasis: Molecular biology and therapeutic implications. *Cancer Biology & Therapy*, *19*(10), 858–868. https://doi.org/10.1080/15384047.2018.1456599

Kang, H. S., Lee, S. C., Park, Y. S., Jeon, Y. E., Lee, J. H., Jung, S.-Y., Park, I. H., Jang, S. H., Park, H. M., Yoo, C. W., Park, S. H., Han, S. Y., Kim, K. P., Kim, Y. H., Ro, J., & Kim, H. K. (2011). Protein and lipid MALDI profiles classify breast cancers according to the intrinsic subtype. *BMC Cancer*, *11*, 465. https://doi.org/10.1186/1471-2407-11-465

Katz-Brull, R., & Degani, H. (1996). Kinetics of choline transport and phosphorylation in human breast cancer cells; NMR application of the zero trans method. *Anticancer Research*, *16*(3B), 1375–1380.

Kennecke, H., Yerushalmi, R., Woods, R., Cheang, M. C. U., Voduc, D., Speers, C. H., Nielsen, T. O., & Gelmon, K. (2010). Metastatic behavior of breast cancer subtypes. *Journal of Clinical*

Oncology: Official Journal of the American Society of Clinical Oncology, *28*(20), 3271–3277. https://doi.org/10.1200/JCO.2009.25.9820

Kennedy, E. P., & Weiss, S. B. (1956). THE FUNCTION OF CYTIDINE COENZYMES IN THE BIOSYNTHESIS OF PHOSPHOLIPIDES. *Journal of Biological Chemistry*, *222*(1), 193–214. https://doi.org/10.1016/S0021-9258(19)50785-2

Knowlden, S., & Georas, S. N. (2014). The autotaxin-LPA axis emerges as a novel regulator of lymphocyte homing and inflammation. *Journal of Immunology (Baltimore, Md.: 1950)*, *192*(3), 851–857. https://doi.org/10.4049/jimmunol.1302831

Lao, C., Kuper-Hommel, M., Elwood, M., Campbell, I., Edwards, M., & Lawrenson, R. (2021). Characteristics and survival of de novo and recurrent metastatic breast cancer in New Zealand. *Breast Cancer (Tokyo, Japan)*, *28*(2), 387–397. https://doi.org/10.1007/s12282-020-01171-3

Law, S.-H., Chan, M.-L., Marathe, G. K., Parveen, F., Chen, C.-H., & Ke, L.-Y. (2019). An Updated Review of Lysophosphatidylcholine Metabolism in Human Diseases. *International Journal of Molecular Sciences*, *20*(5), E1149. https://doi.org/10.3390/ijms20051149

Leone, J. P., & Leone, B. A. (2015). Breast cancer brain metastases: The last frontier. *Experimental Hematology & Oncology*, *4*(1), 33. https://doi.org/10.1186/s40164-015-0028-8

Lesjak, M. S., Marchan, R., Stewart, J. D., Rempel, E., Rahnenführer, J., & Hengstler, J. G. (2014). EDI3 links choline metabolism to integrin expression, cell adhesion and spreading. *Cell Adhesion & Migration*, *8*(5), 499–508. https://doi.org/10.4161/cam.29284

Liang, Y., Zhang, H., Song, X., & Yang, Q. (2020). Metastatic heterogeneity of breast cancer: Molecular mechanism and potential therapeutic targets. *Seminars in Cancer Biology*, *60*, 14–27. https://doi.org/10.1016/j.semcancer.2019.08.012

Lifante, J., Shen, Y., Ximendes, E., Martín Rodríguez, E., & Ortgies, D. H. (2020). The role of tissue fluorescence in in vivo optical bioimaging. *Journal of Applied Physics*, *128*(17), 171101. https://doi.org/10.1063/5.0021854

Lin, N. U., Bellon, J. R., & Winer, E. P. (2004). CNS metastases in breast cancer. *Journal of Clinical Oncology: Official Journal of the American Society of Clinical Oncology*, *22*(17), 3608–3617. https://doi.org/10.1200/JCO.2004.01.175

Liu, S., Umezu-Goto, M., Murph, M., Lu, Y., Liu, W., Zhang, F., Yu, S., Stephens, L. C., Cui, X., Murrow, G., Coombes, K., Muller, W., Hung, M.-C., Perou, C. M., Lee, A. V., Fang, X., & Mills, G. B. (2009). Expression of Autotaxin and Lysophosphatidic Acid Receptors Increases Mammary Tumorigenesis, Invasion, and Metastases. *Cancer Cell*, *15*(6), 539–550. https://doi.org/10.1016/j.ccr.2009.03.027

Liu, Y., & Cao, X. (2016). Characteristics and Significance of the Pre-metastatic Niche. *Cancer Cell*, *30*(5), 668–681. https://doi.org/10.1016/j.ccell.2016.09.011

Livak, K. J., & Schmittgen, T. D. (2001). Analysis of Relative Gene Expression Data Using Real-Time Quantitative PCR and the 2−ΔΔCT Method. *Methods*, *25*(4), 402–408. https://doi.org/10.1006/meth.2001.1262

Loew, R., Heinz, N., Hampf, M., Bujard, H., & Gossen, M. (2010). Improved Tet-responsive promoters with minimized background expression. *BMC Biotechnology*, *10*(1), 81. https://doi.org/10.1186/1472-6750-10-81

Lopez-Albaitero, A., Xu, H., Guo, H., Wang, L., Wu, Z., Tran, H., Chandarlapaty, S., Scaltriti, M., Janjigian, Y., de Stanchina, E., & Cheung, N.-K. V. (2017). Overcoming resistance to HER2-targeted therapy with a novel HER2/CD3 bispecific antibody. *Oncoimmunology*, *6*(3), e1267891. https://doi.org/10.1080/2162402X.2016.1267891

Lu, Y., Lin, Y. Z., LaPushin, R., Cuevas, B., Fang, X., Yu, S. X., Davies, M. A., Khan, H., Furui, T., Mao, M., Zinner, R., Hung, M. C., Steck, P., Siminovitch, K., & Mills, G. B. (1999). The PTEN/MMAC1/TEP tumor suppressor gene decreases cell growth and induces apoptosis and anoikis in breast cancer cells. *Oncogene*, *18*(50), 7034–7045. https://doi.org/10.1038/sj.onc.1203183

Luck, A. A., Evans, A. J., Green, A. R., Rakha, E. A., Paish, C., & Ellis, I. O. (2008). The influence of basal phenotype on the metastatic pattern of breast cancer. *Clinical Oncology (Royal College of Radiologists (Great Britain))*, *20*(1), 40–45. https://doi.org/10.1016/j.clon.2007.10.002

MacDonald, J. I., & Sprecher, H. (1991). Phospholipid fatty acid remodeling in mammalian cells. *Biochimica Et Biophysica Acta*, *1084*(2), 105–121. https://doi.org/10.1016/0005-2760(91)90209-z

Marchan, R., Büttner, B., Lambert, J., Edlund, K., Glaeser, I., Blaszkewicz, M., Leonhardt, G., Marienhoff, L., Kaszta, D., Anft, M., Watzl, C., Madjar, K., Grinberg, M., Rempel, E., Hergenröder, R., Selinski, S., Rahnenführer, J., Lesjak, M. S., Stewart, J. D., … Hengstler, J. G. (2017). Glycerol-3-phosphate Acyltransferase 1 Promotes Tumor Cell Migration and Poor Survival in Ovarian Carcinoma. *Cancer Research*, *77*(17), 4589–4601. https://doi.org/10.1158/0008-5472.CAN-16-2065

Mason, J. A., Cockfield, J. A., Pape, D. J., Meissner, H., Sokolowski, M. T., White, T. C., Valentín López, J. C., Liu, J., Liu, X., Martínez-Reyes, I., Chandel, N. S., Locasale, J. W., & Schafer, Z. T. (2021). SGK1 signaling promotes glucose metabolism and survival in extracellular matrix detached cells. *Cell Reports*, *34*(11), 108821. https://doi.org/10.1016/j.celrep.2021.108821

McMaster, C. R. (2018). From yeast to humans—Roles of the Kennedy pathway for phosphatidylcholine synthesis. *FEBS Letters*, *592*(8), 1256–1272. https://doi.org/10.1002/1873-3468.12919

Meredith, J. E., Fazeli, B., & Schwartz, M. A. (1993). The extracellular matrix as a cell survival factor. *Molecular Biology of the Cell*, *4*(9), 953–961. https://doi.org/10.1091/mbc.4.9.953

Miksicek, R. J. (1993). In situ localization of the estrogen receptor in living cells with the fluorescent phytoestrogen coumestrol. *The Journal of Histochemistry and Cytochemistry: Official Journal of the Histochemistry Society*, *41*(6), 801–810. https://doi.org/10.1177/41.6.8315272

Mills, G. B., & Moolenaar, W. H. (2003). The emerging role of lysophosphatidic acid in cancer. *Nature Reviews. Cancer*, *3*(8), 582–591. https://doi.org/10.1038/nrc1143

Momoi, Y., Nishikimi, A., Du, G., Kataoka, T., & Katagiri, K. (2020). Phosphatidic acid regulates subcellular distribution of RA-GEFs critical for chemokine-dependent migration. *Biochemical and Biophysical Research Communications*, *524*(2), 325–331. https://doi.org/10.1016/j.bbrc.2020.01.080

Moolenaar, W. H., van Meeteren, L. A., & Giepmans, B. N. G. (2004). The ins and outs of lysophosphatidic acid signaling. *BioEssays: News and Reviews in Molecular, Cellular and Developmental Biology*, *26*(8), 870–881. https://doi.org/10.1002/bies.20081

Mori, N., Wildes, F., Takagi, T., Glunde, K., & Bhujwalla, Z. M. (2016). The Tumor Microenvironment Modulates Choline and Lipid Metabolism. *Frontiers in Oncology*, *6*. https://www.frontiersin.org/article/10.3389/fonc.2016.00262

Munshi, A., Hobbs, M., & Meyn, R. E. (2005). Clonogenic cell survival assay. *Methods in Molecular Medicine*, *110*, 21–28. https://doi.org/10.1385/1-59259-869-2:021

Murphy, R. C., & Folco, G. (2019). Lysophospholipid acyltransferases and leukotriene biosynthesis: Intersection of the Lands cycle and the arachidonate PI cycle[S]. *Journal of Lipid Research*, *60*(2), 219–226. https://doi.org/10.1194/jlr.S091371

Na, T.-Y., Schecterson, L., Mendonsa, A. M., & Gumbiner, B. M. (2020). The functional activity of E-cadherin controls tumor cell metastasis at multiple steps. *Proceedings of the National Academy of Sciences of the United States of America*, *117*(11), 5931–5937. https://doi.org/10.1073/pnas.1918167117

Nakamura, K., Takeuchi, T., Ohkawa, R., Okubo, S., Yokota, H., Tozuka, M., Aoki, J., Arai, H., Ikeda, H., Ohshima, N., Kitamura, T., & Yatomi, Y. (2007). Serum lysophospholipase D/autotaxin may be a new nutritional assessment marker: Study on prostate cancer patients. *Annals of Clinical Biochemistry*, *44*(Pt 6), 549–556. https://doi.org/10.1258/000456307782268147

Narayan, P., & Dahiya, R. (1991). Alterations in sphingomyelin and fatty acids in human benign prostatic hyperplasia and prostatic cancer. *Biomedica Biochimica Acta*, *50*(9), 1099–1108.

Navin, N. E., & Hicks, J. (2010). Tracing the tumor lineage. *Molecular Oncology*, *4*(3), 267–283. https://doi.org/10.1016/j.molonc.2010.04.010

Nguyen, D. X., Bos, P. D., & Massagué, J. (2009). Metastasis: From dissemination to organ-specific colonization. *Nature Reviews. Cancer*, *9*(4), 274–284. https://doi.org/10.1038/nrc2622

Noh, D. Y., Ahn, S. J., Lee, R. A., Park, I. A., Kim, J. H., Suh, P. G., Ryu, S. H., Lee, K. H., & Han, J. S. (2000). Overexpression of phospholipase D1 in human breast cancer tissues. *Cancer Letters*, *161*(2), 207–214. https://doi.org/10.1016/s0304-3835(00)00612-1

Ohshima, N., Kudo, T., Yamashita, Y., Mariggiò, S., Araki, M., Honda, A., Nagano, T., Isaji, C., Kato, N., Corda, D., Izumi, T., & Yanaka, N. (2015). New members of the mammalian glycerophosphodiester phosphodiesterase family: GDE4 and GDE7 produce lysophosphatidic acid by lysophospholipase D activity. *The Journal of Biological Chemistry*, *290*(7), 4260–4271. https://doi.org/10.1074/jbc.M114.614537

Okazaki, Y., Ohshima, N., Yoshizawa, I., Kamei, Y., Mariggiò, S., Okamoto, K., Maeda, M., Nogusa, Y., Fujioka, Y., Izumi, T., Ogawa, Y., Shiro, Y., Wada, M., Kato, N., Corda, D., & Yanaka, N. (2010). A novel glycerophosphodiester phosphodiesterase, GDE5, controls skeletal muscle development via a non-enzymatic mechanism. *The Journal of Biological Chemistry*, *285*(36), 27652–27663. https://doi.org/10.1074/jbc.M110.106708

Owen, D. M., Rentero, C., Magenau, A., Abu-Siniyeh, A., & Gaus, K. (2011). Quantitative imaging of membrane lipid order in cells and organisms. *Nature Protocols*, *7*(1), 24–35.

https://doi.org/10.1038/nprot.2011.419

Paddison, P. J., Caudy, A. A., Bernstein, E., Hannon, G. J., & Conklin, D. S. (2002). Short hairpin RNAs (shRNAs) induce sequence-specific silencing in mammalian cells. *Genes & Development*, *16*(8), 948–958. https://doi.org/10.1101/gad.981002

Pagès, C., Simon, M. F., Valet, P., & Saulnier-Blache, J. S. (2001). Lysophosphatidic acid synthesis and release. *Prostaglandins & Other Lipid Mediators*, *64*(1–4), 1–10. https://doi.org/10.1016/s0090-6980(01)00110-1

Paget, S. (1989). The distribution of secondary growths in cancer of the breast. *Cancer Metastasis Reviews*, *8*(2), 98–101.

Palorini, R., Votta, G., Pirola, Y., De Vitto, H., De Palma, S., Airoldi, C., Vasso, M., Ricciardiello, F., Lombardi, P. P., Cirulli, C., Rizzi, R., Nicotra, F., Hiller, K., Gelfi, C., Alberghina, L., & Chiaradonna, F. (2016). Protein Kinase A Activation Promotes Cancer Cell Resistance to Glucose Starvation and Anoikis. *PLoS Genetics*, *12*(3), e1005931. https://doi.org/10.1371/journal.pgen.1005931

Paoli, P., Giannoni, E., & Chiarugi, P. (2013). Anoikis molecular pathways and its role in cancer progression. *Biochimica et Biophysica Acta (BBA) - Molecular Cell Research*, *1833*(12), 3481–3498. https://doi.org/10.1016/j.bbamcr.2013.06.026

Park, M. K., Lee, C. H., & Lee, H. (2018). Mouse models of breast cancer in preclinical research. *Laboratory Animal Research*, *34*(4), 160–165. https://doi.org/10.5625/lar.2018.34.4.160

Parsons, S. L., Watson, S. A., & Steele, R. J. (1996). Malignant ascites. *The British Journal of Surgery*, *83*(1), 6–14. https://doi.org/10.1002/bjs.1800830104

Penry, J. T., & Manore, M. M. (2008). Choline: An important micronutrient for maximal endurance-exercise performance? *International Journal of Sport Nutrition and Exercise Metabolism*, *18*(2), 191–203. https://doi.org/10.1123/ijsnem.18.2.191

Pentheroudakis, G., Fountzilas, G., Bafaloukos, D., Koutsoukou, V., Pectasides, D., Skarlos, D., Samantas, E., Kalofonos, H. P., Gogas, H., & Pavlidis, N. (2006). Metastatic breast cancer with liver metastases: A registry analysis of clinicopathologic, management and outcome characteristics of 500 women. *Breast Cancer Research and Treatment*, *97*(3), 237–244. https://doi.org/10.1007/s10549-005-9117-4

Perou, C. M., Sørlie, T., Eisen, M. B., van de Rijn, M., Jeffrey, S. S., Rees, C. A., Pollack, J. R., Ross, D. T., Johnsen, H., Akslen, L. A., Fluge, O., Pergamenschikov, A., Williams, C., Zhu, S. X., Lønning, P. E., Børresen-Dale, A. L., Brown, P. O., & Botstein, D. (2000). Molecular portraits of human breast tumours. *Nature*, *406*(6797), 747–752. https://doi.org/10.1038/35021093

Perrotti, F., Rosa, C., Cicalini, I., Sacchetta, P., Del Boccio, P., Genovesi, D., & Pieragostino, D. (2016). Advances in Lipidomics for Cancer Biomarkers Discovery. *International Journal of Molecular Sciences*, *17*(12), E1992. https://doi.org/10.3390/ijms17121992

Puck, T. T., & Marcus, P. I. (1956). Action of x-rays on mammalian cells. *The Journal of Experimental Medicine*, *103*(5), 653–666. https://doi.org/10.1084/jem.103.5.653

Quigley, M. R., Fukui, O., Chew, B., Bhatia, S., & Karlovits, S. (2013). The shifting landscape

of metastatic breast cancer to the CNS. *Neurosurgical Review*, *36*(3), 377–382. https://doi.org/10.1007/s10143-012-0446-6

Ramírez de Molina, A., Rodríguez-González, A., Gutiérrez, R., Martínez-Piñeiro, L., Sánchez, J., Bonilla, F., Rosell, R., & Lacal, J. (2002). Overexpression of choline kinase is a frequent feature in human tumor-derived cell lines and in lung, prostate, and colorectal human cancers. *Biochemical and Biophysical Research Communications*, *296*(3), 580–583. https://doi.org/10.1016/s0006-291x(02)00920-8

Reginato, M. J., Mills, K. R., Paulus, J. K., Lynch, D. K., Sgroi, D. C., Debnath, J., Muthuswamy, S. K., & Brugge, J. S. (2003). Integrins and EGFR coordinately regulate the pro-apoptotic protein Bim to prevent anoikis. *Nature Cell Biology*, *5*(8), 733–740. https://doi.org/10.1038/ncb1026

Rettig, G. R., McAnuff, M., Liu, D., Kim, J.-S., & Rice, K. G. (2006). Quantitative bioluminescence imaging of transgene expression in vivo. *Analytical Biochemistry*, *355*(1), 90–94. https://doi.org/10.1016/j.ab.2006.04.026

Rexer, B. N., & Arteaga, C. L. (2012). Intrinsic and acquired resistance to HER2-targeted therapies in HER2 gene-amplified breast cancer: Mechanisms and clinical implications. *Critical Reviews in Oncogenesis*, *17*(1), 1–16. https://doi.org/10.1615/critrevoncog.v17.i1.20

Robert Koch Institut. (2020). *Cancer in Germany in 2015/2016* [Report]. Robert Koch-Institut. https://doi.org/10.25646/6825

Runyon, B. A., Hoefs, J. C., & Morgan, T. R. (1988). Ascitic fluid analysis in malignancy-related ascites. *Hepatology*, *8*(5), 1104–1109. https://doi.org/10.1002/hep.1840080521

Rygaard, J., & Povlsen, C. O. (1969). Heterotransplantation of a human malignant tumour to "Nude" mice. *Acta Pathologica Et Microbiologica Scandinavica*, *77*(4), 758–760. https://doi.org/10.1111/j.1699-0463.1969.tb04520.x

Salic, A., & Mitchison, T. J. (2008). A chemical method for fast and sensitive detection of DNA synthesis *in vivo*. *Proceedings of the National Academy of Sciences*, *105*(7), 2415–2420. https://doi.org/10.1073/pnas.0712168105

Schmid, R., Wolf, K., Robering, J. W., Strauß, S., Strissel, P. L., Strick, R., Rübner, M., Fasching, P. A., Horch, R. E., Kremer, A. E., Boos, A. M., & Weigand, A. (2018). ADSCs and adipocytes are the main producers in the autotaxin-lysophosphatidic acid axis of breast cancer and healthy mammary tissue in vitro. *BMC Cancer*, *18*(1), 1273. https://doi.org/10.1186/s12885-018-5166-z

Schulze, A., & Harris, A. L. (2012). How cancer metabolism is tuned for proliferation and vulnerable to disruption. *Nature*, *491*(7424), 364–373. https://doi.org/10.1038/nature11706

Sears, D., & Hajdu, S. I. (1987). The cytologic diagnosis of malignant neoplasms in pleural and peritoneal effusions. *Acta Cytologica*, *31*(2), 85–97.

Shapiro, A. L., Vinuela, E., & Maizel, J. V. (1967). Molecular weight estimation of polypeptide chains by electrophoresis in SDS-polyacrylamide gels. *Biochemical and Biophysical Research Communications*, *28*(5), 815–820. https://doi.org/10.1016/0006-291X(67)90391-9

Shultz, L. D., Ishikawa, F., & Greiner, D. L. (2007). Humanized mice in translational biomedical research. *Nature Reviews. Immunology*, *7*(2), 118–130.

https://doi.org/10.1038/nri2017

Shultz, L. D., Lyons, B. L., Burzenski, L. M., Gott, B., Chen, X., Chaleff, S., Kotb, M., Gillies, S. D., King, M., Mangada, J., Greiner, D. L., & Handgretinger, R. (2005). Human lymphoid and myeloid cell development in NOD/LtSz-scid IL2R gamma null mice engrafted with mobilized human hemopoietic stem cells. *Journal of Immunology (Baltimore, Md.: 1950)*, *174*(10), 6477–6489. https://doi.org/10.4049/jimmunol.174.10.6477

Shultz, L. D., Schweitzer, P. A., Christianson, S. W., Gott, B., Schweitzer, I. B., Tennent, B., McKenna, S., Mobraaten, L., Rajan, T. V., & Greiner, D. L. (1995). Multiple defects in innate and adaptive immunologic function in NOD/LtSz-scid mice. *Journal of Immunology (Baltimore, Md.: 1950)*, *154*(1), 180–191.

Sim, H., Bibee, K., Wickline, S. A., & Sept, D. (2011). Pharmacokinetic Modeling of Tumor Bioluminescence Implicates Efflux, and Not Influx, as the Bigger Hurdle in Cancer Drug Therapy. *Cancer Research*, *71*(3), 686–692. https://doi.org/10.1158/0008-5472.CAN-10-2666

Simons, K., & Toomre, D. (2000). Lipid rafts and signal transduction. *Nature Reviews Molecular Cell Biology*, *1*(1), Article 1. https://doi.org/10.1038/35036052

Sims, A. H., Ong, K. R., Clarke, R. B., & Howell, A. (2006). High-throughput genomic technology in research and clinical management of breast cancer. Exploiting the potential of gene expression profiling: Is it ready for the clinic? *Breast Cancer Research: BCR*, *8*(5), 214. https://doi.org/10.1186/bcr1605

Skibinski, A., & Kuperwasser, C. (2015). The origin of breast tumor heterogeneity. *Oncogene*, *34*(42), 5309–5316. https://doi.org/10.1038/onc.2014.475

Smid, M., Wang, Y., Zhang, Y., Sieuwerts, A. M., Yu, J., Klijn, J. G. M., Foekens, J. A., & Martens, J. W. M. (2008). Subtypes of breast cancer show preferential site of relapse. *Cancer Research*, *68*(9), 3108–3114. https://doi.org/10.1158/0008-5472.CAN-07-5644

Smith, P. K., Krohn, R. I., Hermanson, G. T., Mallia, A. K., Gartner, F. H., Provenzano, M. D., Fujimoto, E. K., Goeke, N. M., Olson, B. J., & Klenk, D. C. (1985). Measurement of protein using bicinchoninic acid. *Analytical Biochemistry*, *150*(1), 76–85. https://doi.org/10.1016/0003-2697(85)90442-7

Son, K., Fujioka, S., Iida, T., Furukawa, K., Fujita, T., Yamada, H., Chiao, P. J., & Yanaga, K. (2009). Doxycycline induces apoptosis in PANC-1 pancreatic cancer cells. *Anticancer Research*, *29*(10), 3995–4003.

Sonkar, K., Ayyappan, V., Tressler, C. M., Adelaja, O., Cai, R., Cheng, M., & Glunde, K. (2019). Focus on the glycerophosphocholine pathway in choline phospholipid metabolism of cancer. *NMR in Biomedicine*, *32*(10), e4112. https://doi.org/10.1002/nbm.4112

Sørlie, T., Tibshirani, R., Parker, J., Hastie, T., Marron, J. S., Nobel, A., Deng, S., Johnsen, H., Pesich, R., Geisler, S., Demeter, J., Perou, C. M., Lønning, P. E., Brown, P. O., Børresen-Dale, A.-L., & Botstein, D. (2003). Repeated observation of breast tumor subtypes in independent gene expression data sets. *Proceedings of the National Academy of Sciences of the United States of America*, *100*(14), 8418–8423. https://doi.org/10.1073/pnas.0932692100

Soule, H. D., Vazguez, J., Long, A., Albert, S., & Brennan, M. (1973). A human cell line from a pleural effusion derived from a breast carcinoma. *Journal of the National Cancer Institute*,

51(5), 1409–1416. https://doi.org/10.1093/jnci/51.5.1409

Stack, S., & Fishman, D. (2012). *Ovarian Cancer: Second Edition*. Springer.

Stewart, J. D., Marchan, R., Lesjak, M. S., Lambert, J., Hergenroeder, R., Ellis, J. K., Lau, C.-H., Keun, H. C., Schmitz, G., Schiller, J., Eibisch, M., Hedberg, C., Waldmann, H., Lausch, E., Tanner, B., Sehouli, J., Sagemueller, J., Staude, H., Steiner, E., & Hengstler, J. G. (2012). Choline-releasing glycerophosphodiesterase EDI3 drives tumor cell migration and metastasis. *Proceedings of the National Academy of Sciences*, *109*(21), 8155–8160. https://doi.org/10.1073/pnas.1117654109

Sulaiman, S., Arafat, K., Iratni, R., & Attoub, S. (2019). PTC-209 Anti-Cancer Effects Involved the Inhibition of STAT3 Phosphorylation. *Frontiers in Pharmacology*, *10*, 1199. https://doi.org/10.3389/fphar.2019.01199

Tai, W., Mahato, R., & Cheng, K. (2010). The role of HER2 in cancer therapy and targeted drug delivery. *Journal of Controlled Release: Official Journal of the Controlled Release Society*, *146*(3), 264–275. https://doi.org/10.1016/j.jconrel.2010.04.009

Tham, Y.-L., Sexton, K., Kramer, R., Hilsenbeck, S., & Elledge, R. (2006). Primary breast cancer phenotypes associated with propensity for central nervous system metastases. *Cancer*, *107*(4), 696–704. https://doi.org/10.1002/cncr.22041

Thiery, J. P., Acloque, H., Huang, R. Y. J., & Nieto, M. A. (2009). Epithelial-mesenchymal transitions in development and disease. *Cell*, *139*(5), 871–890. https://doi.org/10.1016/j.cell.2009.11.007

Traiffort, E., O'Regan, S., & Ruat, M. (2013). The choline transporter-like family SLC44: Properties and roles in human diseases. *Molecular Aspects of Medicine*, *34*(2), 646–654. https://doi.org/10.1016/j.mam.2012.10.011

Turban, S., & Hajduch, E. (2011). Protein kinase C isoforms: Mediators of reactive lipid metabolites in the development of insulin resistance. *FEBS Letters*, *585*(2), 269–274. https://doi.org/10.1016/j.febslet.2010.12.022

Tuthill, M., Pell, R., Guiliani, R., Lim, A., Gudi, M., Contractor, K. B., Lewis, J. S., Coombes, R. C., & Stebbing, J. (2009). Peritoneal disease in breast cancer: A specific entity with an extremely poor prognosis. *European Journal of Cancer (Oxford, England: 1990)*, *45*(12), 2146–2149. https://doi.org/10.1016/j.ejca.2009.04.027

Vallejos, C. S., Gómez, H. L., Cruz, W. R., Pinto, J. A., Dyer, R. R., Velarde, R., Suazo, J. F., Neciosup, S. P., León, M., de la Cruz, M. A., & Vigil, C. E. (2010). Breast cancer classification according to immunohistochemistry markers: Subtypes and association with clinicopathologic variables in a peruvian hospital database. *Clinical Breast Cancer*, *10*(4), 294–300. https://doi.org/10.3816/CBC.2010.n.038

van der Veen, J. N., Kennelly, J. P., Wan, S., Vance, J. E., Vance, D. E., & Jacobs, R. L. (2017). The critical role of phosphatidylcholine and phosphatidylethanolamine metabolism in health and disease. *Biochimica et Biophysica Acta (BBA) - Biomembranes*, *1859*(9, Part B), 1558–1572. https://doi.org/10.1016/j.bbamem.2017.04.006

van Weverwijk, A., Koundouros, N., Iravani, M., Ashenden, M., Gao, Q., Poulogiannis, G., Jungwirth, U., & Isacke, C. M. (2019). Metabolic adaptability in metastatic breast cancer by

AKR1B10-dependent balancing of glycolysis and fatty acid oxidation. *Nature Communications*, *10*(1), 2698. https://doi.org/10.1038/s41467-019-10592-4

Vance, J. E. (2015). Phospholipid Synthesis and Transport in Mammalian Cells. *Traffic*, *16*(1), 1–18. https://doi.org/10.1111/tra.12230

Waddington, K. E., Pineda-Torra, I., & Jury, E. C. (2019). Analyzing T-Cell Plasma Membrane Lipids by Flow Cytometry. In M. C. Gage & I. Pineda-Torra (Eds.), *Lipid-Activated Nuclear Receptors* (Vol. 1951, pp. 209–216). Springer New York. https://doi.org/10.1007/978-1-4939-9130-3_16

Wang, B., Rong, X., Palladino, E. N. D., Wang, J., Fogelman, A. M., Martín, M. G., Alrefai, W. A., Ford, D. A., & Tontonoz, P. (2018). Phospholipid Remodeling and Cholesterol Availability Regulate Intestinal Stemness and Tumorigenesis. *Cell Stem Cell*, *22*(2), 206-220.e4. https://doi.org/10.1016/j.stem.2017.12.017

Whelan, K. A., Schwab, L. P., Karakashev, S. V., Franchetti, L., Johannes, G. J., Seagroves, T. N., & Reginato, M. J. (2013). The Oncogene HER2/neu (ERBB2) Requires the Hypoxia-inducible Factor HIF-1 for Mammary Tumor Growth and Anoikis Resistance. *The Journal of Biological Chemistry*, *288*(22), 15865–15877. https://doi.org/10.1074/jbc.M112.426999

Wood, R., & Harlow, R. D. (1969). Structural analyses of rat liver phosphoglycerides. *Archives of Biochemistry and Biophysics*, *135*(1), 272–281. https://doi.org/10.1016/0003-9861(69)90540-2

Wu, Q., Li, J., Zhu, S., Wu, J., Chen, C., Liu, Q., Wei, W., Zhang, Y., & Sun, S. (2017). Breast cancer subtypes predict the preferential site of distant metastases: A SEER based study. *Oncotarget*, *8*(17), 27990–27996. https://doi.org/10.18632/oncotarget.15856

Xiong, Z., Deng, G., Huang, X., Li, X., Xie, X., Wang, J., Shuang, Z., & Wang, X. (2018). Bone metastasis pattern in initial metastatic breast cancer: A population-based study. *Cancer Management and Research*, *10*, 287–295. https://doi.org/10.2147/CMAR.S155524

Yamashita, A., Sugiura, T., & Waku, K. (1997). Acyltransferases and transacylases involved in fatty acid remodeling of phospholipids and metabolism of bioactive lipids in mammalian cells. *Journal of Biochemistry*, *122*(1), 1–16. https://doi.org/10.1093/oxfordjournals.jbchem.a021715

Yanaka, N. (2007). Mammalian glycerophosphodiester phosphodiesterases. *Bioscience, Biotechnology, and Biochemistry*, *71*(8), 1811–1818. https://doi.org/10.1271/bbb.70062

Yang, C.-Y., & Frohman, M. A. (2012). Mitochondria: Signaling with phosphatidic acid. *The International Journal of Biochemistry & Cell Biology*, *44*(8), 1346–1350. https://doi.org/10.1016/j.biocel.2012.05.006

Yang, L., He, Z., Yao, J., Tan, R., Zhu, Y., Li, Z., Guo, Q., & Wei, L. (2018). Regulation of AMPK-related glycolipid metabolism imbalances redox homeostasis and inhibits anchorage independent growth in human breast cancer cells. *Redox Biology*, *17*, 180–191. https://doi.org/10.1016/j.redox.2018.04.016

Yeeravalli, R., & Das, A. (2021). Molecular mediators of breast cancer metastasis. *Hematology/Oncology and Stem Cell Therapy*, *14*(4), 275–289. https://doi.org/10.1016/j.hemonc.2021.02.002

Yu, C., Wang, H., Muscarella, A., Goldstein, A., Zeng, H.-C., Bae, Y., Lee, B. H. I., & Zhang, X. H.-F. (2016). Intra-iliac Artery Injection for Efficient and Selective Modeling of Microscopic Bone Metastasis. *Journal of Visualized Experiments: JoVE*, *115*. https://doi.org/10.3791/53982

Yung, Y. C., Stoddard, N. C., & Chun, J. (2014). LPA receptor signaling: Pharmacology, physiology, and pathophysiology. *Journal of Lipid Research*, *55*(7), 1192–1214. https://doi.org/10.1194/jlr.R046458

Zhang, C., Lowery, F. J., & Yu, D. (2017). Intracarotid Cancer Cell Injection to Produce Mouse Models of Brain Metastasis. *Journal of Visualized Experiments: JoVE*, *120*. https://doi.org/10.3791/55085

Zhang, Y., & Du, G. (2009). Phosphatidic acid signaling regulation of Ras superfamily of small guanosine triphosphatases. *Biochimica Et Biophysica Acta*, *1791*(9), 850–855. https://doi.org/10.1016/j.bbalip.2009.05.013

Zhang, Y., Pullambhatla, M., Laterra, J., & Pomper, M. G. (2012). Influence of Bioluminescence Imaging Dynamics by D-Luciferin Uptake and Efflux Mechanisms. *Molecular Imaging*, *11*(6), 499.

Zhang, Y., Zhang, G.-L., Sun, X., Cao, K.-X., Ma, C., Nan, N., Yang, G.-W., Yu, M.-W., & Wang, X.-M. (2018). Establishment of a murine breast tumor model by subcutaneous or orthotopic implantation. *Oncology Letters*, *15*(5), 6233–6240. https://doi.org/10.3892/ol.2018.8113

Zhang, Z., Burnley, P., Coder, B., & Su, D.-M. (2012). Insights on FoxN1 biological significance and usages of the "nude" mouse in studies of T-lymphopoiesis. *International Journal of Biological Sciences*, *8*(8), 1156–1167. https://doi.org/10.7150/ijbs.5033

Zhou, X., Vink, M., Klaver, B., Berkhout, B., & Das, A. T. (2006). Optimization of the Tet-On system for regulated gene expression through viral evolution. *Gene Therapy*, *13*(19), 1382–1390. https://doi.org/10.1038/sj.gt.3302780

Zhukovsky, M. A., Filograna, A., Luini, A., Corda, D., & Valente, C. (2019). The Structure and Function of Acylglycerophosphate Acyltransferase 4/ Lysophosphatidic Acid Acyltransferase Delta (AGPAT4/LPAATδ). *Frontiers in Cell and Developmental Biology*, *7*. https://www.frontiersin.org/article/10.3389/fcell.2019.00147

6 Appendix

6.1 Abbreviations

%	Percent
°C	Degrees Celsius
Adj	Adjusted
ADP	adenosine diphosphate
APS	Ammonium persulfate
ATP	Adenosine triphosphate
ATX	Autotaxin
BCA	Bicinchoninic acid
BSA	Bovine serum albumin
$CaCl_2$	Calcium chloride
CCD	Charge-coupled device
CCT	CTP:phosphocholine cytidylyltransferase
cDNA	Complementary DNA
CDP	Cytidine diphosphate
CDP-DAG	Cytidine diphosphate diacylglycerol
CDS	CDP-DAG synthase
CDX	Cell line-derived xenograft
CHKA	Choline Kinase Alpha
CHT1	High-affinity choline transporter
CHKB	Choline Kinase Beta
CK	Choline kinase
CMP	Cytidine monophosphate
CPT	CDP-choline:DAG cholinephosphotransferase
Ct	Cycle threshold
CTC	Circulating tumor cell
CTL	Choline transporter-like
CTP	Cytidine triphosphate
d/h/min/sec	days/hours/minutes/seconds
Da	Dalton
DAG	Diacylglycerol
DAGAT	Diacylglycerol acyltransferase

DAGK	Diacylglycerol kinase
DEPC	Diethyl pyrocarbonate
DHAP	Dihydroxyacetone phosphate
DMEM	Dulbecco's modified Eagles' medium
DNA/RNA	Deoxyribonucleic acid/Ribonucleic acid
Dox	Doxycycline
ECL	Enhanced chemiluminescent solution
ECM	Extracellular matrix
EDI3	Endometrial Differential 3
EDTA	Ethylenediaminetetraacetic acid
EdU	5-ethynyl-2′-deoxyuridine
e.g.	For example
EMT	Epithelial-to-mesenchymal transition
ER	Estrogen receptor
et al.	And others
FAK	Focal adhesion kinase
FCS	Fetal calf serum
FM	Full media
G3P	Glycerol-3-phosphate
G3PDH	G3P dehydrogenase
G418	Geneticin disulfate
g/mg/µg	gram/milligram/microgram
GDE2	Glycerophosphodiester Phosphodiesterase 2
GDE5	Glycerophosphodiester Phosphodiesterase 5
GDE-PDE	Glycerophosphodiesterase phosphodiesterase
GDPD6	Glycerophosphodiester phosphodiesterase 6
GPAM	Glycerol-3-phosphate acyltransferase
GPC	Glycerophosphocholine
GPCAT	Glycerophosphocholine acyltransferase
GPCPD1	Glycerophosphocholine Phosphodiesterase 1
GPCR	G protein-coupled receptors
GOI	Gene of interest
HCl	Hydrochloric acid
Her2	Human epidermal growth factor receptor 2

HKG	Housekeeping gene
HRMAS	High resolution magic angle spinning
HRP	Horseradish peroxidase
HMDB	Human Metabolome Database
i.e.	That is
IfADo	Leibniz-Institut für Arbeitsforschung an der TU Dortmund
IHC	Immunohistochemistry
ILK	Integrin-linked kinase
i.p.	Intraperitoneal
i.v.	Intravenous
KH_2PO_4	Potassium dihydrogen phosphate
l/ml/µl	Liter/milliliter/microliter
LC-MS/MS	Liquid chromatography-mass spectrometry/mass spectrometry
LPA	Lysophosphatidic acid
LPAAT	Lysophosphatidic acid acyltransferase
LPAR	Lysophosphatidic acid receptor
LPC	Lysophosphatidylcholine
LPCAT	Lysophosphatidylcholine acyltransferase
LPE	Lysophosphatidylethanolamine
LPEAT	Lysophosphatidylethanolamine acyltransferase
LPG	Lysophosphatidylglycerol
LPGAT	Lysophosphatidylglycerol acytransferase
LPI	Lysophosphatidylinositol
LPIAT	Lysophosphatidylinositol acyltransferase
LPLAT	Lysophospholipid acyltransferases
LPS	Lysophosphatidylserine
LPSAT	Lysophosphatidylserine acyltransferase
LSM	Laser scanning microscope
Luc	Luciferase
M/mM/µM/nM	Molar/millimolar/micromolar/nanomolar
MALDI	Matrix-assisted laser desorption/ionization
MEM	Minimum Essential Medium
MET	Mesenchymal-epithelial transition
$MgSO_4$	Magnesium sulphate

MOI	Multiplicity of infection
mRNA	Messenger RNA
MRS	Magnetic resonance spectroscopy
MSI	Mass spectrometry imaging
MTBE	Methyl-tert-butyl-ester
n	Number of biological replicates
Na_2HPO_4	Sodium hydrogen phosphate
NaCl	Sodium chloride
nm	Nanometer
NMR	Nuclear magnetic resonance
NP-40	Nonidet P-40 substitute
NSG	NOD SCID gamma
OCT	Organic cation transporter
ON	Over night
PA	Phosphatidic acid
PAGE	Polyacrylamide gel electrophoresis
PAP	Phosphatidate phosphatase
PBS	Phosphate buffered saline
PCho	Phosphocholine
PDE	Phosphodiesterase
PE	Phosphatidylethanolamine
PEMT	Phosphatidylethanolamine N-methyltransferase
PET	Positron emission tomography
PFA	Paraformaldehyde
PG	Phosphatidylglycerol
PGP	Phosphatidylglycerol phosphate
PGPP	Phosphatidylglycerol phosphate phosphatase
PGPS	Phosphatidylglycerol phosphate synthase
PI	Phosphatidylinositol
PIS	Phosphatidylinositol synthase
PLA	Phospholipase A
PLB	Phospholipase B
PLC	Phospholipase C
PLD	Phospholipase D

PLPP	Phospholipid phosphatase
Poly-HEMA	Poly(2-hydroxyethyl methacrylate)
Ppi	Pyrophosphate
PR	Progesterone receptor
PS	Phosphatidylserine
PSD	Phosphatidylserine decarboxylase
PtdCho	Phosphatidylcholine
PTK2	Protein tyrosine kinase 2
PVDF	Polyvinylidene fluoride
qRT-PCR	Quantitative real-time polymerase chain reaction
RFU	Relative fluorescence units
RFP	Red fluorescence protein
RIPA	Radioimmunoprecipitation assay
RNAseq	RNA-sequencing
RNAi	RNA interference
Rpm	Rounds per minute
RT	Room temperature
s.c.	subcutaneous
SDS	Sodium dodecyl sulphate
shRNA	Short hairpin RNA
SIMPLEX	simultaneous metabolite, protein, lipid extraction
SM	Sphingomyelin
TAG	Triacylglycerol
TBS-T	Tris-buffered saline
tCho	Total choline
TEMED	Tetramethylethylenediamine
tRFP	TurboRFP
Tris	Tris(hydroxymethyl)aminomethane
TSP	Sodium trimethylsilyl propionate
vs.	Versus
v/v; w/v	Volume per volume, weight per volume
WAT	White adipose tissue
x g	Standard gravity

6.2 List of figures

Figure 1.1: Breast cancer subtypes and their prognostic outcome. 1

Figure 1.2: PtdCho *de novo* biosynthesis via the Kennedy pathway. 3

Figure 1.3: Glycerophospholipid structure. 5

Figure 1.4: Schematic illustration showing the metabolism of glycerophospholipids. 7

Figure 1.5: Reaction mechanism catalyzed by the glycerophosphodiesterase EDI3. 9

Figure 1.6: A role for EDI3 as a key enzyme linking different metabolic pathways. 11

Figure 1.7: Schematic illustration of the multiple steps required for metastasis formation. 13

Figure 1.8: Schematic illustration of CDX-models established in this thesis. 15

Figure 1.9: Non-invasive imaging of luciferase-expressing cells in mice. 18

Figure 2.1: Elements of the SMARTvector inducible lentiviral shRNA vector. 34

Figure 3.1: Cell lines stably-transfected with luciferase produce luminescence signal. 53

Figure 3.2: Screening of luciferase-expressing single cell clones reveals most promising clones. 54

Figure 3.3: Tumors formed by luciferase-expressing cancer cell lines can be detected by *in vivo* luminescence imaging. 55

Figure 3.4: Luminescence signal remains stable in HCC1954_Luc cells in the absence of G418. 56

Figure 3.5: Lentiviral transduction of HCC1954_Luc cells with GAPDH-targeting shRNA results in Dox-inducible downregulation of *GAPDH* and increased expression of tRFP. 58

Figure 3.6: Screening of transduced HCC1954_Luc cells revealed efficient Dox-induced downregulation of *EDI3* and increased expression of tRFP with three different EDI3-targeting shRNA oligos. 60

Figure 3.7: Dox-induction of EDI3 knockdown in HCC1954_Luc cells results in a time and dose dependent reduction in EDI3 protein expression and an increase in tRFP. 61

Figure 3.8: Dox-induction of EDI3 knockdown in HCC1954_Luc cells results in a dose-dependent reduction in EDI3 expression on RNA and protein level. 62

Figure 3.9: *EDI3* RNA expression in HCC1954_Luc cells is restored within two days after Dox removal. 63

Figure 3.10: Dox-induced EDI3 knockdown in HCC1954_Luc alters intracellular GPC/PC ratio in a dose dependent manner. 65

Figure 3.11: Inducibly silencing EDI3 in HCC1954_Luc cells alters intracellular glycerophospholipid levels. 66

Figure 3.12: Colony formation assay reveals significant reduction in colony number only in Dox-pretreated cells. 68

Figure 3.13: Dox-induced EDI3 knockdown in HCC1954_Luc reduces colony number and size. 69

Figure 3.14: Dox-induced EDI3 knockdown in HCC1954_Luc reduces cell adhesion compared to Dox-treated control. 71

Figure 3.15: Induced EDI3 knockdown leads to a reduction in cell number per colony over time. 72

Figure 3.16: Induced EDI3 knockdown leads to a reduced number of proliferating cells in colonies..... 73

Figure 3.17: Induced EDI3 knockdown in HCC1954_Luc results in reduced proliferation in a subconfluent cell layer. 74

Figure 3.18: Inducible EDI3 knockdown in HCC1954_Luc reduces cell viability in adherent cells..... 75

Figure 3.19: Inducible EDI3 knockdown decreases viability in HCC1954_Luc cells in suspension. 76

Figure 3.20: Inducibly silencing EDI3 in HCC1954_Luc has no effect on wound closure. ... 78

Figure 3.21: HCC1954_Luc cells form subcutaneous tumors in CD1 nude and NSG mice. .. 80

Figure 3.22: EDI3 knockdown does not decrease growth of subcutaneous tumors. 81

Figure 3.23: *PLB* mRNA expression is significantly reduced upon EDI3 knockdown in subcutaneous tumors. 82

Figure 3.24: Silencing EDI3 has no effect on early attached cells in a mouse model for lung metastasis. 84

Figure 3.25: Growth of i.p. injected HCC1954 cells does not differ between CD1 nude and NSG mice. 85

Figure 3.26: Silencing EDI3 in HCC1954 results in reduced luminescence signal after i.p. injection into mice. 87

Figure 3.27: Induced EDI3 knockdown is associated with higher probability of survival in a peritoneal metastasis model. 88

Figure 3.28: Metastatic organotropism observed in CD1 nude mice after i.p. injection of HCC1954 cells. 89

Figure 3.29: *In vivo* imaging confirms reduced luminescence upon EDI3 knockdown in the i.p. metastasis model for timed organ collection. 91

Figure 3.30: *Ex vivo* imaging of organs reveals metastatic organotropism and reduced metastatic burden in CD1 nude mice injected with EDI3 knockdown cells.. 92

Figure 3.31: Tumor weight and prevalence indicate reduced metastatic burden after EDI3 knockdown induction in HCC1954_Luc. 94

Figure 3.32: Dox-induced EDI3 knockdown in HCC1954_Luc results in reduced ascites in CD1 nude mice eight weeks after i.p. injection. 96

Figure 4.1: Hypothesis for the changes in glycerophospholipid metabolism observed upon EDI3 knockdown induction. 100

6.3 List of tables

Table 2.1: Equipment 21
Table 2.2: Consumables 23
Table 2.3: Chemicals 24
Table 2.4: Commercial buffers, solutions and media 25
Table 2.5: Prepared buffers and solution for gel electrophoresis and western blot 26
Table 2.6: Prepared buffers and solutions for cell assays 27
Table 2.7 Commercial assays and kits 28
Table 2.8: Commercially available cell lines 28
Table 2.9: Cell line generated as part of this thesis 29
Table 2.10: Cell culture medium and additives 29
Table 2.11: Lentiviral vectors 30
Table 2.12: Plasmids 30
Table 2.13: Mice 30
Table 2.14: Mouse feed 31
Table 2.15: Primary antibodies 31
Table 2.16: Secondary antibodies 31
Table 2.17: Concentrations of selection antibiotics tested 33
Table 2.18: Lipofectamine 3000 transfection conditions 34
Table 2.19: Induction conditions for shRNA mediated inhibition of EDI3 expression 36
Table 2.20: Experimental conditions for proliferation assay 40
Table 2.21: Conditions for reverse transcription polymerase chain reaction 46
Table 2.22: Parameters for QuantiFast SYBR® Green assays 46
Table 2.23: Gel preparation for SDS-PAGE 48
Table 2.24: Parameters for antibody incubation (western blotting) 50
Table 2.25: Transition data for measurement of choline-related metabolites 51
Table 2.26: Transition data for measurement of lipids 52

6.4 Publications

6.4.1 Articles

Keller, M.*, Rohlf, K.*, Glotzbach, A.*, Leonhardt, G., Schäfers, S., Derksen, K., AlWahsh, M., Lambert, J., Lindskog, C., Schmidt, M., Brenner, W., Baumann, M., Zent, E., Zischinsky, M., Hellwig, B., Rahnenführer, J., Overbeck, N., Reinders, J., Cadenas, C., Hengstler, J. G., Edlund, K., Marchan, R. (2022). **Inhibiting the glycerophosphodiesterase EDI3 reduces viability and growth of ER-HER2+ breast cancer cells resistant to HER2-targeting therapy.** *In revision.*

Cadenas, C., Vosbeck, S., Edlund, K., Grgas, K., Madjar, K., Hellwig, B., Adawy, A., Glotzbach, A., Stewart, J. D., Lesjak, M. S., Franckenstein, D., Claus, M., Hayen, H., Schriewer, A., Gianmoena, K., Thaler, S., Schmidt, M., Micke, P., Pontén, F., Mardinoglu, A., … Hengstler, J. G. (2019). **LIPG-promoted lipid storage mediates adaptation to oxidative stress in breast cancer.** *International journal of cancer*, *145*(4), 901–915.

Bukhari, H.*, Glotzbach, A.*, Kolbe, K.*, Leonhardt, G., Loosse, C., & Müller, T. (2017). **Small things matter: Implications of APP intracellular domain AICD nuclear signaling in the progression and pathogenesis of Alzheimer's disease.** *Progress in neurobiology*, *156*, 189–213.

Kolbe, K., Bukhari, H., Loosse, C., Leonhardt, G., Glotzbach, A., Pawlas, M., Hess, K., Theiss, C., & Müller, T. (2016). **Extensive nuclear sphere generation in the human Alzheimer's brain.** *Neurobiology of aging*, *48*, 103–113.

* Authors contributed equally to this work

6.4.2 Contribution on congresses

Poster: **Investigating a role for EDI3 in choline metabolism in breast cancer.** Annika Glotzbach, Magdalena Zak, Karolina Edlund, Jörg Reinders, Jörg Lambert, Jan G. Hengstler, Rosemarie Marchan. EACR conference: Mechanisms to Therapies: Innovations in Cancer Metabolism. October 2018 in Bilbao, Spain.

Poster: **Investigating a role for EDI3 in breast cancer using a doxycycline inducible system.** A. Glotzbach, S. Schäfers, M. Zak-Keller, J. Reinders, J.G. Hengstler, R. Marchan. EACR congress: Innovative Cancer Science. June 2021, virtual.

Poster: **Investigating a role for EDI3 in breast cancer metastasis using a doxycycline inducible system.** A. Glotzbach, S. Schäfers, N. Overbeck, J. Reinders, J.G. Hengstler, R. Marchan. EACR conference: Seed and Soil: *In Vivo* Models of Metastasis. January 2022, virtual.

6.5 Eidesstattliche Versicherung (Affidavit)

Name, Vorname
(Surname, first name)

Matrikel-Nr.
(Enrolment number)

Belehrung:

Wer vorsätzlich gegen eine die Täuschung über Prüfungsleistungen betreffende Regelung einer Hochschulprüfungsordnung verstößt, handelt ordnungswidrig. Die Ordnungswidrigkeit kann mit einer Geldbuße von bis zu 50.000,00 € geahndet werden. Zuständige Verwaltungsbehörde für die Verfolgung und Ahndung von Ordnungswidrigkeiten ist der Kanzler/die Kanzlerin der Technischen Universität Dortmund. Im Falle eines mehrfachen oder sonstigen schwerwiegenden Täuschungsversuches kann der Prüfling zudem exmatrikuliert werden, § 63 Abs. 5 Hochschulgesetz NRW.

Die Abgabe einer falschen Versicherung an Eides statt ist strafbar.

Wer vorsätzlich eine falsche Versicherung an Eides statt abgibt, kann mit einer Freiheitsstrafe bis zu drei Jahren oder mit Geldstrafe bestraft werden, § 156 StGB. Die fahrlässige Abgabe einer falschen Versicherung an Eides statt kann mit einer Freiheitsstrafe bis zu einem Jahr oder Geldstrafe bestraft werden, § 161 StGB.

Die oben stehende Belehrung habe ich zur Kenntnis genommen:

Official notification:

Any person who intentionally breaches any regulation of university examination regulations relating to deception in examination performance is acting improperly. This offence can be punished with a fine of up to EUR 50,000.00. The competent administrative authority for the pursuit and prosecution of offences of this type is the chancellor of the TU Dortmund University. In the case of multiple or other serious attempts at deception, the candidate can also be unenrolled, Section 63, paragraph 5 of the Universities Act of North Rhine-Westphalia.

The submission of a false affidavit is punishable.

Any person who intentionally submits a false affidavit can be punished with a prison sentence of up to three years or a fine, Section 156 of the Criminal Code. The negligent submission of a false affidavit can be punished with a prison sentence of up to one year or a fine, Section 161 of the Criminal Code.

I have taken note of the above official notification.

Ort, Datum
(Place, date)

Unterschrift
(Signature)

Titel der Dissertation:
(Title of the thesis):

Ich versichere hiermit an Eides statt, dass ich die vorliegende Dissertation mit dem Titel selbstständig und ohne unzulässige fremde Hilfe angefertigt habe. Ich habe keine anderen als die angegebenen Quellen und Hilfsmittel benutzt sowie wörtliche und sinngemäße Zitate kenntlich gemacht.
Die Arbeit hat in gegenwärtiger oder in einer anderen Fassung weder der TU Dortmund noch einer anderen Hochschule im Zusammenhang mit einer staatlichen oder akademischen Prüfung vorgelegen.

I hereby swear that I have completed the present dissertation independently and without inadmissible external support. I have not used any sources or tools other than those indicated and have identified literal and analogous quotations.

The thesis in its current version or another version has not been presented to the TU Dortmund University or another university in connection with a state or academic examination.*

*Please be aware that solely the German version of the affidavit ("Eidesstattliche Versicherung") for the PhD thesis is the official and legally binding version.

Ort, Datum
(Place, date)

Unterschrift
(Signature)

6.6 Acknowledgement

Completing this PhD thesis was challenging, and I am deeply thankful for the support of numerous people who encouraged me during the whole time.

First of all, I would like to thank Prof. Dr. Jan G. Hengstler for giving me the opportunity to work in his laboratory, for his continuous support and guidance, and for sharing his time for many helpful discussions.

I am deepest grateful to Dr. Rosemarie Marchan for her guidance and for always being there as a supervisor. Thanks to your positive energy you kept me motivated even when EDI3 frequently gave us more questions than answers. Thank you so much for all your helpful ideas and your advice.

I want to thank the team from the Analytical Chemistry Unit at IfADo, in particular, Dr. Jörg Reinders, Dr. Nina Overbeck, Michael Porta and Beate Aust for analyzing hundreds of samples. Moreover, I also want to thank Dr. Maren Claus, Dr. Doris Urlaub and Sabine Wingert from the Immunology Department at IfADo.

Many thanks to my colleagues from the Toxicology Department at IfADo for the lovely working environment and for supporting me in some way or other. My special thanks go to the members of the CellTox working group, Dr. Gregor Leonhardt, Anastasia Oprisko, Katharina Rohlf, Dr. Özlem Demirci, Lisa Marienhoff, Magdalena Keller, Simon Lüke and Katharina Derksen, for all the good times we had together and for the mutual help in the lab, particularly to Simon for his tremendous help with the animal experiments. I thank Katharina Grgas for introducing me to several cell assays and for always being there when I needed her expertise. I also thank Dr. Cristina Cadenas and Dr. Karolina Edlund for their ideas and suggestions. Thank you, Dr. Adelina Jashari, for being a great friend and for all the fun we had.

Mein größter Dank gilt meiner Familie, insbesondere meinen Eltern Andreas und Christiane und meiner Schwester Kristin. Danke, dass ihr immer für mich da seid und mich während dieser Arbeit stets unterstützt und ermutigt habt. Moreover, my deepest gratitude goes to Aniel for his support and encouragement. Merci d'être toi!